UNIVERSITY OF
BIRMINGHAM

Wind Turbine Monitoring Using Short-Range Doppler Radar

by

Manuel Crespo

A thesis submitted to the University of Birmingham for the degree of DOCTOR OF PHILOSOPHY

School of Electronic, Electrical
and Computer Engineering
University of Birmingham
September 2016

Abstract

This thesis summarises the research done on the feasibility of detecting and automatically classifying wind turbine faults using a short-range radar. Two main areas are included in the thesis: the theoretical and experimental analysis of wind turbine blade radar signatures in the near-field and the classification of wind turbine structural faults using machine learning algorithms. In the former, a new theoretical framework has been developed which extends the current far-field models and includes a mathematical and experimental analysis of simple flat blades as well as complex curved blades. The latter area comprises the analysis of the experimental results obtained using faulty wind turbine blades and methods of classifying these faults. This last task has been done in time and frequency domains using, respectively, the signals *Statistical Parameters* and the *Principal Component Analysis* algorithm for features extraction. The classification has been performed employing the *k-Nearest Neighbours* algorithm. Finally, an *Artificial Neural Network* has been used as a more powerful classification tool in both domains.

Acknowledgement

Firstly, I would like to express my sincere gratitude to my supervisors Dr Mike Antoniou and Prof Mike Cherniakov for their continuous support of my PhD study, for their patience, motivation, and knowledge. Their supervision helped me throughout my research and writing of this thesis.

Secondly, I would like to thank my colleagues for their help and for all the fun we have had in the last three years.

I would like to extend my sincerest gratitude to all those who supported me in any respect during this period of my life: Donya, Carmen, Felipe… Thank you.

Last but not the least, a special thanks to my family, my parents and brothers, for their love and support throughout my life. And now, I need to thank them in Spanish…

Gracias a mis padres y mis hermanos por el apoyo que, expresado de diversas formas, me han dado durante toda mi vida.

CONTENTS

Chapter 1 Introduction and Background

Chapter 2 Scattering Centres Model of a Wind Turbine

Chapter 3 Wind Turbine Radar Signature in the Near-Field: Theoretical Model of Curved Blades

Chapter 4 Wind Turbine Radar Signature in the Near-Field: Experimental Confirmation

Chapter 5 Automatic Classification of Wind Turbine Structural Faults

Chapter 6 Conclusions and Future Work

Appendix

List of Figures

List of Tables

Abbreviations

ANN	**Artificial Neural Network**
CEM	**Computational Electromagnetic**
COE	**Cost Of Energy**
CW	**Continuous Wave**
EM	**Electromagnetic**
FFT	**Fast Fourier Transform**
FM	**Frequency Modulation**
FMCW	**Frequency-Modulated Continuous Wave**
FT	**Fourier Transform**
GNSS	**Global Navigation Satellite System**
IF	**Intermediate Frequency-domain**
IQ	**In-phase Quadrature**
k-NN	**k-Nearest-Neighbours**
MISL	**Microwave Integrated Systems Laboratory**
MoM	**Method of Moments**
O&M	**Operation & Maintenance**
PCA	**Principal Component Analysis**
PSD	**Power Spectral Density**
RCS	**Radar Cross Section**
RF	**Radio Frequency**
SCM	**Scattering Centres Model**
SEE	**Spectral Emitted Energy**
SNR	**Signal-to-Noise Ratio**
SPM	**Statistical Parameters Method**
STFT	**Short-Time Fourier Transform**
WT	**Wind Turbine**
WTC	**Wind Turbine Clutter**

List of symbols

$s(t)$	Transmitted radar signal.
$s_r(t)$	Received radar signal.
R_B	Bistatic distance.
f_c	Carried frequency.
ω_c	Carried angular frequency.
λ	Radar signal wavelength.
k	Radar signal wavenumber.
$\theta(t)$	Phase modulation.
φ	Initial phase.
$R(t)$	Range.
c	Speed of light in vacuum.
B	Signal bandwidth.
τ	Pulse width time.
P_r	Received power of the signal at antenna terminals.
P_t	Transmitted power of the signal at antenna terminals.
G	Gain of the antenna
σ	Radar cross-section, RCS.
F	Pattern propagation factor.
$STFT$	Short Time Fourier Transform.
$w(t' - t)$	Window function in the STFT.
ρ_{mn}	Reflectivity of a point-scatterer.
$r_{mn}(t)$	Radial distance from the radar to a scattering point.
Ω	Rotational speed of wind turbine blades.
L_{nm}, l_n	Distance from the wind turbine centre of rotation and a scattering point.
R_N	Radial distance between the radar and the wind turbine nacelle or centre of rotation.
Z_N	Hub height respect to the radar level.
J_p	Bessel functions of the first kind.
$\delta(\cdot)$	Dirac delta function.
$\vec{J}_S$	Surface current density.
$\vec{A}(\vec{x}, t)$	Vector potential in the Lorentz gauge.
μ_0	Permeability of free space.
ε_0	Permittivity of free space.
$\vec{G}(\vec{r}(t), \vec{x}')$	Green function.
$h_l^{(1)}$	Spherical Henkel functions.
j_l	Spherical Bessel functions.
Y_{lm}	Spherical harmonics.
ρ	Surface charge distribution.
$\vec{p}$	Electrostatic electric dipole.
$\vec{E}$	Electric field.
$\vec{B}$	Magnetic field.

Chapter 1 Introduction and Background

1.1 Radar Overview

1.1.1 History background

The term *radar* is an acronym of ***ra****dio* ***d****etection* ***a****nd* ***r****anging.* A radar is an example of those devices that constitute one of the most spectacular accomplishment of the physicist [1]: the scientist creates a situation where all the relevant coordinates are known so that the behaviour of the device can be predicted completely. This fact explains the success of the radar systems in a wide range of applications. In 1865, J. C. Maxwell was the first scientist in theorising about the possibility that an electromagnetic field like light could propagate in form of waves. A few decades later, in 1886, H. R. Hertz discovered the electromagnetic (EM) waves predicted by Maxwell's equations. The work of Maxwell and Hertz stimulated the development of technology to transmit and detect these EM waves. It was in 1904 when the German engineer Christian Hülsmeyer invented the *telemobiloscope* which supposed the first practical usage of radar technology. An overview of the beginning of this technology can be found in reference [2].

Radar technology continued developing nearly simultaneously in different countries, but it was during World War II when investigations in radar accelerated. One of the major innovations was the invention of the *cavity magnetron*. This device made centimeter-band radar practical for the Allies, giving them the capacity of detecting smaller targets from smaller antennas. The first high-power version of the cavity magnetron, the *multicavity-magnetron,* was invented at The University of Birmingham. A summary of the history of the invention of this device and the importance of the work done at the University of Birmingham can be found in [3]-[4].

Radar technology has continued evolving and it is no longer used for military purposes exclusively. The entire society has obtained benefit from radar systems whose applications include: prevention of collision between ships or vessels with land targets using marine radars [5]-[6]; radar astronomy [7]; air traffic control [8]-[9]; medical diagnosis [10]-[11]; automotive radars [12]; etc. Due to the demonstrated utility and versatility of this technology, the radar research community is active and productive and continues working on new and challenging problems.

1.1.2 Radar principles

The basic principles on radar have been widely introduced in scientific literature [13]-[15]. Essentially, a radar is a system that radiates EM waves in the range of radio frequency (RF) and receives the EM energy reflected from any target in the region of interest. The RF spectrum extends approximately from $0.003\ GHz$ to $300\ GHz$ according to the IEEE standard [16].

The exact details of radar design can be found in [17] and [18], but its fundamental elements are sketched in the block diagram of Fig. 1.1. The *transmitter* produces a *signal* $s(t)$ at its output terminals that is transformed to an EM wave with the same time dependence. This EM wave is radiated by the *transmitting antenna* and propagates through space until it undertakes a change in its nature due to the presence of a *target*. This is an object in the radar region that reflects (scatters) part of the transmitted wave's energy back to the *receiving antenna* as a new EM wave. This antenna transforms the received wave into an electric signal $s_r(t)$ of the same time dependence as the scattered wave. This signal can be analysed in several ways to extract information about the target.

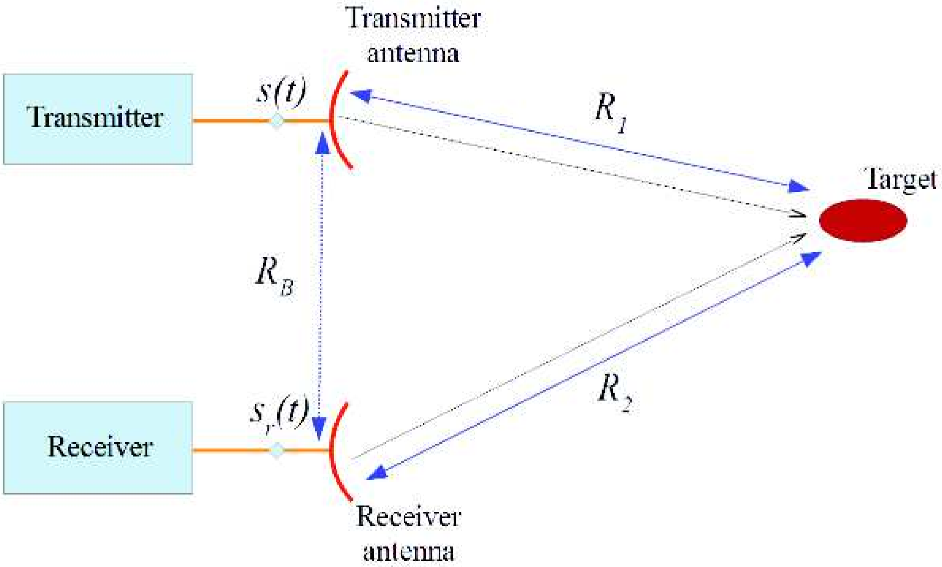

Fig. 1.1: General block diagram of a radar.

In the general situation described in Fig. 1.1, the distance between the transmitter and the receiver is the called *bistatic distance* R_B. If $R_B = 0$, the transmitting and receiving antennas are placed at approximately the same location: *monostatic configuration*. If $R_B \neq 0$ the antennas are located at different places and it is said the system is in a *bistatic configuration*.

The transmitter can be a high-power device that emits EM waves in the order of kW or MW. The receiver instead is a power sensitive system that can detect EM waves in the order of mW or nW. Due to this asymmetry in the power levels between the transmitter and receiver, radar performance can be seriously affected if the receiver is not isolated from the transmitted high-power EM waves. More details about the bistatic configuration and applications can be found in [19] and [20]. Most modern radars are monostatic and it will be the system configuration used during this research.

According to their transmitted signal $s(t)$, radars can be classified in:

- *Continuous wave (CW) radars*: The transmitted wave is continuous over time and its amplitude is, in general, constant. The signal can be frequency modulated (FM) or has a constant frequency. The radar used in this research is a CW radar with constant frequency content.
- *Pulsed radars*: The waveform is transmitted as pulses. The frequency content of the signal can be constant or FM. This kind of radars will not be treated in this dissertation.

Reference [14] defines the general form of the transmitted signal as

$$s(t) = a(t) \cdot \cos[\omega_c t + \theta(t) + \varphi_0] \tag{1.1}$$

The term $a(t)$ is called the *amplitude modulation*. The carrier frequency of the radar is $f_c = \omega_c / 2\pi$ and $\theta(t)$ is the phase modulation. φ_0 represents any arbitrary initial phase.

Although the radar acronym contains the words detection and range, this device can extract knowledge about the target apart from informing of its presence and distance. When the transmitted wave is reflected by the target, its motion modifies the amplitude and phase of the waveform (1.1). The analysis of this “modified” signal can provide information about the target such as range, radial velocity, size, etc. Information about range and frequency content of the received signal will be the topics of the following sections. The phase time-variation of the received signal will be the most important of the two for this research.

1.1.2.1 *Range measurement*

The range R is defined as the distance between radar and target. In the case of a monostatic pulsed radar, the range can be determined by measuring the time difference, ΔT, between the transmission and reception of a pulse. Since EM waves propagate at universal and constant velocity c, the relation between ΔT and R is also constant. Based on this principle, the range must equal

$$R = c\Delta T/2 \tag{1.2}$$

where the factor 2 accounts for the round trip of a pulse. Pulse radars can measure the range of *stationary* and *moving* targets.

CW radars without frequency modulation cannot measure the range of stationary and slow-moving targets. The only way to determine the range of these targets is by using frequency-modulated continuous wave radars, FMCW. Range measurement with CW radar has been broadly used as in aircraft radar altimeters and surveying equipment [21].

An important aspect in range measurement is the *range resolution*. It is defined as the ability of a radar system to distinguish between two targets that are in the same direction but at different ranges. Generally, in pulse radars, two targets can be resolved in range if their separation is greater than the distance corresponding to a pulse width: $R = cB/2$. Here, B is the signal bandwidth defined as $B = 1/\tau$ where τ is the pulse width time. In the case of FM-CW, the range resolution depends on the width of the main lobe of the autocorrelation function of the transmitted signal.

Obviously, the range that a certain radar can achieve for detection is limited. In that sense, expression (1.2) does not set any theoretical *maximum range*. In order to obtain an expression for such range limit, it is necessary to introduce the radar equation [21]:

$$\frac{P_r}{P_t} = G^2\sigma\lambda^2F^4/(4\pi)^3R^4 \tag{1.3}$$

Equation (1.3) describes the monostatic case and the factors in it are:

- P_r corresponds to the received power of the signal at antenna terminals.
- P_t is the transmitted signal power at antenna terminal.
- G is defined as the gain of the antenna.
- σ is the target radar cross section (RCS).
- λ is the radar signal wavelength.
- F corresponds to the called pattern propagation factor.
- R is the range.

Equation (1.3) simply stands that the ratio between the transmitted and received power is inversely proportional to the fourth power of the range. A maximum range equation can be obtained by rewriting this equation and substituting P_r by $P_{r,min}$, the minimum received power detectable by the radar. Consequently,

$$R_{max} = \sqrt[4]{\frac{\sigma\lambda^2 P_t G^2 F^2}{(4\pi)^3 P_{r,min}}}$$

(1.4)

This last equation can be improved by expressing $P_{r,min}$ in terms of the power-to-noise ratio:

$$P_{r,min} = \left(\frac{S}{N}\right)_{min} kT_S B_n$$

(1.5)

where k is the Boltzmann constant, T_S is the receiving-system noise temperature and B_n is the noise bandwidth of the receiver predetection filter [21].

So far, it has been assumed that the transmitted and received EM waves propagate under ideal conditions and without disturbances. In practice, however, the propagation will be affected by a series of loss factors. This factors reduce the strength of the received power and they are also multiplicative, so they can be included in the denominator of equation (1.4) as L.

$$R_{max} = \sqrt[4]{\frac{\sigma\lambda^2 P_t G^2 F^2}{(4\pi)^3 \left(\frac{S}{N}\right)_{min} k T_S B_n L}}$$

(1.6)

Among the factors in equation (1.6), the RCS σ deserves a description because of its importance in radar research.

The portion of the target that is illuminated by the transmitted EM wave disperses the incident energy in all directions: the target scatters this energy. If this energy is scattered back to the source of waves, the process is called *backscattering* and it constitutes the radar echo of the target. The intensity of the object echo is described by its RCS whose formal definition is given by

$$\sigma = \lim_{R\to\infty} 4\pi R^2 \frac{|E_s|^2}{|E_0|^2}$$

(1.7)

where the E_0 is the strength of the incident electric field at the target and E_s is the strength of the scattered electric field at the radar.

The RCS of any object depends on its shape and material, the radar frequency and polarisation, and the radar viewing angle.

The RCS of simple bodies can be obtained exactly by solving the differential wave equation derived from Maxwell's equations, assuming that the electric and magnetic fields need to satisfy certain conditions at the target surface (interface between the interior and exterior target regions). This method has no application to real targets, so it is only used as a guideline for other approximate methods of computing RCS's of more realistic targets.

An alternative is to solve the integral form of the wave equations. This approach corresponds to the called *method of moments* (*MoM*). It basically reduces the integral wave equations to a system of linear homogeneous equations. The relation between the incident and scattered fields have to be specified at the target surface, which will depend on the target material. After defining these boundary conditions, the target surface is divided into a set of small patches. These patches need to be small enough to consider that the currents and charges induced on each patch by the incident field are constant or can be described by simple functions. A weighting function can be assigned to each patch and the problem is computationally solved when the amplitude and phase of these functions are defined. However, although this method is applicable to targets of any shape and not only simple ones, the computer memory and processing time grow with target size. This increment in the computational resources supposes a restriction in the type of targets whose RCS can be computed. In fact, the method is efficient for targets whose dimensions are no larger than several wavelengths, but this will depend on the computational power available.

Alternatives to the MoM to calculate RCS's of realistic targets include physical and geometrical optics, the physical and geometrical theories of diffraction, and the method of equivalent currents. These methods can provide accurate RCS predictions for large targets.

The last way of computing real targets is by directly measuring the scattered fields of such objects. This can be done using the actual target of interest or scaled models.

1.1.2.2 *Doppler frequency shift*

The range of a moving target changes over time, $R = R(t)$, and this motion produces a variation in the frequency of the scattered wave. In the case of a CW radar, the transmitted wave is, based on equation (1.1),

$$s(t) = a \cdot \cos(2\pi f_c t) \tag{1.8}$$

which means that the radar is transmitting without modulation. The phase of the reflected signal at a given time t will be the phase of the transmitted wave at a previous time $t - t_d(t)$where $t_d(t)$ is the time delay, defined as the time that the wavefront takes to reach the target and return to the antenna. In the monostatic case, the time delay is given by

$$t_d\,(t) = 2R(t)/c \tag{1.9}$$

Therefore, the waveform of the reflected signal is given by the transmitted wave (1.8) evaluated at $t - t_d(t)$:

$$s_r(t) = s(t - t_d(t)) = \rho \cdot a \cdot \cos[2\pi f_c(t - t_d(t))] = \rho \cdot a \cdot \cos\left[2\pi f_c\left(t - \frac{2R(t)}{c}\right)\right]$$

(1.10)

where ρ accounts for the change in the amplitude after the transmitted wave is scattered by the target. If only the phase in (1.10) is taken into account, the scattered wave can be rewritten as

$$s_r(t) \propto \cos\left[2\pi f_c t - 2\pi f_c \frac{2R(t)}{c}\right] = \cos\left[2\pi f_c t - \frac{4\pi R(t)}{\lambda}\right] = \cos[2\pi f_c t - \theta(t)]$$

(1.11)

whence $\theta(t) \equiv -\frac{4\pi R(t)}{\lambda}$ is the phase change between the transmitted and received signals due to the target motion. The rate of change of $\theta(t)$is the Doppler frequency, so by taking the time derivative it can be obtained

$$f_d(t) = \frac{1}{2\pi}\frac{d}{dt}\theta(t) = \frac{-2}{\lambda}\frac{dR(t)}{dt} = \frac{-2V(t)}{\lambda} = \frac{-2V(t)}{c} f_c$$

(1.12)

where $V(t)$ is the radial velocity of the target.

The phase change in (1.11) carries the information about the target motion and it can be extracted by a quadrature detector [22]. A diagram of a quadrature detector or IQ demodulator is shown in Fig. 1.2. The received signal $s_r(t)$ is split into two frequency mixers. In the case of a CW radar, the received signal is mixed with the transmitted signal in the I channel. In the Q channel, the transmitted signal is shifted $\frac{\pi}{2} rad$ and mixed with the received signal.

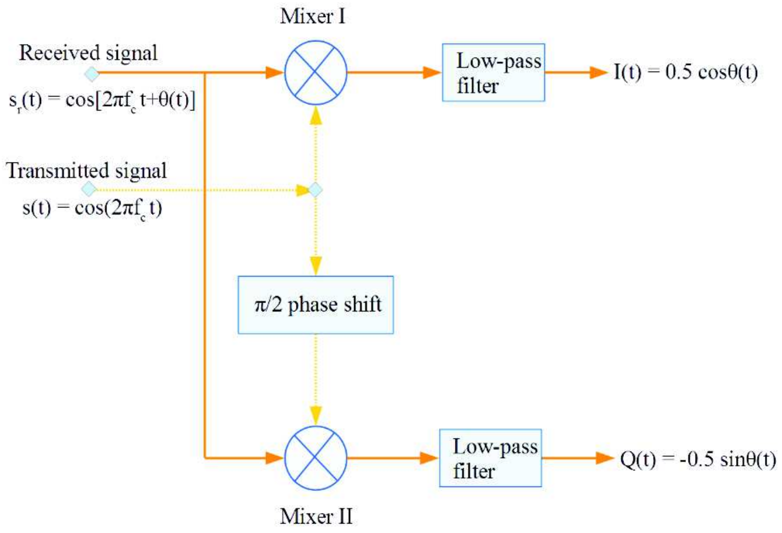

Fig. 1.2: Block diagram of an IQ demodulator or quadrature detector

If the amplitude of the signals is ignored, the result at the output of Mixer I is the product of the received signal (1.11) and the transmitted one (1.8):

$$s_r(t) \cdot s(t) = \cos[2\pi f_c t + \theta(t)] \cdot \cos 2\pi f_c t = \frac{1}{2}\cos\theta(t) + \frac{1}{2}\cos[4\pi f_c t + \theta(t)] \tag{1.13}$$

After the mixing, a low-pass filter is applied. The output of the I channel is thus

$$I(t) = \frac{1}{2}\cos\theta(t)$$

(1.14)

On the other hand, the output at the Mixer II is

$$s_r(t) \cdot s^{\frac{\pi}{2}}(t) = \cos[2\pi f_c t + \theta(t)] \cdot \sin 2\pi f_c t = \frac{1}{2}\sin[4\pi f_c t + \theta(t)] - \frac{1}{2}\sin\theta(t)$$

(1.15)

After low-pass filtering, the output at the Q channel is

$$Q(t) = -\frac{1}{2}\sin\theta(t)$$

(1.16)

Combining I and Q channels, the result is a complex Doppler signal:

$$s_r^{IQ}(t) = I(t) + jQ(t) = \frac{1}{2}e^{-j\theta(t)} = \frac{1}{2}e^{j\frac{4\pi R(t)}{\lambda}}$$

(1.17)

Therefore, the high-frequency component of the transmitted signal has been removed, but the Doppler component is conserved.

The movement of the target may be complicated and not only translational. A rotating target that may be or not moving away from the radar will exhibit a complex Doppler frequency shift $f_d(t)$. This periodical rotation motion will generate side bands Doppler frequency shifts around the centre of the Doppler shifted carrier frequency. These additional Doppler shifts corresponds to the micro-Doppler effect which will be the topic of the next subsection.

1.1.2.3 *Micro-Doppler effect*

The micro-Doppler effect was firstly introduced in LADAR (***la**ser **d**etection **a**nd **r**anging*) systems. A LADAR transmits EM wave in the range of optical wavelengths towards a target and receives the backscattered light to extract information about the object of interest. In the case of vibrating targets, a very small vibration amplitude can produce large phase changes in high-frequency systems. Therefore, Doppler frequency shifts due to very low vibration rates can be easily detected.

It is important to clarify the term “micro” in the context of micro-Doppler signatures in radars. The term “micro motion” includes a wider range of motions of the target or any of its structural components. For example, in addition to the target bulk motion, any oscillatory motion can be called micro-motion [22]-[23]. The source of micro-motion may be a rotating propeller of a fixed-wing aircraft, the rotating rotor blades of a helicopter, the rotating blades of a wind turbine, a rotating antenna, the flapping wings of birds, a walking person with swinging arms and legs, or other causes [24]-[25]. The frequency modulation induced by micro motions can provide information about the kinematic properties of the target.

In case of rotating targets such as rotor blades, the micro-Doppler effect can be observable at even low-frequency bands due to the length of the blades and velocity of their tips. In contrast, if the oscillation rate and displacement of the motion of a target is not high enough, the micro-Doppler effect may not be observable. In this research, the micro-Doppler effect due to blades rotation will be considered.

The micro-Doppler shift is a time-varying frequency shift like in equation (1.11) and it can be extracted by using a quadrature detector as in the case of Doppler processing. In order to analyse the micro-Doppler features, the Fourier transform is not an adequate tool since it cannot provide time-dependent frequency information. In order to describe a signal simultaneously in the time and frequency domains, the instantaneous frequency analysis [26] and the joint time-frequency analysis (first proposed by Gabor in [27]) are the most common methods. In this research, the joint time-frequency analysis will be the technique used, which has been employed for decades to analyse time-varying frequency features of signals.

1.1.3 Representation of Radar Signals

Reference [28] provides a remarkable summary of the three manners in which a radar signal can be represented. The author provides examples of real life signals to illustrate the differences between the domains. The radar signal scattered by the target can be represented in different domains: time, frequency and joint time-frequency.

1.1.3.1 *Time-domain representation*

The time-domain representation is the natural way of writing a signal. Expressions (1.3) and (1.5) are examples of this time representation. However, the time-domain has limitations, as it can be seen in the following example of a sinusoidal FM signal [28]:

$$s(t) = A \cdot \cos\left(2\pi f_c t + \frac{f_d}{f_m} \sin[2\pi f_m t + \varphi] + \psi\right) \tag{1.18}$$

The amplitude of the signal is A and ψ is an arbitrary initial phase; f_d is the peak frequency deviation; f_m corresponds to the modulating frequency; f_c is the carrier frequency and φ allows for the phase of the modulating signal.

Equation (1.18) does not clearly show how the frequency varies with time. The time representation of the signal (1.18) would show a sinusoidal curve changing over time, but it would not be possible to extract the FM law from the graph itself. Therefore, the time-domain representation obscures the information about the frequency since both variables t and f are treated as mutually exclusive. In order to obtain a representation in one domain, for example time, the frequency is eliminated by integration (Fourier transform) and vice versa. The information contained in both domains is complete, but the manner in which the signal is represented can provide access to certain aspects of that information.

1.1.3.2 *Frequency-domain representation*

The Doppler shift of the returned signal is usually obtained by performing the Fourier transform of the signal $s(t)$. This leads to its representation in the frequency-domain, $S(f)$:

$$S(f) = \int_{-\infty}^{\infty} dt\, s(t) e^{-j2\pi f t}$$

(1.19)

As it was already mentioned, the Fourier transform $S(t)$ is a complete representation of the signal. In fact, the original signal in the time-domain can be recovered by performing the Inverse Fourier transform. However, as it occurred in the time-domain representation, $S(t)$ may not be convenient for all purposes.

Expression (1.18) can be expanded into an infinite series, so the signal will be formed by an infinite series of spectral lines in the frequency-domain. The significant spectral lines lie between $f_c \pm (f_d + 2f_m)$ [28]-[29]. This information is useful in radio, TV transmission and other forms of communication such as mobile phones since it allows to design a tuning filter. However, this information is not appropriate to design a modulator or a demodulator.

1.1.3.3 *Joint time-frequency representation*

Instead of the time and frequency domains, the joint time-frequency transforms can be used to fully characterise the time-varying frequency content of the signal. The best-known of these transformations is the Short Time Fourier Transform (STFT) which consists in dividing the time-domain signal into various segments and take the Fourier transform of each of them [28], [30]. Its definition is

$$STFT(t,f) = \int dt' s(t')\, w(t'-t) e^{-j2\pi f t'} \tag{1.20}$$

where $w(\cdots)$ is the called window function. Therefore, the STFT is basically a moving Fourier transform along the signal. The squared magnitude of equation (1.20) is called a spectrogram [22]:

$$Spectrogram(t,f) = |STFT(t,f)|^2 \tag{1.21}$$

A spectrogram is a tool that provides visual information on the time-varying frequency content at different instants of the time-varying signal. This standard representation in the $(t,f) - space$ facilitates the display of different EM mechanism present in a physical system.

1.2 Wind Turbines and Radar Systems

Wind power has been growing since the last 20 years. It has become an alternative energy source; in the UK, it represents the 20% of the total renewable energy produced in 2014 [31]. The use of wind energy is increasing at a rate of 20% every year and it is now an important source of energy in Europe, Asia and United States [32]. The goal in the UK is to install *11,000* wind turbines (WT) until 2020 (there are *6,546* in 2015) to reach the objective of obtain the 20%-25% of the total power from wind farms [33]. Therefore, in recent years, WTs have rapidly increased in number.

In order to increase the energy obtained from a WT, its size has also been increasing since a longer blade results in an increment of the swept area which is proportional to the power output.

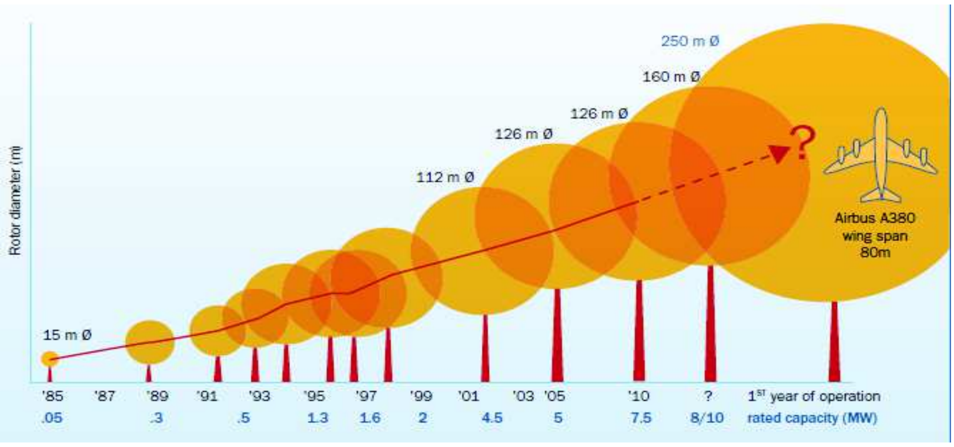

Fig. 1.3: Growth in the size of WT since 1985 [34].

For all these reasons, the interaction between radar and WTs has drawn the increased attention of researchers in recent years and it has supposed a new challenge in the radar community. These structures introduce strong radar clutter which affects the operation of radars in surveillance, air and maritime traffic control, weather monitoring, etc. [35]-[44]; these radars may be located several *km* from a wind farm site.

The radar research community has dedicated substantial efforts in understanding and mitigating WT radar returns. Some examples of this work has focused on the prediction and reduction of WT radar cross-section (RCS). The authors in [45] has presented a new model exclusively designed to model the RCS and Doppler signature of WTs faster than the current commercial computational electromagnetic (CEM) tools. Other examples of the research done on this topic can be found in [46]-[47].

Other authors have concentrated in the suppression of WT radar returns through signal processing. Examples of such work are [48]-[51], among others. In particular, reference [48] is an example of the work done on weather radar interference. WT returns can contaminate the weather radar data and affect forecasts and warnings for severe weather. WTs generate return signals with non-zero Doppler velocity due to the rotation of their blades. Therefore, traditional ground clutter filters are unsuccessful in removing wind turbine clutter (WTC). The authors in [48] have developed and tested a WTC mitigation algorithm by using the range-Doppler spectrum.

Companies have also developed commercial systems to address the problem of WT clutter. Aveillant and its Holographic Radar$^{\text{TM}}$ is an example of this research [52]-[57]. They proposed a system that can obtain an exceptional level of very detailed Doppler information on targets of interest within its search volume. This makes possible the distinction between WTs and aircraft.

1.3 Wind Turbine Monitoring

The statistics provided in the previous section about the current situation of the world wind power industry gives a clearer picture of its importance to society. However, it is necessary to make the generation of wind energy more cost effective to become a more powerful alternative to fossil fuels.

As WTs rapidly increase in size and complexity (see Fig. 1.3), these large structures become increasingly more difficult and expensive to maintain, [58]-[59]. Once installed, WTs currently employ a number of different sensors, installed directly on their blades, and operating at different physical principles: accelerometers to measure vibration, torque and noise; strain gauges for stress analysis to identify weak sections of WTs at an early stage; displacement sensors to detect deflection in blades, nacelle tilt or mass loss damage; etc. However, a great number of these sensors are required for each blade. For example, only displacement sensors should be spaced by typically *1 m* along a blade [60]. With WT blade lengths currently up to *130 m*, such methods become increasingly inefficient.

The costs of wind farms depend on whether they are onshore or offshore. Onshore power is currently dominant, but wind power investments are gradually going to offshore wind farms in the EU, as Fig. 1.4 shows. Among other advantages, offshore WTs are less obstructive than onshore, since their apparent size and noise are mitigated by distance. In addition, the average wind speed in offshore wind farms is considerably higher since the water surface roughness is less than land [61]. However, the construction costs of offshore farms are higher due to the special environmental conditions. In the UK, the capital cost is £0.65 million/MW for onshore and £1.2 million/MW for offshore [32]. The capital cost will contribute to the final price of the energy produced, but the *Operation and Maintenance* (*O&M*) costs will also be taken into account to fix the price of the energy.

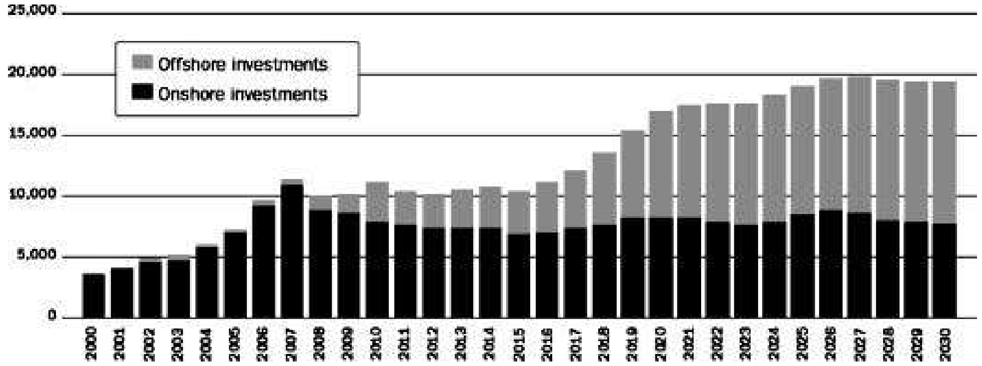

Fig. 1.4: Wind power investments from 2000 to 2030 (€ mio) in the EU [61].

O&M work keeps the structural health and the mechanical and electronic devices of WTs in good condition. Different cost effective O&M methods have been used successfully in onshore wind farms. However, the performance of these methods are not as good as expected in the offshore case. Several specific problems come out in this environment which are not present in onshore farms.

O&M costs contribute to the cost of energy (COE) [62]. In the case of onshore power generation, O&M costs can contribute up to 12% of the COE. For offshore wind, the contribution to the COE is estimated in 30%-35% [32]. Approximately 25%-35% of the O&M costs are associated to preventive maintenance while 65%-75% is related to corrective maintenance [63]. The revenue losses for offshore WTs are estimated in the same order as the direct costs for repair whereas for onshore projects the revenue losses are negligible.

Preventive maintenance is a pre-schedule maintenance. Qualified personnel go to a WT for inspection, detection, and correction of incipient failures either before they occur or before they develop into major defects. During this phase, workers need to operate on the WT, so it has to be switched off and dismantled incurring in downtime costs. These types of operations are much more expensive in offshore wind. As can be seen in Fig. 1.5, the personnel use vessels with access systems or helicopters to reach a WT. In the case of vessels, they may cost £169,804 plus £393/hour [32]. If helicopters are used, the price range from £400/hour to £1,200/hour. Preventive maintenance in offshore farms is also unsafe: of the 161 fatalities 95 were workers related to the wind industry and direct support workers [64].

Fig. 1.5: Vessels and helicopters are used by the personnel to reach a WT.

Corrective maintenance, on the other hand, is done after a failure has taken place. Its objective is to restore the equipment (WT in this case) to the pre-fault status of functioning. One of the approaches to reduce the high costs of corrective maintenance in offshore energy is to use condition monitoring which is a major component of predictive maintenance. References [32], [65] and [66] provide an exhaustive summary of the condition monitoring techniques. Among these techniques, it is possible to highlight the following:

- *Vibration analysis*: It is the most known technology applied for condition monitoring, in particular for rotating machinery. Different sensors are used depending on the frequency range of interest. For example, position transducers are useful in the low frequency range, accelerometers for high frequencies and Spectral Emitted Energy (SEE) are employed in the very high frequency range (acoustic vibrations).
- *Acoustic monitoring:* Acoustic emission has the capability of detecting very small damages and can be used for locating the spatial position and size of evolving damages. Materials subjected to stress or strain may emit sound waves as a result of sudden very small structural changes. The rate and properties of these emissions can be used as indicators of damage growth. The primary initial effect of the rupture of a fibre is the emission of a sound wave in a broad frequency range. The bandwidth can be estimated from the ratio of the speed of sound in the material to a characteristic spatial scale of the rupture. The bandwidth may be several tens of MHz. The high frequency components of such a stress wave are damped very rapidly in polymer composites, whereas lower frequency components travel much further.
- *Thermography*: This type of monitoring can spot a rise in temperature before failure occurs, detecting wear on bearings, shafts, gears and breaks. Thermal imaging is the only technology that allows inspections of components and provides

condition monitoring on the entire electrical circuit, including connectors and cables.

- *Fibre optic transducers*: It has gain interest in the monitoring of WTs. The objective of these sensors is to detect structural faults on the blade itself as well as the build up of ice.

A way to decrease the COE is to reduce the costs of these monitoring techniques. The objective of this research is to obtain the proof-of-concept of a new monitoring technique that can potentially cut the price of the O&M costs.

1.4 Radar for Wind Turbine Monitoring

Instead of treating a WT as radar clutter, these structures can be considered as a radar target. The idea is that radar signatures acquired from a WT may contain useful information about its structural integrity: broken blade, bent blade, vibrations out of control, etc. Therefore, rather than suppressing the radar returns, it may be possible to analyse them to detect and possibly classify the type of fault automatically. A conceptual radar system for this purpose is shown in Fig. 1.6. It involves a compact, short-range Doppler radar attached on the body (presumably the tower or the nacelle) of the WT. The system has a low-gain antenna illuminating the WT blades. The sensor analyses radar returns from the blades in motion to identify potential structural faults.

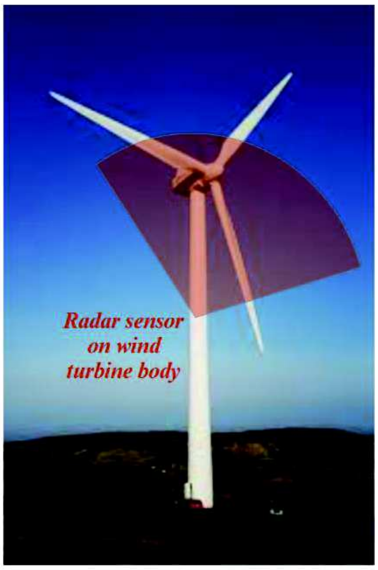

Fig. 1.6: Concept of the system proposed to monitor the WT structural health.

The advantage in this new approach is that a single sensor may monitor larger portions of a blade compared to the traditional WT monitoring techniques commented in the previous section. At the same time, this radar sensor operates at completely different principles and thus complements the existing sensor systems. Since the radar system operates externally, it can be easily installed on already built WTs without the necessity of dismantling them. In fact, the system is cheaper than current monitoring sensors: hardware costs 0.69p. In addition, the sensor proposed may also detect issues such ice accretion in cold climates (Northern Europe) or erosion in hot ones (Southern Europe) since it is based on reflections from WT blades. The ice accretion on WT blades causes a significant impact in the productivity of wind farms in cold climates [67]-[70].

The proposed radar system has the potential of detecting and classifying a wide range of WT faults with only a single sensor instead of using several sensors for each fault.

Furthermore, the conclusions obtained in this research could be potentially extended to monitor the dynamic behaviour of other structures or machinery with rotating parts, e.g. helicopter rotor blades.

1.5 Aims and Objectives

The aim of this research is to demonstrate the feasibility of the new WT structural monitoring system proposed in the previous section.

A number of issues have to be understood and solved, so the first step is to analyse the scattering mechanisms involved in a WT-radar system. Since the radar will be attached to the WT body, or very close to it in any case, the sensor will operate in the near-field of the WT. This means that not only current far-field models do not hold [71]-[72], but also the complex shape of the blades becomes more significant. The analysis of the WT radar signatures in the near-field is presented in this research together with its experimental confirmation.

The next stage is to use this knowledge in the analysis of faulty WTs. Several types of faults have been emulated in a WT scaled model to record their different radar signatures. Finally, the appropriate classification techniques are used to show that WT faults can indeed be distinguished and thus demonstrate that the system proposed can automatically classify faults and monitor the structural health of WTs.

1.6 Main Contributions and Thesis Structure

The hypothesis of this research is that WT radar signatures contain information about its structural integrity. Through the chapters of this dissertation, different aspects of the problem will be addressed in order to gather the necessary information to conclude whether or not the detection and classification of WT faults is possible.

Chapter 2 presents the theoretical analysis of WT radar signatures. As it can be observed in Fig. 1.6, the distance between the sensor and the WT is comparable to the blade length, so the radar sensor will operate in the near-field of the WT. In Chapter 2, the WT blades are modelled as a group of scattering points; the name given to this model is *Scattering Centres Model (SCM)*. The complexity of the WT blades model is gradually increased through the different sections. The analysis will begin by analysing the radar signature of a single point-scatterer in section 2.3 and it will finish in section 2.5 studying the case of three WT blades modelled as flat plates. The three domains or representations of the backscattered signals will be analysed for each case or sub-model (three scattering points, one blade, etc.).

The theoretical analysis of WT blades radar signatures will continue in Chapter 3, where a more realistic scenario is considered. In this case, the complex curved shape of the blades will be taken into account. The model will address the effect in the amplitude of the curvature of WT blades. As well as in Chapter 2, the backscattered signal will be analysed in three domains: time, frequency and joint time-frequency.

The first part of Chapter 4 presents details of the experimental set-up and methodology employed to collect experimental data that will be used to confirm the theoretical models of Chapters 2 and 3: the theoretical signatures in the three domains will be compared with the corresponding recorded signal from a scaled WT model in an anechoic chamber.

The goal of the second part of Chapter 4 is to demonstrate that WT structural faults can be detected by using radar sensors. A description of the different types of mechanical faults induced on a scaled WT model are presented in first place. Subsequently, the observation and analysis of the effect of these faults in the radar signatures is studied.

Finally, Chapter 5 is focused on analysing the feasibility of WT structural faults classification. In this chapter, different classification algorithms are presented and applied to the the time and frequency domains of the faulty WT signals. The performance of the different classifiers used is assessed with the help of confusion matrices.

References

[1] E. P. Wigner, “The unreasonable effectiveness of mathematics in the natural sciences,” *Comm. Pure Appl. Math*., vol. 13, no. 1, pp. 1-14, Feb., 1960.

[2] J. McKinney, “Radar: a case history of an invention,” *IEEE AES Systems Magazine*, vol. 21, no. 8, Part II, 2006.

[3] Y. Blanchard, G. Galati and P. van Genderen, “The Cavity Magnetron: Not Just a British Invention,” *IEEE Antennas Propagat. Mag.,* vol. 55, no. 5, pp. 244-254, Oct., 2013.

[4] P. Redhead, “The Invention of the cavity magnetron and its introduction into Canada and the U.S.A.,” *La Physique au Canada*, pp. 321-328, Nov., 2001.

[5] L. Sevgi, A. Ponsford and H. Chan, “An integrated maritime surveillance system based on high-frequency surface-wave radars. 1. Theoretical background and numerical simulations.,” *IEEE Antennas Propagat. Mag*., vol. 43, no. 4, pp. 28-43, Aug., 2001.

[6] A. Ponsford, L. Sevgi and H. Chan, “An integrated maritime surveillance system based on high-frequency surface-wave radars. 2. Operational status and system performance,” *IEEE Antennas Propagat. Mag.*, vol. 43, no. 5, pp. 52-63, Oct., 2001.

[7] Raney R.K. et al., “The lunar mini-RF radars: Hybrid polarimetric architecture and initial results,” *Proc. IEEE*, vol. 99, no. 5, pp. 808-823, Dec. 2010.

[8] M. Skolnik, G. Linde and K. Meads, “Senrad: an advanced wideband air-surveillance radar,” *IEEE Trans. Aerosp. Electron. Syst.*, vol. 37, no. 4, pp. 1163-1175, Oct. 2001.

[9] O'Hagan D.W. et al., “A multi-frequency hybrid passive radar concept for medium range air surveillance,” *IEEE Aerosp. Electron. Syst. Mag.*, vol. 27, no. 10, pp. 6-15, Oct., 2012.

[10] A. Mobashsher et al., “Microwave system to detect traumatic brain injuries using compact unidirectional antenna and wideband tranceiver with verification on realistic head phantom,” *IEEE Trans. Microw. Theory Tech.,* vol. 62, no. 9, pp. 1826-1836, Aug., 2014.

[11] Changzhan Gu et al., “A multi-radar wireless system for respiratory gating and accurate tumor tracking in lung cancer radiotherapy” in *Annual International Conference of the IEEE Engineering in Medicine and Biology Society*, Boston, MA, 2011, pp. 417-420.

[12] J. Hasch et al., “Millimiter-wave technology for automotive radar sensors in the 77 GHz frequency band” *IEEE Trans. Microw. Theory Tech*., vol. 60, no. 3, pp. 845-860, Jan. 2012.

[13] M. I. Skolnik, *Radar Handbook*, 3rd ed. New York; London, UK: McGraw-Hill, 2008.

[14] J. Peyton and Z. Peebles, *Radar principles*, New York; Chichester: Wiley, 1998.

[15] F. E. Nathanson, *Radar design principles: signal processing and the environment*, New York; Maidenhead: McGraw-Hill, 1969.

[16] IEEE Standard Letter Designations for Radar-Frequency Bands, *IEEE Standard* 521-2002, 2003.

[17] M. A. Richards et al., *Principles of modern radar. Volume 1, Basic principles*, Edison, N.J.: SciTech Publishing, 2010.

[18] R. G. Curry, *Radar Essentials: a concise handbook for radar design and performance analysis*, SciTech Publishing, 2011.

[19] N. J. Willis, *Bistatic radar*, Silver Spring MD: Technology Service Corp, 1995.

[20] M. Cherniakov and V. D. Nezlin, *Bistatic radar: principles and practice*, Chichester: John Wiley, 2007.

[21] M. I. Skolnik, *Introduction to Radar Systems*, 3rd ed.: McGraw Hill, third edition 2002

[22] V. C. Chen, *The Micro-Doppler Effect in Radar*, Boston; London, UK: Artech House, 2010.

[23] V. C. Chen, “Analysis of Radar Micro-Doppler Signature with Time-Frequency Transform,” *Proc. of the IEEE Workshop on Statistical Signal and Array Processing (SSAP)*, Pocono, PA, 2000, pp. 463–466

[24] V. C. Chen and H. Ling, *Time-Frequency Transforms for Radar Imaging and Signal Analysis*, Norwood, MA: Artech House, 2002

[25] V. C. Chen *et al*., “Micro-Doppler Effect in Radar: Phenomenon, Model, and Simulation Study,” *IEEE Trans. Aerosp. Electron. Syst.*, vol. 42, no. 1, pp. 2–21, Jan. 2006

[26] N. E. Huang *et al*., “The Empirical Mode Decomposition and the Hilbert Spectrum for Nonlinear and Non-Stationary Time Series Analysis,” *Proc. Roy. Soc. London*, Ser. A, vol. 454, pp. 903–995, 1998

[27] D. Gabor, “Theory of Communication,” *J. IEE (London)*, vol. 93, Part III, no. 26, pp. 429–457, Nov. 1946

[28] B. Boashash, “Time-Frequency Concepts” in *Time Frequency Signal Analysis and Processing*, Brisbane, Australia: Elsevier, 2003, ch. 1, sec. 1.1, pp. 3-11.

[29] B. A. Carlson *et al.*, “Signals and Spectra” in *Communication Systems*, 4th ed., New York, NY: McGraw-Hill, 2002, ch. 2, sec. 2.1, pp. 19-21

[30] V. C. Chen and H. Ling, “Time-Frequency Transforms” in *Time-Frequency Transforms for Radar Imaging and Signal Analysis*, 1st ed., Norwood, MA: Artech House, 2002, ch. 2, sec. 2.1.1, pp. 28-31.

[31] D. o. E. &. C. Change (2015, July 30). *gov.uk: Statistics - National Statistics* [Online]. Available: https://www.gov.uk/government/uploads/system/uploads/attachment_data/file/449426/Chapter_6_Renewables.pdf.

[32] P. Tavner, *Offshore Wind Turbines: Reliability, Availability and Maintenance*, The Institution of Engineering & Technology, 2012.

[33] T. E. W. Association. *Pure Power. Wind Energy Targets for 2020 and 2030* [Online]. Available: http://www.ewea.org/fileadmin/files/library/publications/reports/Pure_Power_III.pdf.

[34] IRENA (2012, June). *Renewable energy technologies: cost analysis series* [Online]. Available: https://www.irena.org/documentdownloads/publications/re_technologies_cost_analysis-wind_power.pdf

[35] J. Perry and A. Biss, “Wind Farm Clutter Mitigation in Air Surveillance Radar”, *IEEE Radar Conf.*, Boston, MA, 2007, pp. 93-98

[36] L. Sergey *et al.*, “Advanced Mitigating Techniques to Remove the Effects of Wind Turbines and Wind Farms on Primary Surveillance Radars”, *IEEE Radar Conf.*, Rome, 2008, pp. 1-6

[37] Gavin J. Poupart, “Wind Farms Impact on Radar Aviation Interests - Final Report”, QinetiQ, UK. FES W/14/00614/00/REP. 2003

[38] B. Gallardo-Hernando *et al.*, “Wind turbine clutter observations and theoretical validation for meteorological radar applications”, *IET Radar, Sonar & Navigation*, vol. 5, Iss. 2, pp. 111-117, Feb. 2011

[39] B. Gallardo-Hernando *et al.*, “Detection and Mitigation of Wind Turbine Clutter in C-band Meteorological Radar”, *IET Radar, Sonar & Navigation*, vol. 4, Iss. 4, pp. 520-527, Aug. 2010

[40] B. Gallardo-Hernando *et al.*, “Super-resolution techniques for wind turbine clutter spectrum enhancement in meteorological radars”, *IET Radar, Sonar & Navigation*, vol. 5, Iss. 9, pp. 924-933, Dec. 2011

[41] A. Belmonte and X. Fabregas, “Analysis of Blockage on Doppler Weather Radar Beams”, *IEEE Antennas and Wireless Propag. Lett.*, vol. 9, pp. 670-673, Jul., 2010

[42] S. M. Yucedag *et al.*, “Analytical method for monostatic radar cross section calculation of a perfectly conducting wind turbine model located over dielectric lossy half space”, *IET Radar, Sonar and Navigation*, vol. 8, Iss. 8, pp. 965-970, Oct., 2014

[43] M. Ritchie *et al.*, “Measurement and analysis of multiband bistatic and monostatic radar signatures of wind turbines”, *Electronics Letters*, vol. 51, Iss. 14, pp. 1112-1113, Jul. 2015.

[44] A. Balleri *et al*., “Measurements and analysis of the radar signature of a new wind turbine design at X-band”, *IET Radar, Sonar & Navigation*, vol. 7, Iss. 2, pp. 170 – 177, Feb., 2013.

[45] L. R. Danoon and A. K. Brown, “Modeling Methodology for Computing the Radar Cross Section and Doppler Signature of Wind Farms,” *IEEE Trans. on Antennas Propag.*, vol. 61, no. 10, pp. 5166-5174, Oct., 2013.

[46] R. Rudd and B. Rhandawa, “RCS Measurement of Wind Turbines,” in *EuCAP 2009 Antennas and Propagation*, Berlin, 2009, pp. 3642-3644.

[47] J. Pinto *et al.*, “Stealth Technology for Wind Turbines,” *IET Radar, Sonar & Navigation*, vol. 4, Iss. 1, pp. 126-133, Feb. 2010.

[48] Feng Nai *et al.*, “On the mitigation of wind turbine clutter for weather radars using range-Doppler spectral processing,” *IET Radar, Sonar and Navigation*, vol. 7, Iss. 2, pp. 178-190, Feb., 2013.

[49] Y. Zhang *et al.,* “On the effects of rotating blades on DS/SS communication systems”, *IEEE Statistical Signal and Array Processing (SSAP 2000)*, Pocono Manor, PA, 2000, pp. 682-686.

[50] O. Karabayir *et al*., “Wind turbine signal modelling approach for pulse Doppler radars and applications,” *IET Radar, Sonar & Navigation*, vol. 9, Iss. 3, pp. 276 – 284, Feb., 2013.

[51] C. A. Jackson and M.M. Butler, “Options for Mitigation of the Effects of Wind Farms on Radar Systems,” in *IET International Conference on Radar Systems*, Edinburgh, 2007, pp. 1-6

[52] M. Jahangir, “Target centric wide-area 3-D surveillance using a non-scanning multibeam receiver array,” in *2015 IEEE Radar Conference (RadarCon)*, Arlington, VA, 2015, pp. 652-657.

[53] T. Quilter and M. Jahangir, “Performance of a 3D non-scanning array to detect targets in the presence of wind turbines — A step change for air traffic control,” in *2014 Tyrrhenian International Workshop on Digital Communications - Enhanced Surveillance of Aircraft and Vehicles (TIWDC/ESAV)*, Rome, 2014, pp. 116-121.

[54] M. Jahangir and T. Quilter, “The practicality and benefit of a 3-D wide-area persistent surveillance micro-Doppler radar,” in *16th International Radar Symposium (IRS)*, Dresden, 2015, pp. 271-277.

[55] G. K. A. Oswald, C. D. Webster and A. G. Smithson, “Radar system and method”, U. S. Patent 20110241928 A1, Oct., 6, 2011

[56] C. D. Webster and G. K. A. Oswald, “Radar filter”, U.S. Patent 20130127656 A1, May, 23, 2013

[57] G. K. A. Oswald, “Radar system”, U.S. Patent 8860604 B2, Oct., 14, 2014

[58] R. Poore and C. Walford, “Development of an operations and maintenance cost model to identify cost of energy savings for low wind speed turbines”, National Renewable Energy Laboratory, Subcontract report, Jan., 2008.

[59] S. Tegen *et al.*, “2010 Cost of wind energy review”, National Renewable Energy Laboratory, Technical report, April, 2012.

[60] B. F. Sorensen *et al.*, “Fundamentals for remote structural health monitoring of wind turbine blades”, RisØ National Laboratory Technical Report, May, 2002.

[61] M. Bilgili *et al.*, “Offshore wind power development in Europe and its comparison with onshore counterpart”, Renewable and Sustainable Energy Reviews 15 (2011) 905–915.

[62] L. Fingersh *et al.*, “Wind turbine design cost and scaling model”, National Renewable Energy Laboratory, Technical report, Dec., 2006.

[63] T. W. Verbruggen, “Wind Turbine Operation & Maintenance based on Condition Monitoring WT-Ω”, Energy research Centre of the Netherlands (ECN), Final report, April, 2003.

[64] Caithness Windfarm Information Forum, *Summary of wind turbine accident data to 31 May 2015* [Online]. Available: http://www.caithnesswindfarms.co.uk/AccidentStatistics.htm

[65] C. J. Crabtree, “Condition Monitoring Techniques for Wind Turbines”, PhD dissertation, Durham theses, Durham University.

[66] Chia Chen Ciang *et al.*, “Structural health monitoring for a wind turbine system: a review of damage detection methods,” *Measurement Science and Technology*, vol. 19, no. 12, 2008.

[67] Yan Li *et al.*, “Computer simulation on the icing accretions on a static straight blade used for the vertical axis wind turbine,” in *International Conference on Computer Design and Applications*, Qinhuangdao, 2010, pp. 291-294.

[68] Minghao Zhao *et al.*, “Research on fault mechanism of icing of wind turbine blades,” in *World Non-Grid-Connected Wind Power and Energy Conference*, Nanjing, 2009, pp. 1-4.

[69] S. Shajiee, “Direct ice sensing and localised closed-loop heating for active de-icing of wind turbine blades,” in *American Control Conference*, Washington, DC, 2013, pp. 634-639.

[70] M. Akhloufi and N. Benmesbah, “Outdoor ice accretion estimation of wind turbine blades using computer vision,” in *Canadian Conference on Computer and Robot Vision*, Montreal, QC, 2014, pp. 246-253.

[71] Yan Zhang *et al.*, “Using Scaled Models for Wind Turbine EM Scattering Characterization Techniques and Experiments,” *IEEE Trans. Instrum. Meas.*, vol. 60, no. 4, April, 2011.

[72] H. Trzaska, “The Near Field and the Far Field” in *Electromagnetic Field Measurements in the Near Field*, 2nd ed., Atlanta, GA: Noble, 2001, ch. 2, pp. 14-19.

Chapter 2 Scattering Centres Model of a Wind Turbine

2.1 Introduction

As has been introduced in Chapter 1, the detection of incipient WT faults is becoming more important and for this reason a large number of monitoring techniques have been developed. The new radar system proposed in this dissertation may be used to reduce the cost of WT condition monitoring.

In order to study the feasibility of the proposed radar sensor, it would be necessary to induce different types of faults on actual operating WTs for experimental purposes exclusively. However, this procedure is clearly not realisable since its cost would be certainly high. Instead, at this stage of the research, all the experiments were performed by using a scaled WT model inside an anechoic chamber. This approach makes feasible the emulation of structural faults with a low cost, which allows the analysis of the radar signature of WT faults in time, frequency and joint time-frequency domains.

First of all, it is necessary to understand all the characteristics of the radar signature of a WT, regardless of its structural health, before performing any experiment. The mathematical description of the radar signature of a complex target such as WT blade is a difficult task. Due to the curved and complex shape of WT blades, their reflectivity has to be analysed along with the Doppler shift. Before going into the reflectivity issue, WT blades will first be treated as rectangular targets. In this manner, the physics of the problem can be understood by analysing their dynamic behaviour in different domains.

This chapter introduces a theoretical model of the radar signature of WT blades in the near-field. The approach consisted in using the called *scattering centres model* (SCM) which considers a target, a WT blade in this case, as formed by a group of point-scatterers. The electromagnetic (EM) wave reflected can be conceived as the sum of the scattered waves emanating from such points. This method takes into account the phases of the reflected waves. However, the reflectivity is not predicted by the SCM, which will be the topic of the next chapter where a curved blade will be analysed. Although the idea proposed in section 1.4 is to place the radar on the WT body, the actual position of this type of sensor is not completely determined. A more profound study on the adventages and disadventages of the different position options would clarify this question. However, the goal of the theoretical model presented on this chapter and chapter 3 is to better understand the dynamic behaviour of WT blades respect to the research done so far. Therefore, a Taylor approximation will be considered but keeping terms that are usually discarded in research literature.

The radar signature of WT blades was studied step by step, starting from simple targets and finishing with a model of rectangular blades. The analysis begins in section 2.2 where the results obtained from a single point-scatterer on one of the blades are explained. The complexity of the target was increased, considering a WT formed by three point-scatterers, corresponding to each blade tip; the results are analysed in section 2.3. The next step was to model one blade as a line of point-scatterers or wire; this is the topic of section 2.4. Section 2.5 presents the results from the analysis of the radar signature of WT blades modeled as three wires. The last step was taken by modelling the WT blades as rectangular plates and this is the topic of section 2.6. Finally, the micro-Doppler signature of a WT blade is analysed in section 2.7.

2.2 Single Blade-Single Point Target

The first assumption in the analysis was to presume that the incident EM field can be considered as a plane wave over the localised regions of the WT blades. This is justified by the fact that the antenna dimensions are of the order of magnitude of the frequency wavelength λ, which is consistent with the experimental conditions described in Chapter 4. This means that the WT blades are in the far-field of the antenna. Therefore, in the analysis of the radar signature of all the different cases considered in this chapter, the transmitted signal will have a plane wave form (CW form), this is

$$s(t) = e^{j\omega_0 t} \tag{2.1}$$

The first step in the construction of a theoretical model based on the SCM was the study of a single point target illuminated by the plane wave (2.1). The backscattered signal has the form (2.1) but shifted in time. This shift is the round-trip time delay between the radar and the target. Formally, the backscattered signal from a generic n^{th}-point on the m^{th} -blade can be written as

$$s_{R;mn}(t) = \rho_{mn} \cdot s_T\big(t - t_r(t)\big) = \rho_{mn} \cdot e^{j\omega_0\left(t - t_r(t)\right)} = \rho_{mn} \cdot s_T(t) \cdot e^{-j\omega_0 t_r(t)} \tag{2.2}$$

The reflectivity ρ_{mn} in (2.2) takes into account the intensity of the backscattered signal associated to that particular point-scatterer. Since these are point targets, the reflectivity was set to1 for all the points.

The time $t_r(t)$ is the time delay between the signal transmission and echo reception. It is a function of time because the radar-target distance changes as the point rotates about its axis. In the monostatic case, this time delay is given by

$$t_r(t) = \frac{2|\vec{r}_{mn}(t)|}{c} \tag{2.3}$$

where $r_{mn}(t)$ is the radial distance between the radar and the scattering centre [1]-[2].

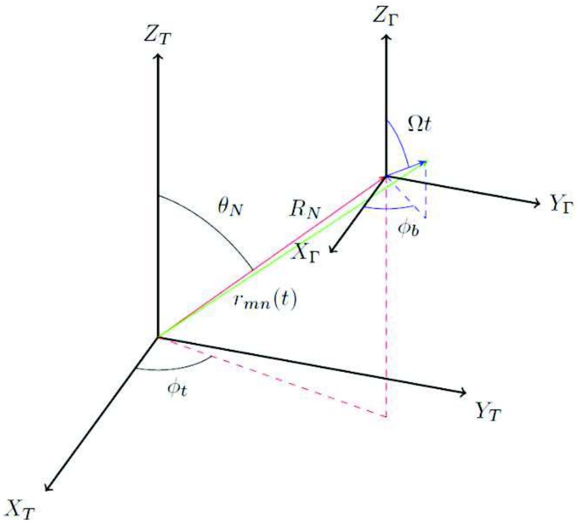

Fig. 2.1: General geometric configuration of a point target on a WT arbitrarily orientated.

In order to compute this time delay and consequently the backscattered signal, it was necessary to obtain an explicit expression of the radial distance $r_{mn}(t)$. Fig. 2.1 shows the general geometry of the problem addressed where the radar coordinate system, *S_T*, is centred at the radar position. $S_\Gamma$is the WT coordinate system which is placed at the centre of rotation of the blades (the nacelle). The angles θ_N, ϕ_tdetermine the position of the WT system with respect to *S_T* , while $\Omega t, \phi_b$ set the position of an arbitrary scattering point on the blade. Ω is the rotational speed of the WT blades. The distance between the radar and the origin of the turbine system is defined as $\vec{R}_N$. Finally, $\vec{r}_{mn}^{T}$ and $\vec{r}_{mn}^{\Gamma}$label the position of a generic *n*-point on the *m*-blade in the radar and WT systems respectively.

From Fig. 2.1, it is clear that

$$r(t) = \vec{R}_N + \vec{r}_{mn}^{\Gamma}(t)$$

(2.4)

whose modulus is the radial distance $r_{mn}(t)$ necessary to calculate the time delay in the backscattered signal (2.2). Defining the components of $\vec{R}_N$ as (X_N, Y_N, Z_N), the coordinates of the scattering point in the radar system are

$$x_{mn}^{T}(t) = X_N + l_n \cdot \cos\phi_b \cdot \sin\left(\theta_0 + \frac{2\pi}{3}(m-1) + \Omega t\right)$$

$$y_{mn}^{T}(t) = Y_N + l_n \cdot \sin\phi_b \cdot \sin\left(\theta_0 + \frac{2\pi}{3}(m-1) + \Omega t\right)$$

$$z_{mn}^{T}(t) = Z_N + l_n \cdot \cos\left(\theta_0 + \frac{2\pi}{3}(m-1) + \Omega t\right)$$

(2.5)

where l_n is the modulus of $\vec{r}^{\Gamma}_{mn}$, i.e., the distance between the point-scatterer and the centre of rotation. The polar angle θ_0 takes into account any initial angle of the blade. From equations (2.4), the square of the radial distance, which corresponds to$r^2_{mn}(t) = (x^T_{mn}(t))^2 + (y^T_{mn}(t))^2 + (z^T_{mn}(t))^2$, can be expressed by

$$r^2_{mn}(t) = R^2_N + l^2_n + 2l_n \sin\left(\theta_0 + \frac{2\pi}{3}(m-1) + \Omega t\right)\left[X_N \cos\phi_b + Y_N \sin\phi_b + Z_N \cot\left(\theta_0 + \frac{2\pi}{3}(m-1) + \Omega t\right)\right] \tag{2.6}$$

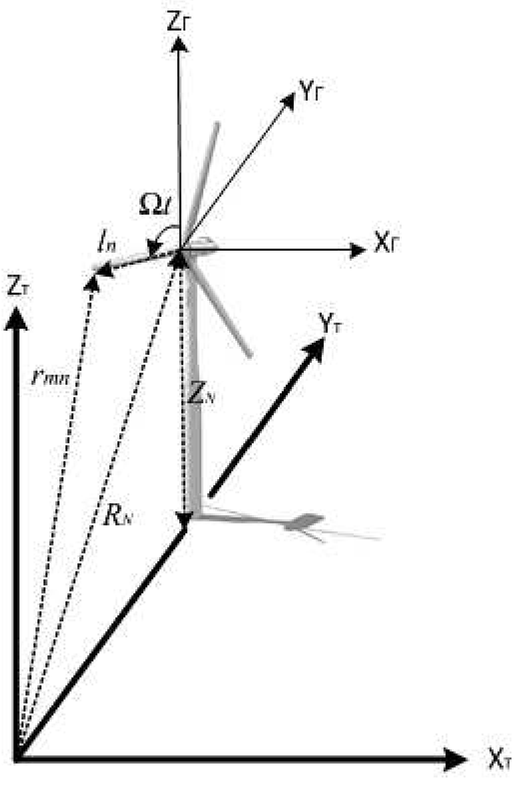

Fig. 2.2: Specific geometric configuration of the problem analysed.

Expression (2.6) determines the radial distance to the scattering centre in a general monostatic configuration. In the developing of the theoretical models presented in this chapter and in Chapter 3, it was assumed that the radar is facing the WT like in Fig. 2.2. This special situation corresponds to the following values of the angular coordinates introduced in Fig. 2.1: $\phi_t = 0$ ($\phi_b = \frac{\pi}{2}$) and $\phi_b = \frac{\pi}{2}$ ($\phi_t = 0$). The radial distance (2.5) is then simplified to obtain

$$r_{mn}(t) = \sqrt{R_N^2 + l_n^2 + 2 l_n Z_N \cos\left(\theta_0 + \frac{2\pi}{3}(m-1) + \Omega t\right)}$$

(2.7)

Once the radar-to-target distance is known, expression (2.2) can be written as

$$s_R(t) = s_T(t) \cdot e^{-j\frac{2\omega_0}{c}\sqrt{R_N^2 + l_n^2 + 2 l_n Z_N \cos(\Omega t)}}$$

(2.8)

which corresponds to the backscattered signal from a single point in the blade labelled as *m = 1.*

In order to extract the Doppler frequency shift from the experimental signals, an I/Q demodulation was used. Theoretically, this can be expressed as

$$s_{R;1n}(t) \equiv s_{R;1n}^{IQ}(t) = r(t) = e^{-j\frac{4\pi}{\lambda}\sqrt{R_N^2 + l_n^2 + 2 l_n Z_N \cos(\Omega t)}} \quad (2.9)$$

No further conclusions or mathematical analysis can be obtained directly from expression (2.9), so it is necessary to deal with an approximation of this equation to manipulate it. The accuracy of such approximation depends on the physical parameters of the system under study. However, it is important to notice that the comparison with the experimental results presented in Chapter 4 was done using the exact analytical expression (2.9).

The phase of the signal can be defined as

$$\theta(t) \overset{\text{def}}{=} -\frac{4\pi}{\lambda}\sqrt{R_N^2 + l_n^2 + 2l_nZ_N\cos(\Omega t)} = \frac{4\pi}{\lambda}R_N\sqrt{1 + \frac{l_n^2}{R_N^2} + \frac{2l_nZ_N}{R_N}\cos\Omega t} \tag{2.10}$$

If $R_N \gg Z_N > max\{l_b\} = l_b$, where l_b is the blade length, the square root can be expanded in Taylor series and approximate it to the first order term:

$$\theta(t) \cong -\frac{4\pi}{\lambda}R_N\left(1 + \frac{l_n^2}{2R_N^2} + \frac{2l_nZ_N}{R_N^2}\cos\Omega t\right) \tag{2.11}$$

Therefore, the backscattered signal (2.9) can be written as

$$s_{R;1n}(t) \simeq e^{-\frac{4\pi}{\lambda}R_N\left(1+\frac{l_n^2}{2R_N^2}\right)} \cdot e^{-j\frac{4\pi}{\lambda}\frac{l_nZ_N}{R_N}\cos\Omega t} = C_n e^{jk_n\cos\Omega t} \tag{2.12}$$

where the constants C_n and k_n are defined by

$$C_n \equiv e^{-\frac{4\pi}{\lambda}R_N\left(1+\frac{l_n^2}{2R_N^2}\right)}$$

(2.13a)

$$k_n \equiv -j\frac{4\pi}{\lambda}\frac{l_n Z_N}{R_N}\cos \Omega t$$

(2.13b)

If the centre of rotation is at $l_{n=0} = 0$, it is clear that $C_{n=0} = cte$ and $k_{n=0} = 0$. Therefore, the real part of the signal (2.12) will be constant, as it is expected for any stationary target. For any other point-scatterer along the blade, the backscattered signal will oscillate in time due to the term $\cos \Omega t$.

At this stage, the Jacobi-Anger expansion [3] can be invoked in the the last term of (2.12) to write

$$s_{R;1n}(t) \simeq C_n e^{jk_n \cos \Omega t} = C_n \sum_{p=-\infty}^{\infty} j^p J_p(k_n) e^{jp\Omega t}$$

(2.14)

where the terms $J_p(k_n)$ correspond to the Bessel functions. This is an exact expansion of the approximated backscattered signal (2.12) in the basis of its harmonics. This series expansion will be useful to interpret the features of the time and frequency domains not only of (2.11) but of the rest of the signals obtained in this chapter. Actually, the representation of (2.11) in the time-domain is simply an oscillating signal without major interest to the analysis. On the other hand, the frequency-domain representation reveals interesting characteristics that will be useful to the analysis of more complicated targets.

Since the single point target is rotating, the signal (2.12) (and of course (2.11)) has to be periodic with period $T = \frac{2\pi}{\Omega}\ s$ which corresponds to a full rotation of the blade. Consequently, the signal (2.12) can be considered as formed by a train of pulses. For an arbitrary finite number of periods $l \cdot T$, or pulses, its Fourier transform is

$$\Phi(\omega) \equiv F\{s_{R;1n}(t)\}(\omega) = \frac{1}{\sqrt{2\pi}} \int_{-\infty}^{+\infty} dt\ C_n e^{jk_n \cos \Omega t} \cdot e^{-j\omega t} = \frac{1}{\sqrt{2\pi}} \int_{0}^{l\cdot T} dt\ C_n e^{jk_n \cos \Omega t} \cdot e^{-j\omega t}$$

(2.15)

The last equality takes into account the fact that the signal is zero outside the train of pulses. After inserting the expansion (2.14), the spectrum of the signal can be written as

$$\Phi_{R;1n}(\omega) = \frac{C_n}{\sqrt{2\pi}} \int_{0}^{l\cdot T} dt \sum_{p=-\infty}^{\infty} j^p J_p(k_n) e^{jp\Omega t} \cdot e^{-j\omega t}$$

(2.16)

In order to obtain an analytical expression of the Fourier transform (2.16), the infinite summation in p has to be interchanged with the integral sign. This operation is legitimate if Fubini's theorem can be applied. Therefore, the conditions that the function $f_{n,p}(t,\omega) \equiv j^p J_p(k_n) e^{jp\Omega t} e^{-j\omega t}$ has to satisfy are

$$\sum_{p=-\infty}^{\infty} \int_0^{lT} \left| f_{n,p}(t,\omega) \right| < \infty$$

(2.17a)

$$\int_0^{lT} dt \sum_{p=-\infty}^{\infty} \left| f_{n,p}(t,\omega) \right| < \infty$$

(2.17b)

The absolute value of the function under analysis in both of the previous conditions is

$$\left| f_{n,p}(t,\omega) \right| = \sqrt{f_{n,p}(t,\omega) \cdot \overline{f_{n,p}(t,\omega)}} = |J_p(k_n)|$$

(2.18)

where $\overline{f_{n,p}(t,\omega)}$ denotes the complex conjugate. Substituting this expression into the inequalities (2.17a) and (2.17b), these conditions become

$$\sum_{p=-\infty}^{\infty}\int_{0}^{lT}\left|J_p(k_n)\right| = \sum_{p=-\infty}^{\infty}\left|J_p(k_n)\right|\int_{0}^{lT}dt = lT\cdot\sum_{p=-\infty}^{\infty}\left|J_p(k_n)\right| < \infty$$

(2.19a)

$$\int_{0}^{lT}dt\sum_{p=-\infty}^{\infty}\left|f_{n,p}(t,\omega)\right| < \infty$$

(2.19b)

Therefore, the validity or not of these inequalities are reduced to ensure the convergence of the series $\sum_{p=-\infty}^{\infty}\left|J_p(k_n)\right|$. In order to verify the convergence, a comparison test can be used. The Bessel functions satisfy the following inequality when $p \geq 0$ [3]:

$$\left|J_p(k_n)\right| \leq \left|\frac{k_n}{2}\right|^{p}\frac{e^{\left|\frac{k_n}{2}\right|^{2}}}{p!}$$

(2.20)

The series whose general term is given by (2.20) is convergent by d'Alambert criteria [4]. Therefore, using the fact that

$$\left|J_p(k_n)\right| = \left|(-1)^{p}J_p(k_n)\right| = \left|J_p(k_n))\right|, \forall p \geq 0$$

(2.21)

the series in (2.19a) and (2.19b) are also convergent, which demonstrates the validity of interchanging the integral and summation signs. Consequently, the Fourier transform (2.16) can be computed as follows:

$$\Phi_{R;1n}(\omega) = \frac{C_n}{\sqrt{2\pi}} \int_0^{l\cdot T} dt \sum_{p=-\infty}^{\infty} j^p J_p(k_n) e^{jp\Omega t} \cdot e^{-j\omega t} = \frac{C_n}{\sqrt{2\pi}} \sum_{p=-\infty}^{\infty} j^p J_p(k_n) \int_0^{l\cdot T} dt\, e^{j(p\Omega-\omega)t} = \frac{C_n}{\sqrt{2\pi}} \sum_{p=-\infty}^{\infty} j^p J_p(k_n) \frac{e^{j(p\Omega-\omega)lT} - 1}{j(p\Omega-\omega)} \tag{2.22}$$

The two graphs in Fig. 2.3 correspond to the cases $l = 1$ (one revolution) and $l = 2$ (two revolutions) in equation (2.22). The signal corresponding to one rotation is equivalent to a single pulse signal, so it can be considered as a non-periodic function of time and, consequently, it has a continuous frequency spectrum. If more revolutions are taken into account, the signal can be considered as formed by several pulses. In this case, the signal spectrum becomes discrete due to modulation [5].

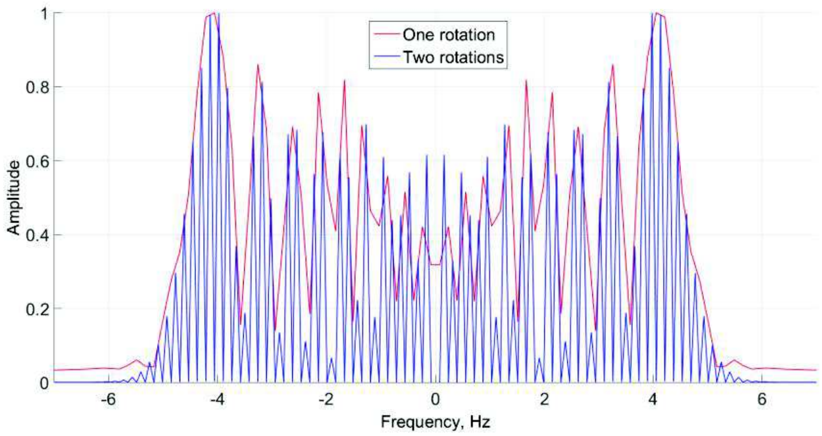

Fig. 2.3: Spectra of signals formed of one (red) and two (blue) pulses.

If the number of periods l is increased, the signal can be considered as a continuous train of pulses extended to all times t. In this situation, condition (2.19a) is not satisfied since the integral is not bounded when $l \rightarrow \infty$ and thus the summation and integration signs cannot be interchangeable.

In order to calculate the Fourier transform of the continuous signal (point target constantly rotating), it is necessary to use the theory of generalised functions and their relation with the Fourier transform. It can be demonstrated that the Fourier transform of an infinite series can be taken term by term [6]. Applying this to the signal (2.14), its spectrum can be written

$$\Phi_{R;1n}(\omega) \equiv F\{s_{R;1n}(t)\}(\omega) = F\left\{C_n \sum_{p=-\infty}^{\infty} j^p J_p(k_n) e^{jp\Omega t}\right\}(\omega) = C_n \sum_{p=-\infty}^{\infty} F\{j^p J_p(k_n) e^{jp\Omega t}\}(\omega)$$

$$= C_n \sum_{p=-\infty}^{\infty} j^p J_p(k_n) \delta(p\Omega - \omega)$$

(2.23)

whence it can be concluded that the spectrum of the backscattered signal of a single point on one blade consists of an infinite number of sideband lines at definite frequencies given by

$$p\Omega - \omega = 0 \leftrightarrow f_p = \frac{\Omega}{2\pi} p$$

(2.24)

It is important to notice that the carrier frequency f_0 has been removed by the I/Q demodulator, so the actual spectral lines are situated at $f_0 \pm p\frac{\Omega}{2\pi}$. Fig. 2.4a corresponds to the spectrum of a single point target during one rotation which is continuous as expression (2.19) predicted. The spectrum in Fig. 2.4b corresponds to a signal formed by several rotations. In both cases, the exact expression (2.9) was used to simulate the signals.

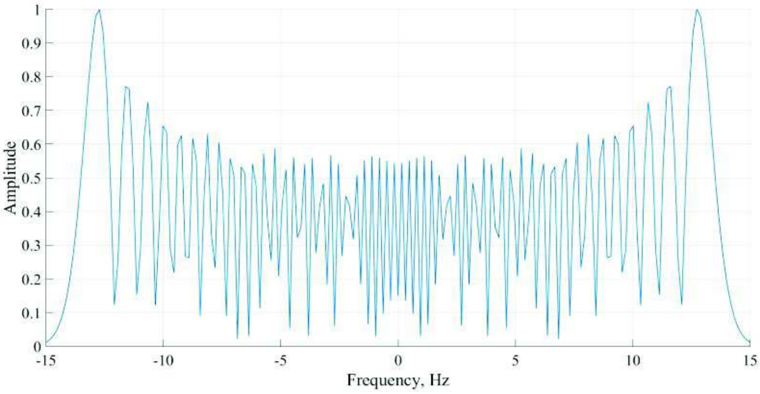

(a)

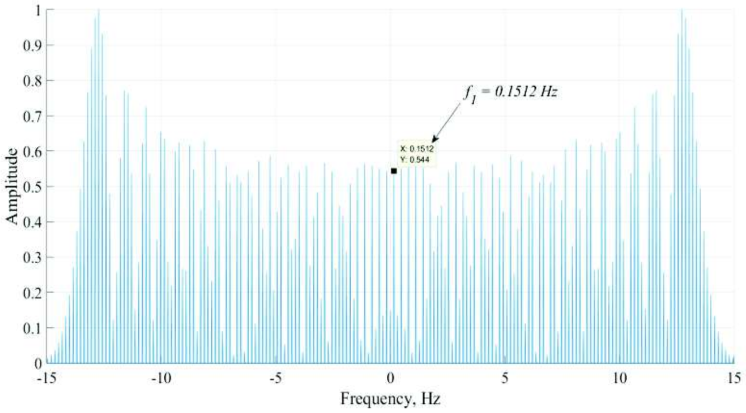

(b)

Fig. 2.4: Spectrum of one rotating point target. Simulation parameters: $f_0 = 2\ GHz$, $Z_N = 100\ m$, $l_b = 50\ m$, $R_N = 5\ km$, $\Omega = 1\ rad/s$. The number of rotations are (a) one revolution and (b) ten revolutions.

The simulated target corresponded to the blade tip of a WT with a hub height $Z_N = 100\,m$ and blade length $l_b = 50\,m$ illuminated by a $f_0 = 2\ GHz$ radar. The radar-target distance was $R_N = 5\ km$ and the rotation velocity was set to $\Omega = 1\ rad/S$. Based on the formula (2.24), the frequency $f_1 = 0.159\ Hz$ is approximately the frequency of the first peak marked on Fig. 2.4b.

The amplitude of the frequencies in the spectrum depends on the Bessel functions $J_p(k_n)$, so it is necessary to examine them to get more insight into the structure of the frequency-domain. Fig. 2.5a represents how the Bessel functions varies with their argument k_n [7]. Based on this graph, it is clear that the amplitude of the spectral lines will rely on the value of k_n which ultimately depends on the specific physical parameters of the radar-WT system. If $k_n \ll 1$, which corresponds to the far-field situation, J_0 and $J_{\pm 1}$ are the only relevant functions as it can be seen on Fig. 2.5a; the spectrum is then formed by just few spectral lines. However, if $k_n \gg 1$, various $J_p(k_n)$ are significant as Fig. 2.5a shows, so the spectrum is formed by a great number of spectral lines. This situation corresponds to the near-field region and it is the case of interest in this research.

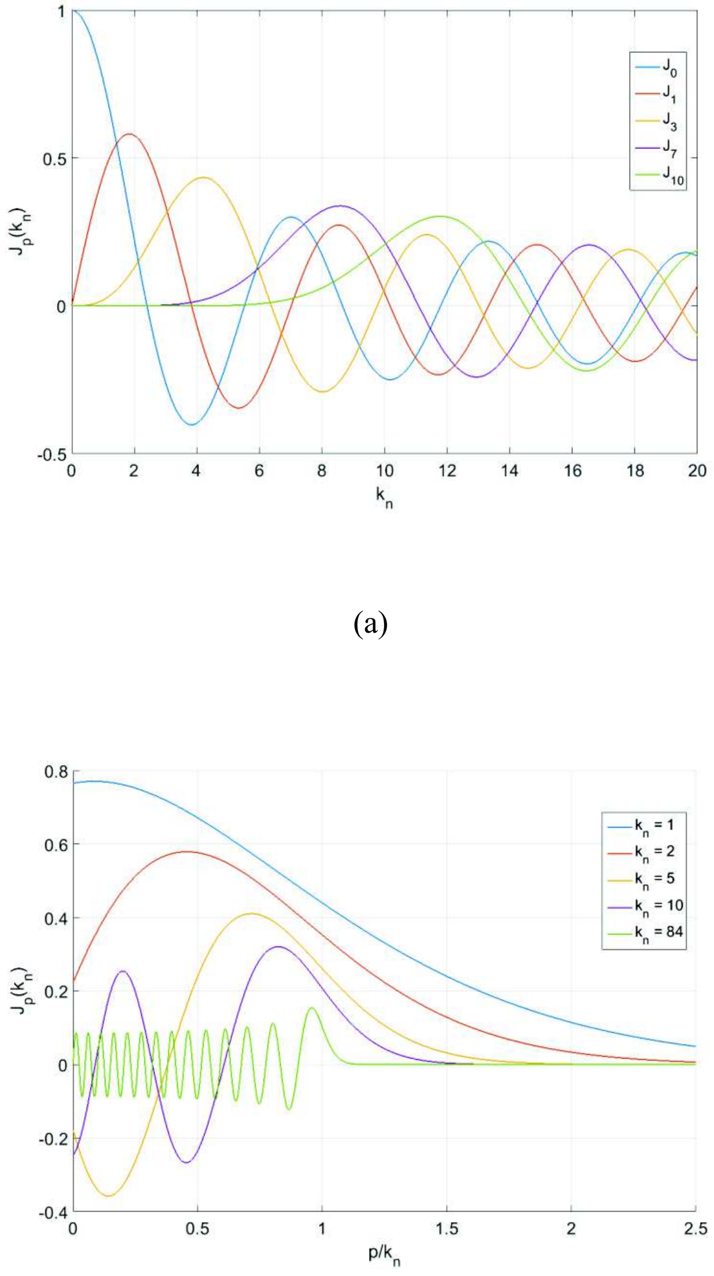

(a)

(b)

Fig. 2.5: The plots in (a) correspond to several orders of the Bessel functions for different values of k_n. The graphs in (b) show the variation in the order of the Bessel functions for several values of k_n.

It is possible to determine the significant frequencies that appear in the near-field spectrum. In order to do so, the Bessel functions $J_p(k_n)$ were plotted against the ratio p/k_n for several fixed values of the coefficient k_n, which corresponds to Fig. 2.5b. If the horizontal axis is multiplied by $k_n\frac{\Omega}{2\pi}$, the positions of the spectral lines relative to f_0 are obtained and the curves represent the envelope of the spectrum of the signal. As Fig. 2.5b shows, the curves decay monotonically and satisfy that $|J_p(k_n)| \ll 1$ if $|\frac{p}{k_n}| \gg 1$. As an example, let us consider the following radar-target system parameters: $R_N = 5\,km,\ l_b = 50\,m,\ Z_N = 100\,m,$ and $\lambda = 0.15\,m.$ In this case, the argument of the Bessel functions is $k_n = 84$ (this case is plotted in Fig. 2.5b) and their amplitude can be neglected for orders $p > 1.25 \cdot 84 \approx 105.$ As can be observed in Fig. 2.4b, frequencies larger than $15\,Hz$are not significant, which is consistent with the results obtained in Fig. 2.5b since $105 \cdot \frac{\Omega}{2\pi} \approx 17\,Hz.$

2.3 Three Point Targets. Blade Tips.

The case of a single point-scatterer on one blade has been analysed in the previous section. The next step towards the construction of a more complex model of a WT was to consider three point-scatterers, one on each blade, as Fig. 2.6 shows. In this section, and without loss of generality, the three blade tips will be analysed.

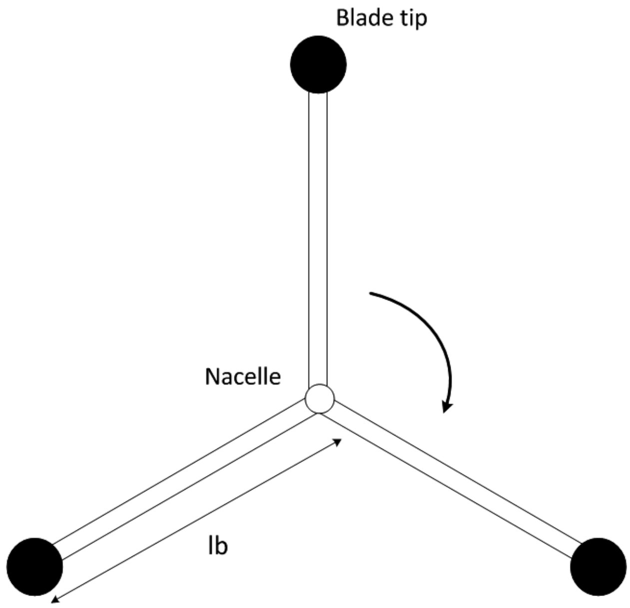

Fig. 2.6: WT modelled as three point targets.

It is important to remember that expression (2.9) represents the signal of an EM wave. Ultimately, this wave is a solution of Maxwell's equations. Since these equations are linear, the principle of superposition guarantees that the full backscattered signal is the sum of the individual waves emanating from each one of the three blade tips. This is, by adding the three possible expressions (2.9) (one for each blade *m*), the backscattered signal can be written

$$s_{R;tip}(t) = \sum_{m=1}^{3} e^{-j\frac{4\pi}{\lambda}\sqrt{R_N^2 + l_n^2 + 2l_n Z_N \cos\left(\frac{2\pi}{3}(m-1) + \Omega t\right)}} \tag{2.25}$$

As it was done in section 2.2, the square root in (2.25) can be approximated by Taylor to write:

$$s_{R;tip}(t) \cong C \sum_{m=1}^{3} e^{jk\cos\left(\frac{2\pi}{3}(m-1)+\Omega t\right)} = C\left[e^{jk\cos(\Omega t)} + e^{jk\cos\left(\frac{2\pi}{3}+\Omega t\right)} + e^{jk\cos\left(\frac{4\pi}{3}+\Omega t\right)}\right]$$

(2.26)

where the constants C and k are given by (2.13) after setting $l_n = l_b$. The Jacobi-Anger formula expands each one of the exponentials in (2.26) in the basis of their harmonics as follows

$$s_{R;tip}(t) \cong C\left[\sum_{p=-\infty}^{\infty} j^p J_p(k)\, e^{jp\Omega t} + \sum_{p=-\infty}^{\infty} j^p J_p(k)\, e^{jp\left(\frac{2\pi}{3}+\Omega t\right)} + \sum_{p=-\infty}^{\infty} j^p J_p(k)\, e^{jp\left(\frac{4\pi}{3}+\Omega t\right)}\right]$$

(2.27)

The summations run over the same dummy index, so the three terms can be reorganised to obtain a more compact expression:

$$s_{R;tip}(t) \cong C \sum_{p=-\infty}^{\infty} j^p J_p(k)\left(1 + e^{jp\frac{2\pi}{3}} + e^{jp\frac{4\pi}{3}}\right) e^{jp\Omega t} = C \sum_{p=-\infty}^{\infty} C_p\, e^{jp\Omega t} = \sum_{p=-\infty}^{\infty} \chi_p\, e^{jp\Omega t}$$

(2.28)

where $\chi_p \stackrel{\text{def}}{=} C\, j^p J_p(k)\left(1 + e^{jp\frac{2\pi}{3}} + e^{jp\frac{4\pi}{3}}\right)$ can be regarded as the coefficients of the expansion of the signal in the basis of its harmonics. The signal (2.28) is similar to (2.14); both are expansions in terms of the same basis, but with different coefficients for each component of the basis.

The same mathematical analysis performed in section 2.2 can be applied here in order to extract information about the spectrum. Experimentally, the signal is comprised of a large number of cycles: the signal replicates itself periodically. The Fourier transform of (2.28) is then given by

$$\Phi_{R;tips}(\omega) \equiv F\left\{\sum_{p=-\infty}^{\infty} \chi_p\, e^{jp\Omega t}\right\}(\omega) = \sum_{p=-\infty}^{\infty} \chi_p \delta(p\Omega - \omega)$$

(2.29)

Therefore, the spectrum of the signal will be constituted of several spectral lines at frequencies $f_p = \frac{\Omega}{2\pi} p$. The amplitude of each spectral line is related to the module of the coefficients χ_p whose analysis will be important in the comparison between the simulated and experimental signals. The modulus of χ_p is given by

$$|\chi_p| = |J_p(k)| \sqrt{3 + 2\cos\left(\frac{4\pi}{3} p\right) + 4\cos\left(\frac{2\pi}{3} p\right)}$$

(2.30)

The value of these coefficients depends partly on the Bessel function, so the conclusions obtained for the spectrum of a single point target are valid in this case. The amplitude given by $J_p(k)$is modified by the square root which is zero if the cosines satisfy the following condition:

$$\cos\left(\frac{4\pi}{3}p\right) = \cos\left(\frac{2\pi}{3}p\right) = \frac{-1}{2} \rightarrow |\chi_p| = 0$$

(2.31)

This occurs certain values of the integer p: $p \neq 3 \cdot q$, where $q \in N$. Consequently, the coefficients related to multiples of the number of blades will appear in the spectrum. The rest of the frequencies will disappear as Fig. 2.7 shows.

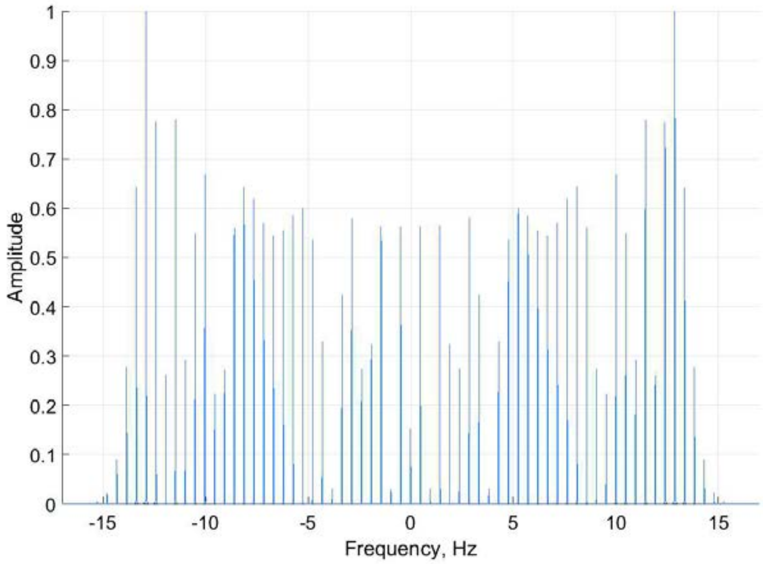

(a)

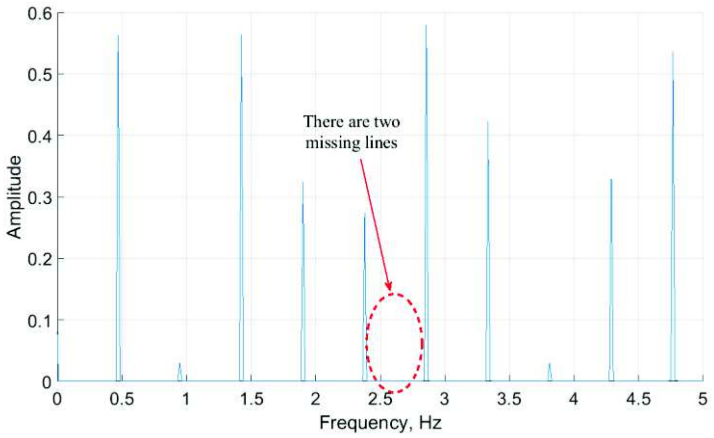

(b)

Fig. 2.7: Spectrum of the backscattered signal from the three tips of a WT. The parameters of the simulation are the same as in Fig. 2.4b. In (a) there are missing peaks that were present in the spectrum of a single target. Graph (b) is a close look at the spectrum of the three tips.

The same mechanical and physical parameters used in Fig. 2.4b have been employed to plot the spectrum in Fig. 2.7. A visual comparison between them indicates there are missing frequencies in the spectrum of the blade tips that appeared in the spectrum of a single point target, which is clearer in Fig. 2.7b. This phenomenon, which is purely theoretical, is due to the assumption of three perfectly aligned identical blades. In order to compare with the experimental spectra, it was necessary to introduce deviations from this symmetric situation in equation (2.25).

2.4 One Blade Modelled as a Line of Point Targets

The next step to reach a realistic WT model was to consider one blade as a straight line of point targets similar to a wire, i.e., a line of N scattering centres as Fig. 2.8 represents.

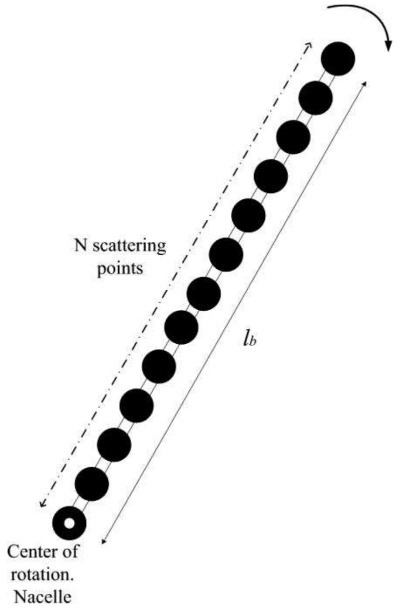

Fig. 2.8: WT blade modelled as a straight line of point-scatterers.

If the blade length is l_b, the separation between two consecutive scattering centres is $h \equiv \frac{l_b}{(N-1)} < \lambda$. Consequently, the distance from the centre of rotation to a particular point n is given by $l_n = n \cdot h$, where $n = 0, 1, \ldots, N-1$.

2.4.1 Time-domain signature

Using the superposition principle once again, the backscattered signal is the sum of the waves radiated by each individual point-scatterer which are given by the expression (2.9). Without loss of generality, the blade $m = 1$ is considered. The signal can be written as

$$s_{R;1}(t) = \sum_{n=0}^{N-1} e^{-j\frac{4\pi}{\lambda}\sqrt{R_N^2+l_n^2+2l_nZ_N\cos\Omega t}} = \sum_{n=0}^{N-1} e^{-j\frac{4\pi}{\lambda}R_N\sqrt{1+\frac{l_n^2}{R_N^2}+\frac{2l_nZ_N}{R_N^2}\cos\Omega t}} \tag{2.32}$$

In order to continue with the analysis, it is important first to make an important distinction between the far-field of the antenna and the far-field of the WT. The first postulation at the beginning of this chapter was that the WT is in the far-field of the antenna, which means that the incident field can be considered as a plane wave over the localised regions of the WT. This presumption is guaranteed if (1) the radar is actually placed far from the turbine or (2) if the radar wavelength is comparable to the transmitter antenna dimensions. The latter corresponds to the experimental system used during the research and explained in Chapter 4 to confirm the theoretical results. However, the wave reflected by the WT needs a more careful analysis. It is important to remember that the goal of this research is to demonstrate the feasibility of monitoring a WT by using radar sensors. In order to do so, the idea is to place the receiver antenna in the vicinity of the WT. Therefore, in this situation, the receiver antenna is located in the near-field of the WT and assumptions on the backscattered wave radiated by the blades have to be taken cautiously.

The research done so far on the characterisation of WT radar signature has assumed a far-field approximation for both the transmitted and received signals. Examples of this work can be found in references [8]-[9]. In this far-field approach, the radial distance R_N is considered much larger than the blade length l_b and after approximating the square root in (2.32) by Taylor

$$s_{R;1}(t) \cong \sum_{n=0}^{N-1} e^{-j\frac{4\pi}{\lambda}R_N\left(1+\frac{l_n^2}{2R_N^2}+\frac{l_n Z_N}{R_N^2}\cos\Omega t\right)}$$

(2.33)

the quadratic term in l_n, $\frac{l_n^2}{2R_N^2}$, is eliminated to write the backscattered signal as

$$s_{R;1}(t) \cong e^{-j\frac{4\pi}{\lambda}R_N} \sum_{n=0}^{N-1} e^{-j\frac{4\pi}{\lambda}\frac{l_n Z_N}{R_N}\cos\Omega t} = C \sum_{n=0}^{N-1} e^{-jB(t)l_n}$$

(2.34)

where $B(t) \equiv \frac{4\pi}{\lambda}\frac{Z_N}{R_N}\cos\Omega t$. In this case, it is straightforward to find a closed form for the backscattered signal if the summation is changed by integration over all the lengths▯▯:

$$s_{R;1}(t) \cong C \int_0^{l_b} dl_n \, e^{-jB(t)l_n} = jC\left[\frac{e^{-jB(t)l_b}}{B(t)} - \frac{1}{B(t)}\right]$$

(2.35)

The real part of the previous expression is the actual signal which can be written as

$$Re\left\{jC\left[\frac{e^{-jB(t)l_b}}{B(t)} - \frac{1}{B(t)}\right]\right\} = Re\left\{\frac{j\cos[B(t)l_b] - \sin[B(t)l_b]}{B(t)}\right\} = -l_b sinc[B(t)l_b]$$

(2.36)

The approximation (2.36) is adequate for the radar-WT distances considered so far in scientific literature. However, the far-field border for a typical WT is given by the Fraunhofer distance $d = 2D^2/\lambda$, where *D* is the largest dimension of the radiator (the WT in this case) and λ is the wavelength of the transmitted signal. The distance *d* is further than the distances considered in the published research studies. In the case of a WT $Z_N = 80\,m$ tall with a blade length of $l_b = 40\,m$ $(D = 80\,m)$ and using a radar frequency of few *GHz*, the far-field is at approximately $80\,km$ which doubles the 40 km considered in experimental literature [9]. Depending on the importance of the accuracy, the approximation (2.36) may be perfectly adequate. Nevertheless, this expression is no longer valid at shorter ranges where this research is interested. A comparison between both solutions, (2.32) and (2.36), for two different distances can be seen in Fig. 2.9. At a distance $R_N = 15\,km$, both expressions give similar results. The approximated solution is offset respect the exact one, but both follow a similar pattern. If the distance is reduced to $R_N = 5\,km$, equation (2.36) does not predict the pattern of the exact expression (2.32). Both graphs represent one revolution of the blade at $\Omega = 2\,rad/s$.

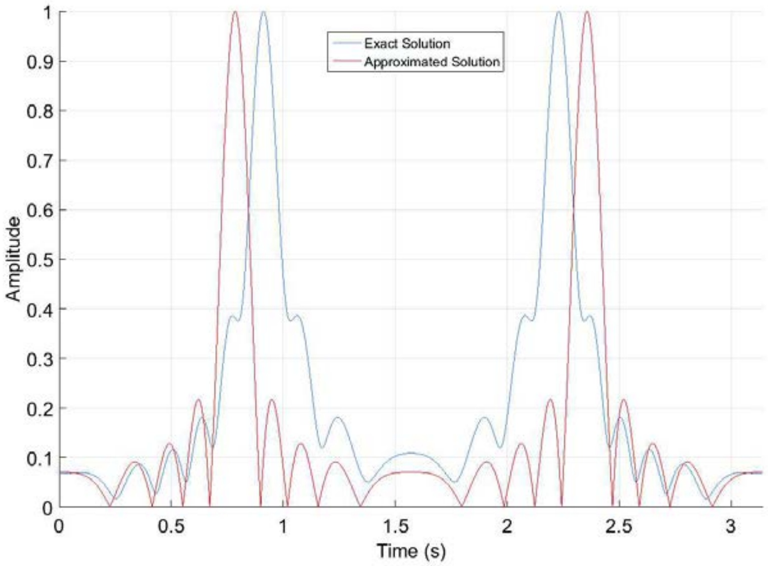

(a)

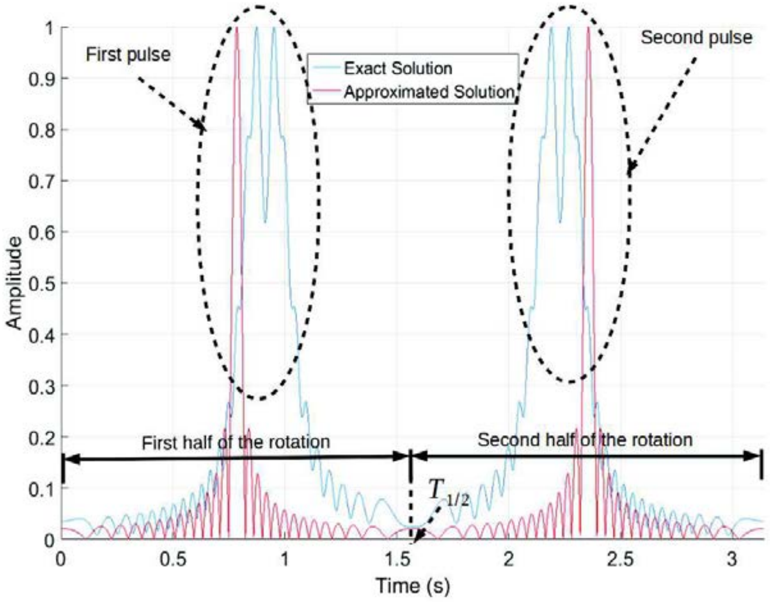

(b)

Fig. 2.9: Exact and approximated solution of the backscattered signal from a wind turbine blade modelled as a wire. (a) $R_N = 15\ km$; (b) $R_N = 5\ km$.

The signals in Fig. 2.9 exhibit two intense returns or pulses in a single period. In the case of Fig. 2.9b, the pulses of the exact solution (2.32) are wider than those predicted by the approximation (2.36). These pulses or returns from (2.32) also exhibit oscillations or sequences of maxima around a central value. The shorter the distance to the radar, the wider and more oscillatory these returns are. On the other hand, the *sinc* function solution has two sharp peaks which are narrower as R_N decreases as can be observed in Fig. 2.9b. Another characteristic of the backscattered signals plotted in Fig. 2.9 is that the pulses are symmetric with respect the half period time, $T_{1/2} = \frac{\pi}{\Omega} = \frac{\pi}{2}\ s$. This reflects the fact that the WT is symmetric respect to the vertical axis that passes through the centre of rotation (nacelle) as Fig. 2.10 shows. Each half of the signal in Fig. 2.9 corresponds to a half rotation.

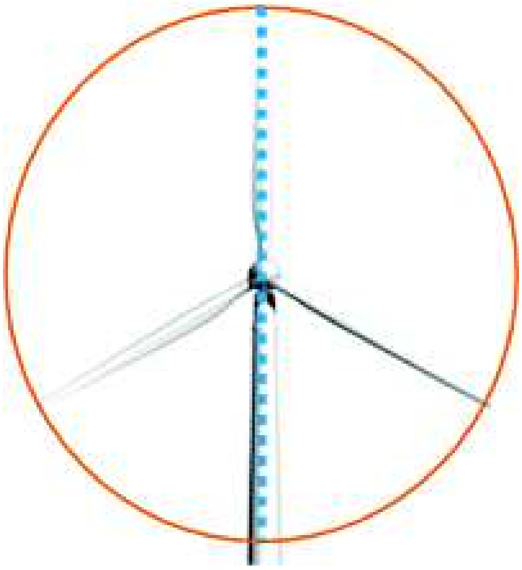

Fig. 2.10: Symmetry of rotation of a WT.

There are several manners of understanding the time-domain pattern of the backscattered signal (2.32). One way is to analyse, in the complex field, the vectors associated to the EM waves reflected by each scattering point (see expression 2.9). All these vectors (or phasors) have the same magnitude (it was assumed the same reflectivity for all the points), but their orientation in the complex field depend on their phases:

$$\theta_n(t) \equiv -\frac{4\pi}{\lambda} R_N \sqrt{1 + \frac{l_n^2}{R_N^2} + \frac{2 l_n Z_N}{R_N^2} \cos \Omega t} \tag{2.37}$$

The resultant signal at a specific time can be constructed by adding up all these vectors at that time. A large vector (a large signal response) might be built if all the individual phasors were aligned at that time. However, this would be only possible if the phase (2.31) were constant.

If the vectors whose phases are larger tan $\theta_0(t) = \frac{-4\pi}{\lambda} R_N$ (the phase of the non-rotating point corresponding to the nacelle) compensate those with smaller phases, the configuration is symmetric and a large resultant vector may be formed. A sketch of this situation is shown in Fig. 2.11. When this situation occurs, the backscattered signal reaches a maximum; at any other instant, the sum results in a smaller total vector.

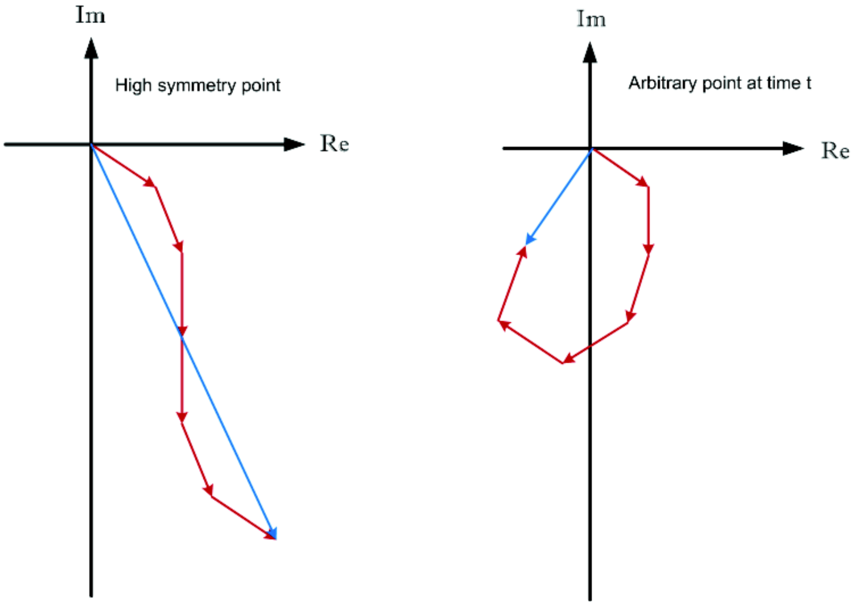

(a) (b)

Fig. 2.11: Phasors in the complex plane.

The symmetric situation observed in Fig. 2.11a is possible due to the quadratic form in l_n of the phase (2.37). If this phase is approximated by Taylor, the real part of the complex signal (2.9) can be expressed by

$$\cos\left[\frac{4\pi}{\lambda}R_N + \frac{2\pi}{\lambda}R_N\left(\frac{l_n^2}{R_N^2} + \frac{2l_nZ_N}{R_N^2}\cos\Omega t\right)\right] = \cos\left[\theta_0 + 2\pi\left(l_n^2\,\frac{1}{\lambda R_N} + l_n\frac{2Z_N}{\lambda R_N}\cos\Omega t\right)\right] \tag{2.38}$$

$$\text{At certain time } t_0,\ \cos\left[\theta_0 + 2\pi\left(p_{t_0} + \delta_{t_0}\right)\right] \tag{2.39}$$

Where $p_{t_0} \in \mathbb{Z}$ and $\delta_{t_0} \in \mathbb{R}$. The term $2\pi\left(p_{t_0} + \delta_{t_0}\right)$ in (2.39) suggests that the phase of the signal has an initial phase θ_0 plus a number of extra p_{t_0}cycles and/or a small fraction of a cycle given by δ_{t_0}. If a great number of phasors are aligned at t_0, as in Fig. 2.11a, the signal will exhibit a maximum in the time-domain. The extra phase in (2.38) may be written as

$$y(l_n) \equiv l_n^2\,\frac{1}{\lambda R_N} + l_n\frac{2Z_N}{\lambda R_N}\cos\Omega t \tag{2.40}$$

This function was plotted in Fig. 2.12 at three different times: $0, t_c, \frac{T}{2}$. The value $t_c$will be given later. T is the period of a WT revolution. At $t = 0$, all the individual signals from each scattering centre have a quadratic decreasing phase. The resultant vector has a small magnitude as in Fig. 2.11b. A similar situation occurs if $t = \frac{T}{2}$, but the phases have a increasing character in this case. Therefore, there are two extreme situations: $y(l_b)]_{t=0} > 0$ and $y(l_b)]_{t=\frac{T}{2}} < 0$. It is clear that there has to be a time such that $y(l_b)]_t = 0$. This time is t_c and it will be called the centre time of the pulse or return in the first half of the blade rotation (see Fig. 2.9b). For large R_N, the signal reaches its maximum at exactly t_c. At closer distances, the signal return gets wider and t_c simply gives its centre time position. This can be observed in Fig. 2.12.

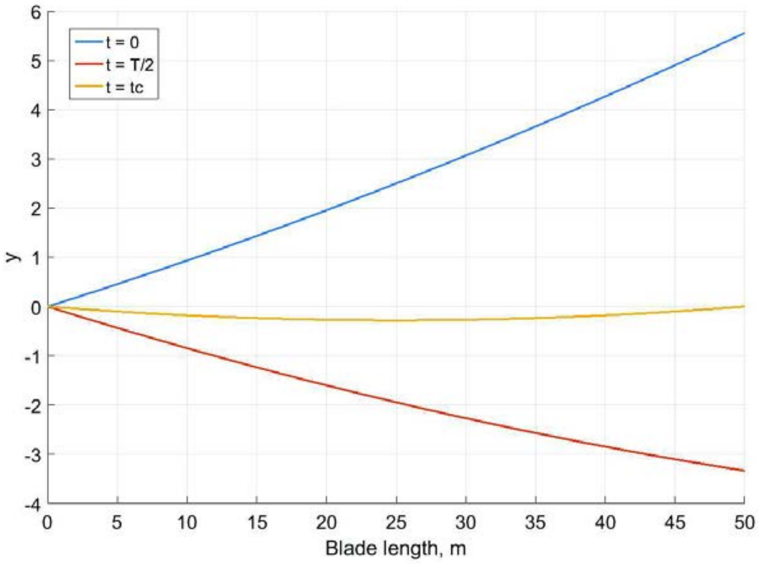

Fig. 2.12: Phase increment for each scattering point and three different times: $t = 0, t_c, \frac{T}{2}$.

It is possible to get an explicit expression for t_c from the condition $y(l_b)]_{t=t_c} = 0$:

$$l_b^2 \frac{1}{\lambda R_N} + l_b \frac{2Z_N}{\lambda R_N} \cos \Omega t_c = 0 \rightarrow t_c = \frac{1}{\Omega} \cos^{-1}\left(\frac{-l_b}{2Z_N}\right) \tag{2.41}$$

This time is independent of the distance R_N and it is only a function of the physical parameters of the WT. The graphs in Fig. 2.13 corresponds to the same signals plotted in Fig. 2.9 (only the exact solutions (2.32)) where the positions of the centre of the pulses have been marked. The numerical value of these times are, in both situations,

$$t_c = \frac{1}{\Omega} \cos^{-1}\left(\frac{-l_b}{2Z_N}\right) = \frac{1}{2} \cos^{-1}\left(\frac{-50}{2 \cdot 100}\right) \approx 0.91\ s$$

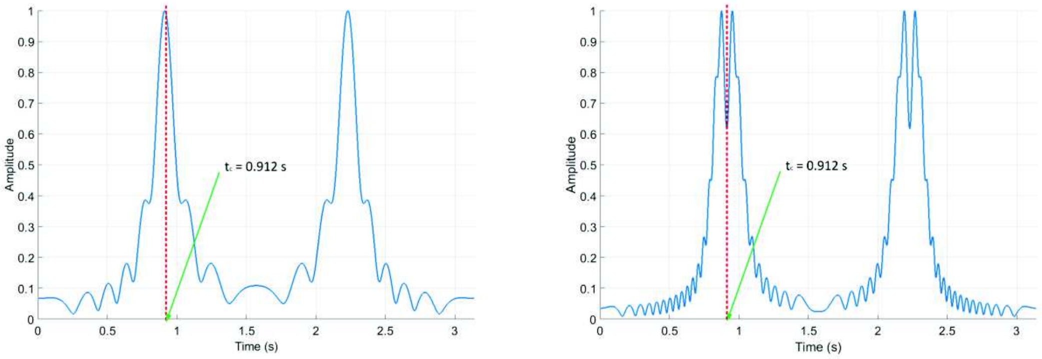

(a) (b)

Fig. 2.13: Centre time of the pulses for two distances: (a) $R_N = 15\ km$, (b) $R_N = 5\ km$.

It is clear that, in the far-field case (Fig. 2.13a), t_c corresponds to the maximum of the first signal return (first half rotation). In the near-field situation (Fig. 2.13b), t_c gives the position in time of the centre of the first signal return.

The formation of the two returns or pulses observed in Fig. 2.13 has a clear physical explanation when R_N is large enough (the meaning of this statement will be explained later). If the individual backscattering signals that form (2.32) follow the same optical path, their interference at the radar position is constructive and, consequently, a strong response can be measured. Although geometrically it can be argued that not all the signals can have the same phase, there is a situation where all the waves are in phase by pairs, as it will be explained shortly.

The distances radar-blade tip and radar-nacelle (centre of rotation) are

$$\begin{gathered} r_{tip}^2(t) = R_N^2 + l_b^2 + 2l_b^2 Z_N \cos \Omega t \\ r_{nacelle}^2(t) = R_N^2 \end{gathered} \tag{2.42}$$

If both distances are the same, the backscattered waves associated to these two point-scatterers are in phase; they are forming an isosceles triangle. This takes place at t_c:

$$r_{tip}^2(t) - r_{nacelle}^2(t) = 0 \rightarrow t = \frac{1}{\Omega} \cos^{-1}\left(\frac{-l_b}{2Z_N}\right) = t_c \tag{2.43}$$

Therefore, the expression for t_c has been recovered by physical argumentation exclusively. It is important to notice that t_c in (2.43) has been obtained from the exact expression of the phase (2.37) and not from its approximation.

The rest of the scattering points that are symmetric respect to the centre of the blade are also in phase. This last statement is geometrically clear and it can be demonstrated mathematically. From Fig. 2.14, two symmetric points a and b can be label as

$$n_a = \frac{N}{2} - p - 1 \text{ and } n_b = \frac{N}{2} + p \tag{2.44}$$

Where $p = 0, 1, 2, \dots, \frac{N}{2} - 1$. Therefore, the distances between these scattering centres and the radar are

$$r_a^2(t) = R_N^2 + h^2\left(\frac{N}{2} - p - 1\right)^2 + 2h\left(\frac{N}{2} - p - 1\right) Z_N \cos \Omega t$$

$$r_b^2(t) = R_N^2 + h^2\left(\frac{N}{2} + p\right)^2 + 2h\left(\frac{N}{2} + p\right) Z_N \cos \Omega t \tag{2.45}$$

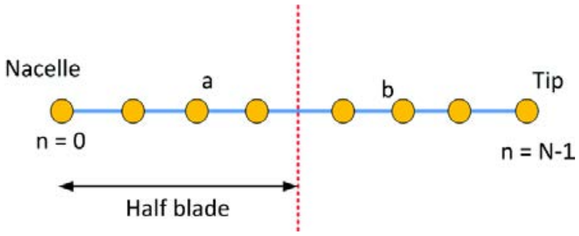

Fig. 2.14: Sketch of the blade modelled as a line of scattering points.

It the two distances in (2.45) are the same, their corresponding waves are in phase, i.e. when

$$r_a^2(t) - r_b^2(t) = 0$$

(2.46)

After the appropriate mathematical manipulation, this last condition can be written as

$$r_a^2(t) - r_b^2(t) = h^2[(2p + 1)(N - 1)] + 2hZ_N \cos \Omega t \, [2p + 1] = 0$$

(2.47)

The distance between two consecutive scattering centres, as stated at the beginning of this section, is $h = \frac{l_b}{(N-1)}$. Introducing this expression into the condition (2.47):

$$r_b^2(t) - r_a^2(t) = \frac{l_b^2}{(N-1)^2}[(2p+1)(N-1)] + 2\frac{l_b}{N-1}Z_N \cos \Omega t\,[2p+1] = 0$$

$$r_b^2(t) - r_a^2(t) = l_b^2 + 2l_b^2 Z_N \cos \Omega t = 0 \rightarrow t = \frac{1}{\Omega}\cos^{-1}\left(\frac{-l_b}{2Z_N}\right) = t_c$$

(2.48)

Therefore, it can be concluded that at t_c all the backscattered waves are in phase by pairs.

As the value of R_N decreases, the pulses in the time-domain become wider and other maxima and minima appear around the central time, as it is observed in Fig. 2.13b where two maxima appear at each side of t_c. In fact, the value of these maxima exceed the value of the signal at t_c.

In order to understand this behaviour, a further analysis of the function (2.40) is necessary. The minimum of this function at t_c, which corresponds to a maximum in the phase change (2.38), is

$$y_{min}(t_c) = \frac{-l_b^2}{4\lambda R_N}$$

(2.49)

A shorter R_N corresponds to a deeper minimum of the function y at t_c. This implies that the vectors of Fig. 2.11a will exhibit a larger deviation from the initial phase and, consequently, the resulting vector will have a smaller magnitude: the intensity of the signal will diminish.

Another implication of a shorter t_c is that there are blade positions of high symmetry apart from the one at t_c. In Fig. 2.15, the function $y(l_n)$has been plotted at t_c and $t_1 = 0.951\ s$ which is the instant of time when the first maximum takes place in Fig. 2.13b just before the centre time. At t_1, the phasors of the point-scatterers between $l_n = 15\ m$ and $l_n = l_b = 50\ m$ have already completed one revolution in the complex field since $y(l_n = 15)]_{t_1} = y(l_n = 50)]_{t_1} = -1$. The curve corresponding to t_1 below $y = -1$ is geometrically equivalent to the curved corresponding to t_c. Therefore, the conclusions obtained in the case of t_c can be applied in the situation of t_1. This implies that another maximum is expected, although it will be "dimmer" since only part of the blade (from $l_n = 15\ m$ to $l_n = 50\ m$) is producing a constructive interference. The same situation will occur when the phasors complete any integer number of revolutions in the complex field and, consequently, peaks of different intensities will be produced.

Although these secondary peaks are necessarily less intense than the maximum in Fig. 2.13a, the value of the signal at t_c diminishes as R_N decreases. Therefore, it is possible that the secondary maxima are more intense than the central peak in relative terms, as it occurs in Fig. 2.13b. Consequently, the pulses observed in the time-domain signature of a single blade will get wider. This effect is consistent with the principle of conservation of energy.

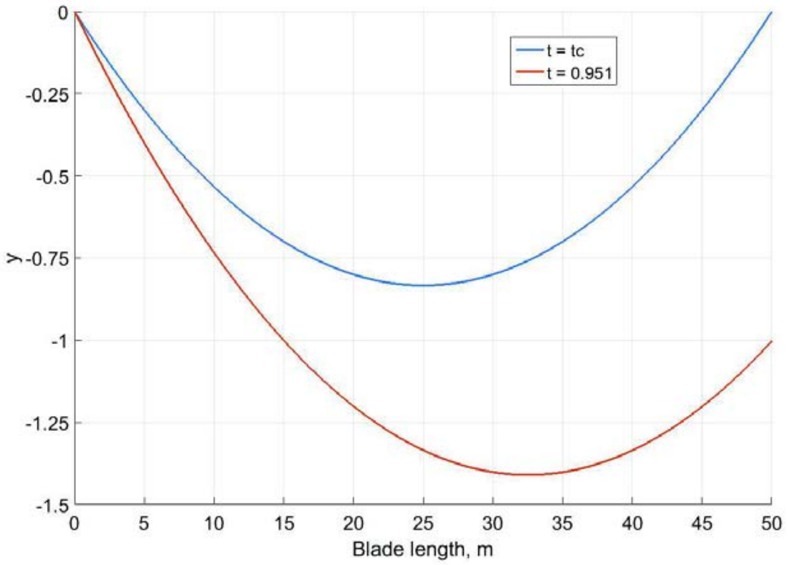

Fig. 2.15: Curve y at two different times.

There is another way of understanding the behaviour of the signal (2.32) in the time-domain. The frequency of each individual backscattered signal is, by definition, the time derivative of the individual phases (2.37). The approximation by Taylor of this phase is the argument of the cosine in (2.38). Therefore, the oscillation rate of the signal corresponding to a particular scattering-centre *n* is approximately given by

$$f_n(t) \equiv \frac{1}{2\pi}\frac{d}{dt}\theta_n(t) \approx \frac{2l_n Z_N}{\lambda R_N}\Omega \sin \Omega t \tag{2.50}$$

The frequency (2.50) has two important features:

- Its value at a fixed time depends on the specific point n: $f_n(t) \propto l_n$. Larger n implies higher frequency.

- It varies with time.

Each individual backscattered signal has a different initial phase at $t = 0$ and its frequency corresponds to $f_n(t = 0) = 0\ Hz$. The time-domain of two of these signals, $l_{n=15} = 2.5\ m$ and $l_{n=50} = 8.4\ m$, has been plotted in Fig. 2.16. In this case, the $50\ m$ blade has been divided into $N = 300$ points ($\lambda \sim 0.25\ m\ \rightarrow N\ > 200$). The signal corresponding to $n = 50$ oscillates faster than the other one since, based on (2.50), a longer l_n implies a higher frequency. Consequently, the relative phases between different signals change continuously: they move at different speeds. The signals will not be synchronised in general, so their interference will be partly destructive. However, a group of signals that performs an integer number of oscillations after a certain time will be synchronised; they will cause constructive interference. Therefore, an intense response in the total signal can be produced if this group of waves is large enough.

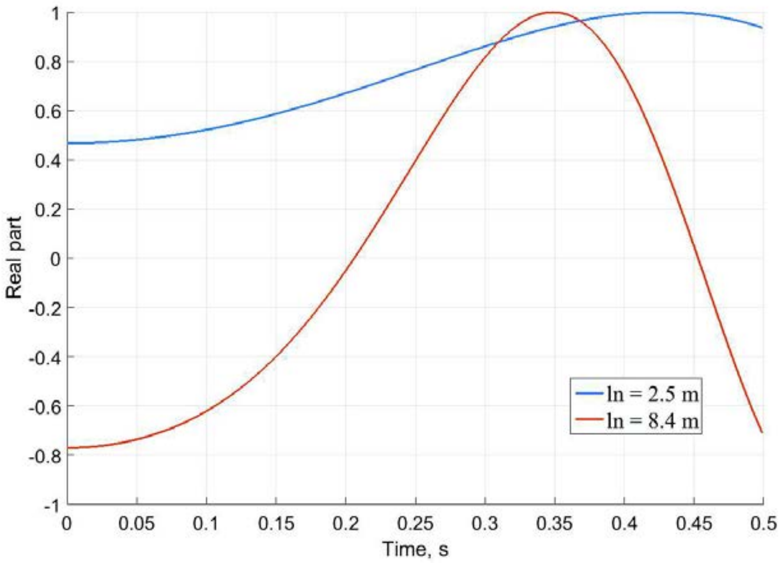

Fig. 2.16: Real parts of the signals from two different point-scatterers.

It can be showed that, in the time interval from $0.8\ s$ to $1\ s$ approximately, an important portion of individual signals from different scattering points are nearly in phase. Consequently, an intense response will take place in that interval. The particular pattern of the response will depend on the physical parameters of the system radar-WT. This synchronisation of a great portion of individual waves at the interval $t \in [0.8, 1.0]$ can be explained mathematically by analysing the phase in (2.38). Each individual signal reaches its maxima when the phase equals $2\pi p$, $p \in \mathbb{Z}$. The instants of time when the maxima take place are

$$\tilde{\theta}_n(t) \equiv -\frac{4\pi}{\lambda R_N}\left(\frac{l_n^2}{2} + l_n Z_N \cos \Omega t\right) = 2\pi p \rightarrow t = \frac{1}{\Omega}\cos^{-1}\left(\frac{-p\lambda R_N + l_n^2}{2 l_n Z_N}\right) \tag{2.51}$$

There is a restriction in the values of p since it is necessary to select the correct branch for the *arc cosine* function. Thus,

$$\left|\frac{-p\lambda R_N + l_n^2}{2 l_n Z_N}\right| \leq 1 \leftrightarrow p_{n;min} \equiv -\frac{2}{\lambda R_N}\left\lceil l_n Z_N + \frac{l_n^2}{2}\right\rceil \leq p \leq \frac{2}{\lambda R_N}\left\lfloor l_n Z_N - \frac{l_n^2}{2}\right\rfloor \equiv p_{n;max} \tag{2.52}$$

The expression (2.51) versus p has been plotted in Fig. 2.17 for several point-scatterers between the centre of rotation $l_n = 0$ and the blade tip $l_n = l_b$. Although the curves in Fig. 2.17 are continuous, the function (2.51) is evaluated only at the integer values given by (2.52). Approximately, all the signals have maxima from $0.8\ s$ to $1.0\ s$. Therefore, the total signal will present an intense backscattered response, which is observed in the time domain of Fig. 2.13b.

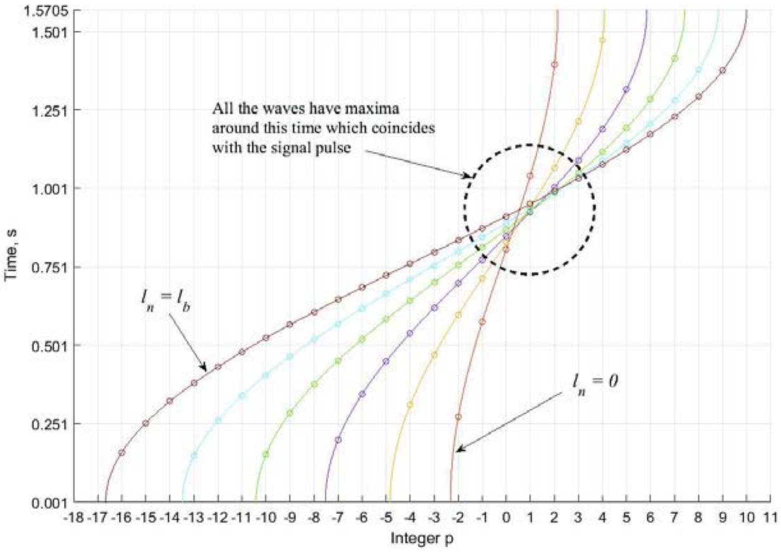

Fig. 2.17: Maxima of signals from different parts of the blade.

2.4.2 Frequency-domain signature

As has been done in section 2.2 and 2.3, the Jacobi-Anger expansion can be used to obtain information about the spectrum of the backscattered signal (2.32). Therefore, the expansion of this signal is

$$s_{R;1}(t) = \sum_{n=0}^{N-1} e^{-j\frac{4\pi}{\lambda}R_N\sqrt{1+\frac{l_n^2}{R_N^2}+\frac{2l_nZ_N}{R_N^2}\cos\Omega t}} \cong \sum_{n=0}^{N-1} e^{-j\frac{4\pi}{\lambda}R_N\left(1+\frac{l_n^2}{2R_N^2}+\frac{l_nZ_N}{R_N^2}\cos\Omega t\right)} = \sum_{n=0}^{N-1} C_n e^{jk_n\cos\Omega t}$$

$$s_{R;1}(t) = \sum_{n=0}^{N-1}\sum_{p=-\infty}^{\infty} C_n j^p J_p(k_n) e^{jp\Omega t} = \sum_{n=0}^{N-1}\sum_{p=-\infty}^{\infty} \chi_{np} e^{jp\Omega t}$$

(2.53)

The Fourier transform, in the sense explained in section 2.2 equation (2.23), can be computed from the last term in (2.53):

$$F\{s_{R;1}(t)\}(\omega) \equiv \Phi_{R;1n}(\omega) = \sum_{n=0}^{N-1} \sum_{p=-\infty}^{\infty} \chi_{np} \delta(p\Omega - \omega) \tag{2.54}$$

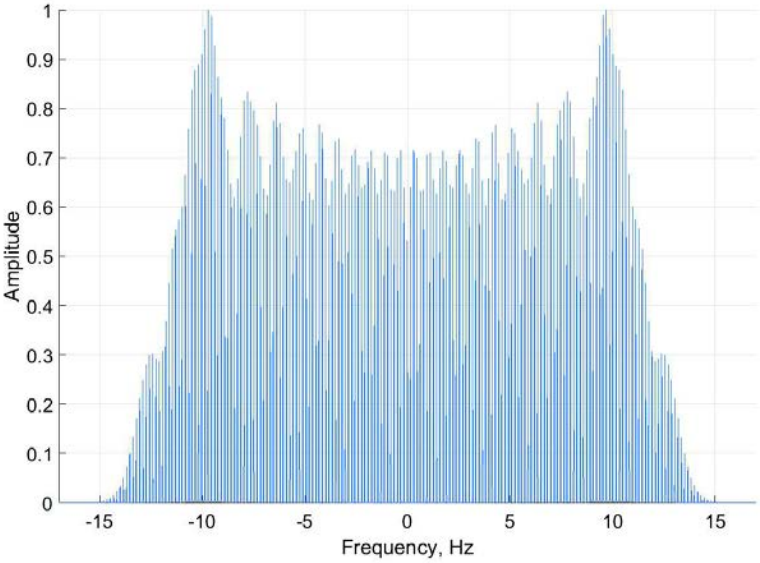

Fig. 2.18: Spectrum of a single blade modelled as a line of scattering points.

Fig. 2.18 corresponds to the spectrum of the signal (2.32) for several revolutions with the following parameters of the radar-WT system: $R_N = 5\,km$, $Z_N = 2l_b = 100\,m$, $f_0 = 2\,GHz$ and $\Omega = 1\,rad/s$. The spectrum is formed by spectral lines at frequencies $f_p = \frac{\Omega}{2\pi} p$ whose amplitudes depend on the coefficients χ_{np}, as was the case of one and three scattering points. The same conclusions obtained in section 2.2 can be applied in this situation.

2.5 Three Blades Modelled as Wires

The first simple full model of a WT consists of three blades modelled as straight lines of scattering points, in the same way as in section 2.4.

2.5.1 Time-domain signature

The signals of two consecutive blades are shifted in time $\frac{2\pi}{3\Omega}$ s, as expression (2.7) takes into account. Therefore, the full backscattered signal is the linear combination of three expressions like (2.32), each one shifted in time adequately:

$$s_R(t) = \sum_{m=1}^{3} s_{R;m}(t) = \sum_{m=1}^{3}\sum_{n=0}^{N-1} e^{-j\frac{4\pi}{\lambda}R_N\sqrt{1+\frac{l_n^2}{R_N^2}+\frac{2l_nZ_N}{R_N^2}\cos\left[\Omega t+\frac{2\pi}{3}(m-1)\right]}} \tag{2.55}$$

Expression (2.55) can be approximated by Taylor to write

$$s_R(t) \cong \sum_{m=1}^{3}\sum_{n=0}^{N-1} e^{-j\frac{4\pi}{\lambda}R_N\left(1+\frac{l_n^2}{2R_N^2}+\frac{l_nZ_N}{R_N^2}\cos\left[\Omega t+\frac{2\pi}{3}(m-1)\right]\right)} \tag{2.56}$$

After using the Jacobi-Anger expansion and rearranging the terms corresponding to the three blades signals, the previous expression becomes

$$s_R(t) \cong \sum_{n=0}^{N-1} C_n \left[\sum_{p=-\infty}^{\infty} j^p J_p(k_n)\, e^{jp\Omega t} + \sum_{p=-\infty}^{\infty} j^p J_p(k_n)\, e^{jp\left(\frac{2\pi}{3}+\Omega t\right)} + \sum_{p=-\infty}^{\infty} j^p J_p(k_n)\, e^{jp\left(\frac{4\pi}{3}+\Omega t\right)} \right]$$

$$s_R(t) \cong \sum_{n=0}^{N-1} C_n \left[\sum_{p=-\infty}^{\infty} j^p J_p(k_n) \left(e^{jp\Omega t} + e^{jp\left(\frac{2\pi}{3}+\Omega t\right)} + e^{jp\left(\frac{4\pi}{3}+\Omega t\right)} \right) \right]$$

(2.57)

where the constants C_n and k_n are the same expressions given by (2.13). Regrouping all the constants in a single one, the approximated total backscattered signal can be written as

$$s_R(t) \cong \sum_{n=0}^{N-1} \sum_{p=-\infty}^{\infty} \chi_{np} e^{jp\Omega t}$$

(2.58)

This signal is formally identical to (2.12), (2.28) and (2.53) which correspond to the signals of a single point, the three blade tips and a single blade, respectively. They differ in the value of the coefficients χ_{np} associated to each component of the expansion.

Fig. 2.19 corresponds to the time-domain signature of the signal (2.55) over one full period $T = \frac{2\pi}{\Omega}\ s$. The backscattered signal is formed by a train of pulses with a pulse repetition time of $\frac{2\pi}{3\Omega}\ s$, the shift between two blade signals. This characteristic is expected since the WT position at a given time is replicated every $\frac{2\pi}{3} rad$ (the angle between two consecutive blades).

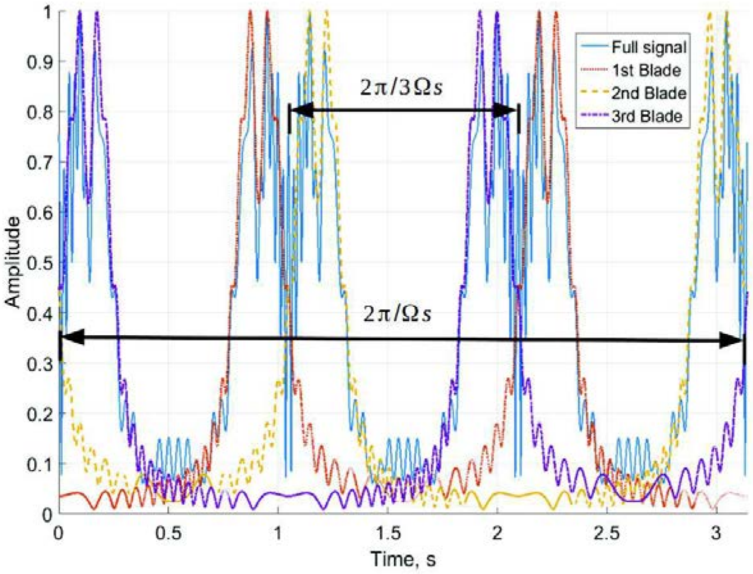

Fig. 2.19: Time-domain signature of WT blades modelled as wires.

Fig. 2.19 also shows that the full signal is a combination of the individual signals from each one of the three blades. In fact, each pulse in the total backscattered signal (in blue in Fig. 2.19) is the union of two returns of two blades, which can be explained as follows. The centre of the first pulse in the signal associated to the first blade is produced when it is at the angular position Ωt_c. Thus, this blade contributes considerably to the total signal. The second blade will reach the symmetrical position (respect to the vertical axis) at a different time, but immediately after. Consequently, the two near individual returns produce a wide and intense response in the full signal. The contribution of the third blade can be neglected as it is in a geometrical position that produces a small signal amplitude. The situation described can be geometrically visualised in Fig. 2.20.

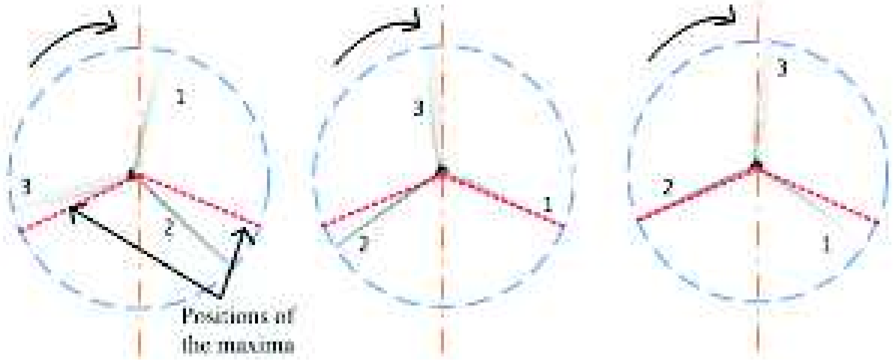

Fig. 2.20: Positions of maximum in the radar echo signal.

2.5.2 Frequency-domain signature

As has already been stated, the approximated signal (2.58) is formally similar to the rest of the signals studied in this chapter so far. Therefore, the same conclusions about the frequency domain obtained in previous sections are now valid. The approximated spectrum is given in this case by

$$\Phi_R(\omega) = F\left\{\sum_{n=0}^{N-1}\sum_{p=-\infty}^{\infty}\chi_{np}e^{jp\Omega t}\right\}(\omega) = \sum_{n=0}^{N-1}\sum_{p=-\infty}^{\infty}\chi_{np}\delta(p\Omega-\omega)$$

(2.59)

The spectral lines in the spectrum are the same as in the case of a single blade. However, the amplitude of each particular frequency differs in both cases. The module of the coefficients in (2.59) are

$$|\chi_{np}| = |J_p(k_n)|\sqrt{3 + 2\cos\left(\frac{4\pi}{3}p\right) + 4\cos\left(\frac{2\pi}{3}p\right)}$$

(2.60)

and, as it happened in the case of the three blade tips (section 2.3), the coefficients are zero for certain values of the integer p:

$$\cos\left(\frac{4\pi}{3}p\right) = \cos\left(\frac{2\pi}{3}p\right) = \frac{-1}{2} \rightarrow |\chi_{np}| = 0$$

(2.61)

These frequencies do not appear in the spectrum, but it was explained in section 2.2 this phenomenon is purely theoretical and it emerges from the supposition that blades are exactly separated by $\frac{2\pi}{3}\ rad$. This phenomenon can be observed in Fig. 2.21 where the spectra for several revolutions of a single blade and a full WT are compared.

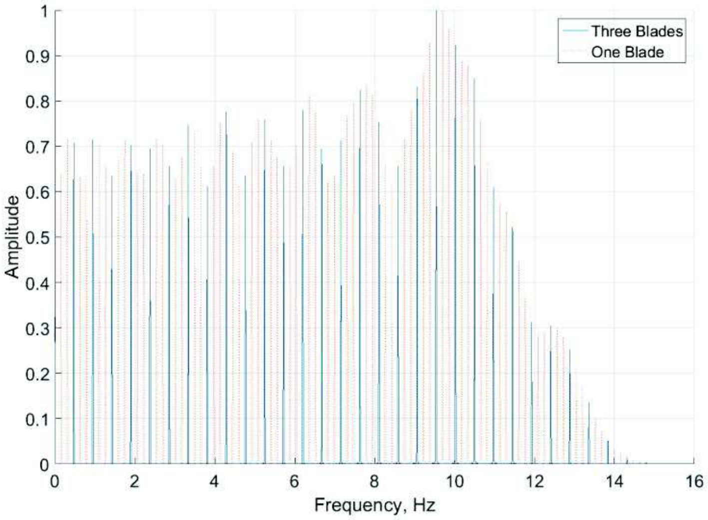

Fig. 2.21: One-sided spectra of three blades and one blade.

2.6 One and Three Blades Modelled as Rectangular Plates

There are three main reasons why the analysis of this type of blades was important for the research. Firstly, the mathematical study of such blades was easily approachable. Secondly, the shape of these blades could be easily programmed on Matlab in order to simulate the backscattered signal and compare it to the experimental results. Finally, this kind of blade could be built easily for experimental purposes.

In this section, a WT blade is modelled as a group of scattering points that form a rectangular plate, as it is sketched in Fig. 2.22. This model is a better representation of an actual WT blade.

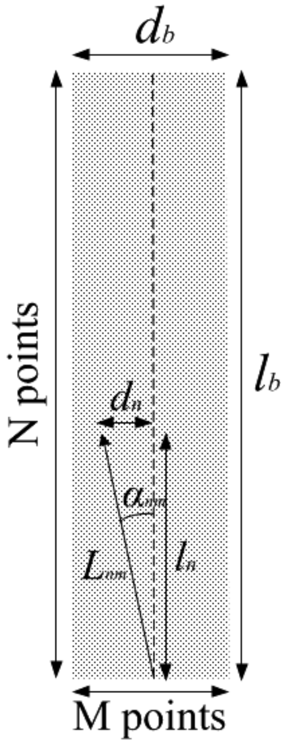

Fig. 2.22: WT blade modelled as a group of scattering points forming a rectangular plate.

The distance between any point-scatterer and the radar has to be modified with respect to the case described in section 2.2. If the blade dimensions are⍰⍰×⍰⍰and they are divided in both directions into $N \in \mathbb{Z}^+$ and $M \in (2\mathbb{Z}^+ + 1)$ points respectively, the separation between two scattering centres in each direction is

$$h_V = \frac{l_b}{N-1}$$

$$h_H = \frac{d_b}{M-1}$$

(2.62)

The coordinates of each point-scatterer in the WT system, whose origin is the centre of rotation of the blades, can be written as

$$l_n = N \cdot h_V$$

$$d_m = M \cdot h_H$$

$$L_{nm} = \sqrt{l_n^2 + d_m^2}$$

(2.63)

2.6.1 Time-domain signature

If the WT is facing the radar, the distance radar-point is given by

$$r_{q;nm}(t) = \sqrt{R_N^2 + L_{nm}^2 + 2L_{nm}Z_N \cos\left[\Omega t + \alpha_{nm} + \frac{2\pi}{3}(q-1)\right]}$$

(2.64)

where index $q = 1,2,3$ labels the blade and $\alpha_{nm} \equiv \sin^{-1}\left(\frac{d_m}{L_{nm}}\right)$. The backscattered signal associated to an arbitrary scattering point is now given by

$$s_{R;qnm}(t) = e^{-j\frac{4\pi}{\lambda}\sqrt{R_N^2+L_{nm}^2+2L_{nm}Z_N \cos\left[\Omega t+\alpha_{nm}+\frac{2\pi}{3}(q-1)\right]}}$$

(2.65)

and the full signal of a single blade is obtained by the addition of all the scattering centres:

$$s_{R;q}(t) = \sum_{n=0}^{n=N-1} \sum_{m=\frac{-(M-1)}{2}}^{m=\frac{M-1}{2}} e^{-j\frac{4\pi}{\lambda}\sqrt{R_N^2+L_{nm}^2+2L_{nm}Z_N \cos\left[\Omega t+\alpha_{nm}+\frac{2\pi}{3}(q-1)\right]}}$$

(2.66)

The complete backscattered signal of a WT whose blades are modelled as a rectangular plate is the sum of the three possible signals (2.66):

$$s_R(t) = \sum_{q=1}^{3} \sum_{n=0}^{n=N-1} \sum_{m=\frac{-(M-1)}{2}}^{m=\frac{M-1}{2}} e^{-j\frac{4\pi}{\lambda}\sqrt{R_N^2+L_{nm}^2+2L_{nm}Z_N \cos\left[\Omega t+\alpha_{nm}+\frac{2\pi}{3}(q-1)\right]}}$$

(2.67)

The signals (2.66) and (2.67) can be approximated by Taylor in the same way done in previous sections. Subsequently, the Jacobi-Anger expansion can be invoked to expand these signals in the basis of their harmonics. In this case, the coefficients associated to each component of the expansion will depend on three indexes:

$$s_{R;q}(t) = \sum_{n=0}^{n=N-1} \sum_{m=\frac{-(M-1)}{2}}^{m=\frac{M-1}{2}} \sum_{p=-\infty}^{\infty} \chi_{nmp} e^{jp\Omega t} \tag{2.68}$$

The time-domain signature of one blade does not change drastically with respect to the case of a “wire blade” as it can be seen in Fig. 2.23. The phase difference is small between a scattering point on the central line of the plate ($d_m = 0, \forall n$, i.e. the “wire blade”) and a point out of this line. Therefore, the signal of the rectangular plate blade differs slightly from the wire blade signal. However, the signal response is more intense since the rectangular blade has a larger surface and therefore it reflects more energy. If the width of the blade d_b is large, the pattern of the signal might change, but in general it is much smaller that its length l_b.

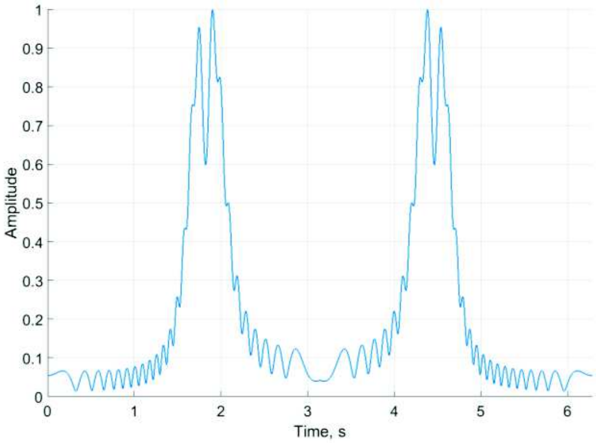

Fig. 2.23: Time-domain signature of a rectangular blade. The physical parameters are: $R_N = 5\,km$, $Z_N = 2l_b = 100\,m$, $\Omega = 1\,rad/s$ and $f_0 = 2\,GHz$.

2.6.2 Frequency-domain signature

The same general conclusions obtained in sections 2.4 and 2.5 about the spectrum are valid in this case. The expression (2.68) has the same analytical form as the functions studied in previous sections. Fig. 2.24 corresponds to the spectra of one and three rectangular blades. As it can be observed, there is no great difference with respect to Fig. 2.21.

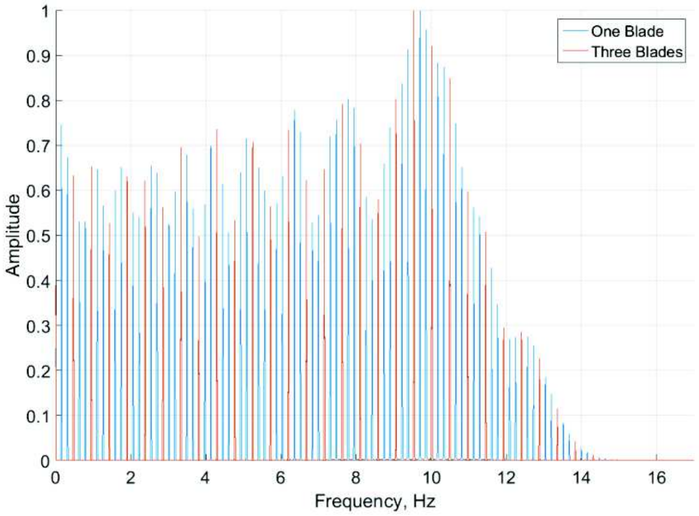

Fig. 2.24: Positive-side spectra of one and three rectangular blades. The physical parameters are the same as in Fig. 2.23.

2.7 Micro-Doppler Signature

As was introduced in Chapter 1, the time and frequency domains are not the only representations of the radar signature of a target. Moreover, they are not the most adequate representations if the frequency content of the signal varies over time, as it was the case studied in this research. This time variation in the frequency was clear in the time-domain signatures analysed in previous sections. For example, the signal produced by the rotation of a single scattering point on one of the blades was given by (2.9):

$$s_{R;1n}(t) = e^{-j\frac{4\pi}{\lambda}\sqrt{R_N^2+l_n^2+2l_nZ_N\cos\Omega t}}$$

This signal exhibits a time-dependent variation of the frequency, although it does not show manifestly this variation. Obtaining an expression of the frequency as a function of time is not a straightforward task since the time-domain representation conceals information about the frequency.

The approximated Fourier transform of the prior function is given by the equation (2.23):

$$\Phi_{R;1n}(t) = C_n \sum_{p=-\infty}^{\infty} j^p J_p(k_n)\, \delta(p\Omega - \omega)$$

This expression shows that the spectrum is formed by an infinite series of delta functions, although only a limited number of them are significant (this has been analysed in section 2.2). Therefore, the frequency representation hides (even more than the time-domain) information about the variation of the frequency over time; the spectrum shows what are the frequencies present in the signal, but not when they take place.

Instead of using the time and frequency domains, the joint time-frequency transforms can be applied to fully characterise the time-varying frequency content of the signal. The best-known of these transformations is the called *Short Time Fourier Transform* (STFT) which consists in dividing the time-domain signal into various segments and take the Fourier transform of each of them [10]-[11]. Its mathematical definition is

$$STFT(t,f) = \int dt' s(t') w(t'-t) e^{-j2\pi f t'}$$

(2.69)

The window function $w(t)$ selects part of the signal $s(t)$ and computes its spectrum. Therefore, the STFT is basically a moving Fourier transform along the signal. The squared magnitude of equation (2.69) forms spectrogram [12]:

$$Spectrogram(t,f) = |STFT(t,f)|^2$$

(2.70)

A spectrogram is a technique that provides visual information on the time-varying frequency content of a signal at different instants of time. This standard representation in the $(t,f)-space$ facilitates the display of different EM mechanism present in the physical system under analysis.

Fig. 2.25a corresponds to the spectrogram of a single point-scatterer. It simply represents the trace of the sinusoidal time-variation of the frequency as the target rotates.

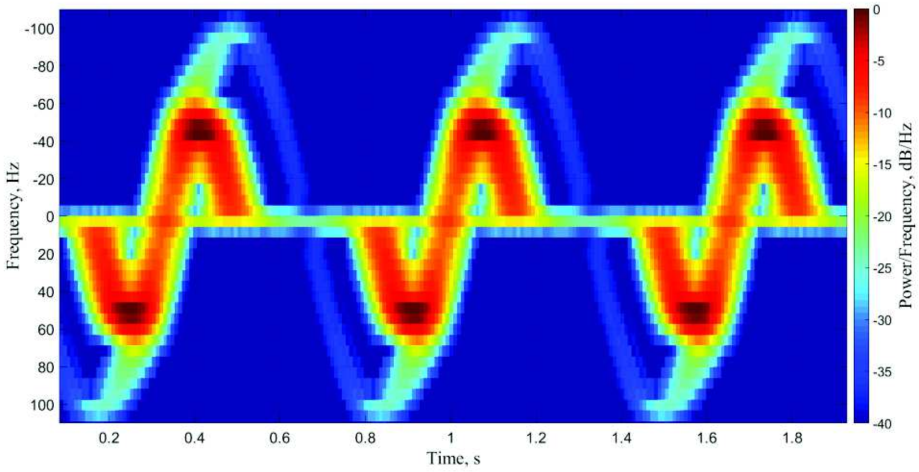

Fig. 2.25: Spectrogram of a blade modelled as a line of points.

Fig. 2.25 corresponds to the spectrogram of a blade modelled as a line of scattering points where different features can be observed. It was derived using blocks of data equal to 7680 samples each, using a Gaussian window and a 5% overlap between consecutive blocks. First of all, the sinusoidal pattern observed corresponds to returns from the blade tip for two rotations. A bright flash due to the maximum backscattered energy at t_c can be observed and, as may be expected, it is not associated to the blade tip. The explanation of this phenomenon lies in the nature of the spectrum of the signal. It was shown in section 2.2 that the amplitudes of the frequencies in the spectrum depend on the Bessel functions whose value ultimately relies on the WT physical parameters its distance to the radar. Therefore, and as can be seen in the spectrum of the different targets studied in this chapter, the maximum amplitude is not associated to the blade tip.

The instantaneous frequency of a signal is given by

$$f_I(t) \equiv \frac{1}{2\pi}\frac{d}{2\pi}\theta(t)$$

(2.71)

In the case of a single scattering point, the previous formula represents its micro-Doppler frequency and it can be written

$$f_{\mu D;n}(t) = \frac{2\Omega l_n Z_N}{\lambda}\frac{\sin \Omega t}{\sqrt{R_N^2 + l_n^2 + 2 l_n Z_N \cos \Omega t}}$$

(2.72)

In general, the maximum frequency associated to the tip is calculated by approximating the phase of the signal by Taylor which results in an instantaneous frequency given by

$$f_{I;tip}(t) \cong \frac{2\Omega l_n Z_N}{\lambda R_N}\sin \Omega t$$

(2.73)

For the physical parameters used to simulate the spectrum and spectrogram of a single blade (Fig. 2.18 and 2.25 respectively), the maximum frequency is given when $\sin \Omega t = 1$ and it is $f_{max;tip} \approx 13\ Hz$. However, the strongest response in the spectrogram is at $10\ Hz$. The same occurs in the spectrum where the maximum amplitude are around the same frequency value.

The discrepancy between the expected maximum and the actual one is also due to the approximation (2.51). The maximum in this expression takes place when $\sin \Omega t = 1$, but this is not the case for the equation (2.50). When the sine is equal to the unit, the cosine in the denominator is zero. However, that is not the maximum that (2.50) can reach; there is a trade-off between the sine and cosine to maximise the frequency value.

2.8 Summary

In this chapter, a theoretical model to describe WT radar returns in the near-field has been developed. This model has received the name of Scattering Centres Model or SCM and it considers the WT blades as formed by a group of point-scatterers. By computing the backscattered signal from an individual scattering centre, the full WT radar echo has been modelled and simulated.

The time and frequency domains, as well as the joint time-frequency domain, of the different targets considered has been analysed. The radar returns from a WT in the near-field has not been studied in prior literature and this research has revealed specific characteristics associated to this regime. Although these features has been observed in real experiments, their theoretical studied has not been explored. The SCM developed in this chapter offers an explanation to these and others features exhibited by WT radar echoes.

References

[1] P. Z. Peebles, *Radar Principles*, 1st ed., New York; Chichester: Wiley, 1998.

[2] M. Cherniakov, *Bistatic Radar: Principles and Practice*, 1st ed., Chichester: Wiley, 2007.

[3] G. N. Watson, *A Treatise on the Theory of Bessel Functions*, Cambridge: Cambridge University Press, 1922.

[4] W. Kaplan, *Advanced Calculus*, 3rd ed., Reading, Mass.; London: Addison-Wesley, 2002.

[5] J. C. Lozier, "Spectrum Analysis of Pulse Modulated Waves," *Bell System Technical Journal*, vol. 26, pp. 360-387, 1947.

[6] M. J. Lighthill, "The theory of generalised functions and their Fourier transforms- Theorem 15," in *An Introduction to Fourier Analysis and Generalised Functions*, Cambridge: Cambridge University Press, 1958, pp. 28.

[7] B. A. Carlson and P. B. Crilly, "Phase and Frequency Modulation," in *Communication Systems*, 4th ed., New York, NY: McGraw-Hill, ch. 5, sec. 5.1, pp. 184-199.

[8] A. Tennant and B. Chambers, "Signature Management of Radar Returns from Wind Turbine Generators," *Smart Mater. Struct.*, vol. 15, no. 2, pp. 468, 2006.

[9] B. Gallardo-Hernando *et al.,* "Wind turbine clutter observations and theoretical validation for meteorological radar applications", *IET Radar, Sonar & Navigation*, vol. 5, Iss. 2, pp. 111-117, Feb. 2011.

[10] B. Boashash, "Time-Frequency Concepts" in *Time Frequency Signal Analysis and Processing*, Brisbane, Australia: Elsevier, 2003, ch. 1, sec. 1.1, pp. 3-11.

[11] V. C. Chen and H. Ling, "Time-Frequency Transforms" in *Time-Frequency Transforms for Radar Imaging and Signal Analysis*, 1st ed., Norwood, MA: Artech House, 2002, ch. 2, sec. 2.1.1, pp. 28-31.

[12] V. C. Chen, *The Micro-Doppler Effect in Radar*, Boston; London, UK: Artech House, 2010.

Chapter 3 Wind Turbine Radar Signature in the Near-Field: Theoretical Model of Curved Blades.

3.1 Introduction

This chapter is the continuation of the theoretical analysis of the radar signature of WT blades in the near-field. In Chapter 2, the WT blades were modelled as a group of scattering points forming a rectangular plate, which facilitated the mathematical analysis of the backscattered signal.

In addition, this type of blade could be easily manufactured for experimental purposes in order to confirm the validity of the theoretical model. The experimental analysis with these flat blades will be presented in Chapter 4.

Although the flat blades were easy to treat experimental and theoretically, they are not the most realistic blade model. Actual blades have a curved contour in order to optimise their aerodynamic functioning [1]. Therefore, in order to fully characterise the radar signature of WT blades, it is necessary to analyse the scattering process of these complex targets, which is the aim of this chapter.

The first attempt to characterise the radar signature of a curved blade consisted in measuring its radar echo and compare it with the theoretical signature of flat blades. This comparison revealed clear differences in the signatures of these two types of blades. In order to improve the results, a CAD model of one of the curved blade was manually created. When the SCM was applied to the points of this CAD model, the match between theory and experiment was not improved; furthermore, worse results were obtained.

The failure of the SCM applied to curved blades suggested the necessity of developing a model to take into account the effects produced by their complex shape. The method considered the EM fields radiated by the charges and currents induced on the WT blade

3.2 Motivation

The SCM explained in Chapter 2 predicts the radar signature of flat blades as it will be confirmed experimentally in Chapter 4. However, this model does not characterise the radar signature of curved blades as it will be shown shortly. Although the experimental study of flat and curved blades is the topic of Chapter 4, part of the results will be shown here in order to provide a motivation for the theoretical analysis presented in this chapter.

Fig. 3.1 corresponds to one of the curved blades used during the experimental analysis and its CAD model created manually; the methodology employed to obtain this model will be explained in detail in the next chapter.

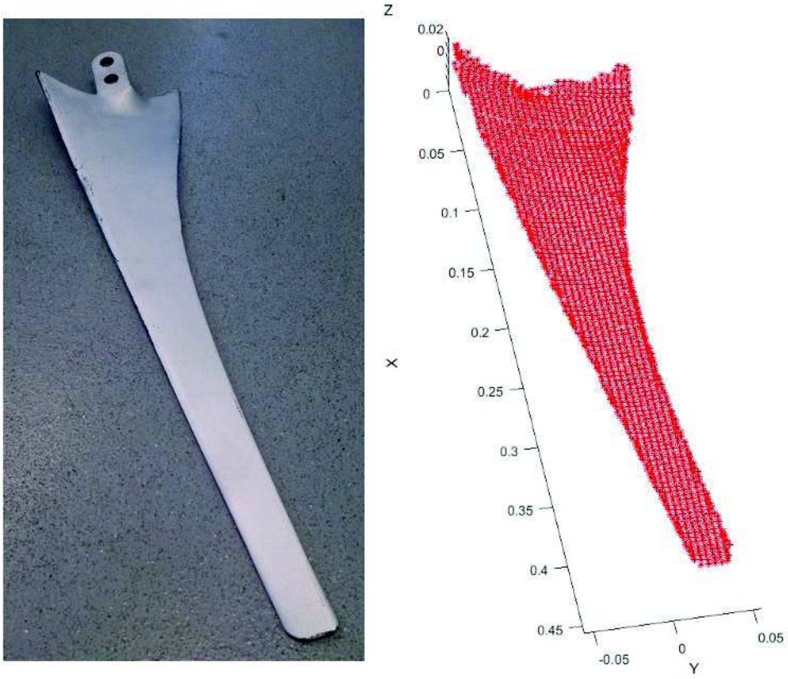

(a) (b)

Fig. 3.1: (a) Curved blade and (b) its CAD model.

The first attempt to characterise the radar signature of the blade in Fig. 3.1a was to compare the simulated signal of a flat blade using the SCM with the experimental signature obtained from the curved blade. The length of the curved blade in Fig. 3.1a is $50\ cm$ and the width at its wider part is $12\ cm$. The dimensions of the flat blade used to simulate the time-domain signal were $50 \times 3\ cm$. The result of this comparison over one WT blade revolution can be seen in Fig. 3.2. The theoretical and experimental signals exhibit several differences that cannot be explained in the framework of the SCM. The theoretical signal in Fig. 3.2 displays the two symmetric peaks already analysed in Chapter 2, although there are several features that will be explained in Chapter 4. The experimental signal however exhibits only one these symmetric peaks. The correlation coefficient between both signals is 0.64.

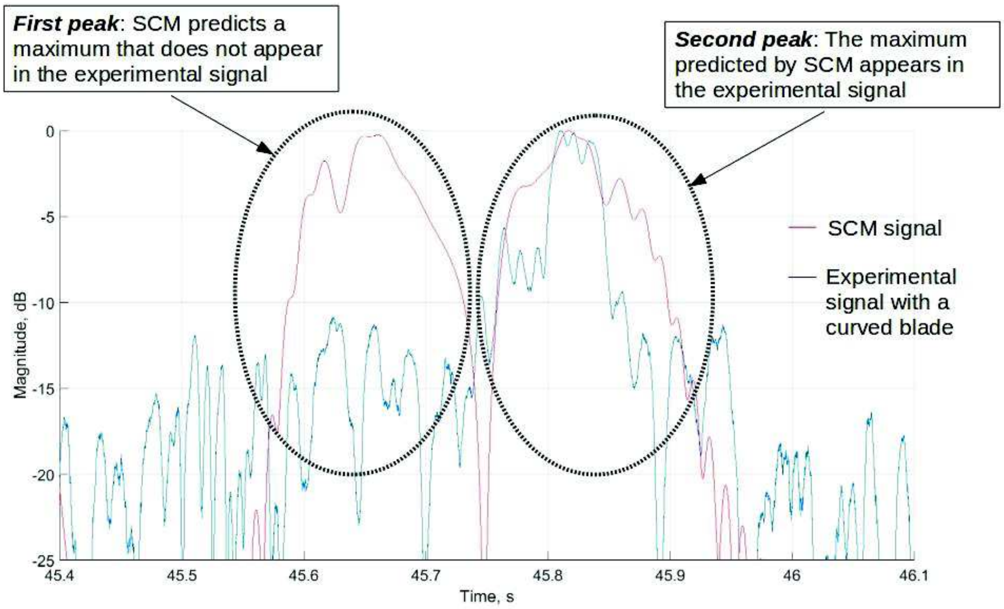

Fig. 3.2: Theoretical signal of a flat blade vs. experimental signal of a curved blade.

During the research, there have been different attempts to reproduce the experimental results with curved blades. For example, instead of a rectangular flat blade, a triangular flat blade was used to simulate the theoretical backscattered signal. However, the comparison with the experimental measurements using curved blades was not satisfactory either in this case.

The disagreement between theory and experiment is however expected because, at the operating frequency used during the experiments (*24 GHz*), the constructive and destructive patterns formed by the backscattered waves from different parts of the blade are sensitive to the blade curvature.

When the SCM was applied to the point-scatterers that form the CAD model of Fig. 3.2b, the result was even worse than the comparison in Fig. 3.2.

In conclusion, the shape of a curved blade causes the discrepancies between theory and experiment and the reason for this relies on the amplitudes of the backscattered waves from the different parts of a curved blade. In the flat blades case, the amplitude of the return wave from a scattering centre is not important in relative terms. All the points lie on the same plane, so there are no major differences in the backscattered energy between nearby point-scatterers. This is the reason why, as will be shown in Chapter 4, the SCM accurately represents the experimental signal of a flat blade. That model only takes into account the phase that affects the signal.

The difference between the two peaks of the curved blade signature in Fig. 3.2 is expected since the symmetry of the system is broken and the intensity of the signal is not necessarily the same at each side of the vertical axis, as it was in the case of flat blades. Fig. 3.3 explains the EM scattering mechanism that produces the asymmetry in the time-domain signature of a curved blade.

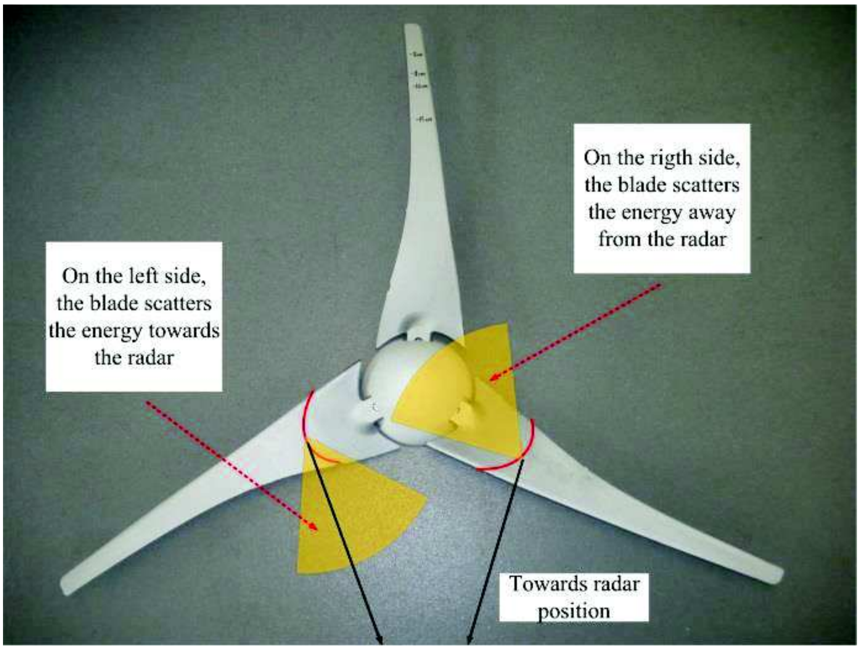

Fig. 3.3: Energy scattered away from a curved blade.

Therefore, in order to move to the realistic shape of the blades, it became necessary to complete the theoretical framework to include the effects of the amplitude on the backscattered signal.

3.3 Electromagnetic Fields Radiated by a Wind Turbine Blade

The typical approach to this problem would have been to use the physical optics (PO) approximation $\vec{J}_{inc} = 2\hat{n}\times\vec{H}_{inc}$where $\vec{H}_{inc}$ is the incident magnetic field intensity – examples of this method applied to the scattering of a rectangle plate can be found in [2]. In the derivation of the far-field expressions, it is generally assumed that the far field region begins at $r = 2D^2/\lambda$ where D is the largest dimension of the radiation source, given that D is larger than the wavelength. However, it will be shown later that the size of the sources considered in this model (secondary radiators) are several times smaller than the wavelength. The existence of currents on the blade surface is assumed in first place. The idea is to calculate the fields produced by these currents at the observation point, where the radar was placed. The incident field that induces the surface currents is phase-modulated through the radial distance r that varies with time due to rotating blade surface. This situation differs from the case in [2] where the author assumes a time-harmonic incident field and a static scattering surface. The phase-modulated incident field might be somehow included in this approach, but the calculations would be more complicated and might not have analytic solutions.

The idea of the theoretical framework developed here is to obtain the WT radar signal from EM first principles. This include a detailed understanding of the physics of the problem and aspects like the time varying phase of the incident field through the radial distance. The reasoning presented here recovers the phase of the radar echo from a single blade, expression (2.32), from first principles but with a non constant amplitude, including the $2r/c$ term typical of the monostatic case.

The assumption of plane wave illumination (far-field of the antenna) is still valid in this situation. Therefore, the electric field of the transmitted wave has the form

$$E_T(t) = e^{-j\omega t} \tag{3.1}$$

This incident field will excite the charges on the blade surface to produce a current density $\vec{J}_S$ on it. This surface current will have a certain amplitude depending on the blade material and the intensity of the incident field. If the blade were not moving, the time dependence of the surface current density would be the same as in (3.1), i.e. $e^{-j\omega t}$. However, due to the rotation of the blades, $\vec{J}_S$ will oscillate in time with a delay given by $\frac{r(t)}{c}$, where $r(t)$ is the radial distance between the radar and a point on the blade. Therefore, the surface current density induced on the WT blade will have the general form

$$\vec{J}_S(\vec{x},t) = \vec{J}_S(\vec{x})\, e^{-j\omega(t-\frac{r(t)}{c})} \tag{3.2}$$

where $\{\vec{x}\}$ are the coordinates of the surface current density in certain coordinate system. If the origin of this system is the centre of rotation of the blades, the coordinates $\{\vec{x}\}$ coincide with the vector $\vec{L}_{nm}$ already introduced in Chapter 2, section 2.6 and $r(t) = |\vec{R}_N - \vec{L}_{nm}|$.

The surface current density $\vec{J}_S$ can be considered as forming a vector field defined on the 2D surface *S* as Fig. 3.4 shows. A vector field on a surface *S* is defined, in general, as a smooth map between *S* and the tangent bundle *TS*, the collection of all the tangent spaces at *S*. This map satisfies that for each point *P* on *S* there is an associated vector that lies on TS_P, the tangent space at the point *P* [3]. It is then possible to define a vector $\vec{J}_S$ on the tangent plane corresponding to each point of *S* building thus a vector field which has a physical meaning. For a sufficient smooth surface, as it is the case of the turbine blade in Fig. 3.1a, the vectors $\vec{J}_S$ in the neighbourhood of a point *P* can be considered to lie on the same tangent plane TS_P. Therefore, the blade can be divided into *flat* regions with a particular charge and current density distributions that will depend on the phase of the incident field (3.1) at that specific point. These currents are the sources of the EM fields that produce the backscattered waves detected by the radar.

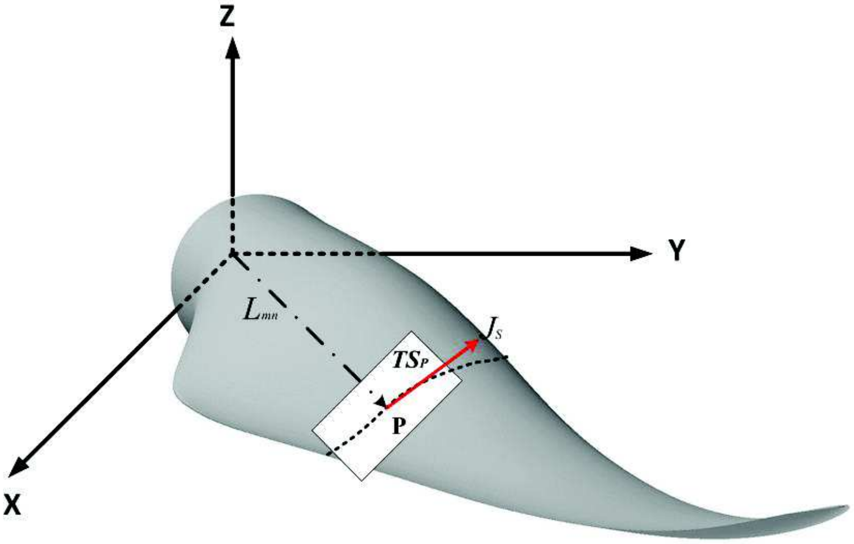

Fig. 3.4: Current density vector at point *P*.

The method suggested in this chapter consisted on computing the radiated field of each source, or secondary radiator, independently. The linearity of the Maxwell's equations guarantees that the superposition of these individual contributions will form the total field at the radar position. Two consequences can be inferred from this idea. On the one hand, a far-field approximation can be assumed as the distance between the radar and a point on the blade is much larger than the size of the individual, elementary sources; the calculations will be thus highly simplified. On the other hand, these calculations can be performed in a 2D Euclidean space instead of dealing with curved surfaces.

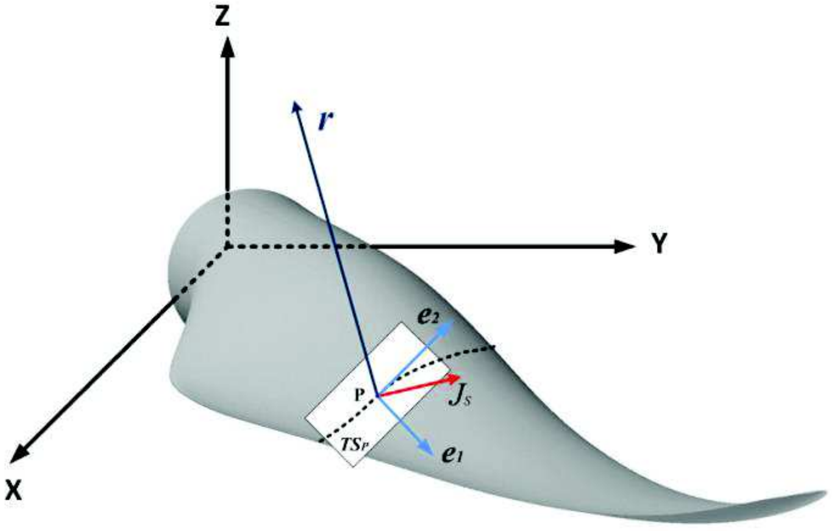

Fig. 3.5: The surface current density vector can be expanded by the tangent plane vector basis.

The aim now is to build the tangent bundle TS or, to be more precise, to construct the individual tangent spaces and associate to each one the corresponding current distribution $\vec{J}_S$. In order to do it, the tangent plane at an arbitrary point P, TS_P,can be expanded by in terms of the vector basis $\{\hat{e}_1(P), \hat{e}_2(P)\}$which are the tangent vectors at the blade point P in the x^1, x^2 directions, the generalised coordinates that parametrise the surface. This approach can be seen schematically in Fig. 3.5. Any vector lying on TS_P is by definition a linear combination of the vectors $\{\hat{e}_1(P), \hat{e}_2(P)\}$, so the current density $\vec{J}_S$ can be expanded in the terms of this basis. In order to evaluate the EM fields at the radar position, the origin of a global Cartesian coordinates *(X,Y,Z)* system is placed at the centre of rotation of the WT blades as Fig. 3.5 shows. The basis $\{\hat{e}_1(P), \hat{e}_2(P)\}$ is defined at each point $P := (x', y', z')$ on the blade given by the vector $\vec{L}_{nm}$. Fig. 3.6 represents the basis $\{\hat{e}_1(P), \hat{e}_2(P)\}$ at different points on the blade surface, where the normal vector to the surface at *P* is defined as $\hat{e}_3(P)$. The orientation of these vectors varies along the profile of the blade.

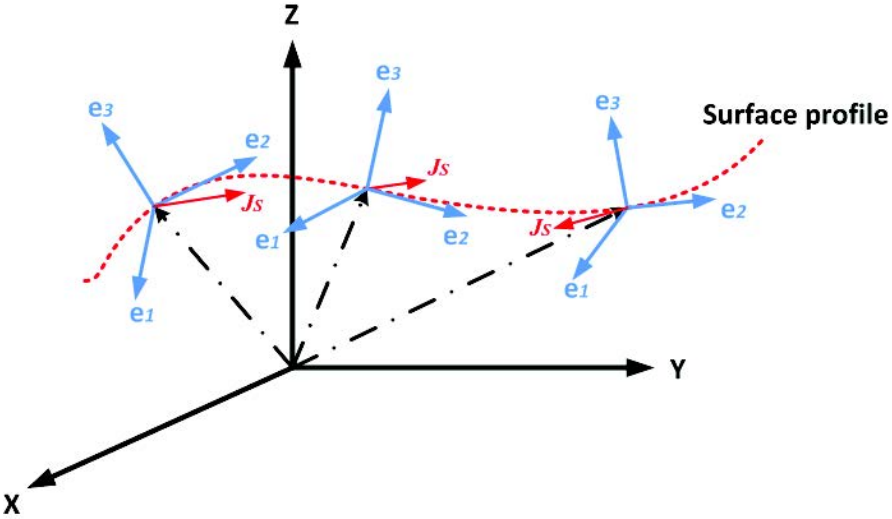

Fig. 3.6: Vectors of the tangent planes basis at different points along the blade surface.

The EM fields created by each individual source can be determined by calculating the vector potential $\vec{A}(\vec{x}, t)$ which solution in the Lorentz gauge is [4]

$$\vec{A}(\vec{x}, t) = \frac{\mu_0}{4\pi} \int ds' \int dt' \frac{\vec{J}_S(\vec{x}', t')}{|\vec{x} - \vec{x}'|} \delta\left(t' + \frac{|\vec{x} - \vec{x}'|}{c} - t\right) \tag{3.3}$$

where μ_0 is the permeability of free space. $\vec{x}'$ are the coordinates of the charge and current density distributions on the tangent plane TS_P. The radial distance between the radar and a particular point on the blade is given by the module of $\vec{r}(t)$, as indicated in Fig. 3.5. The Dirac delta function δ accounts for the correct time delayed in the signal. The surface element is ds'. The transmitted radar signal will be incident on the blade at a certain angle due to the geometrical configuration of the system and/or the curvature of the WT blade. Therefore, the signal will reach different points at distinct phases which means that separated parts of the blade will experience different field intensities and orientations. Consequently, a complex charge and current distribution will be induced over the blade. The current amplitude $\vec{J}_S(\vec{x}')$ must vary over each flat area considered as a source in order to satisfy the boundary conditions between different regions.

A further analysis on the physical process that takes place on the blade surface can provide more insight into the problem before continuing the calculations. Fig. 3.7 shows that, depending on the relative position radar-WT, the transmitted EM wave will reach the blade at a certain angle. Consequently, the phase of the incident field (3.1) will vary along the blade. This means that different points of the blade surface will experience different field intensities and orientations, inducing a complex charge and current distribution. The current amplitude $\vec{J}_S(\vec{x})$ must vary over each flat area considered as a source in order to satisfy the boundary conditions between different regions.

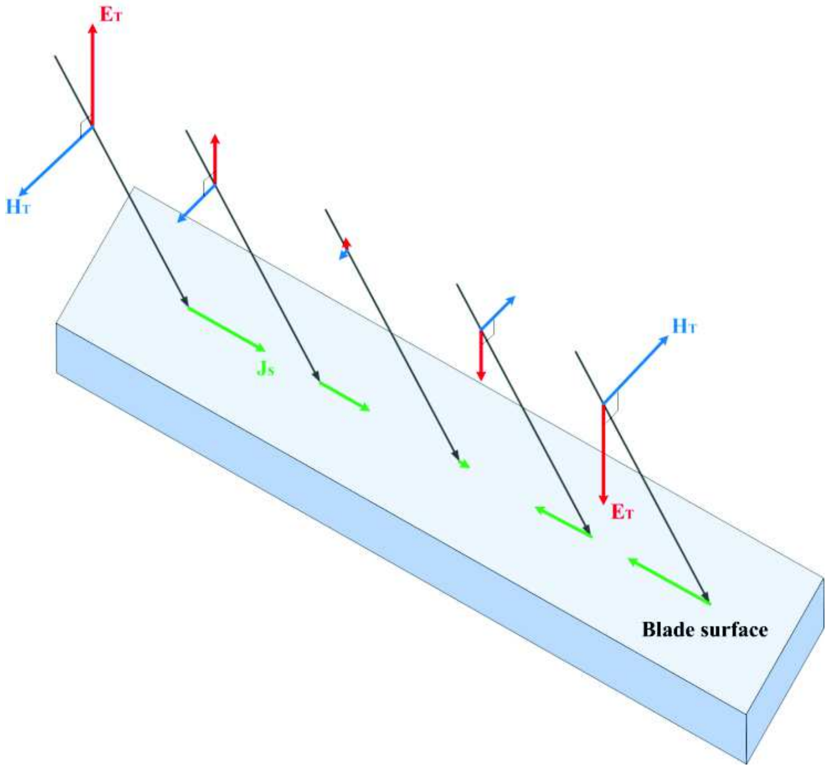

Fig. 3.7: Phase of the incident EM fields at different points on the blade surface.

In published work on radar reflections from WTs (see [5]-[8]), a common practice is to use CAD models of WT blades in commercial EM simulators to determine their RCS in static conditions. Although such practice is technically possible here for near-field simulations, it was not preferred for a number of reasons. First of all, the objective of this research is to model the dynamic near-field signature of WT blades as they rotate, rather than their RCS in static conditions. Using EM simulator to do this would be computationally costly. Secondly, the final goal of this thesis is to use dynamic behaviours derived here as a model for characterising faulty blades, where computationally expensive EM simulations could well turn out to be impractical. The concepts described in this chapter, therefore, could be potentially extended to monitor the dynamic behaviour of other rotating mechanical parts in the near-field, such as helicopter rotor blades, for example.

After substituting the current distribution (3.2) into the vector potential (3.3), this can be written as

$$\vec{A}(\vec{r}(t),t) = \frac{\mu_0}{4\pi}\int ds' \int dt' \frac{\vec{J}_S(\vec{x}')e^{-j\omega(t\prime - \frac{r(t)}{c})}}{|\vec{r}(t)-\vec{x}'|}\delta\left(t' + \frac{|\vec{r}(t)-\vec{x}'|}{c} - t\right)$$

(3.4)

Any disturbance in the electromagnetic fields propagates at c, so the propagation time is approximately $t_d = \frac{r}{c} \sim 10^{-8}s$. The variation in the charge and current density distributions due to the rotation of the blade is of the order of $t_r = 1/\Omega \sim 10^{-1}s$. Therefore, the sources are practically constant during the propagation of the EM fields. Once the radial distance $r(t)$ is known for each point, the current density in (3.2) can be considered as an independent source that oscillates deterministically in time producing electric and magnetic fields that propagate through space. Therefore, the radial distance enters into the equation (3.4) simply as a function of time ⍰ and it is not necessary to take into account any extra delay inside $r(t)$.

After evaluating the delta function in equation (3.4), the vector potential is given by

$$\vec{A}(\vec{r}(t),t) = \mu_0 e^{-j\omega(t - \frac{r(t)}{c})}\int ds' \vec{J}_S(\vec{x}')\frac{e^{-jk|\vec{r}(t)-\vec{x}\prime|}}{4\pi|\vec{r}(t)-\vec{x}'|}$$

(3.5)

The so-called Green function [4]

$$G(\vec{r}(t),\vec{x}') \equiv \frac{e^{-jk|\vec{r}(t)-\vec{x}'|}}{4\pi|\vec{r}(t)-\vec{x}'|}$$

(3.6)

can be introduced in order to write the vector potential (3.5) as

$$\vec{A}(\vec{r}(t),t) = \mu_0 e^{-j\omega(t-\frac{r(t)}{c})} \int ds' \vec{J}_S(\vec{x}') G(\vec{r}(t),\vec{x}')$$

(3.7)

The radiated EM fields are given only in terms of spatial derivatives of $\vec{A}(\vec{r}(t),t)$, so the phase $e^{-j\omega t}$ can be ignored in the subsequent calculations. This will lead to an expression of the backscattered electric field whose phase is the one predicted by the SCM. Its amplitude will depend on the blade point and its orientation respect to the radar.

The exact expansion of the Green function $G(\vec{r},\vec{x}')$ for points outside the source allows to write the vector potential (3.7) in spherical coordinates as [4]

$$\vec{A}(\vec{r}) = j\mu_0 k e^{jkr} \sum_{l,m} h_l^{(1)}(kr) Y_{lm}(\theta,\phi) \int ds' \vec{J}_S(\vec{r}') j_l(kr') \bar{Y}_{lm}(\theta',\phi')$$

(3.8)

where the time dependence of the observation position has been omitted to simplify the notation and $k = \omega/c$. The terms $h_l^{(1)}(kr)$ and $j_l(kr')$ are the spherical Hankel and Bessel functions and $Y_{lm}(\theta, \phi)$ are the spherical harmonics.

The isotropic terms of the series (3.8) can be considered in first place. It will be shown later that this will be enough to obtain an accurate prediction of the radar signature of a curved WT blade. Therefore, if only the term $l = 0$ (and consequently $m = 0$) of the series (3.8) is retained, the vector potential becomes

$$\vec{A}(\vec{r}) = j\mu_0 k e^{jkr} \left[h_0^{(1)}(kr) Y_{00}(\theta, \phi) \int ds' \vec{J}_S(\vec{r}') j_0(kr') \bar{Y}_{00}(\theta', \phi') \right] \tag{3.9}$$

The isotropic spherical harmonics and the Hankel and Bessel functions are, respectively,

$$Y_{00}(\theta, \phi) = \bar{Y}_{00}(\theta', \phi') = \frac{1}{\sqrt{4\pi}} \tag{3.10a}$$

$$h_0^{(1)}(kr) = \frac{e^{jkr}}{jkr} \tag{3.10b}$$

$$j_0(kr') = \frac{\sin kr'}{kr'}$$

(3.10c)

Expression (3.10c) can be, in general, approximated by $sinc(kr') \approx 1$ since the maximum value of the size of the source r' is several times smaller than the wavelength. This approximation will be as closer to *1* as the size of the source decreases. This will depend on the incident angle of the transmitted field. Based on the CAD model of the blade created, the maximum value of r' is of the order of $\lambda/6$ which suggests that the range for the value of (3.10c) is $[0.86, 1]$. In order to obtain an analytical expression for the integral (3.9) and to avoid interpolating the measured points, the Bessel function will be approximated by *1*. There is information missing since this approximation is equivalent to consider a smaller source without filling the gap between two measured points by interpolating an extra source. However, the comparison between theoretical and experimental results in Chapter 4 will validate the appropriateness of this assumption.

Introducing the expressions (3.10a)-(3.10c) in (3.9), the vector potential can be written as

$$\vec{A}(\vec{r}) = \frac{\mu_0}{4\pi}\frac{e^{j2kr}}{r}\int ds'\vec{J}_S(\vec{r}')$$

(3.11)

This last expression of the vector potential can also be obtained by assuming $|\vec{r}(t) - \vec{x}'| = r$ in (3.5). However, this approximation does not mean the same when it is taken in the denominator or in the exponential. In the former case, the approximation rightly takes into account the fact that the distance to the radar is larger than the dimensions of the source. On the other hand, the term $e^{-jk|\vec{r}(t)-\vec{x}'|} \cong e^{-jkr}$ means that the whole current density distribution over the considered integration area is being taken at the same delayed time $(t-\frac{r}{c})$. The source is oscillating and moving in circles as the blade rotates, so the current distribution is travelling at certain velocity as a whole. If the velocity were close to c, the current at one side of the area considered should be evaluated at a delayed time different from the time at the opposite side. This difference would propagate at c and the fields would be certainly affected. However, the rotational velocity of the WT blade is several orders of magnitude slower than the speed of light, so the approximation in the exponential is valid.

The dependence of $\vec{A}(\vec{r})$ only on the radial distance implies that the EM fields will depend on r as well. Any angular dependence will appear as a result of the cross-products necessary to calculate $\vec{E}(\vec{r})$ and $\vec{B}(\vec{r})$. Furthermore, due to fact that the vector potential falls off as r^{-1} in (3.11), the fields will present the same behaviour as expected in the radiation zone (higher orders in r will be discarded).

The expression for the current distribution is not known, so the surface integral in (3.11) cannot be calculated analytically. However, the integral in the vector potential can be expressed as

$$\vec{A}(\vec{r}) = \frac{-\mu_0}{4\pi}\frac{e^{j2kr}}{r}\int ds'\vec{x}'\nabla\cdot\vec{J}_S(\vec{x}')$$

(3.12)

which suggests the use of the continuity equation: $\nabla \cdot \vec{J}_S = \frac{-\partial \rho}{\partial t}$. As it has already mentioned, the incident electric field creates a complex charge and current distribution over the blade. The charge distribution, as in the case of the current in (3.2), will have the form

$$\rho(\vec{x}', t) = \rho(\vec{x}')\, e^{-j\omega(t-\frac{r(t)}{c})}$$

(3.13)

Using these distributions, the continuity equation can be written as

$$\nabla \cdot \left[\vec{J}_S(\vec{x}')e^{-j\omega\left(t-\frac{r(t)}{c}\right)}\right] = \frac{-\partial}{\partial t}\left[\rho(\vec{x}')\, e^{-j\omega(t-\frac{r(t)}{c})}\right]$$

(3.14)

Since the spatial derivatives in the left side of (3.14) are performed on the source coordinates $\vec{x}'$, they do not affect the radial distance in the exponential. Consequently, equation (3.14) becomes

$$e^{-j\omega(t-\frac{r(t)}{c})}\, \nabla \cdot \vec{J}_S(\vec{x}') = j\omega\rho(\vec{x}')\left(1 - \frac{1}{c}\frac{\partial r(t)}{\partial t}\right) e^{-j\omega(t-\frac{r(t)}{c})}$$

(3.15)

and after ruling out the common exponential on both sides, the previous equation is then written as

$$\nabla \cdot \vec{J}_S(\vec{x}') = j\omega\rho(\vec{x}')\left(1 + \frac{\Omega L_{nm} Z_N}{c}\frac{\sin \Omega t}{r(t)}\right)$$

(3.16)

Substituting the divergence of the current distribution in expression (3.12), the vector potential is given by

$$\vec{A}(\vec{r}) = \frac{-\mu_0}{4\pi}\frac{e^{j2kr}}{r}\int ds'\vec{x}' j\omega\rho(\vec{x}')\left(1 + \frac{\Omega L_{nm} Z_N}{c}\frac{\sin \Omega t}{r}\right) = -j\frac{k}{4\pi c\varepsilon_0}\frac{e^{j2kr}}{r}\vec{p}\left(1 + \frac{\Omega L_{nm} Z_N}{c}\frac{\sin \Omega t}{r}\right)$$

(3.17)

where $\vec{p} \equiv \int ds'\vec{x}'\rho(\vec{x}')$ is the electrostatic electric dipole [4]. The second term in parenthesis in (3.17) produces a contribution of order r^{-2}. Since only the radiation contribution to the fields will be considered, those that vary with r^{-1}, a sufficient accurate approximation of the vector field is given by

$$\vec{A}(\vec{r}) = -j\frac{k}{4\pi c\varepsilon_0}\frac{e^{j2kr}}{r}\vec{p}$$

(3.18)

The radiated electric and magnetic field can now be computed through their relations with the vector potential (3.18). The magnetic field $\vec{B}$ is given, in terms of $\vec{A}(\vec{r})$, by

$$\vec{B}(\vec{r}) = \nabla \times \vec{A}(\vec{r})$$

(3.19)

which is valid everywhere in space.

In order to obtain the electric field in terms of $\vec{A}(\vec{r})$, Ampère's law can be invoked. Outside the source (at the radar position), the rotational of the magnetic field is given by

$$\nabla\times\vec{B}(\vec{r},t) = \mu_0(\vec{J}_S + \varepsilon_0\frac{\partial\vec{E}(\vec{r},t)}{\partial t}) = 0 + \frac{1}{c^2}\frac{\partial\vec{E}(\vec{r},t)}{\partial t}$$

(3.20)

The time dependence of $\vec{B}(\vec{r},t)$ and $\vec{E}(\vec{r},t)$ will have the same form as the current and charges distributions, that is

$$\vec{B}(\vec{r},t) = \vec{B}(\vec{r})\cdot e^{-j\omega(t-\frac{r}{c})}$$

$$\vec{E}(\vec{r},t) = \vec{E}(\vec{r})\cdot e^{-j\omega(t-\frac{r}{c})}$$

(3.21)

After including these last expressions in (3.20), Ampère's law can be written as

$$\nabla\times[\vec{B}(\vec{r})\cdot e^{-j\omega(t-\frac{r}{c})}]=\frac{1}{c^2}\frac{\partial}{\partial t}[\vec{E}(\vec{r})\cdot e^{-j\omega(t-\frac{r}{c})}]$$

(3.22)

If $\vec{F}$ is a vector field and ψ is a scalar valued function, then $\nabla\times[\psi\vec{F}]=\nabla\psi\times\vec{F}+\psi\nabla\times\vec{F}$. Therefore, using this property, the left side in (3.22) can be expressed as

$$\nabla\times\left[\vec{B}(\vec{r})\cdot e^{-j\omega\left(t-\frac{r}{c}\right)}\right]=\nabla e^{-j\omega\left(t-\frac{r}{c}\right)}\times\vec{B}(\vec{r})+\nabla\times\left[\vec{B}(\vec{r})\cdot e^{-j\omega\left(t-\frac{r}{c}\right)}\right]$$

(3.23)

The gradient of the complex exponential in (3.23) is given by

$$\nabla e^{-j\omega\left(t-\frac{r}{c}\right)}=jk\hat{r}e^{-j\omega\left(t-\frac{r}{c}\right)}$$

(3.24)

where $\hat{r}$ is the unit radial vector in the direction of the observation point. The rotational of the magnetic field (3.23) can now be written as

$$\nabla\times\left[\vec{B}(\vec{r})\cdot e^{-j\omega\left(t-\frac{r}{c}\right)}\right]=\left[jk\left(\hat{r}\times\vec{B}(\vec{r})\right)+\nabla\times\vec{B}(\vec{r})\right]\cdot e^{-j\omega\left(t-\frac{r}{c}\right)}$$

(3.25)

Let us now to consider the right side of Ampère's law (3.22). Here, after performing the partial time derivative over the terms in the parenthesis, the rate of change with time of the electric field is given by

$$\frac{1}{c^2}\frac{\partial}{\partial t}\left[\vec{E}(\vec{r})\cdot e^{-j\omega\left(t-\frac{r}{c}\right)}\right]=\frac{1}{c^2}\left[e^{-j\omega\left(t-\frac{r}{c}\right)}\frac{\partial\vec{E}(\vec{r})}{\partial t}+\vec{E}(\vec{r})\frac{\partial}{\partial t}\left(e^{-j\omega\left(t-\frac{r}{c}\right)}\right)\right]$$

(3.26)

The time dependence of $\vec{E}(\vec{r})$ is only through r, so the first of the derivative in (3.26) is

$$\frac{\partial\vec{E}(\vec{r})}{\partial t}=\frac{\partial\vec{E}(\vec{r})}{\partial r}\frac{\partial r}{\partial t}=\frac{-\Omega L_{nm}Z_N\sin\Omega t}{r}\frac{\partial\vec{E}(\vec{r})}{\partial r}=\frac{f(t)}{r}\frac{\partial\vec{E}(\vec{r})}{\partial r},where\ f(t)\equiv-\Omega L_{nm}Z_N\sin\Omega t$$

(3.27)

The partial time derivative of the exponential in (3.26) can be calculated straightaway and, using the definition for $f(t)$ given in (3.27), it is obtained

$$\frac{\partial}{\partial t}\left(e^{-j\omega\left(t-\frac{r}{c}\right)}\right)=-j\omega e^{-j\omega\left(t-\frac{r}{c}\right)}\left[1-\frac{f(t)}{cr}\right]$$

(3.28)

After substituting the previous calculations into (3.22), the right term in Ampère's law (3.22) can be written as

$$\frac{1}{c^2}\frac{\partial}{\partial t}\left[\vec{E}(\vec{r})\cdot e^{-j\omega\left(t-\frac{r}{c}\right)}\right]=\frac{1}{c^2}e^{-j\omega\left(t-\frac{r}{c}\right)}\left\{\frac{f(t)}{r}\left[j\omega\vec{E}(\vec{r})+\frac{\partial\vec{E}(\vec{r})}{\partial r}\right]-j\omega\vec{E}(\vec{r})\right\}$$

(3.29)

The electric and magnetic fields will decay at the rate of r^{-1} and higher orders. However, the latter will not contribute to the radiation part of the EM fields, so the expression (3.29) can be correctly approximated by

$$\frac{1}{c^2}\frac{\partial}{\partial t}\left[\vec{E}(\vec{r})\cdot e^{-j\omega\left(t-\frac{r}{c}\right)}\right]\cong -j\frac{1}{c^2}\omega\vec{E}(\vec{r})e^{-j\omega\left(t-\frac{r}{c}\right)}$$

(3.30)

Finally, Ampère's law is, in this case, given by

$$\left[jk\left(\hat{r}\times\vec{B}(\vec{r})\right)+\nabla\times\vec{B}(\vec{r})\right]\cdot e^{-j\omega\left(t-\frac{r}{c}\right)}=-j\frac{1}{c^2}\omega\vec{E}(\vec{r})e^{-j\omega\left(t-\frac{r}{c}\right)}$$

(3.31)

and after eliminating the common exponentials, the electric field at the radar position is

$$\vec{E}(\vec{r})=c\left[\frac{j}{k}\nabla\times\vec{B}(\vec{r})-\hat{r}\times\vec{B}(\vec{r})\right]$$

(3.32)

The first term on the right side in (3.32) simply expresses that an electric field is the source of a magnetic field; this term appears in the case of sinusoidal time-varying sources. The second term, however, can be related to the rotational motion of the blade. As it rotates, the charge and current distributions experiences an extra movement that contributes to the variation of the magnetic field and, consequently, to the production of an electric field. Both terms in (3.32) have the correct direction of the electric field for a plane wave propagation: right angle to the direction of propagation. Furthermore, the imaginary unit in the first term can be associated to the underlying dynamics of the field that oscillates in time while the second term is a kind of torque.

Since the magnetic field is given by $\vec{B}(\vec{r}) = \nabla\times\vec{A}(\vec{r})$, the electric field can be written in terms of the vector potential as

$$\vec{E}(\vec{r}) = c\left[\frac{j}{k}\nabla\times\left(\nabla\times\vec{A}(\vec{r})\right) - \hat{r}\times\left(\nabla\times\vec{A}(\vec{r})\right)\right] \tag{3.33}$$

Using the expression obtained for the vector potential in the magnetic field equation:

$$\vec{B}(\vec{r}) = \nabla\times\vec{A}(\vec{r}) = -j\frac{k}{4\pi c\varepsilon_0}\nabla\times\left(\frac{e^{j2kr}}{r}\vec{p}\right) = -j\frac{k}{4\pi c\varepsilon_0}\left[\nabla\left(\frac{e^{j2kr}}{r}\right)\times\vec{p} + \frac{e^{j2kr}}{r}\nabla\times\vec{p}\right] = -j\frac{k}{4\pi c\varepsilon_0}\nabla\left(\frac{e^{j2kr}}{r}\right)\times\vec{p} \tag{3.34}$$

where it is implied the fact that the electric dipole does not depend on the observation coordinates. After performing the gradient in (3.34), the magnetic field becomes

$$\vec{B}(\vec{r}) = \frac{k^2}{2\pi c\varepsilon_0}\frac{e^{j2kr}}{r}\left(1-\frac{1}{j2kr}\right)\hat{r}\times\vec{p}$$

(3.35)

If similar calculations for the electric field (3.33) are performed, it can be obtained:

$$\vec{E}(\vec{r}) = c\left\{\frac{j}{k}\nabla\times\left[\frac{k^2}{2\pi c\varepsilon_0}\frac{e^{j2kr}}{r}\left(1-\frac{1}{j2kr}\right)\hat{r}\times\vec{p}\right]-\frac{k^2}{2\pi c\varepsilon_0}\frac{e^{j2kr}}{r}\left(1-\frac{1}{j2kr}\right)\hat{r}\times(\hat{r}\times\vec{p})\right\}$$

(3.36)

Once again, since the terms that fall off as r^{-2} do not contribute to the radiation fields, the electric field has the form

$$\vec{E}(\vec{r}) = \frac{k^2}{2\pi\varepsilon_0}\left\{\frac{j}{k}\nabla\times\left[\frac{e^{j2kr}}{r}\hat{r}\times\vec{p}\right]-\frac{e^{j2kr}}{r}\hat{r}\times(\hat{r}\times\vec{p})\right\}$$

(3.37)

The curl in (3.37) can be expanded in two terms to write:

$$\vec{E}(\vec{r}) = \frac{k^2}{2\pi\varepsilon_0}\left\{\frac{j}{k}\left[\nabla\left(\frac{e^{j2kr}}{r}\right)\times(\hat{r}\times\vec{p})+\frac{e^{j2kr}}{r}\nabla\times(\hat{r}\times\vec{p})\right]-\frac{e^{j2kr}}{r}\hat{r}\times(\hat{r}\times\vec{p})\right\}$$

(3.38)

Any arbitrary vector $\vec{a}$ and a unit radial vector $\hat{r}$ satisfy the following two vector formulae:

$$\nabla \cdot \hat{r} = \frac{2}{r}$$

(3.39a)

$$(\vec{a} \cdot \nabla)\, \hat{r} = \frac{1}{r}[\vec{a} \; - \; \hat{r}\; (\vec{a} \cdot \hat{r})]$$

(3.39b)

The curl and gradient in (3.38) produce expressions of the form of (3.39a) and (3.39b), so these can be used to write the electric field as

$$\vec{E}(\vec{r}) = \frac{k^2}{2\pi\varepsilon_0}\left\{\frac{j}{k}\left[\left(j2k\frac{e^{j2kr}}{r}\left(1-\frac{1}{j2kr}\right)\right)\hat{r}\times(\hat{r}\times\vec{p}) - \frac{e^{j2kr}}{r^2}[\vec{p}+\hat{r}(\vec{p}\cdot\hat{r})]\right] - \frac{e^{j2kr}}{r}\hat{r}\times(\hat{r}\times\vec{p})\right\}$$

(3.40)

After rearranging the terms in (3.40), it can be obtained:

$$\vec{E}(\vec{r}) = \frac{k^2}{2\pi\varepsilon_0}\frac{e^{j2kr}}{r}\left\{\left[2\left(1-\frac{1}{jkr}\right)(\hat{r}\times\vec{p})\times\hat{r} - j\frac{1}{kr}[\vec{p}+\hat{r}(\vec{p}\cdot\hat{r})]\right] + (\hat{r}\times\vec{p})\times\hat{r}\right\}$$

(3.41)

and if terms that fall of as r^{-1} are conserved exclusively:

$$\vec{E}(\vec{r}) = \frac{3}{2}\frac{k^2}{\pi\varepsilon_0}\frac{e^{j2kr}}{r}(\hat{r}\times\vec{p})\times\hat{r}$$

(3.42)

Finally, after recovering the time oscillation, the electric field vector is given by

$$\vec{E}(\vec{r},t) = \frac{3}{2}\frac{k^2}{\pi\varepsilon_0}\frac{(\hat{r}\times\vec{p})\times\hat{r}}{r}\cdot e^{-j\omega\left(t-\frac{2r}{c}\right)}$$

(3.43)

In principle, the modulus of the electric dipole $|\vec{p}|$ in (3.43) would depend on the material of the blade surface and the strength of the incident field. The orientation of the dipole will be aligned to the current orientation which has the orientation as the electric field. Therefore, in a coordinate system that rotates with the blade, the electric dipole is seen as a vector that slowly rotates and rapidly oscillates with time on the tangent plane associated to a specific point on the blade. On the other hand, since $\hat{r}(t)$ changes its orientation as the blade moves, the rotation produces a time-varying relative angle between the source and the direction of observation. The cross-products in (3.43) take into account only the component that is perpendicular to the line of sight, as it must be. As the relative orientation between $\hat{r}$ and $\vec{p}$ varies, the strength of the backscattered signal will also change.

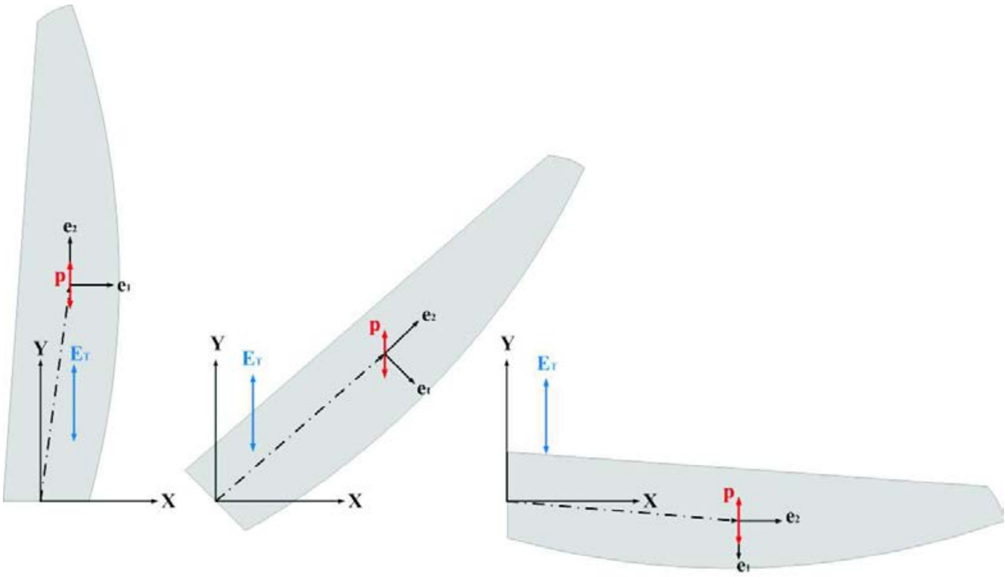

Fig. 3.8: Orientation of the electric dipole as the blade rotates when the incident electric field is vertically polarised.

In order to complete the theoretical framework, it is necessary to obtain an expression for the rotation of the dipole. In order to do this, the polarisation of the incident electric field has to be defined. The monostatic radar used for experimental measurements is linearly vertical polarised. Therefore, the dipole will point in the same direction and will rotate on the tangent plane as the blade moves, as Fig. 3.8 shows, and only the vertical component of the field (3.43) will be taken into account. At this stage it should be stated that a natural extension of the models developed in this chapter and in Chapter 2 could be to consider their full polarimetric implementation.

A rotating dipole can be obtained by superimposing two perpendicular oscillating dipoles. The frequency of oscillation must be the angular velocity of the blade. In order to compare the theoretical and experimental signals, the components of the electric dipole on the tangent plane in terms of the basis vectors $\hat{e}_1(P), \hat{e}_2(P)$ should be, for the specific electric field polarisation,

$$\vec{p} = p_0[-\sin \Omega t \cdot \hat{e}_1(P) + \cos \Omega t \cdot \hat{e}_2(P)]$$

(3.44)

which is equivalent to a rotation opposing the blade spinning. The specific value for p_0 does not affect the final result in relative terms as long as it is the same for all the points.

Since (3.43) corresponds to the radiated field from an arbitrary source point on the blade, the sum of all these individual contributions will form the total backscattered field at the radar position:

$$\vec{E}_{total} = \sum_{\forall n} \vec{E}_n(\vec{r}_n, t) = \frac{3}{2}\frac{k^2}{\pi \varepsilon_0} \sum_{\forall n} \frac{(\hat{r}_n \times \vec{p}_n) \times \hat{r}_n}{r_n} \cdot e^{-j\omega\left(t - \frac{2r_n}{c}\right)}$$

(3.45)

The intensity of the total field will change as a result of the different amplitude of the sources at different blade positions. Expression (3.45) is the desired formula for the amplitude of the backscattered wave.

3.4 Experimental Predictions

Chapter 4 is dedicated to confirm experimentally both the SCM and the model developed in this chapter. However, it is important to show that the theoretical analysis elaborated in the previous section predicts the features observed in the time-domain signature of curved blades.

In order to simulate the theoretical signal, equation (3.43) is applied to each of the points that form the CAD model of the curved blade displayed in Fig. 3.1b. Therefore, equation (3.43) is applied to each point measured in the way explained in section 4.2.2. The basis vectors to define the orientation of the electric dipoles were obtained by a first order approximation of the partial derivatives in x and y directions. Fig. 3.9 corresponds to the measured time-domain signature of a single curved blade rotating at a fixed speed in both clockwise and anticlockwise directions; the corresponding theoretical signals have been superimposed. The initial time shift of the experimental signal have been removed to make it overlay with the theoretical signature.

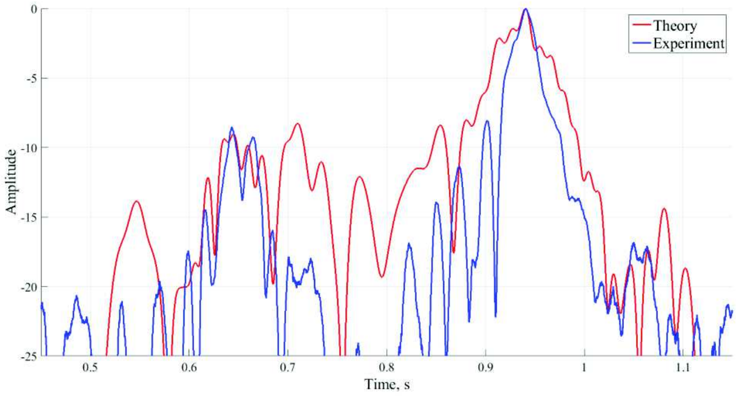

(a)

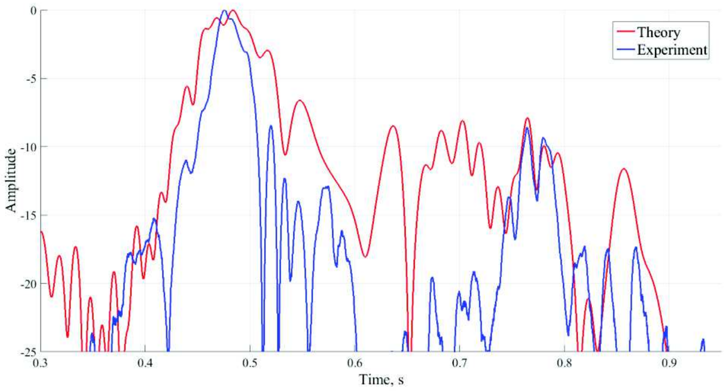

(b)

Fig. 3.9: Theoretical and experimental time-domain signatures of a single curved blade. (a) Clockwise rotation. (b) Anticlockwise rotation.

Fig. 3.3 showed that, if the rotation is clockwise, the blades will sequentially sweep the right side of the WT. Therefore, the blades will reach, in first place, the position indicated in Fig. 3.3 that backscatters the energy away from the radar. Consequently, the first of the symmetric peaks predicted by the SCM in Fig. 3.2 has to be less intense when curved blades are used and this is what can be also seen in Fig. 3.2. The model developed in this chapter predicts this behaviour as can be observed in Fig. 3.9a. If the rotation is anticlockwise, the opposite will occur: the second of the symmetric peak will be less intense. This is also predicted by the model as Fig. 3.9b shows. The correlation coefficients are 0.92 in the case of Fig. 3.9a and 0.91 in Fig. 3.9b.

3.5 Summary

The SCM was useful to predict the radar signature from WT flat blades, where the amplitude associated to each of the point-scatterers can be discarded. However, when more realistic blades were used for experiments, the SCM was not able to predict specific features present in the time-domain signature of these types of blades. Therefore, the theoretical framework had to be expanded to take into account the characteristics in the backscattered signals introduced by curved blades.

The result of the model developed is the expression (3.45) which were used to simulate the backscattered signal from a curved blade. This expression predicted the drop in the signal observed in experiments. This phenomenon is due to the asymmetries introduced by the curvature of the blades. The SCM was not able to foresee this characteristic. The prediction of this behaviour is the main contribution of the model developed in this chapter.

References

[1] P. Z. Peebles, *Radar Principles*, 1st ed., New York; Chichester: Wiley, 1998.

[2] M. Cherniakov, *Bistatic Radar: Principles and Practice*, 1st ed., Chichester: Wiley, 2007.

[3] M. O. Hansen, "3D Aerodynamics," in *Aerodynamics of wind turbine*, 2nd ed., Sterling, VA, London: Earthscan, 2008.

[4] C. A. Balanis, "Radiation and Scattering Equations," in *Advanced Engineering Electromagnetics*, 2nd ed., Hoboken, NJ: Wiley, 2012.

[5] J. M. Lee, "The Tangent Structure," in *Manifolds and Differential Geometry*, Providence, Rhode Island: American Mathematical Society, 2009.

[6] J. D. Jackson, "Radiating Systems, Multipole Fields and Radiation," in *Classical Electrodynamics*, 2rd ed., New York, London: Wiley, 1975.

[7] G. J. Poupart, "Wind Farms Impact on Radar Aviation Interests - Final Report," QinetiQ, UK. FES W/14/00614/00/REP. 2003

[8] L. R. Danoon *et al.*, "Modeling Methodology for Computing the Radar Cross Section and Doppler Signature of Wind Farms," *IEEE Trans. Antennas Propag.,* vol 61, no. 10, pp. 5166-5174, Oct., 2013.

[9] B. M. Kent *et al.*, “Dynamic Radar cross section and radar Doppler measurements of commercial General Electric windmill power turbines - Part 1: predicted and measured radar signatures,” IEEE Antennas Propag. Mag., vol. 50, Iss. 2, pp. 211-219, April, 2008.

[10] M. Bryanton *et al.*, “Stealth Technologies for Wind Turbines Final Report,” BAE, Rep. TES101865, 2007.

Chapter 4 Wind Turbine Blade Radar Signatures in the Near-Field: Experimental Confirmation

4.1. Introduction

In Chapters 2 and 3, a theoretical framework has been developed to predict and explain the radar signatures of WT blades. This chapter is divided into two parts: the first part is dedicated to confirm the theoretical results and the second part analyses the radar echoes from faulty WTs.

Section 4.2 describes the experimental set-up used which includes the RF system (Doppler-radar and laptop for acquisition), two types of blades - flat plates for testing purposes as well as blades from a real, small wind turbine - and a DC motor to set the rotational velocity of these blades. The experimental radar signatures in the time, frequency and joint time-frequency domains are analysed and compared with their corresponding theoretical signals in sections 4.3, 4.4 and 4.5 respectively.

Section 4.6 is dedicated to the experimental observation of the radar signature from faulty WTs. The objective sought by these experiments is to demonstrate the capability of a radar system to detect WT faults. The simplicity of the equipment used during experiments is in accordance with the idea of developing a low-cost system to detect structural problems in WTs.

4.2. Experimental set-up

The experimental set-up designed to study the radar signature of a WT was not excessively complicated in terms of technology and configuration. This is in accordance with the final goal of the project which is to study the feasibility of detecting WT faults employing a Doppler radar as a low-cost and easy-to-use system. This last idea will be explored in detail in section 4.6 where the tests using this Doppler radar are shown and analysed.

The following subsections describe the experimental configuration designed to perform the measurements as well as all the elements that form this experimental set-up.

4.2.1. Experimental configuration

A scaled WT model was used to record the radar echoes from WTs in laboratory and controlled conditions. Fig. 4.1 represents a diagram of the experimental configuration. The scaled WT model was placed facing into the Doppler radar inside an anechoic chamber as the picture in Fig. 4.2 shows. Inside this chamber, the WT radar signature could be recorded avoiding ground reflections. The WT dimensions, its rotational speed and the WT-radar distance are specified in Fig. 4.1. The different auxiliary devices, which will be explained in more detail in the following subsections, are also sketched in Fig. 4.1.

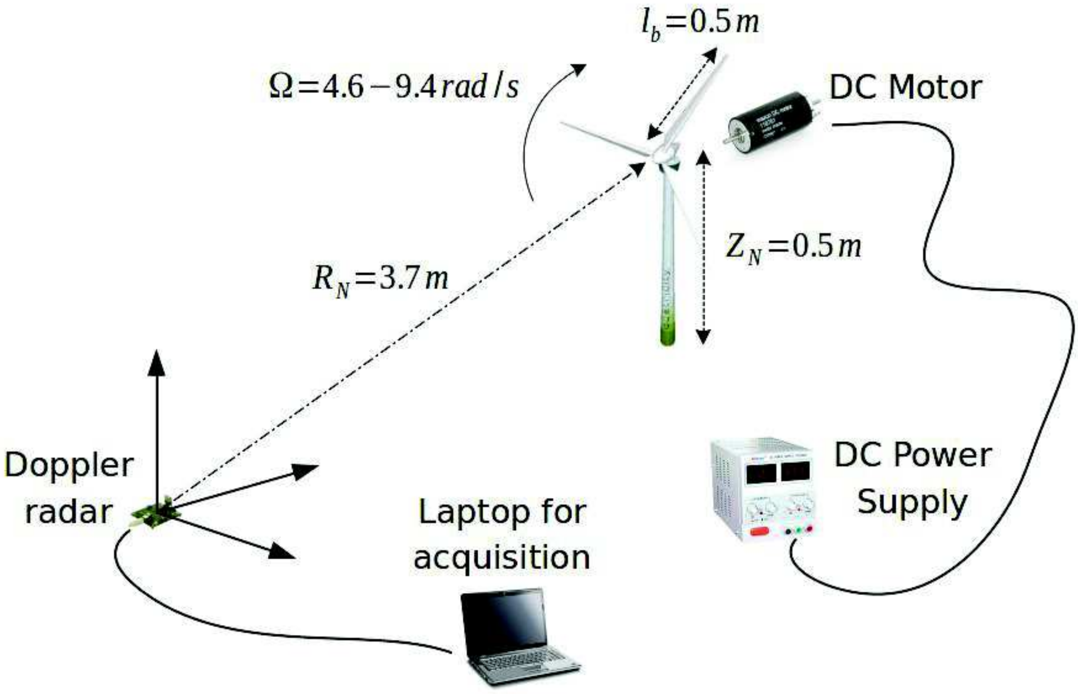

Fig. 4.1: Sketch of the experimental set-up.

The scaled WT was mounted on a wooden tripod. The radar was connected to a laptop through a USB connector with two purposes: to provide power supply to the radar and to acquire the data from measurements. An external power supply was placed outside the chamber to feed a DC motor that set the rotational velocity of the WT at a known value.

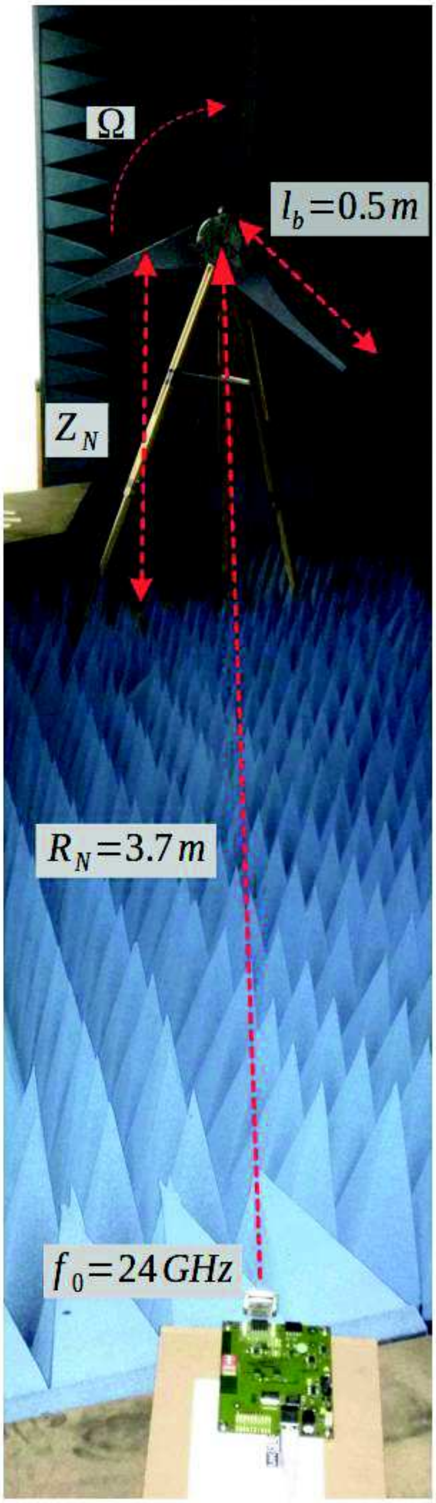

Fig. 4.2: Doppler radar in front of the WT in one of the experiments.

4.2.2. Scaled Wind Turbine

Two types of blades were used for experiments, having different purposes. The aluminium flat rectangular blades showed in Fig. 4.3a were built to verify the results predicted by the SCM developed in Chapter 2. The length of each blade is $l_b = 0.50\,m$ and its width is $d_b = 0.03\,m$. The curved blades displayed in Fig. 4.3b are a more realistic model of a WT. In order to improve their reflectivity, these curved blades, originally made of plastic, were covered with aluminium paint. The blade length is also $l_b = 0.50\,m$, although the shape and width varies along the blade.

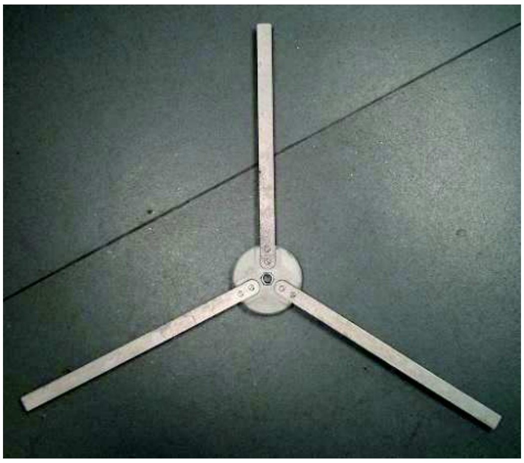

(a)

(b)

Fig. 4.3: WT blades used during the experiments. (a) Flat blades. (b) Curved blades.

The backscattered signal from the flat blades was simulated on Matlab using the SCM. This model assumes that the amplitudes of the echo signals from the different point-scatterers have the same amplitude. The signals differ only in their phases which depend on the position of the particular scattering centre on the blade.

The theoretical model of Chapter 3 was developed to explain the features observed in the time-domain signature of the curved blades showed in Fig. 4.3b. In order to compare the experimental signature from the curved blades with the corresponding theoretical signal, a CAD model of one of these blades was manually created. The system used to obtain the coordinates of different points on the blade is displayed in Fig. 4.4. The separation between two points in the x and y direction was $4\ mm$ maximum which is equivalent to $\lambda/3\ m$. The height or z coordinate was measured with the help of a calliper. The blade surface can then be represented by a set of points with three components: height and directions along and transversal to the blade. The result is shown in Fig. 4.5. The expression (3.43) derived in section 3.3 was applied to each of these points to obtain the theoretical signal. The radar antenna transmits and receives in vertical polarization, so only the component E_y in equation (3.43) was used to simulate the backscattered signal.

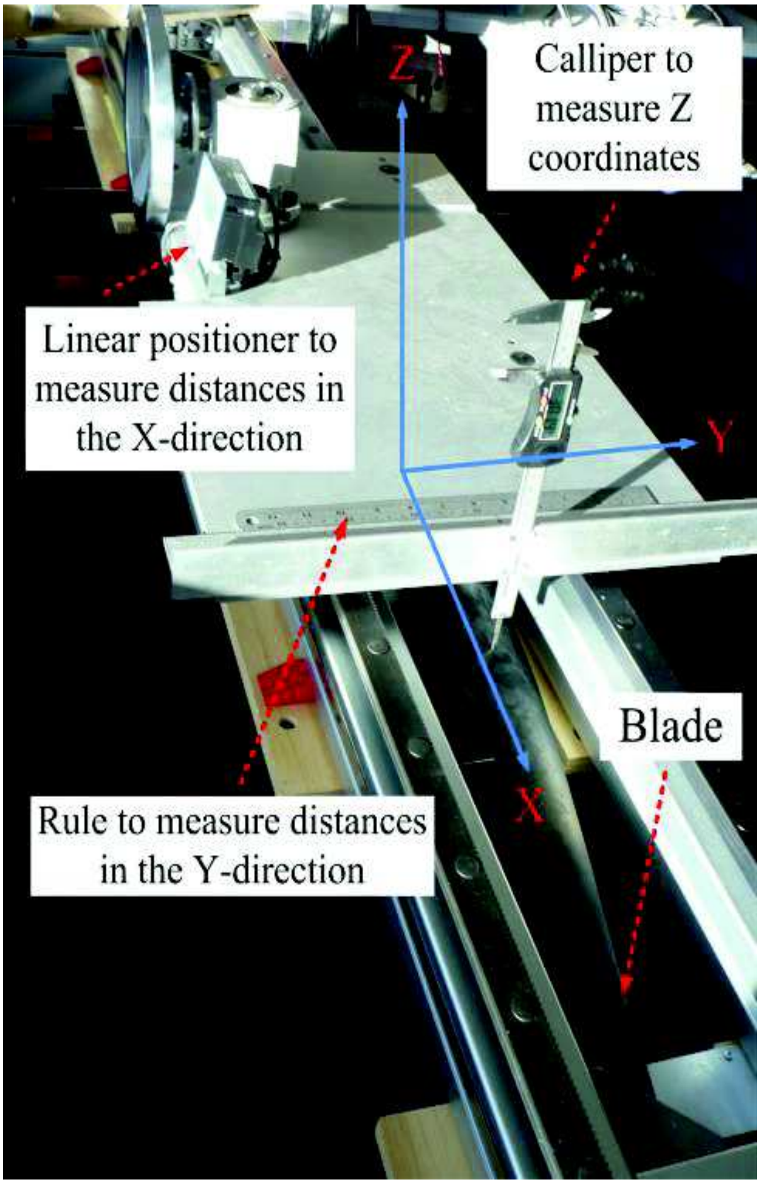

Fig. 4.4: Experimental set-up to measure the curved blade profile.

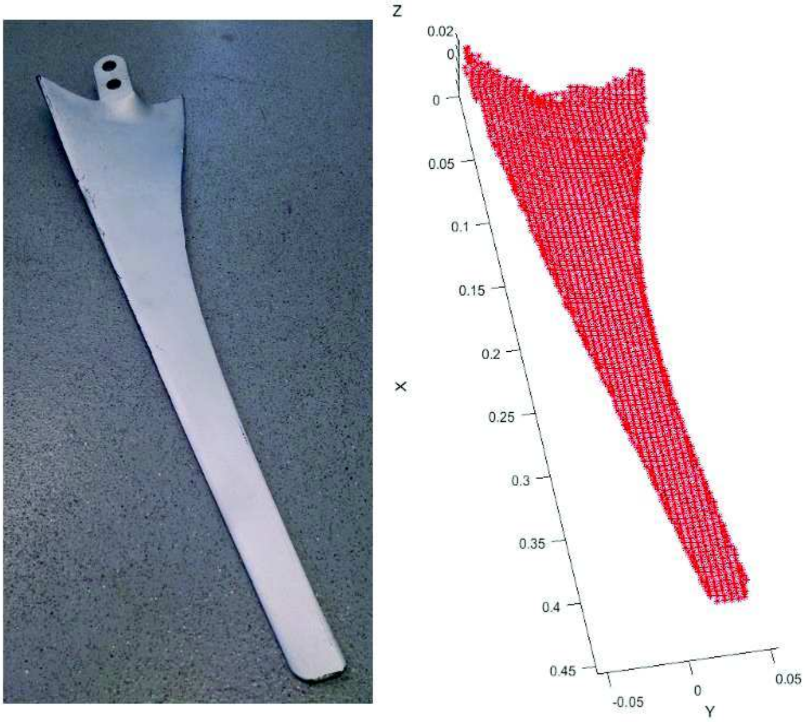

Fig. 4.5: Curved blade compared to its CAD model.

The DC motor in Fig. 4.6 corresponds to the model EMG49 bought from [1]. This is a $24\,V$ motor fully equipped with encoders and a 49:1 reduction gearbox. The motor was placed inside a metal box and, subsequently, this box was attached to the back of the WT hub through the motor shaft to set the rotational velocity at a known value.

Fig. 4.6: DC motor used to set the rotational speed of the WT at a known value.

The voltage of the power supply fixes the WT rotational speed. Two voltages were used during the experiments: 16V and 8V, corresponding to maximum and minimum velocities respectively. This rotational velocity, measured in rad/s, was calculated using a video record of the spinning WT. In this way, it was possible to establish the relation voltage-angular velocity: $\Omega = 9.4\ rad/s$ (16V) and $\Omega = 4.6\, rad/s$ (8V).

At this stage, it is worth mentioning that this set of experiments does not represent a scaled anechoic chamber experiment in the traditional sense, where there is a scaling ratio between frequency and target size. The reason for this is that at this early stage in the research of the overarching problem of trying to detect WT faults, there is no set recommendation on the frequency to be used (even the 24 GHz considered here could ultimately be used), where at the same time WT blade lengths could vary from a few tens of meters to more than $120\ m$. Instead, the experimental set-up was built to test the major objective of this research, which is the modelling of WT radar signatures in the near-field, with a CW radar device and WTs of an appropriate size for the anechoic chamber.

As a summary, the experimental parameters are listed in Table 4.1.

Parameter	Symbol	Minimum	Typical	Maximum	Units
Blade length	l_b		0.50		m
Blade width	d_b		0.03 (flat blades)		m
Height of the hub respect to the radar	Z_N	0.0	0.47	1.15	m
Radial distance from the radar to the hub	R_N	3.65	3.70	3.80	m
Rotational speed	Ω	4.60		9.40	rad/s

Table 4.1: Experimental parameters.

4.2.3. Doppler-radar

The radar employed was a *24 GHz* Doppler radar with I/Q digital outputs and a sampling frequency of *44.1 kHz*, with the unambiguous Doppler range being half the sampling frequency. The radar used was their old version of the K-LC2 which is shown in Fig. 4.7. The main features of the K-LC2 version employed during experimental measurements are explained in this section. These are slightly different from the characteristics of the current version of the module. The datasheet of the current version of the K-LC2 can be found on [2].

The K-LC2 module used was a 4 patch Doppler radar of $24\,GHz$ with an asymmetrical beam useful for short distance applications. The main features of the radar module are listed in Table 4.2.

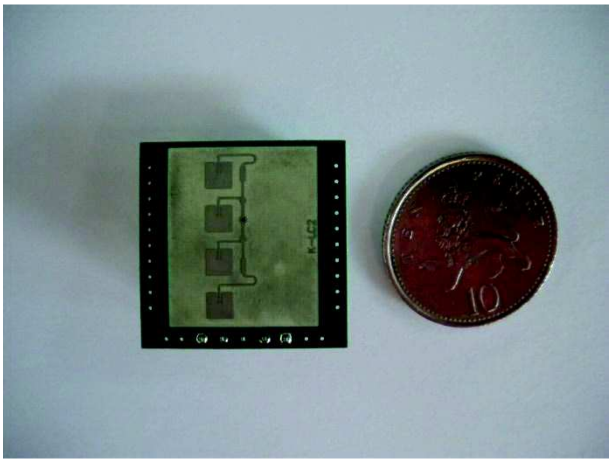

Fig. 4.7: K-LC2 Doppler module compared with a 10p coin.

Parameter	Minimum	Typical	Maximum	Units
Transmitter Frequency	24.050	24.125	24.250	GHz
Horizontal -3dB beamwidth E-plane		80		deg
Vertical -3dB beamwidth H-plane		34		deg
Outline dimensions		25 x 25 x 6		mm^2

Table 4.2: K-LC2 Doppler transceiver features.

The K-LC2 radar was directly connected to a PCB motherboard as shown in Fig. 4.8. The hardware, called ST100 StarterKit [3], consists of two dual-channel low noise amplifiers, a dual 16Bit ADC, a dual 16 Bit DAC and a USB interface. Radar signals are converted by the 16 Bit ADC and transmitted by a standard USB audio protocol. The 16 Bit DAC drives the FM inputs of the radar modules and is also driven by a standard USB audio protocol. No driver software is necessary to operate the audio protocol. Fig. 4.9 corresponds to the block diagram of the ST100 StarterKit.

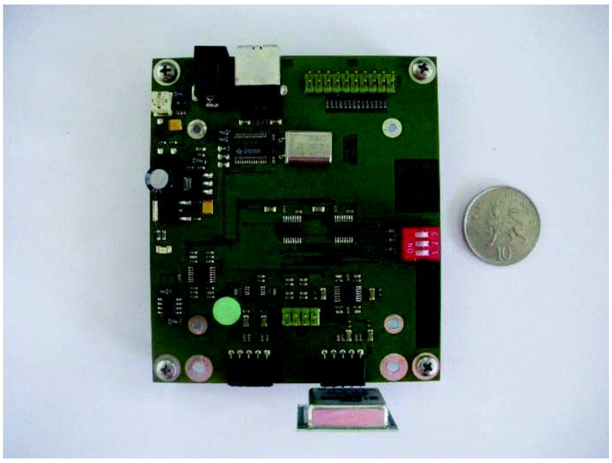

Fig. 4.8: ST100 StarterKit PCB motherboard with the K-LC2 module connected.

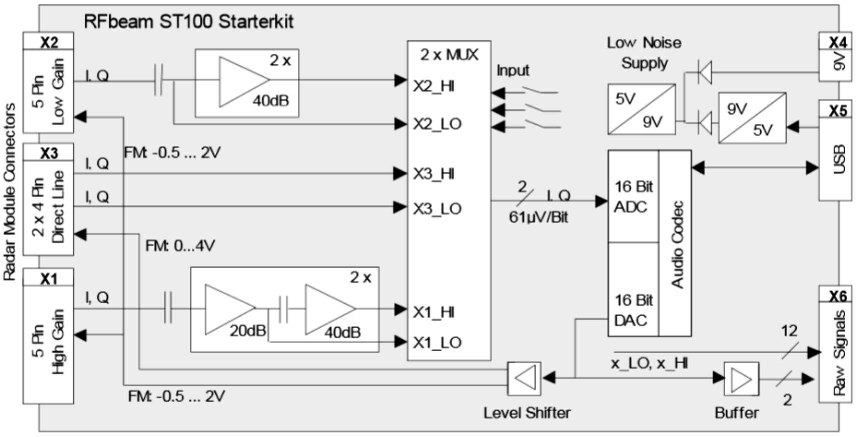

Fig. 4.9: ST100 StarterKit block diagram [3].

As it can be seen in the block diagram, the ST100 StarterKit provides 3 connectors (X1-X3) for different types of radar modules. The K-LC2 module is connected to the connector X1, the high gain input. This connector is optimised for radar modules without IF amplifier like the K-LC2.

The frequency response of the ST100 StarterKit was experimentally measured. The points in Fig. 4.10 correspond to the frequency response of channels 1 and 2 (I and Q) while the solid line is the frequency response of two cascaded first-order Butterworth high-pass filters and cut-off frequency 6 Hz each.

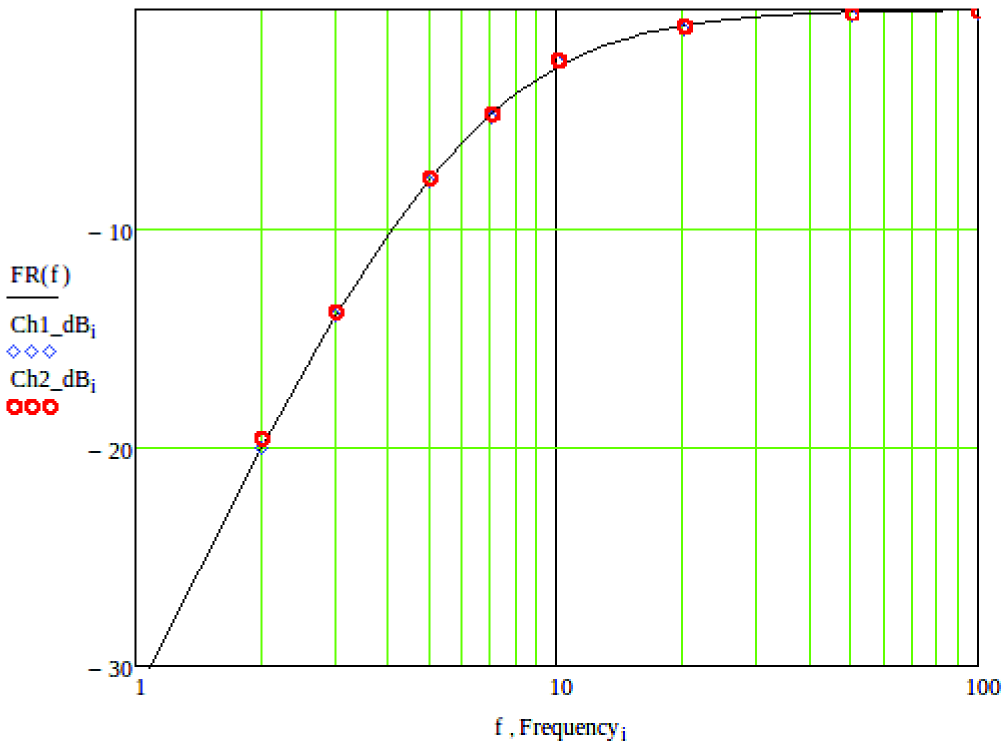

Fig. 4.10: Frequency response of channels I and Q and two cascaded Butterworth filters.

Power supply is derived from the USB port and converted to low noise supply voltage. Codec and radar modules at X1-X3 are supplied by this low noise voltage.

The horizontal and vertical beamwidths of the radar forced to place the WT at certain distance to be completely covered by the transmitted signal. The most critical situation is related to the horizontal beamwidth, *34°*. A safe criterion to calculate the distance □ that allows the radar to cover the whole WT is $R > \frac{1\,m}{\tan 17} = 3.33\,m$. This means that the half beamwidth covers the area expanded by the WT blades. However, due to the restricted dimensions of the anechoic chamber, the WT could only be placed at a maximum distance of $R = 3.8\,m$, approximately.

4.3. Time-domain Signatures

In this section, the methodology employed to compare the theoretical and experimental time-domain signatures is explained and, subsequently, the results are analysed. The flat and curved blades cases are treated separately in two different subsections.

In order to remove high frequency noise, a low-pass filter was applied to the experimental signals. The experimental parameters are in the range of values indicated in Table 4.1, so the same parameters were used in equations (2.4) and (3.43) to simulate the backscattered signals. The theoretical signatures had to be filtered to simulate the two cascaded Butterworth filters that the ST100 StarterKit contains. The effect of this filtering reproduced certain features exhibited by the experimental signals that were not explained by the theoretical models. Fig. 4.11 corresponds to the block diagram of the signal processing performed to compare the theoretical and experimental signatures.

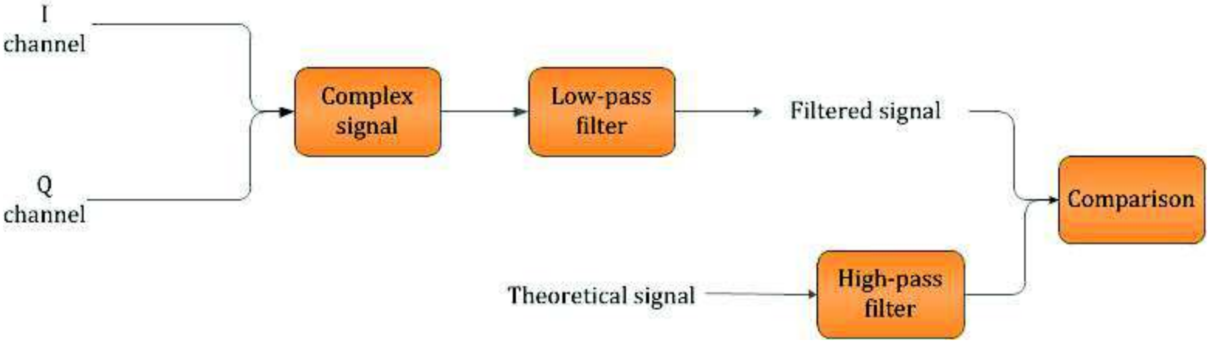

Fig. 4.11: Signal processing performed to compare simulated and experimental results.

The correlation coefficient between the theoretical signatures, A, and the experimental signals, B, was used to assess the accuracy of the theoretical models. This correlation coefficient is defined as:

$$r_{coeff} = \frac{\sum_m \sum_n (A_{mn} - \bar{A})(B_{mn} - \bar{B})}{\sqrt{\sum_m \sum_n (A_{mn} - \bar{A})^2 \sum_m \sum_n (B_{mn} - \bar{B})^2}}$$

where $\bar{A}$ and $\bar{B}$ are the mean (DC) values of the signals and n, m are the indices of the signals points (in MATLAB, the elements of the vectors that form the signals).

4.3.1. Results for flat blades.

Fig. 4.12 shows the experimental time-domain signature of a single flat blade corresponding to the typical parameters of Table 4.1: $l_b \times d_b = 0.50 \times 0.03\, m$, $Z_N = 0.47\, m$, $R_N = 3.70\, m$, $f_0 = 24\, GHz$. The rotational speed was Ω=4.6 *rad/s*. The theoretical signal simulated using the same parameters has been plot on top of the experimental signal.

The graph shows nearly one-to-one coincidence between the signals. The correlation coefficient between both signatures is, indeed, high: 0.92. The experimental signal exhibits the features predicted by the analysis done in sections 2.4 and 2.6 of equations (2.32) and (2.66). Two symmetric wide peaks separated by a dip in the signal can be observed. This pattern repeats itself forming a train of pulses whose duration is, theoretically, $T = \frac{2\pi}{\Omega} = \frac{2\pi}{4.6} = 1.366\, s$, the rotational period. This value coincides with the duration of the experimental signal. All plots are normalized to their respective highest intensity.

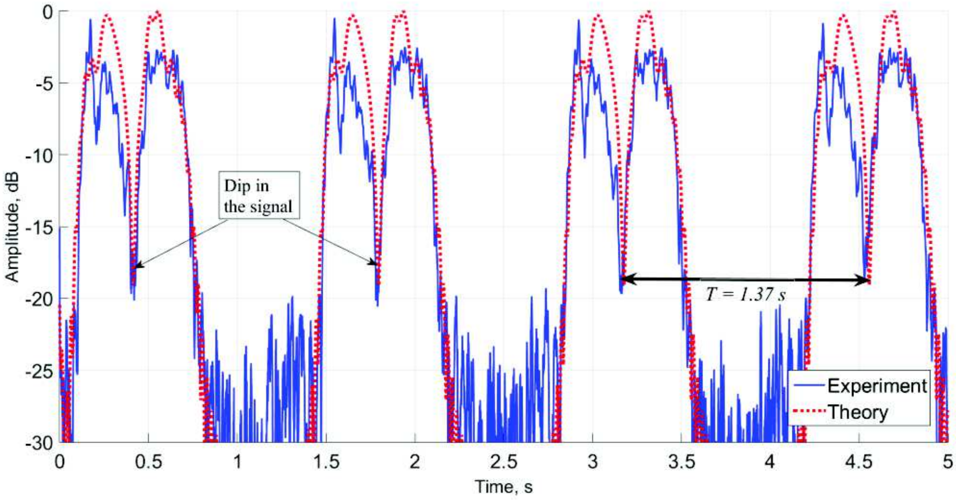

(a)

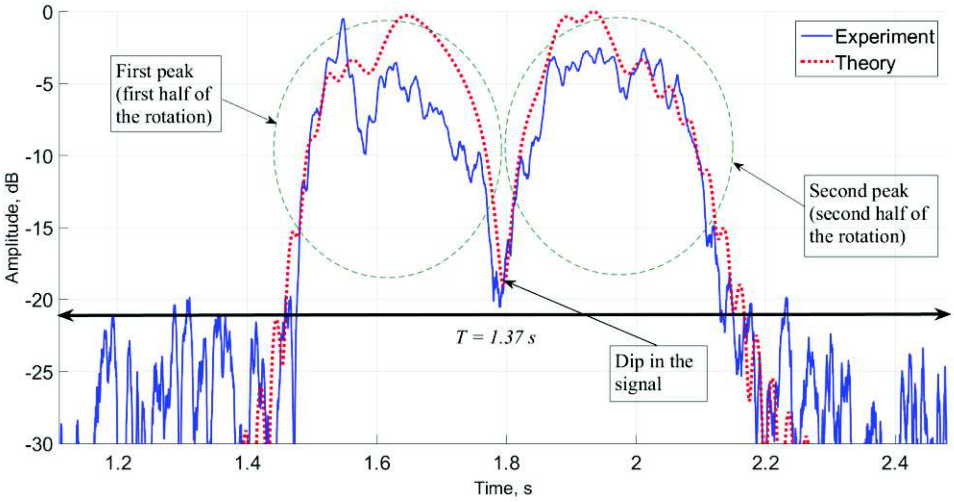

(b)

Fig. 4.12: Theoretical and experimental time-domain signatures. $l_b \times d_b = 0.50\times 0.03\ m$, $Z_N = 0.47\ m$, $R_N = 3.70\ m$, $f_0 = 24\ GHz$, Ω=4.6 rad/s

The dip in the pulses observed in both signatures separates the two symmetric wide peaks (Fig. 4.12b). Although the signal is symmetric respect to its centre, the dip observed is not part of the signal itself. It is a consequence of the effect of the two cascaded Butterworth high-pass filter mentioned in section 4.2.3. Fig. 4.13 correspond to the experimental and theoretical signatures of one flat blade, but the high-pass filter was not applied to the theoretical signal in this case. Although Fig. 4.12 and Fig. 4.13 are highly similar, the drop in the amplitude has disappeared in the theoretical signal, but it is still present in the experimental curve. The explanation for this resides in the fact that the centre of the signal is associated to frequencies of few Hz,so it exhibits a flat zone. Therefore, when the high-pass filter is applied, it eliminates these frequencies and produces the dip observed in the signal.

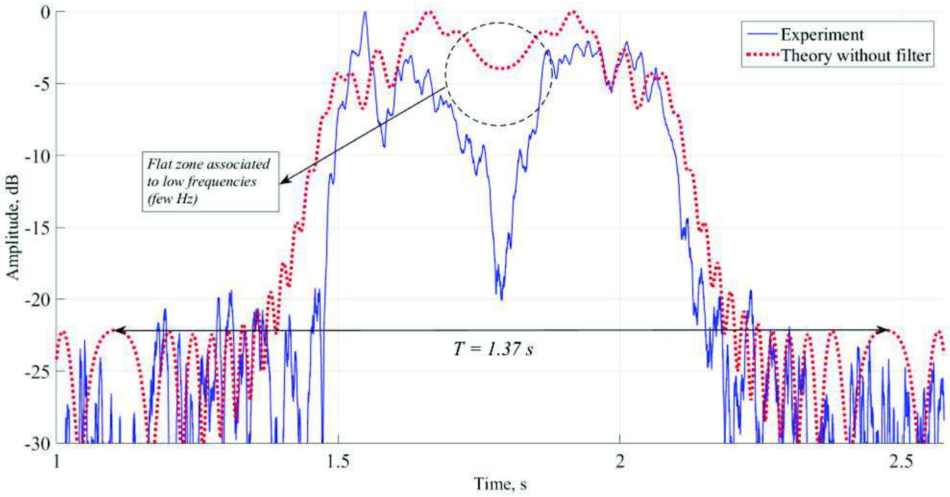

Fig. 4.13: No high-pass filter is applied to the theoretical signal. Experimental and simulation parameters: $l_b \times d_b = 0.50 \times 0.03\ m$, $Z_N = 0.47\ m$, $R_N = 3.70\ m$, $f_0 = 24\ GHz$, **Ω**=4.6 rad/s

The graph in Fig. 4.14 corresponds to the case of three flat blades. The features observed are also well-predicted by the SCM. The correlation coefficient is, in this case, 0.89 which is high as expected from visual comparison. The time-domain signature is formed by a train of pulses and it replicates itself every $T = \frac{2\pi}{\Omega} = \frac{2\pi}{9.4} = 0.668\ s$, the period of one full turbine revolution which coincides with the time measured in Fig. 14a.

Two consecutive pulses are separated in time by the period $T_3 = \frac{2\pi}{3\Omega} = \frac{2\pi}{3 \cdot 9.4} = 0.223\ s$ which is similar to the time measured on Fig. 4.14a. T and T_3 are related to the two WT's rotational symmetries. The former is associated to the $360°$ rotational symmetry while the latter is a consequence of the $120°$ geometrical symmetry. However, as it was described in section 2.5 in Chapter 2, the individual backscattered signals of two blades combine to form one single return in the three blades signature. Therefore, the inevitable physical differences between the blades themselves produce discrepancies among the individual pulses in the experimental signal.

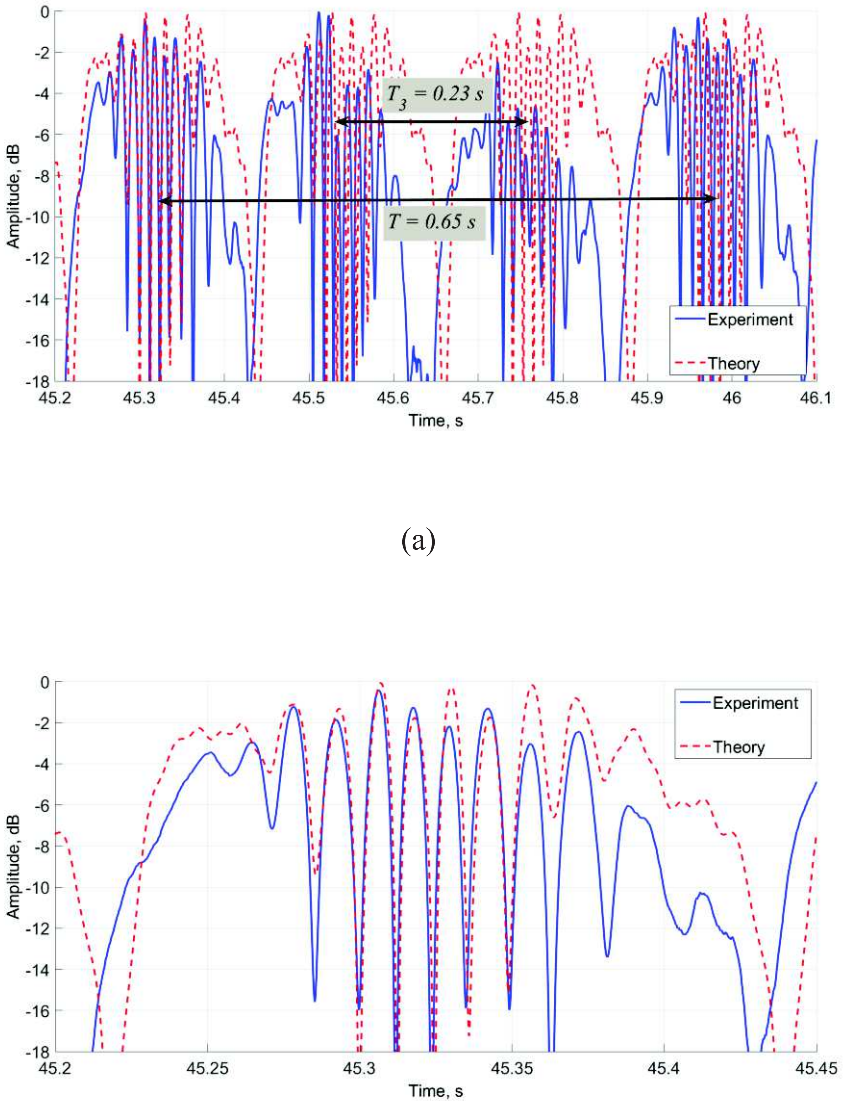

(a)

(b)

Fig. 4.14: Theoretical and experimental time-domain signatures of three blades. $l_b \times d_b = 0.50 \times 0.03\ m$, $Z_N = 0.47\ m$, $R_N = 3.77\ m$, $f_0 = 24\ GHz$, Ω=9.4 rad/s

4.3.2. Results for curved blades.

Fig. 4.15 corresponds to the simulated backscattered signal from a single flat blade using the SCM on top of the measured time-domain signature from a curved blade. The graph has already been shown in Chapter 3 and it served there as a motivation to expand the theoretical framework beyond the SCM. The correlation coefficient between the simulated and experimental signatures is in this case 0.61, a lower value than those obtained in the previous section. The reason for this behaviour has been already explained in section 3.2.

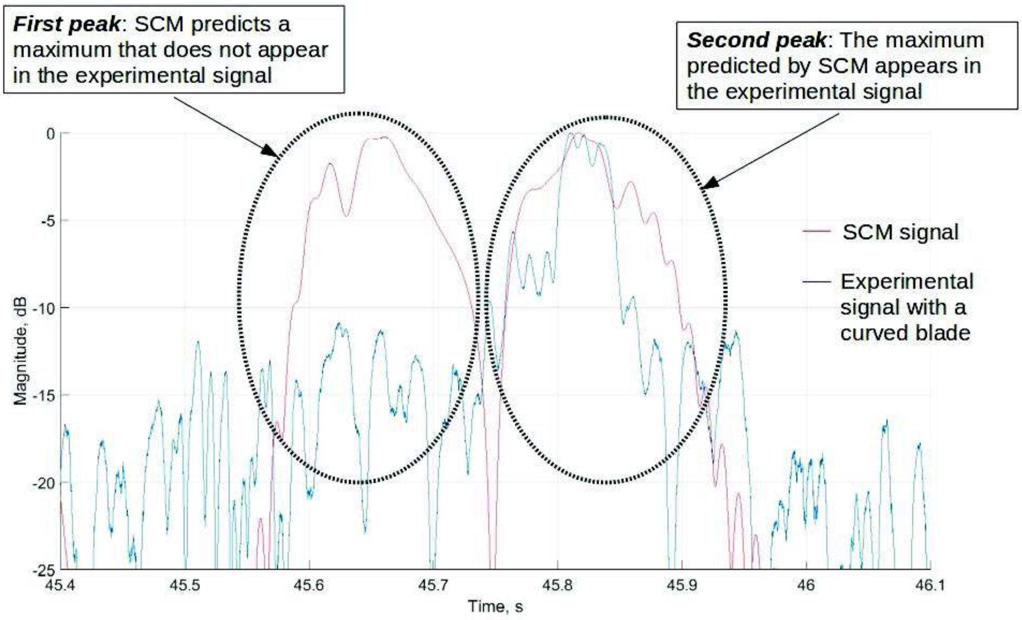

Fig. 4.15: Comparison between the signal predicted by the SCM for a single flat blade and the measured signal from a curved blade.

Expression (3.43) can now be applied to each point in the CAD model of a curved blade (see Fig. 4.5) to obtain the theoretical signal. The radar antenna transmits and receives in vertical polarization, so only the component E_y in equation (3.43) has been used to simulate the signal. The graphs in Fig. 4.16 correspond to the theoretical and experimental results for a single blade.

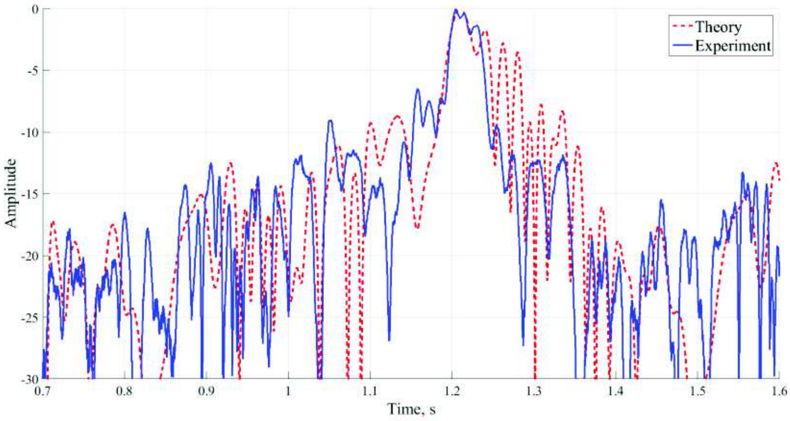

Fig. 4.16: Theoretical and experimental time-domain signatures of a single curved blade. Experimental parameters: $l_b = 0.50m$, $Z_N = 0.47\ m$, $R_N = 3.70\ m$, $f_0 = 24\ GHz$ and Ω=9.4 rad/s

The correlation coefficient between the theoretical and experimental signals in Fig. 4.16 is 0.92. This results shows how equation (3.43) predicts the asymmetry in the time-domain signature of a single curved blade: the peak predicted by the SCM in Fig. 4.15 has now disappeared.

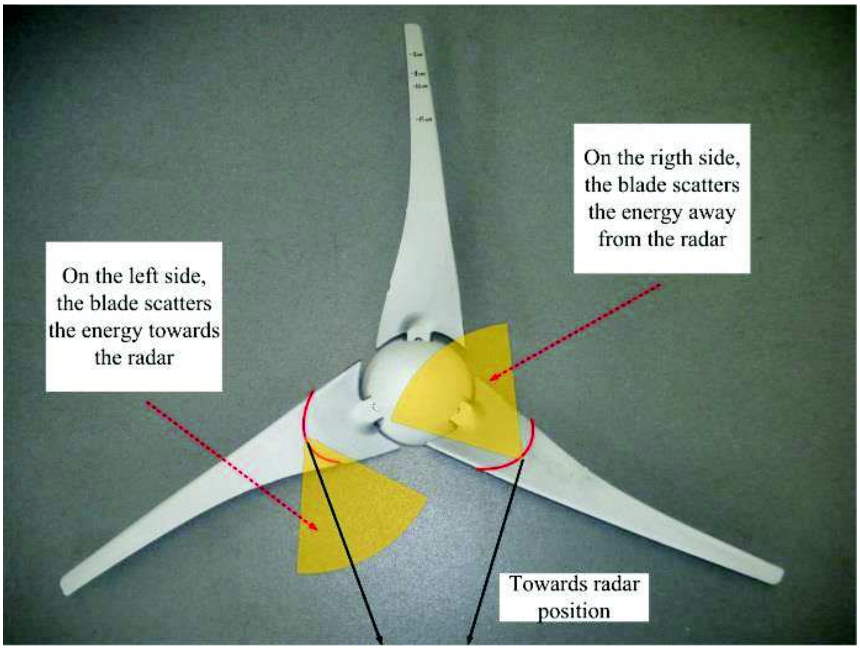

Fig. 4.17: Scattering mechanism that produces an asymmetry in the time-domain signature of a curved blade.

Fig. 4.17 has been already analysed in section 3.2, but it is shown again here for the sake of clarity. The curved shape of the blade scatters the EM energy asymmetrically and that is the reason why one of the peaks predicted by the SCM disappeared. If the blade rotates clockwise or anticlockwise, this maximum peak will take place at different moments. If the blade rotates clockwise, the second maximum peak observed in Fig. 4.15 remains which correspond to the maximum reflection towards the radar in Fig. 4.17. However, when the WT rotates anticlockwise, the maximum return position will be reached first and consequently the first maximum peak will appear. This phenomenon has been measured using a single curved blade rotating at the speed ($\Omega = 9.4\, rad/s$) in both clockwise and anticlockwise directions and the results shown in Fig. 4.18.

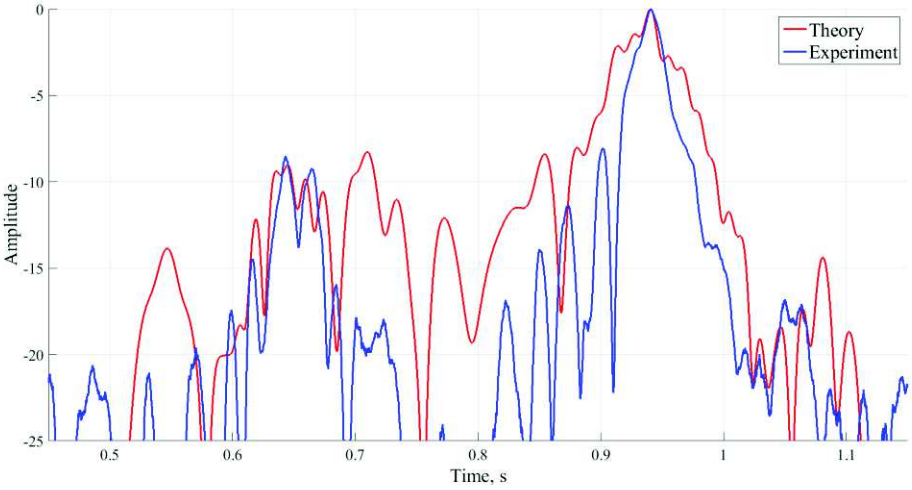

(a)

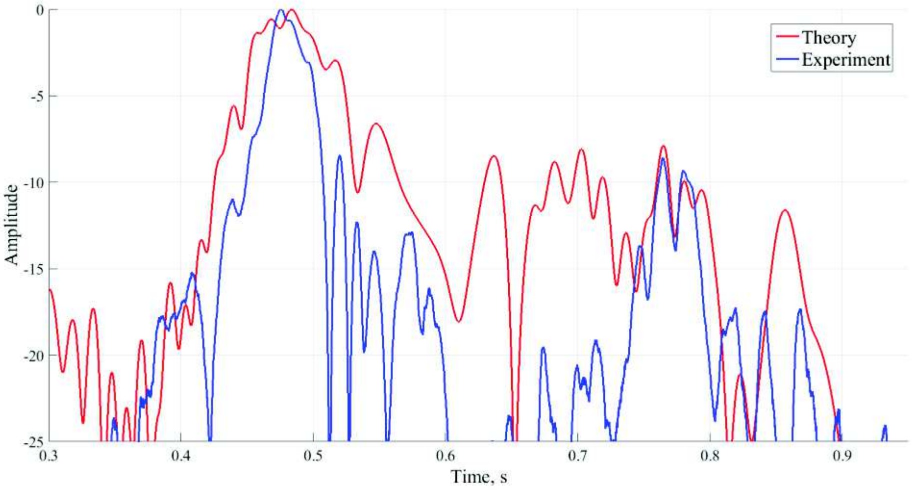

(b)

Fig. 4.18: Comparison between the theoretical and experimental signal of a single curved blade rotating (a) clockwise, (b) anticlockwise.

Fig. 4.18a corresponds to the time-domain signal of a single curved blade rotating clockwise. As expected, the first peak that would appear in the SCM (Fig. 4.15) vanishes but the second maximum remains. Fig. 4.18b represents to the opposite case when the direction of rotation is anticlockwise. The correlation coefficients are 0.92 for Fig. 4.18a and 0.91 in the case of Fig. 4.18b.

The theoretical expression (3.43) predicts the drop in the signal due to the asymmetries introduced by the curvature of the blades. The scattering centres model was not able to foresee this phenomenon. The prediction of this behaviour is the main contribution of the model developed in Chapter 3.

The experimental and theoretical time-domain signatures of a full WT (three curved blades) is shown in Fig. 4.19. The correlation coefficient is, in this case, 0.87. As in the case of flat blades (Fig. 4.14a), the signal is formed by a train of pulse separated by $T_3 = \frac{2\pi}{3\Omega} = \frac{2\pi}{3\cdot 9.4} = 0.223\ s$. The signal repeats itself every $T = \frac{2\pi}{\Omega} = \frac{2\pi}{9.4} = 0.668\ s$.

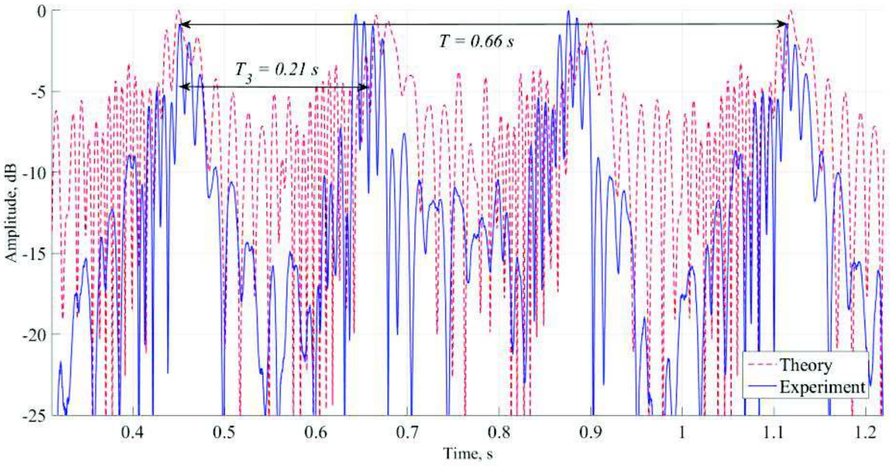

Fig. 4.19: Theoretical and experimental time-domain signatures from three curved blades. Experimental parameters: $l_b = 0.50\ m$, $Z_N = 0.48\ m$, $R_N = 3.70\ m$, $f_0 = 24\ GHz$ and $\Omega =$ 9.4 rad/s

4.4. Frequency-domain Signatures

In Chapter 2, the theoretical analysis predicted that the backscattered signal spectrum from flat blades was formed by a series of spectral lines. The amplitude of these lines depended on the Bessel functions whose argument was a function of the geometrical parameters of the system WT-radar. Although this was an approximated result, the comparison with the experimental spectrum will show enough accuracy in this prediction.

In the case of curved blades, the theoretical spectrum is harder to obtain, but no major differences should be expected with respect to the flat blades case.

4.4.1. Results for Flat Blades.

Fig. 4.20a corresponds to the two-side spectrum of a single flat blade. The theoretical spectrum is the result of applying the FFT to the signal (2.66). It can be observed how the envelopes of the theoretical and experimental spectra highly coincide. The amplitude of the spectral lines in the theoretical signature has a maximum in the amplitude at approximately $20\,Hz$ and decays after this. The maximum in the experimental spectrum is less clear but it is produced at around $20\,Hz$; the decaying behaviour is similar in both cases. The last observable frequency in the theoretical spectrum is $47\,Hz$ approximately while the experimental spectrum presents spectral lines until $60\,Hz$. This may be due to a not perfect alignment between the radar and the WT or to vibrations in the wooden tripod while the blade rotates.

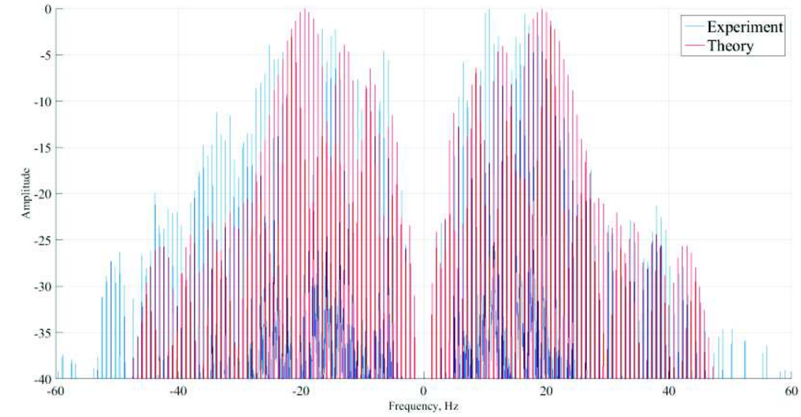

(a)

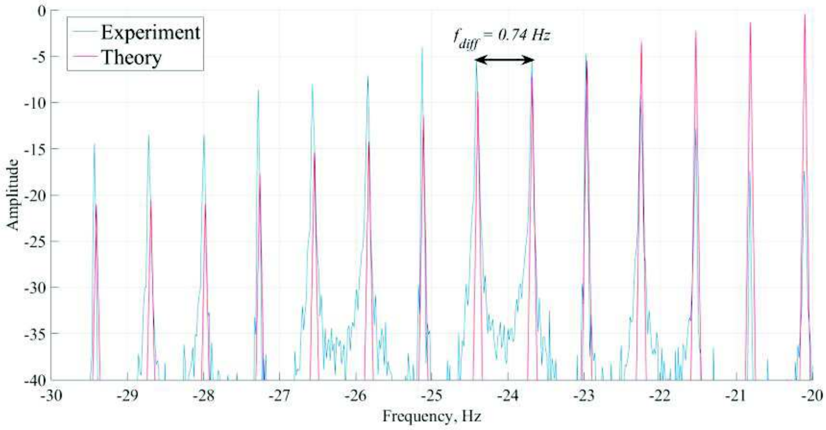

(b)

Fig. 4.20: (a) Theoretical and experimental spectrum of a single flat blade. (b) A portion of *10 Hz* in the spectrum. The parameters of the experiment are $l_b \times d_b = 0.50 \times 0.03\ m$, $Z_N = 0.47\ m$, $R_N = 3.70\ m$, $f_0 = 24\ GHz$, Ω=4.6 rad/s

The drop in the amplitude of the first frequencies around $0\ Hz$ is however artificial and it is caused by two cascaded Butterworth high pass filters mentioned in section 4.2.3. Without this filtering, the spectrum would resemble the theoretical spectra studied in Chapter 2.

A portion of $10\ Hz$ of the spectrum has been plotted in Fig. 4.20b. The amplitudes for each spectral line differ slightly between theory and experiment, but both take place at the same frequency. The SCM predicts that the separation between two consecutive frequencies is given by equation (2.24) when $p = 1$. It only depends on the angular velocity of the turbine and its value is, in this case, $f_{diff} = \frac{\Omega}{2\pi} = \frac{4.6}{2\pi} = 0.73\ Hz$ which corresponds to the difference between the spectral lines marked on Fig. 4.20b.

4.4.2. Results for Curved Blades

The graphs in Fig. 4.21 correspond to the theoretical and experimental spectra of a single curved blade. The theoretical spectrum has been obtained by applying the FFT to the signal (3.45). The bandwidth is approximately $100\,Hz$ in both cases (the rotational velocity used was $\Omega = 9.4\,rad/s$). As in the flat blade case, it is reasonable to believe that the amplitude of the spectral lines also depends on the geometrical parameters of the system WT-radar through the Bessel functions. However, this dependence would be hard if not impossible to obtain, but the idea that each part of the blade contributes differently to the spectrum is still valid.

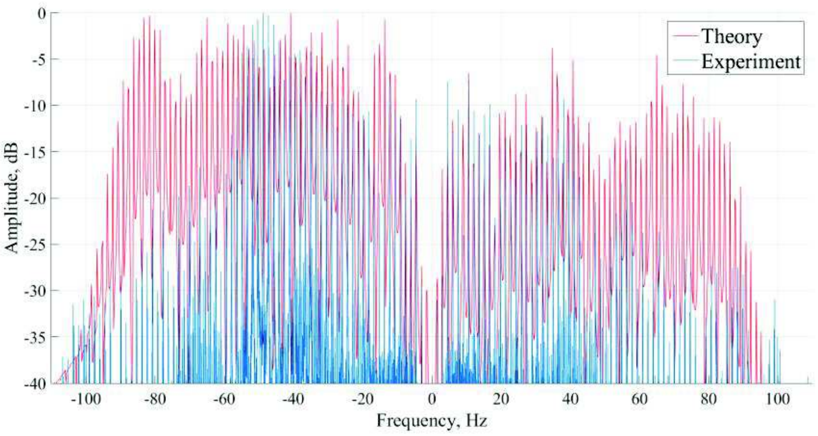

(a)

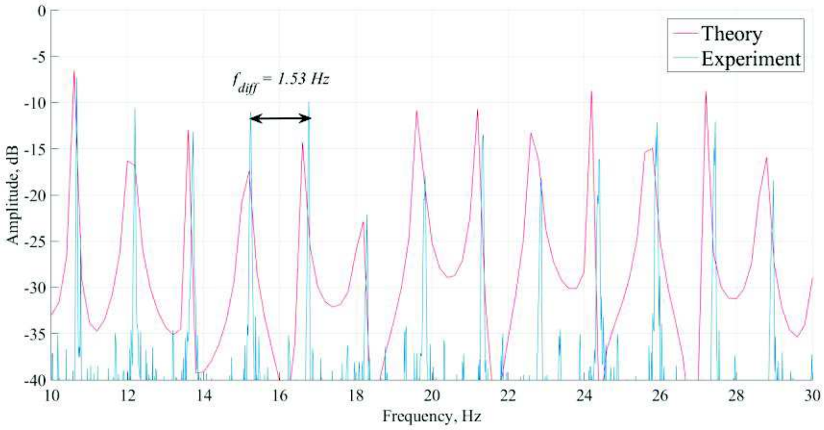

(b)

Fig. 4.21: (a) Theoretical and experimental spectrum of a single curved blade. (b) A portion of the spectrum. The physical parameters of the experiment are $l_b = 0.5\ m$, $Z_N = 0.47\ m$, $R_N = 3.70\ m$, $f_0 = 24\ GHz$ and Ω=9.4 rad/s

Although equation (2.24) was obtained in the context of flat blades, it still valid in the case of the radar signal from curved blades. The equation predicts that the difference between two consecutive spectral lines is $f_{diff} = \frac{\Omega}{2\pi} = \frac{9.4}{2\pi} = 1.50\ Hz$ which is close to the value observed in Fig. 4.21b.

4.5. Micro-Doppler Signatures

The last relevant part of the analysis is the joint time-frequency domain or micro-Doppler signature. As in previous sections, the simulated micro-Doppler signatures from flat and curved blades were obtained by applying the STFT to the theoretical signals (2.66) and (3.45) respectively.

4.5.1. Results for Flat Blades

The graphs in Fig. 22 correspond to the theoretical and experimental spectrograms of a single flat blade. It can be verified from Fig. 22b that the period of the signal is the predicted by the SCM, i.e $T = \frac{2\pi}{\Omega} = \frac{2\pi}{9.4} = 0.668\ s$. As it was explained in section 2.7, when the blade reaches its position of maximum backscattered energy, the micro-Doppler signature exhibits an intense response which takes place at $t_c = \frac{1}{\Omega}\cos^{-1}\left(\frac{-l_b}{2Z_N}\right) = 0.227\ s$. A comparison with the theoretical spectrogram shows that this flash occurs at a frequency of $45\ Hz$ approximately and it is inclined. This behaviour has been observed in previous investigations done on WT radar signature, e.g. [4]. In particular, the theoretical approach in [4] consisted in eliminating the term $\frac{L_{nm}^2}{R_N^2}$ from a similar equation like (2.66). The paper [4] contains the spectrogram of an actual WT and shows the inclined flash predicted by the SCM. This phenomenon is directly associated to the neglected term $\frac{L_{nm}^2}{R_N^2}$.

The power of the frequencies below this bright flash is also intense as expected from the signal spectrum. The trace of the blade tip can also be seen above the $45\ Hz$ bright point in the experimental micro-Doppler.

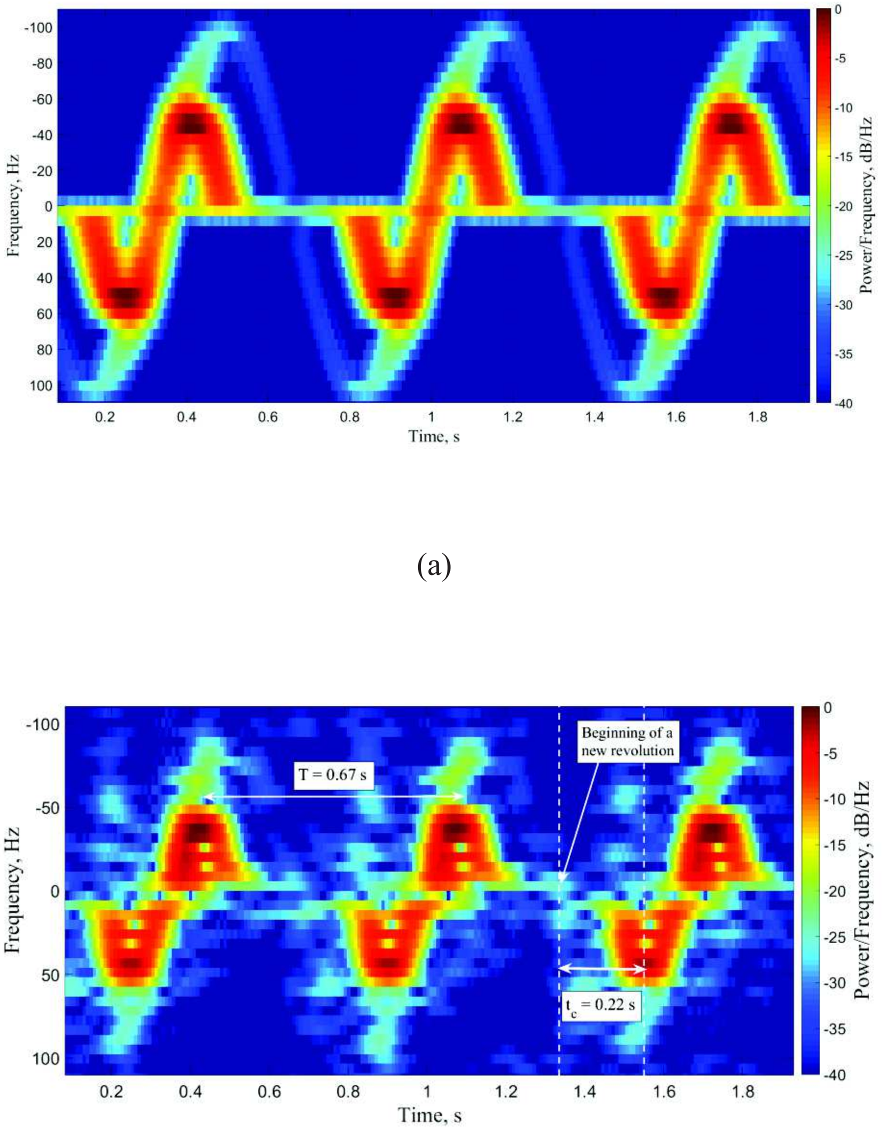

(a)

(b)

Fig. 4.22: Micro-Doppler signature of a single flat blade. (a) Theoretical signature. (b) Experimental signature. Parameters: $l_b \times d_b = 0.50 \times 0.03\ m$, $Z_N = 0.47\ m$, $R_N = 3.77\ m$, $f_0 = 24\ GHz$, Ω=9.4 rad/s

The spectrograms from the simulated and experimental backscattered signals of a full WT with flat blades can be seen in Fig. 4.23. The pattern observed in the case of a single flat blade replicates itself three times in one period, one for each blade. Therefore, no complicated EM effects are taken place and each blade generates its own signature. However, part of these individuals signals overlap on the spectrogram producing a dense graph where the clear sinusoidal trace of Fig. 4.22 cannot be distinguished. This is due to the experimental set-up restrictions and it may not be necessarily representative of what it would be obtained in real conditions experiments. Note that two different rotational velocities have been used to generate Fig. 4.22 (9.4 rad/s) and Fig. 4.23 (4.6 rad/s)

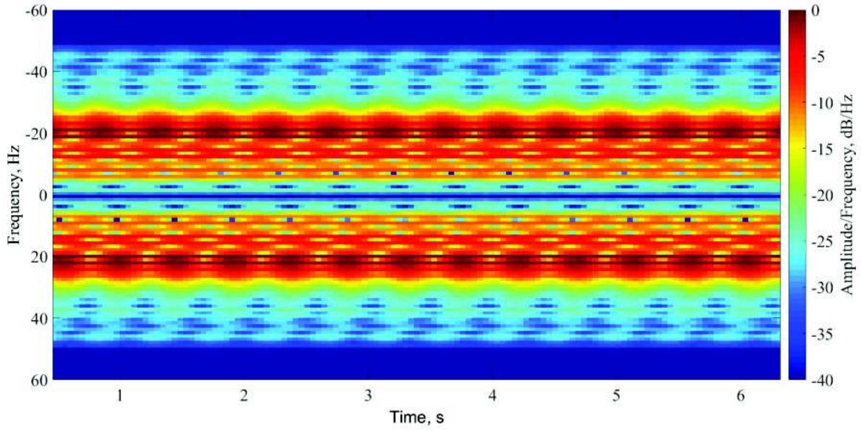

(a)

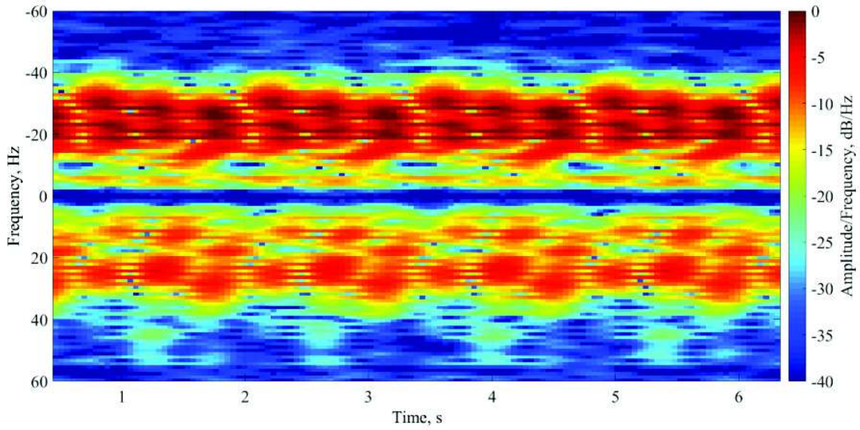

(b)

Fig. 4.23: Micro-Doppler signature of the full WT with flat blades. (a) Theoretical signature. (b) Experimental signature. Experimental parameters: $l_b \times d_b = 0.50 \times 0.03\ m$, $Z_N = 0.48\ m$, $R_N = 3.75\ m$, $f_0 = 24\ GHz$, Ω=4.6 rad/s

The results presented in the figures above are difficult, if possible at all, to compare to existing experimental results such as those in [5] and [6], as they are focused on monostatic and bistatic measurements in the far-field whereas the results presented here focus on monostatic measurements in the near-field. However, some comments could be made on qualitative aspects of the results obtained here. For example, the theoretical spectrograms of Fig. 4.22a and Fig. 4.23a predicts the same intensity in both upper and lower halves of the graph, as expected from the symmetry of the WT with respect to the vertical axis. If the alignment is not perfect during the measurement, part of the energy is scattered away from the radar in one side of the turbine and towards the radar in the symmetric side. Even if the alignment is perfect, this phenomenon would still be more pronounced if the blades are curved, as will be discussed in more detail in the next section.

4.5.2. Results for Curved Blades

A comparison between the theoretical and experimental spectrograms of a single curved blade is displayed in Fig. 4.24. The upper and lower halves of the experimental micro-Doppler differ in the power/frequency levels. This is a consequence of the complex shape of the blade: the energy is scattered away from the radar in one side of the WT and towards the radar in the symmetric side (see Fig. 4.17). The theoretical micro-Doppler in Fig. 4.24a was obtained from equation (3.45) and it predicts the same behaviour. An intense response takes place at around $50\ Hz$ in the experimental spectrogram, Fig. 4.24b. Since the time and frequency of this response depends on the geometrical parameters of the set-up and these are similar to the flat blades case (Fig. 4.22b), the flash takes place at a similar position in the spectrogram.

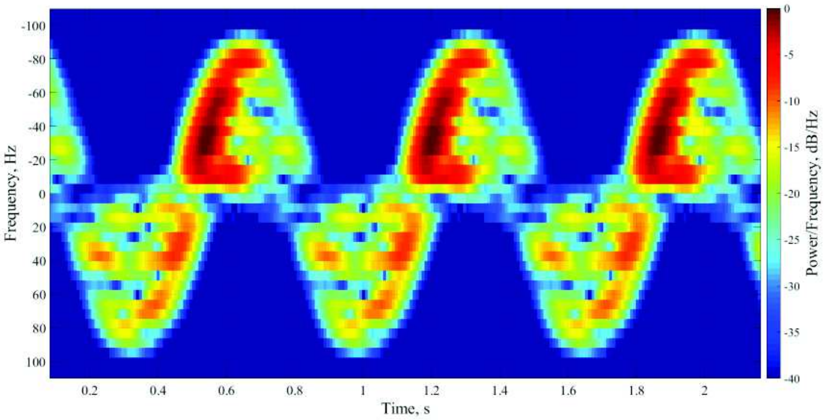

(a)

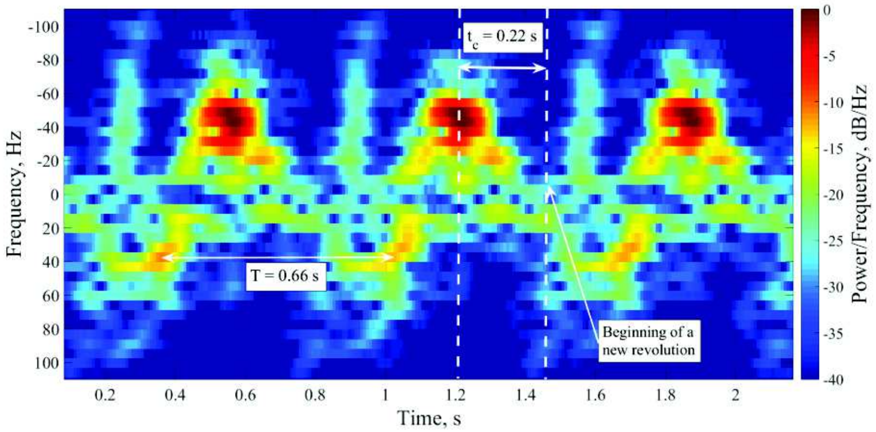

(b)

Fig. 4.24: Micro-Doppler signature of a single curved blade. (a) Theoretical spectrogram. (b) Experimental spectrogram. The physical parameters of the experiment are $l_b = 0.50\,m$, $Z_N = 0.48\,m$, $R_N = 3.70\,m$, $f_0 = 24\,GHz$ and Ω=9.4 rad/s

The shape of the spectrograms in Fig. 4.24 is not as simple as in the case of a flat blade. As it can be seen from equation (2.68), the amplitude of each frequency will depend in general on the physical parameters of the set-up. The curved shape introduces a complex dependence of these amplitudes on the geometrical properties of the blade. Even so, the resemblance between the theoretical and experimental results is clear.

The graphs in Fig. 4.25 correspond to the theoretical and experimental micro-Doppler signatures of a full WT. Both spectrograms show a similar pattern. In the experimental case, it is clear how the pattern replicates itself every $T = \frac{2\pi}{\Omega} = \frac{2\pi}{9.4} = 0.67\,s$. Again, the separation in time between each individual signal is $T_3 = \frac{2\pi}{3\Omega} = \frac{2\pi}{3 \cdot 9.4} = 0.22\,s$. The blade flash commented in the flat blade case can be observed here at $75\,Hz$ in both the theoretical and experimental spectrograms.

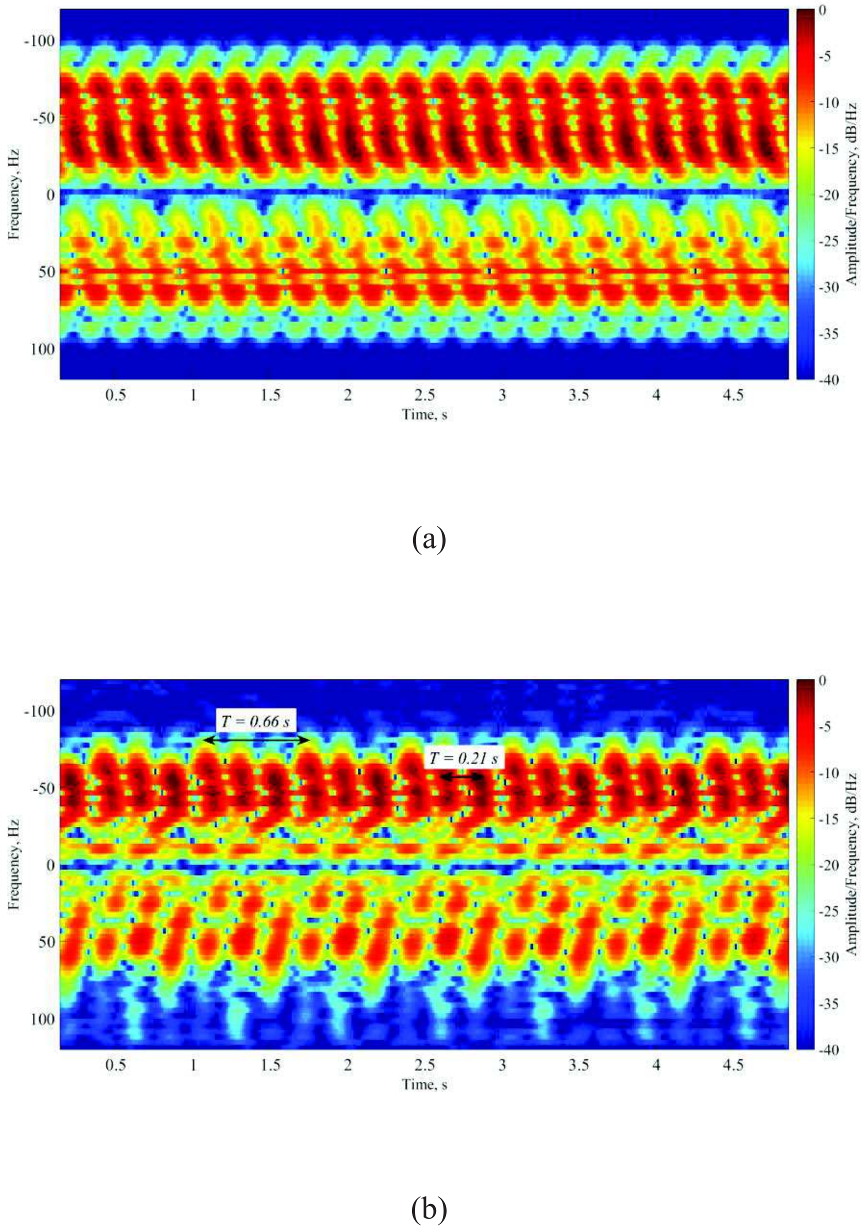

Fig. 4.25: Theoretical and experimental micro-Doppler signatures of three curved blades. Experimental parameters: $l_b = 0.50\,m$, $Z_N = 0.48\,m$, $R_N = 3.70\,m$, $f_0 = 24\,GHz$ and Ω=9.4 rad/s.

4.6. Detection of Wind Turbine Faults

The theoretical analysis of WT radar signatures in the near-field has now been experimentally tested and verified. This analysis has been useful to understand the physics behind the problem and relate different physical parameters of the system radar-WT to the observed signal. Therefore, the research done so far represents a new body of knowledge about the radar signature of a WT in the near-field.

This section begins the feasibility study of the detection and classification of structural faults in WT's. The capability to detect structural problems in WT's will be approached first in this chapter while the classification of faults will be the aim of Chapter 5. It is important to remember that the research done so far on the relation WT-radar has been focused on mitigation. The results of this thesis represents the first study where WT's are considered as radar targets and not merely as clutter. Preliminary results in WT faults classification has been published in international conferences [7].

An experimental analysis of the radar signature from faulty WT's will be shown in the next subctions. Several mechanical defects were artificially induced on the blades to emulate the measured radar echo signal from faulty WT's. The analysis of the radar signatures from these faulty turbines will be exclusively observational and it will show how the radar system can detect the mechanical faults. The different faulty WT's signals will display patterns that can be understood based on the theoretical models developed in Chapter 2 and 3.

4.6.1. Wind turbine faults

The experimental set-up used to record the radar signature from faulty WTs was the same one described in Section 4.2. The faults were induced on the curved blades exclusively. The geometrical parameters used during the experiments are listed in Table 4.3:

Parameter	Symbol	Value	Units
Blade length	l_b	0.50	m
Height of the hub respect to the radar	Z_N	0.5	m
Radial distance from the radar to the hub	R_N	3.70	m
Rotational speed	Ω	9.4	rad/s

Table 4.3: Experimental parameters for recording faulty WTs radar signatures.

The blades displayed in Fig. 4.3b are considered as healthy, this is, with no physical defects. The mechanical blade faults analysed, which are displayed in Fig. 4.26, were the following:

- One blade 25 mm shorter than a healthy one (5% of the blade).
- One blade 50 mm shorter (10% of the blade).
- One blade 100 mm shorter (15% of the blade).
- One blade 150 mm shorter (20% of the blade).
- One blade was bent.
- One blade was completely removed.
- One blade was scratched all over its surface (*rough surface*).

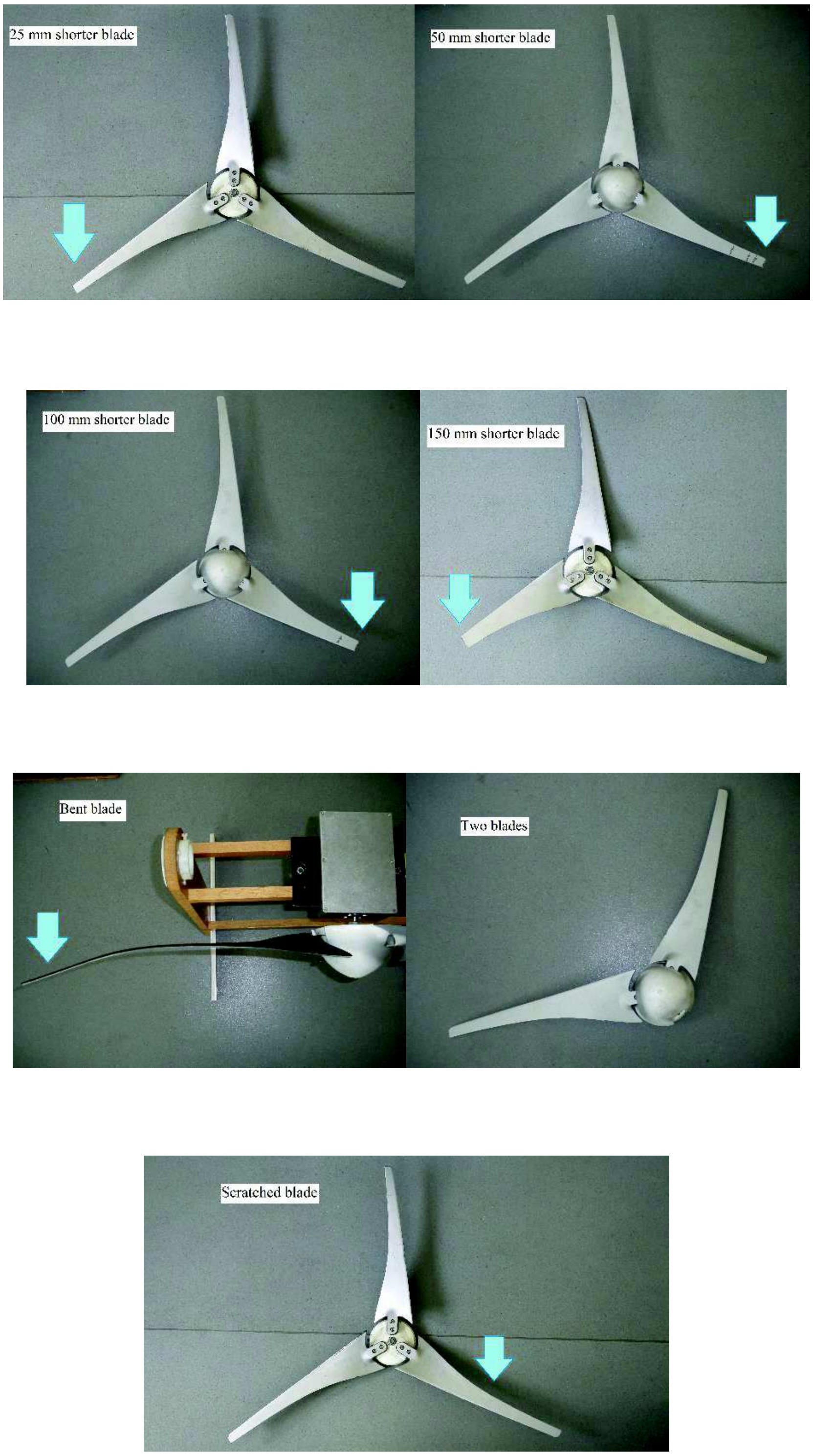

Fig. 4.26: Types of faults induced on WT blades.

The WT models shown in Fig. 4.26 have only one faulty blade while the other two are healthy. The backscattered signal from each one of these WTs was recorded without changing the experimental parameters of Table 4.3.

4.6.2. Time-domain signature of faulty blades

The graph in Fig. 4.27 corresponds to the time-domain signature of a healthy WT. The signal exhibits the same features already commented in section 4.3: four individual pulses can be distinguished where the first and the last one are the same, i.e. when the WT is in the same position. The difference in time between these two pulses corresponds to the period of the signal (the angular velocity is $\Omega = 9.4\, rad/s$, so $T = \frac{2\pi}{\Omega} = \frac{2\pi}{9.4} = 0.67\, s$) and two consecutive returns are separated by $T_3 = \frac{2\pi}{3\Omega} = \frac{2\pi}{3 \cdot 9.4} = 0.22\, s$.

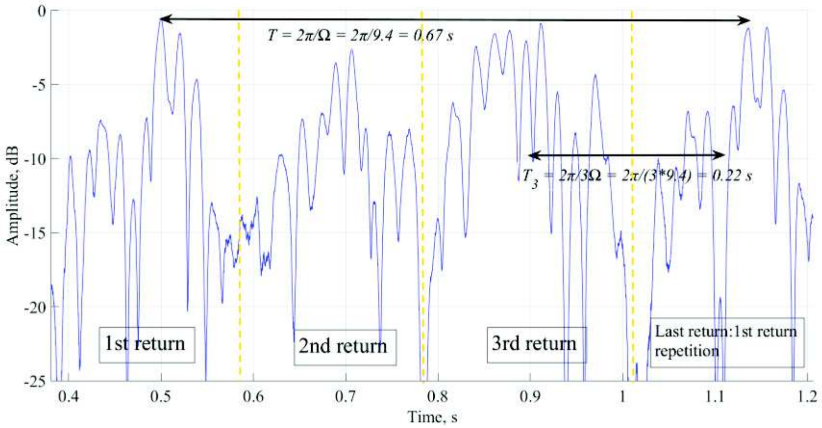

Fig. 4.27: Time-domain signature of healthy blades. Experimental parameters: $l_b = 0.50\, m$, $Z_N = 0.50\, m$, $R_N = 3.70\, m$, $f_0 = 24\, GHz$ and Ω=9.4 rad/s.

The healthy blades signature can be compared with the signals from the different faulty blades to observe any change in the pattern. If any, these variations in the pattern of the time-domain signatures may be associated to the mechanical faults induced on the blades. Fig. 4.28-4.34 show the healthy WT signature superimposed to the different faulty blade signals. All the signals are normalised to their own maximum value. As will be observed, Fig. 4.28-4.34 show visual differences between the healthy blade signal (in blue) and the faulty blade signal (in red). These differences in the time-domain imply that parameter like power or mean amplitude will vary from fault to fault and with respect to healthy blades. As will be shown in Chapter 5, these parameters can be used to differenciate and therefore classify WT with faults.

The case of a WT with one blade *25 mm* shorter than a healthy blade is displayed in Fig. 4.28. The first and last pulses in the faulty signal coincide almost perfectly with the returns of the healthy WT signature.

The second pulse also exhibits the same pattern and amplitude. However, small differences are observed in the third pulse: the signal is slightly shifted and the amplitude varies respect to the healthy signature. It will be clear in the rest of the types of faults how the same return exhibits a variation in its amplitude and shape.

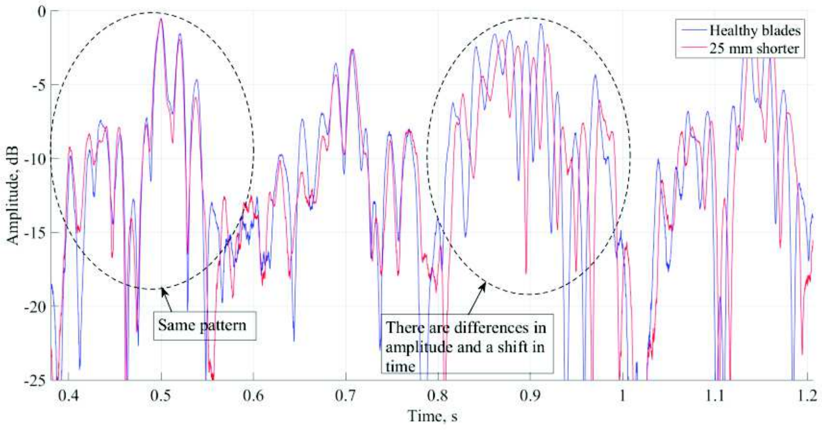

Fig. 4.28: Healthy blades vs. faulty WT with one blade *25 mm* shorter.

Fig. 4.29 shows the signature of a WT with one of its blades $50\,mm$ shorter on top of the healthy WT signal. As in the previous case, the clearest differences are observed in the third pulse while the first and last returns are practically the same.

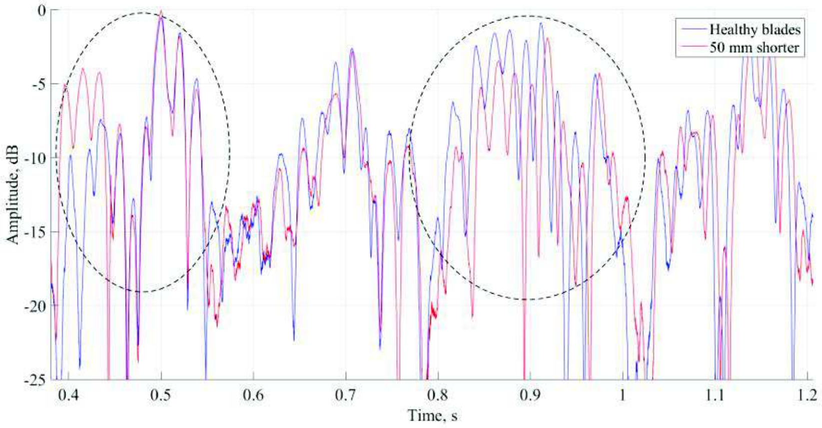

Fig. 4.29: Healthy blades vs. faulty WT with one blade $50\,mm$ shorter.

Using an even shorter blade, $100\,mm$, the difference is obvious as Fig. 4.30 shows. The first and last pulses of the two signals coincide almost one-to-one. However, the second and third pulses exhibit clear discrepancies between both signatures.

In section 2.5, it was shown how the returns observed in the time-domain signature of three blades were actually formed by the individual signals of two of the blades. Fig. 4.30 shows how the total signal is affected when one of the blades is mechanically different. The first and last pulses are formed by the same two healthy blades. However, the second and third pulses are product of a healthy blade and the faulty one and thus the signature differs from the healthy signal. It was also observed in section 4.3.2 that, when curved blades are used, one of the two symmetric peaks of a single blade signature is smaller than the other (Fig. 4.15). It is reasonable to think that the second return in Fig. 4.30 is formed by the strongest response from a healthy blade and the weakest peak of the faulty blade; therefore, there are changes but they are not significant. Nevertheless, the third return is formed by the weakest response of one of the healthy blades and the strongest response of the faulty blade. This is the reason why this third peak in Fig. 4.30 (and in the subsequent figures) is clearly affected by the physical change in the blade.

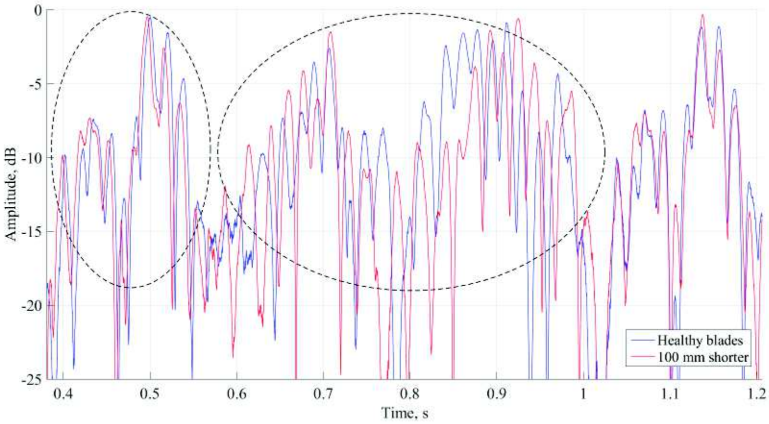

Fig. 4.30: Healthy blades vs. faulty WT with one blade *100 mm* shorter.

If *20%* of one blade is removed (blade *150 mm* shorter), the time-domain signature resembles like Fig. 4.31. As it was explained in the previous paragraph, the first and last returns exhibit the same pattern while the third (and the second in a smaller degree) manifestly differs from the healthy signal.

The pattern observed so far continues appearing in the rest of the faults. Fig. 4.32 corresponds to the case of a bent blade. The signature is similar to the one in Fig. 4.31

which is reasonable since the curvature of the bent blade may resemble as a shorter blade from the point of view of the radar.

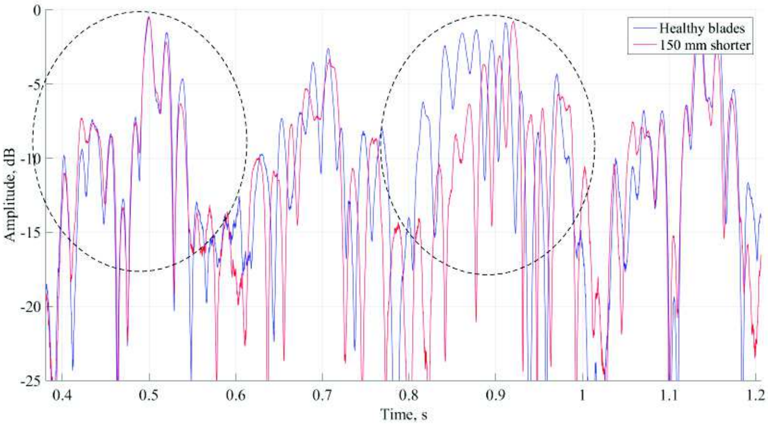

Fig. 4.31: Healthy blades vs. faulty WT with one blade *150 mm* shorter.

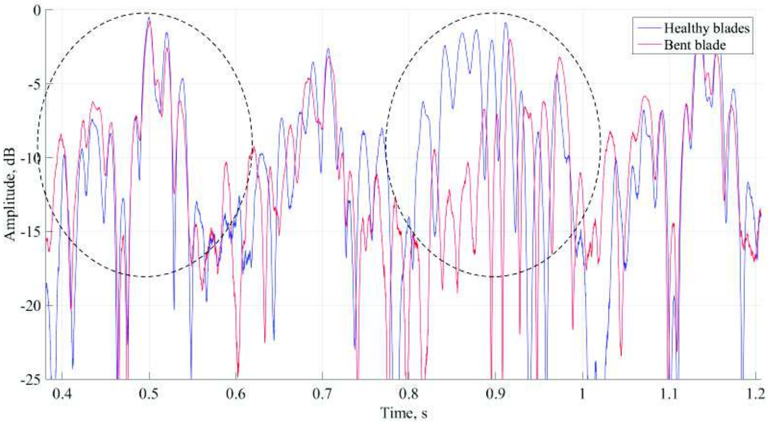

Fig. 4.32: Healthy blades vs. faulty WT with one bent blade.

The most extreme type of fault is when one the blades is completely removed leaving only two healthy blades. Fig. 4.33 shows how the first and last returns of both signals coincide nearly one-to-one. The second peak is manifestly different from the healthy signature and the third return of the faulty signal has almost disappeared.

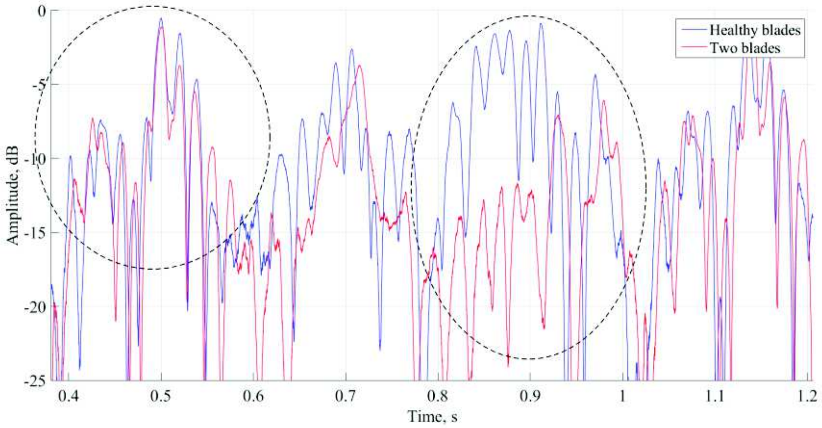

Fig. 4.33: Healthy blades vs. faulty WT with only two blades.

The last fault considered was the case of a scratched blade which may be similar to blade surface erosion or accumulation of ice. The signature, compared to the healthy blades signal, can be seen in Fig. 4.34. There are differences in the second and third returns while the rest of the signature remains almost similar. The physical change in the blade is small, but it is reasonable to believe that the rough surface affects the amplitude of the backscattered signal at the frequency used ($24\ GHz \rightarrow 0.0125\ m$ wavelength).

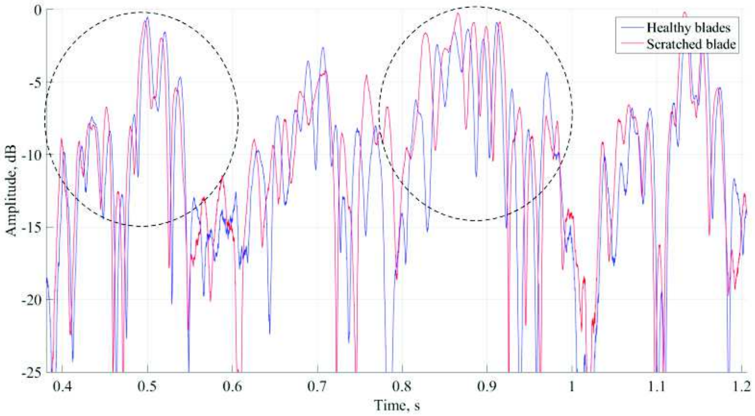

Fig. 4.34: Healthy blades vs. faulty WT with one scratched blade.

4.6.3. Frequency-domain Signature of Faulty Blades

The frequency-domain signatures analysed in Chapters 2 and 3 and observed experimentally in section 4.4 do not provide much information about the system radar-WT. It was demonstrated in Chapter 2 that, in the case of flat blades, the amplitude of the spectral lines is related to the physical parameters of the experiment. The same is expected when curved blades are used, although an analytic form has not been obtained. Furthermore, the equation obtained in the case of flat blades is rather complex, so an even more complicated relation would be expected when realistic blade is employed.

The experimental spectra of the different faulty signals are superimposed to the healthy blades spectrum in Fig. 4.35. Although there are certain differences among the spectra, there is no visual and direct pattern that can be related to the mechanical defects induced on the blades.

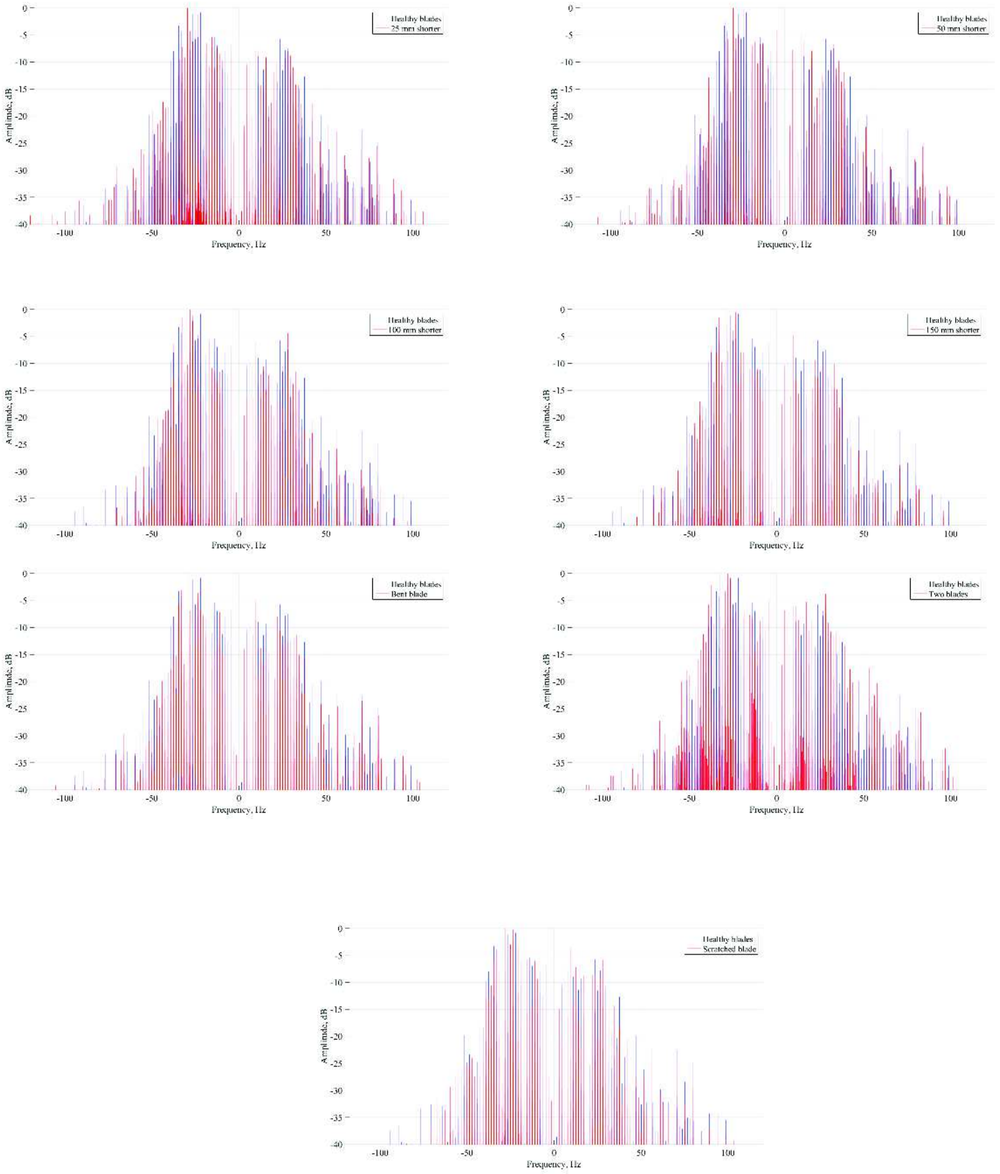

Fig. 4.35: Spectra of faulty WT's vs. spectrum of healthy blades.

The spectra in Fig. 4.35 are calculated for the complete signal duration: 3 minutes, which is equal to approximately 270 revolutions. It is reasonable to believe that the frequency-domain signature of a single revolution may reveal differences between the faults. For this purpose, the Power Spectral Density (PSD) of a single revolution (duration T) for the different types of faults was calculated and the results are shown in Fig. 4.36 together with the healthy blades PSD. The signals certainly differ one from each other, but these dissimilarities do not show a clear pattern and may be associated to the particular revolution. In fact, the PSD of different revolutions extracted from the same signal are as different as the signature of another type of fault. However, it will be showed in Chapter 5 that the PSD can be employed to classify WTs faults.

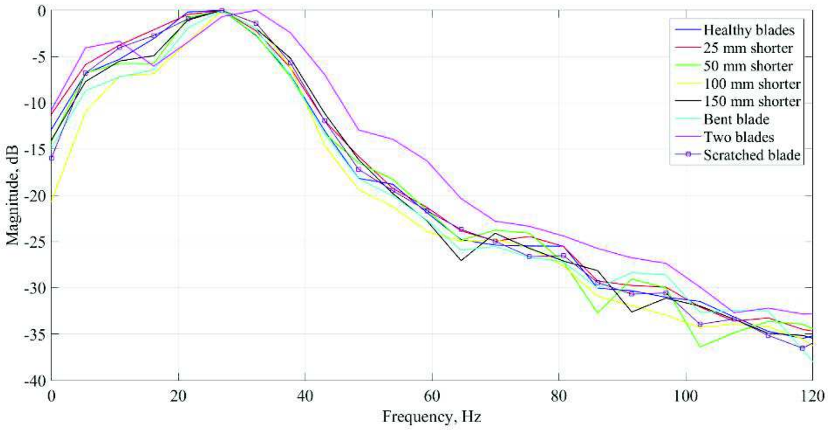

Fig. 4.36: PSD for one revolution of faulty blades.

4.6.4. Micro-Doppler signature of faulty blades

The effect of the mechanical faults on the backscattered signals can also be observed in the joint time-frequency domain. Fig. 4.37 corresponds to the spectrogram of healthy blades where several revolutions can be observed. The returns from each single blade have been marked on the graph.

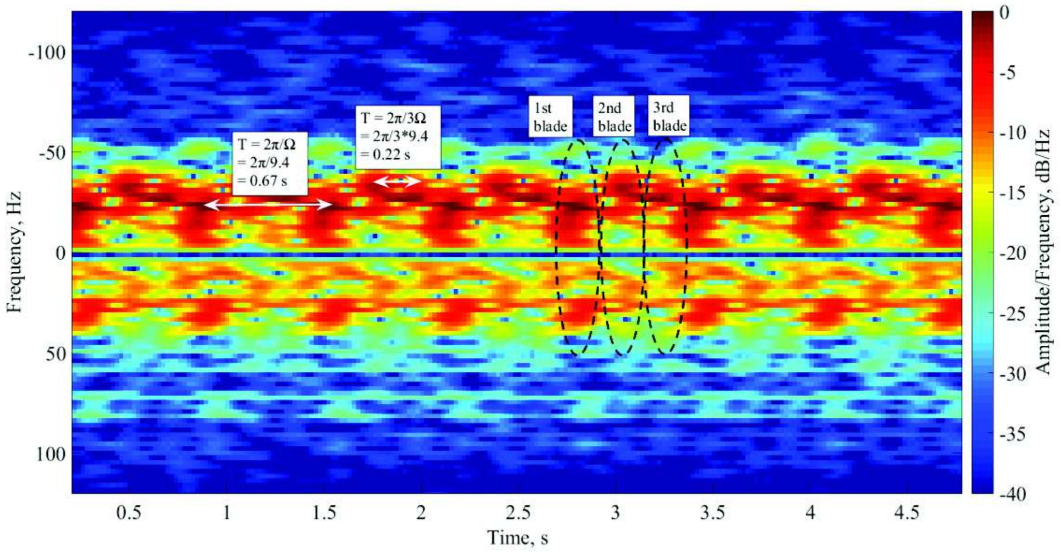

Fig. 4.37: Micro-Doppler signature of healthy blades.

Fig. 4.38 corresponds to the micro-Doppler signature of a WT with a blade $25\,mm$ shorter together with the healthy spectrogram for comparison. In this case, the differences respect to the healthy WT is not appreciable by simple visualisation.

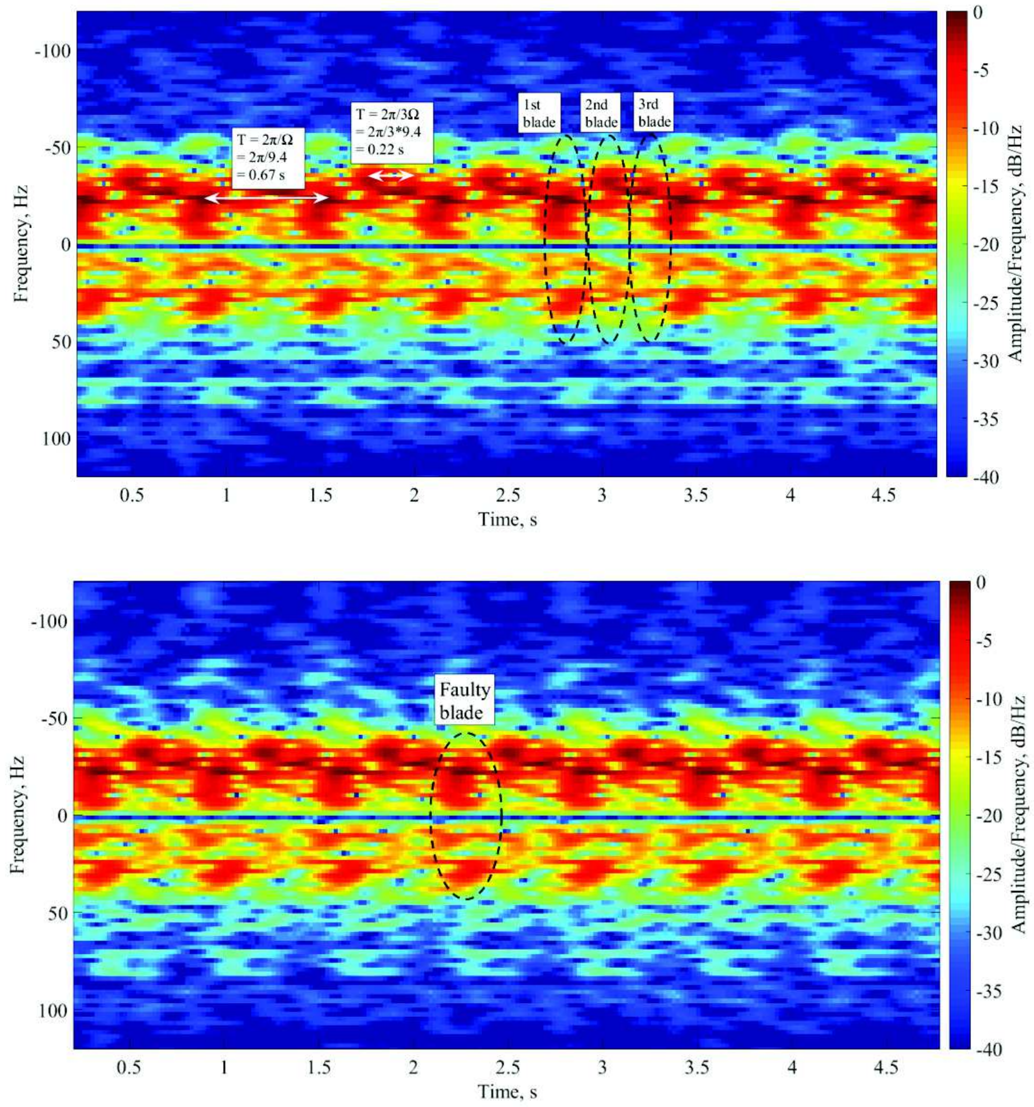

Fig. 4.38: Micro-Doppler of healthy blades vs. faulty WT with one blade *25 mm* shorter.

Changes in the spectrogram start being appreciable when one of the blades is $50\,mm$ shorter. Fig. 4.39 shows that the return corresponding to what it has been called “1st blade” is less intense in the up part of the spectrogram in the case of the faulty blade. The differences respect to the healthy blades spectrogram increase as the faulty blade becomes shorter.

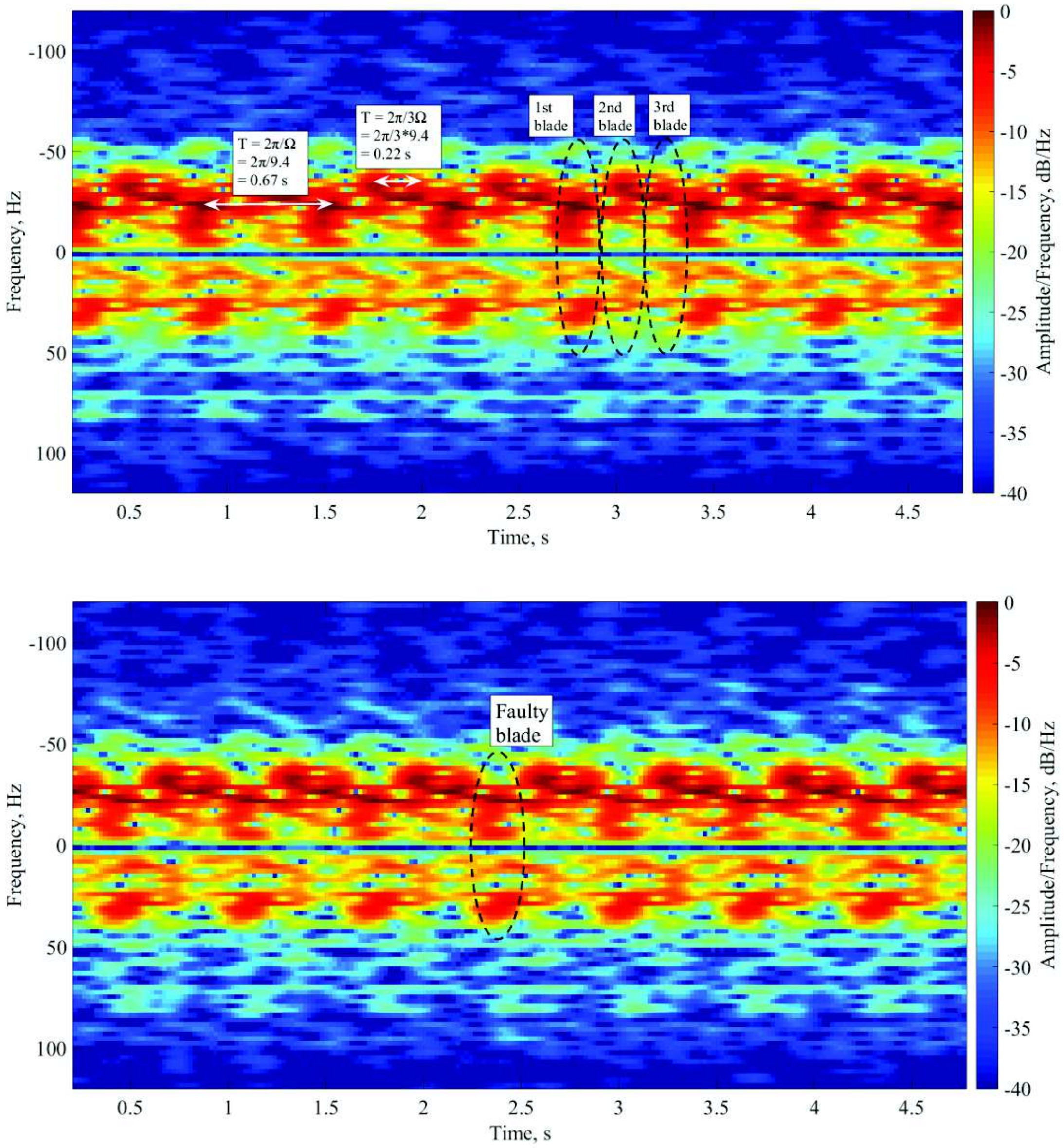

Fig. 4.39: Micro-Doppler of healthy blades vs. faulty WT with one blade *50 mm* shorter.

The case of *100 mm* and *150 mm* shorter blades are shown in Fig. 4.40 and Fig. 4.41 respectively. It is visually clear the differences between the healthy and faulty signatures, although the pattern is complicated to distinguish since it seems that the whole spectrogram is affected by the faulty blade.

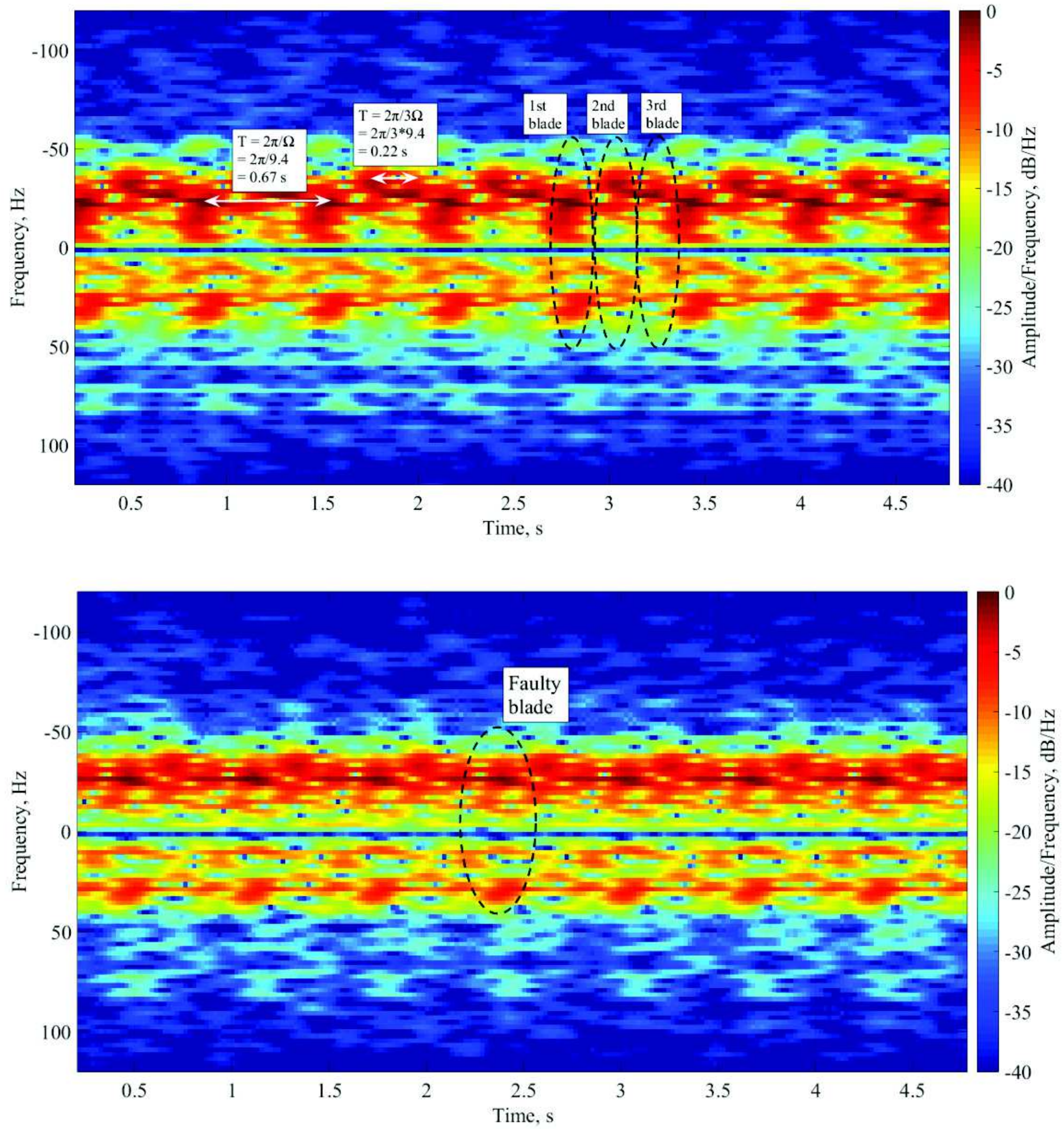

Fig. 4.40: Micro-Doppler of healthy blades vs. faulty WT with one blade *100 mm* shorter.

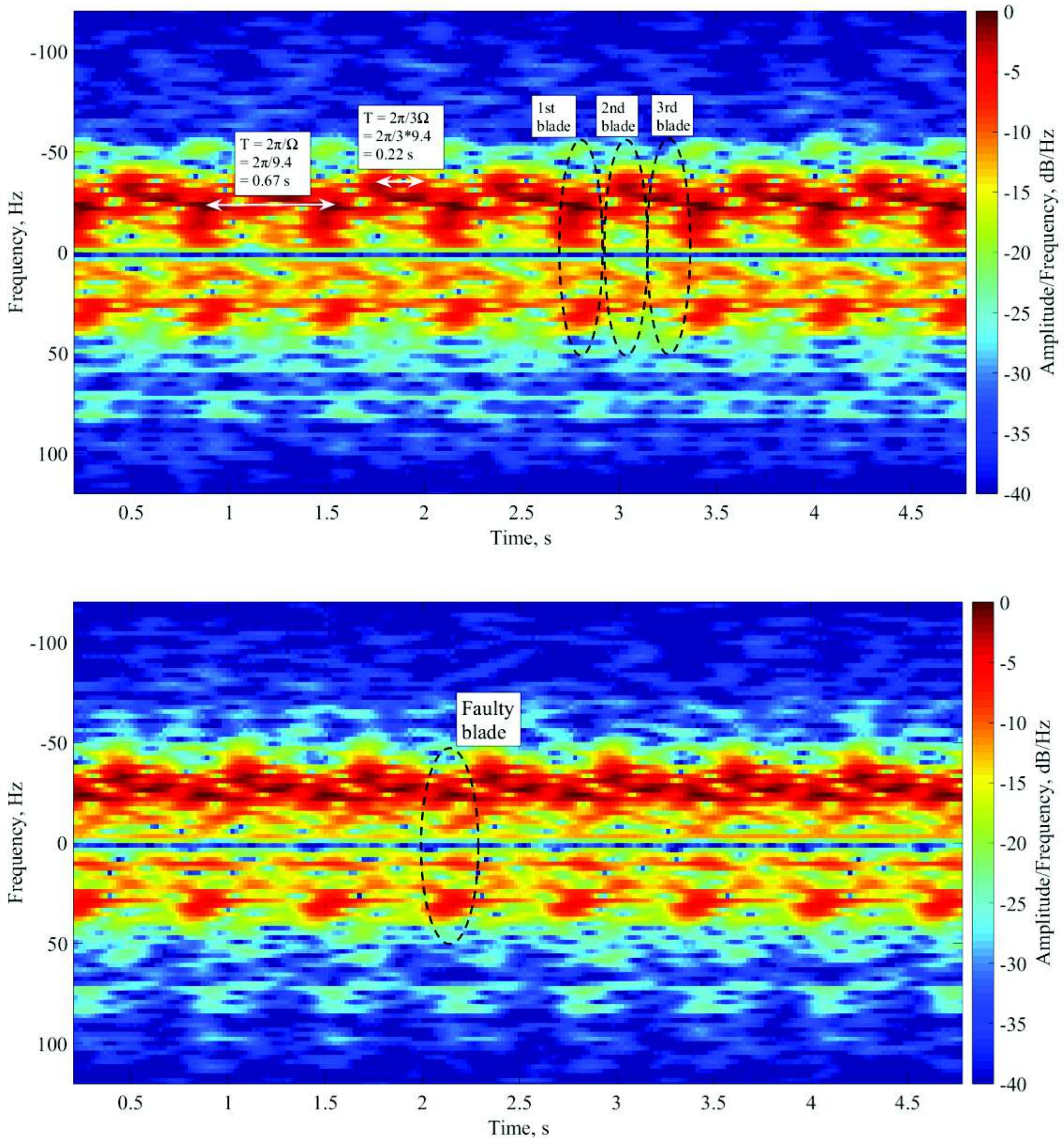

Fig. 4.41: Micro-Doppler of healthy blades vs. faulty WT with one blade *150 mm* shorter.

The graph in Fig. 4.42 corresponds to the spectrogram of a bent blade. It is visually clear that the complete revolution has been affected by the mechanical change induced on the blade. One of the returns has almost disappeared from the spectrogram.

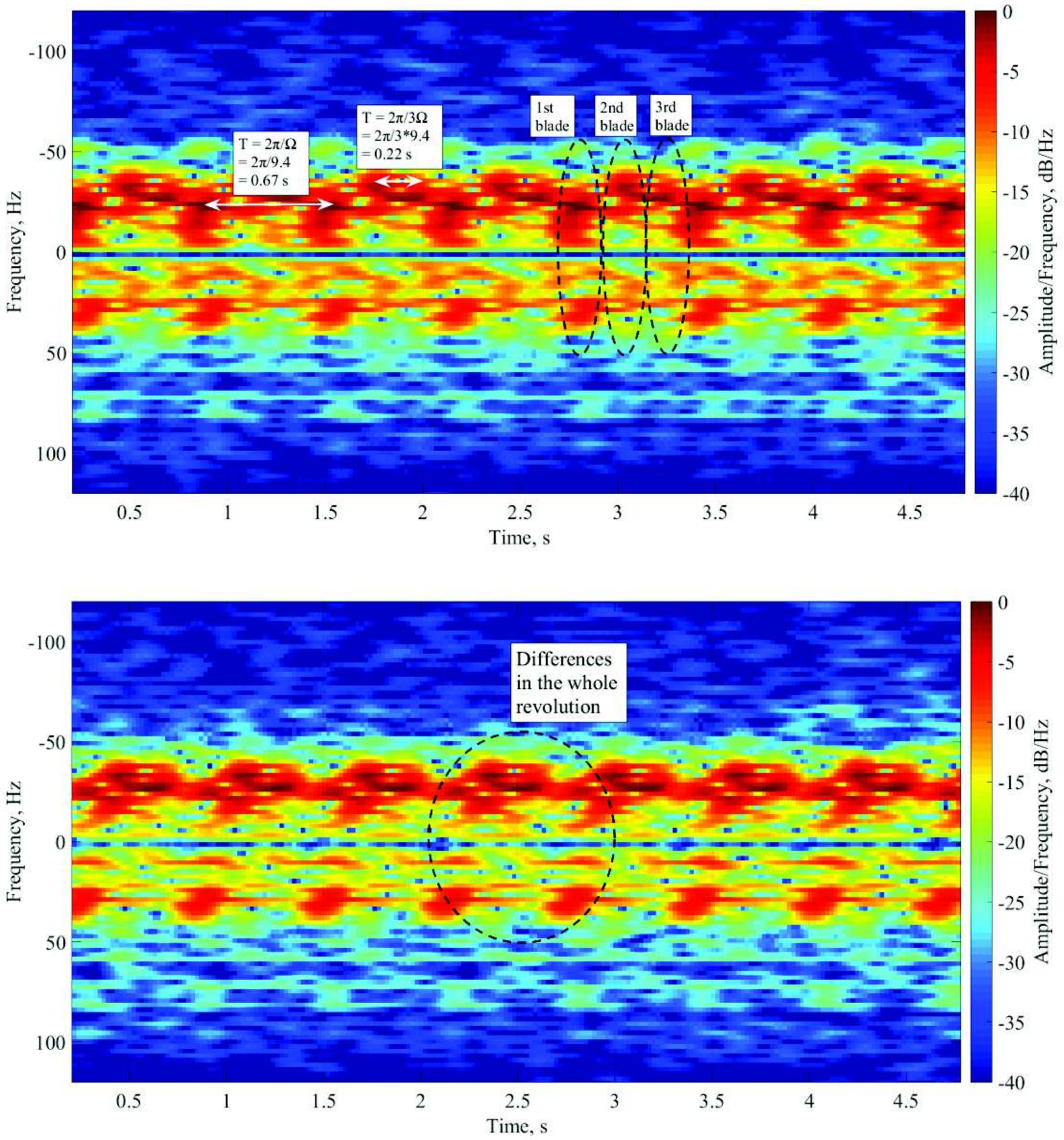

Fig. 4.42: Micro-Doppler of healthy blades vs. faulty WT with one bent blade.

The most dramatic difference respect to the healthy turbine spectrogram corresponds to the case of two blades, as it could be expected. It is clear in Fig. 4.43 that one of the returns has disappeared completely.

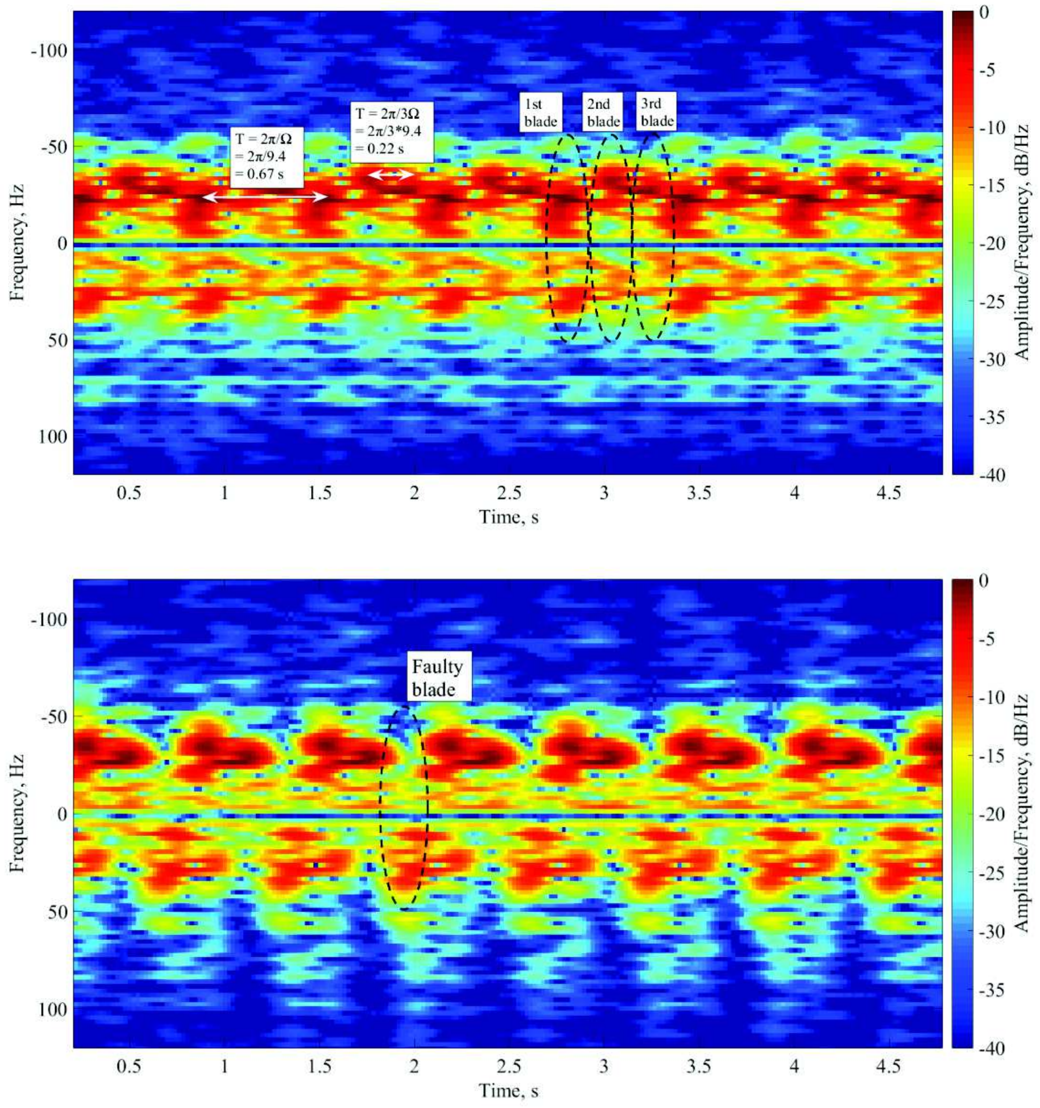

Fig. 4.43: Micro-Doppler of healthy blades vs. faulty WT with only two blades.

The spectrogram of the scratched blade is shown in Fig. 4.44. In this case, the pattern is practically similar to the healthy blades spectrogram, although it is not exactly the same. In the faulty spectrogram, the bottom part of the graph exhibits a slightly more intense response. This may be related to a complex scattering process due to the rough surface of the scratched blade. It can be concluded that the different spectrogram shows differences between faults and with respect to healthy blades. However, these differences are not as clearer as in the time-domain. This just shows that the time-frequency respond from WT's is affected by structural faults. The use of the information carried by the spectrograms for WT faults classification has not been implemented in this thesis. This would need more complex classification techniques that are out of the scope of this research. Nevertheless, the classification methods presented in Chapter 5 show enough accuracy in classifiying these faults.

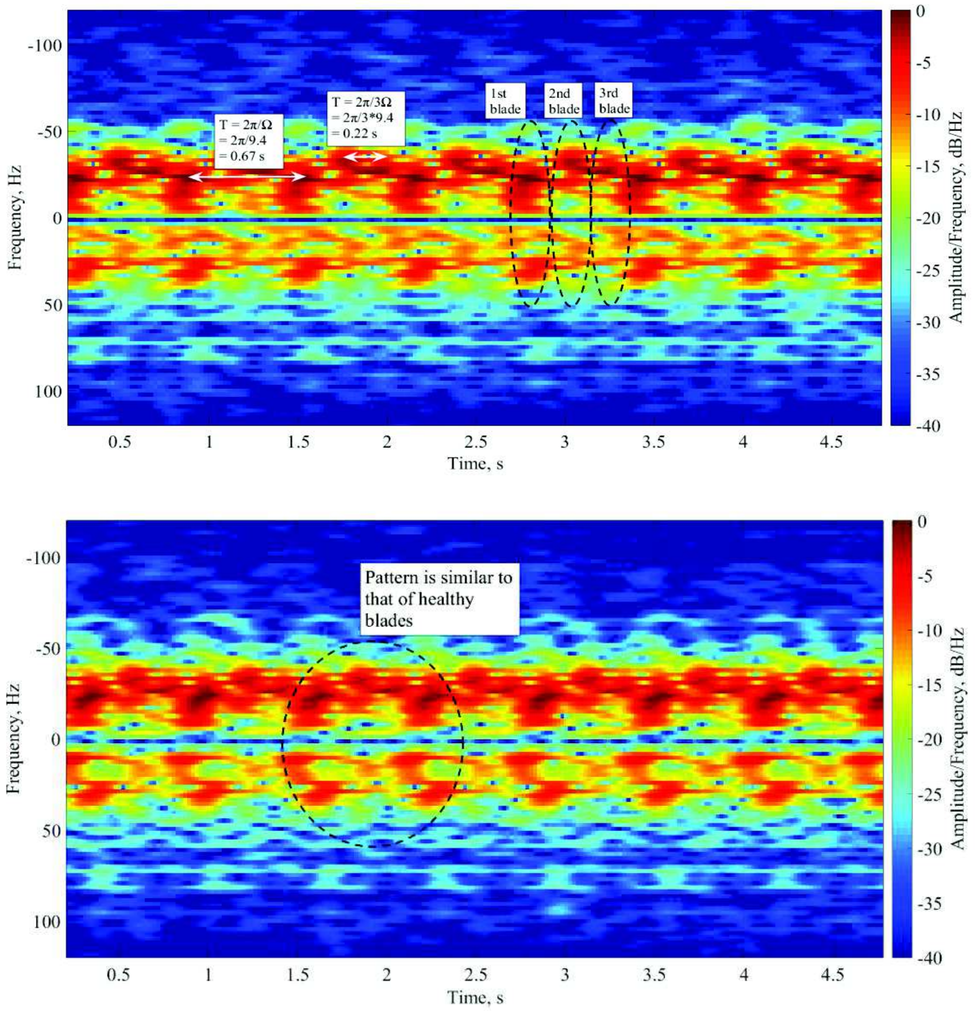

Fig. 4.44: Micro-Doppler of healthy blades vs. faulty WT with a scratched blade.

4.7. Summary

The aim of this chapter was to verify experimentally the theoretical models developed in Chapter 2 and Chapter 3. For this purpose, a simple experiment was designed using a scaled WT model with two types of blades: flat and curved. The radar signatures from these two kinds of blades were compared with their corresponding simulated echo signals using the equations obtained in the theoretical analysis.

The measurements were performed in ideal and controlled, but representative experimental conditions within an anechoic chamber, showing a correlation coefficient of ~ 0.9 between theoretical and experimental results. The good agreement between theory and experiment confirms the validity of the theoretical framework developed in this research.

The experimental time-domain signals exhibit the main features predicted by the theoretical models. Their characteristics can be associated to the physical parameters of the WT such as blade length, relative height radar-WT hub and rotational speed.

The spectrogram is fundamentally related to the angular velocity, Ω, of the WT. This speed determines the separation between two consecutive spectral lines. The amplitude of these lines are related to the geometrical characteristics of the system radar-WT through the Bessel function of the first kind. However, due to this complex dependence, it is complicated to extract any geometrical information from the spectrogram.

The micro-Doppler obtained from the experimental signal shows features predicted by the theoretical model. As in the case of the time-domain, the micro-Doppler signature replicates itself periodically, where the period is given by the angular velocity Ω. Information about the physical parameters of the system radar-WT can be extracted from the spectrograms, although this information would be the same obtained from the time representation.

In order to take advantage of the micro-Doppler signature, a higher frequency radar may be employed: it would provide a better resolution and more details could be observed in the spectrogram. Future work should focus on this idea together with conducting measurements outside the anechoic chamber to study how the theoretical models are affected by real conditions.

The last part of the chapter, section 4.6, corresponds to the analysis of radar signatures from faulty WTs. The results show how the different mechanical faults affect the signals in the time and joint time-frequency domains. The theoretical study carried out in Chapter 2 and Chapter 3 has helped understand the features observed in the signatures and how these are related to the mechanical faults.

Finally, the information obtained about the radar echo from WTs can be used to understand the radar signatures from faulty blades in the near-field, and how the corresponding signal properties may be used to diagnose or classify a particular WT fault using a short-range radar sensor in the vicinity of the turbine blades. This is the goal of Chapter 5.

References

[1] *EMG49: encoder, motor, gearbox 49:1* [Online]. Available: http://www.robot-electronics.co.uk/htm/emg49.htm

[2] *RFbeam Microwave K-LC2 datasheet* [Online]. Available: http://www.rfbeam.ch/fileadmin/downloads/datasheets/Datasheet_K-LC2.pdf

[3] *RFbeam Microwave ST100 StarterKit* [Online]. Available: http://www.rfbeam.ch/fileadmin/downloads/datasheets/ProductBrief_ST100.pdf.

[4] B. Gallardo-Hernando *et al*., "Wind turbine clutter observations and theoretical validation for meteorological radar applications", *IET Radar, Sonar & Navigation*, vol. 5, Iss. 2, pp. 111-117, Feb. 2011.

[5] M. Ritchie *et al.*, "Measurement and analysis of multiband bistatic and monostatic radar signatures of wind turbines", *Electronics Letters*, vol. 51, Iss. 14, pp. 1112-1113, Jul. 2015.

[6] F. Fioranelli *et al.*, "Analysis of multiband monostatic and bistatic radar signatures of wind turbines," in *IEEE Radar Conf.*, Johannesburg, 2015, pp.277-282.

[7] M. Crespo-Ballesteros and M. Antoniou (2015, May), "Automatic classification of wind turbine structural faults using Doppler radar: proof of concept study," *IEEE Radar Conf.*, Arlington, VA, 2015, pp. 286-291.

Chapter 5 Automatic Classification of Wind Turbine Structural Faults

5.1 Introduction

An observational analysis of the radar signatures of faulty WT has been done at the end of Chapter 4. It has been demonstrated the capability of a radar sensor to detect different WT structural faults. In this chapter, the radar echoes from the faulty WTs are used to build a method capable of classifying these faults.

Two different types of features were used to classify WT faults. The first type of these features was the time-domain statistical parameters from faulty blades, which were purposely selected. This method has been called Statistical Parameters Method (SPM). This technique is the simplest and easiest to visualise. The second type was the frequency-domain features, where the well-known Principal Components Analysis (PCA) method were used to reduce the dimensionality of the problem by automatically selecting the features that help differentiate the types of WT faults.

After selecting the appropriate features, two classification algorithms were applied: k-Nearest Neighbours (k-NN) and Artificial Neural Networks (ANN). Several confusion matrices were built to assess the capacity of these algorithms to correctly classify WT faults.

5.2 Classification of Wind Turbine Faults. Methodology.

A database was created before performing any classification. The data points in this database were the different characteristics extracted from radar signatures of faulty WTs. In the case of SPM, the data were precisely the statistical parameters obtained from the faulty time-domain signals. On the other hand, the PSD of faulty WT signatures constituted the data points in the case of PCA. It is important to notice that, in both cases, the data points were extracted from the same faulty WT signals; the only difference was their representation in time and frequency domains.

The signals were recorded in three different positions using four types of faults. Another measurement was performed using seven kinds of faults. The experimental parameters are listed in Table 5.1

		Four Faults			**Seven Faults**	
Parameter	**Symbol**	**Exp1**	**Exp2**	**Exp3**		**Units**
Radial distance	R_N	3.70	3.85	3.55	3.60	*m*
Blade length (healthy)	l_b	0.50				*m*
Height of the hub	Z_N	0.48				*m*
Rotational speed	Ω	9.4				*rad/s*

Table 5.1: Experimental parameters with faulty WTs.

Subsequently, the database was divided into two sets: training and test datasets. The data points in both sets were chosen randomly from the database. A supervised learning approach was considered in this analysis, [1]-[2]. Each WT fault was associated to a particular category label or class θ_i, where the index i corresponds to the different types of faults: $25\ mm$ shorter blade, two blades, bent blade, etc. In supervised learning, the data points of the training set are automatically categorised in one of the classes since this information is known a priori. A good method of categorising or clustering selects the features of the training set that group or cluster the points of the same class well-separated from the rest of the classes. The output from the training stage is therefore a group of clusters, each one related to one of the classes, distributed around the called *feature space*.

In the case of SPM, the features were purposely selected from the time-domain signatures to build the corresponding feature space. On the other hand, the PCA algorithm was applied to the frequency-domain to reduce the dimensionality of the training set by selecting the principal components, representing the data in a compact form easy to visualise. The ANN technique did not provide a visual feature space; the process of training occurred internally and the output was a trained network that was used to classify the test data points.

The data points that were not used for training formed the test datasets. Two classification algorithms were applied to the test points for classification in time and frequency domains: k-NN and ANN.

In the case of SPM and PCA, the training set was formed by 90% of the database while the rest 10% was employed to test the performance of the k-NN. On the other hand, 80% of the database was used to train the neural network and the 20% left was used to validate and test the output.

Confusion matrices were built in order to evaluate the performance of the classification algorithms in time and frequency domains.

5.3 k-Nearest Neighbours to Classify Wind Turbine Faults

As it is explained in sections 5.4 and 5.5, SPM and PCA are used to cluster the data points of the training set in different classes, one for each WT fault. These classes are known a priori in the supervised learning approach employed, so a particular label is associated to each cluster. The k-NN technique was used to classify the data of the test set and therefore assess the performance of the classification. The explanation of how the k-NN algorithm works is the goal of this section.

For a given test point $\bar{x}_{test}$, the algorithm selects its k nearest points in the training set and assigns to the test point the most frequent class among its neighbours. In other words, a test sample can be classified by counting the number of neighbours that belong to a particular cluster and decide by majority [3]-[4].

As an example, Fig. 5.1 shows a possible scenario where there are three classes in a 2D feature space. The classes are well separated from each other forming definite clusters; the ellipses in Fig. 5.1 represents a collection of points. In this example, the test point $\bar{x}_{test}$ is inside class 3 (θ_3). Therefore, all its nearest neighbours (with k less than the number of elements in θ_3) belong to class 3. In this case, the k-NN algorithm will label the test point as a class 3 member, i.e. $\bar{x}_{test} \in \theta_3$. In general, due to the clear class clustering of this example, the test points will be correctly classified. However, it might occur that a statistically non representative point fall inside or near another cluster and were classified wrongly.

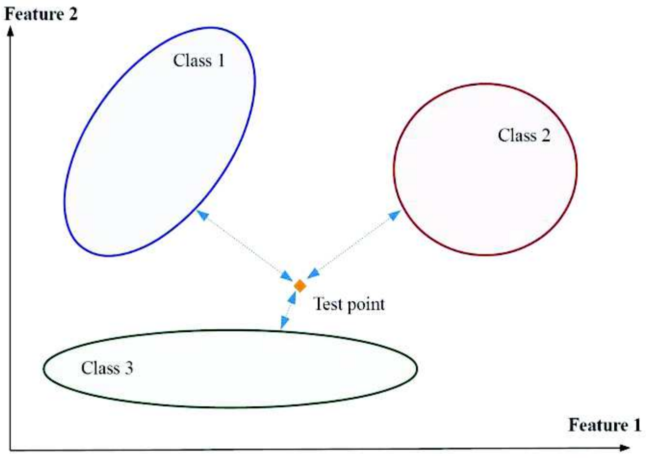

Fig. 5.1: 2D feature space with three classes. Correct classification.

The situation described in Fig. 5.1 is the most favourable. However, it can occur that two of the clusters overlap in the feature space; Fig. 5.2 represents this situation. Assume that the test point $\bar{x}_{test}$ belongs to class 1 and it falls in the overlapping region of classes 1 and 2. It could happen that, for k = 5 for example, three of the nearest neighbours to $\bar{x}_{test}$ belonged to θ_2 and the other two were members of θ_1. In this situation, the k-NN algorithm would misclassify the test point as part of the class 2, i.e. $\bar{x}_{test} \in \theta_2$. The opposite could happen and the test point might be classified as a member of the correct cluster. Therefore, the correct classification will depend on the value of k and the statistical variability of the data in the overlapping region. It is clear that, when two or more clusters overlap or they are very close to each other, there will be a percentage of misclassification.

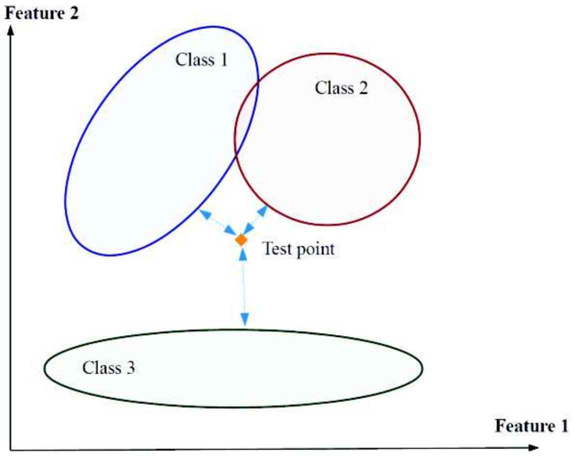

Fig 5.2: 2D feature space with three classes. Misclassification.

The metric used to calculate the nearest points is in general the Euclidean norm and k must be an odd number to take a decision based on the majority. The number of closest neighbours k has been studied in theory [5]-[6], but the optimal election of this number depends on the specific problem and data set. A great number of neighbours k can degrade the performance of the classifier and increase the computational resources needed to perform the classification. On the other hand, a low value for k can induce wrong conclusions.

5.4 Classification in the Time-Domain. Statistical Parameters Method

This is a basic technique that was used as a first method of data clustering. SPM consisted in selecting directly the features from the time-domain signatures that better clustered the data points. The method allowed a direct visualization of the relationships in the information carried by the radar signals. It was shown in Chapter 4 that the time-domain signals of faulty blades exhibited different signal properties. Therefore, it was reasonable to use a number of statistical parameters of the signals as features for clustering. All these parameters were values per cycle, i.e., per WT revolution. If the signal during one rotation is called *s,* having *N* elements, the statistical variables calculated for each individual fault were:

- Mean amplitude $\mu = \frac{1}{N}\sum_{i=1}^{N} s_i$
- Power $P = \frac{1}{N}\sum_{i=1}^{N} s_i^2$
- Standard deviation $S = \sqrt{\frac{1}{N-1}\sum_{i=1}^{N}|s_i - \mu|^2}$
- Maximum of the signal

As was explained in section 4.6, the radar signatures from the different faulty blades were recorded in the same experimental conditions. A total of three experiments in different positions were performed using four types of faulty blades: *5 cm* and *10 cm* shorter blades, one *bent blade* and a WT with only *two blades*. Each of these signals contains approximately $N = 180$ revolutions. The signal can be split into these individual revolutions; the statistical parameters are calculated for each of these subsignals. In this way, a database of $N{\times}F$ elements can be built, with F the number of faults or classes included the *healthy blades* group. Another experiment was performed using three more faults: *2.5 cm* and *15 cm* shorter blades, and a *scratched blade* with sand paper. Since the number of faults has increased, the number of samples for each class has to be increased as well. In this case, the number of revolutions per fault is $N = 270$.

As it was stated in section 5.2, the training set was built by randomly selecting 90% of the database samples. These samples or data points can be seen as vector of *d*-dimensions where d is the number of statistical parameters calculated for each data point or revolution. The feature selection that better cluster the data was performed by picking and combining different statistical variables from this d options. Therefore, if only two of these parameters are selected, each data from the training set can be represented by a point in a 2D feature space like the examples in Fig. 5.1 and Fig. 5.2. If three parameters are employed instead, the points can be located in a 3D feature space.

Data points of the same type of fault are expected to present similar characteristics and, consequently, they will group in the same class cluster. The combination of several statistical parameters can lead to different cluster configurations, resulting in either well-separated groups or overlapping classes. The separation between clusters determines the performance of the classifier. If clusters are well-separated from each other, the accuracy of the classification method will be high since most of the neighbours will belong to the correct class. On the other hand, if the clusters are close to each other or the points are mixed, the classifier will not be able to assign the correct class to the test samples with enough degree of accuracy.

Fig. 5.3 corresponds to a 2D clustering using statistical parameters as features. The number of classes is 5: *four faults* plus *healthy blades signals*. The data corresponds to the called Exp3 in Table 5.1. The statistical parameters used were the mean amplitude and total power per revolution. Each dot on the figure corresponds to a single WT revolution. The training data clusters are concentrated and well separated one from each other, so, under ideal conditions, automatic fault classification might be feasible using this method. The relation between the amplitude and the power seems to be linear in this case. The mean amplitude and power of the *healthy blades* samples are more intense than, for example, the *two blades* points. This is expected since the reflecting surface is greater in the former than in the latter case.

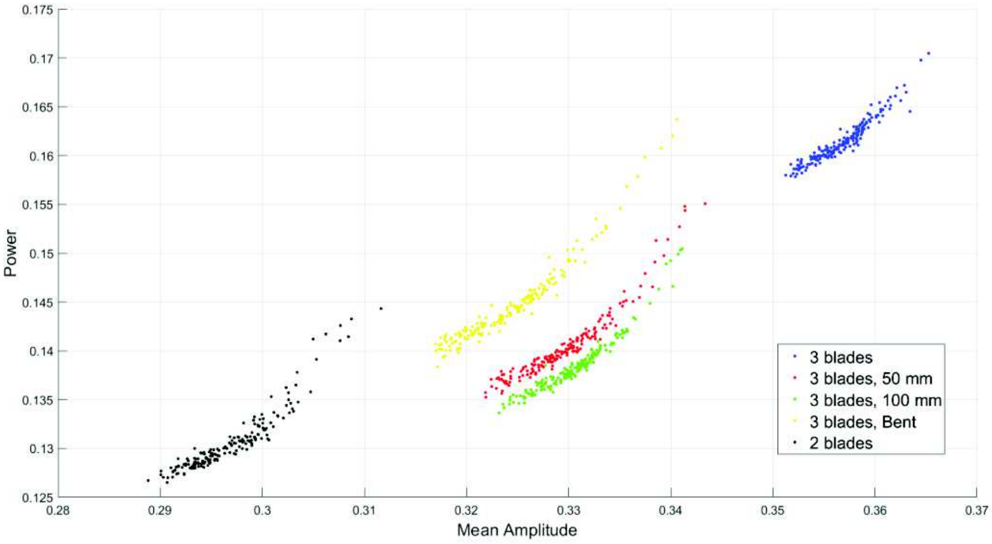

Fig. 5.3: 2D feature space using SPM: Power vs Mean amplitude. Data from Exp3.

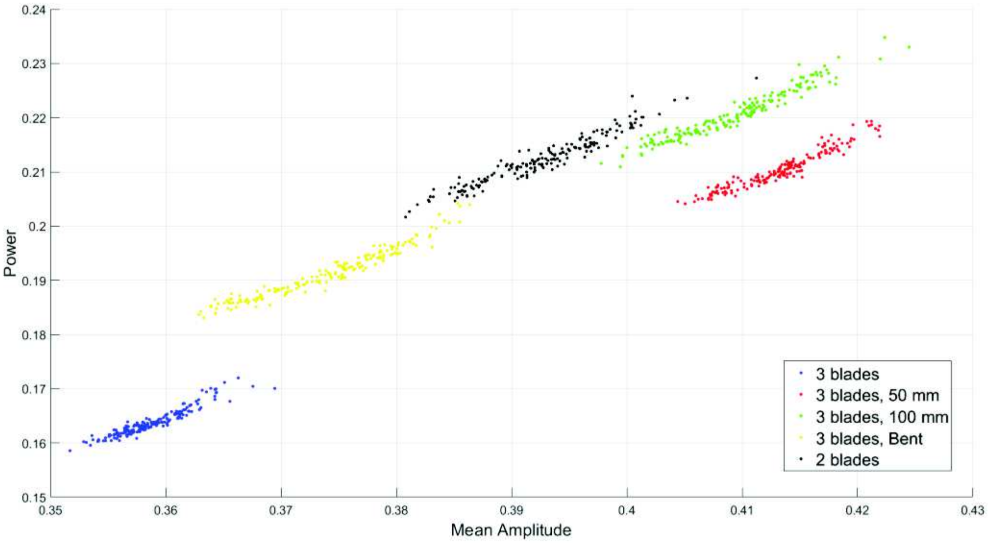

Fig. 5.4: 2D feature space using SPM: Power vs Mean amplitude. Data from Exp2.

Fig. 5.4 and Fig. 5.5 show the result of applying the same methodology to the measurements Exp1 and Exp2 (see Table 5.1). In these cases, the faults group in different clusters but the linear relationship between mean amplitude and power is not present. This is due to the inevitable error introduced when the faulty blades were changed or the radar was moved during measurements. These small modifications could have varied slightly the distance R_N or the orientation of the WT/radar and consequently, due to the high frequency used, have affected the values of the statistical parameters.

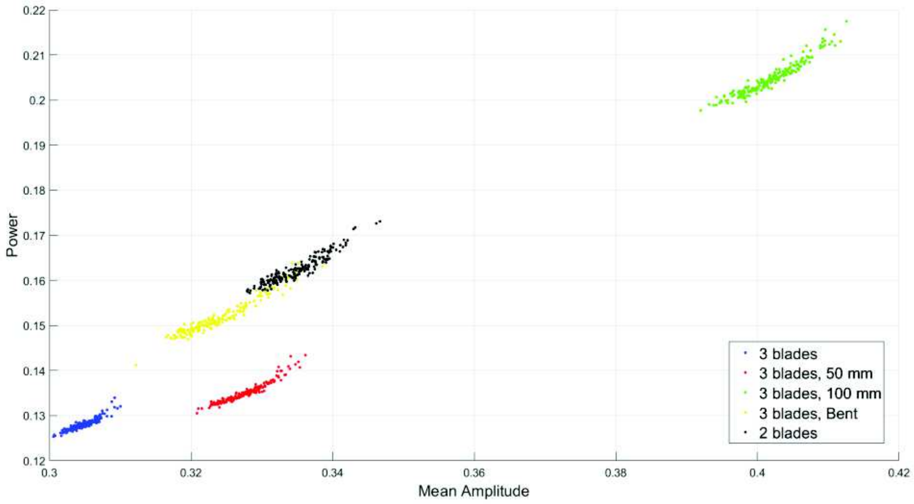

Fig. 5.5: 2D feature space using SPM: Power vs Mean amplitude. Data from Exp1.

The corresponding confusion matrices to these trained sets are presented in Fig. 5.6-5.8. A confusion matrix is a special type of table that permits to evaluate the performance of a classification algorithm. The rows correspond to the actual class (type of fault) while the columns represent the predicted one, the type of fault that the classification algorithm assigns to a test point. For example, Fig. 5.6a shows that the k-NN algorithm classified 20% of the test points as *two blades* instead of the correct class, the *bent blade* group.

Fig. 5.6 corresponds to the confusion matrices that assess the performance of the k-NN algorithm when it was applied to the training data of Fig. 5.5. The confusion matrices were built for different number of neighbours: *k=3, 5, 7* and *9.* The row corresponding to the *bent blade* class shows that there is a percentage of misclassification between the *two blades* and *bent blade* clusters. This is expected due to the similarities in the time-domain between these two kinds of faults. The different number of neighbours used does not change drastically the performance of the k-NN algorithm.

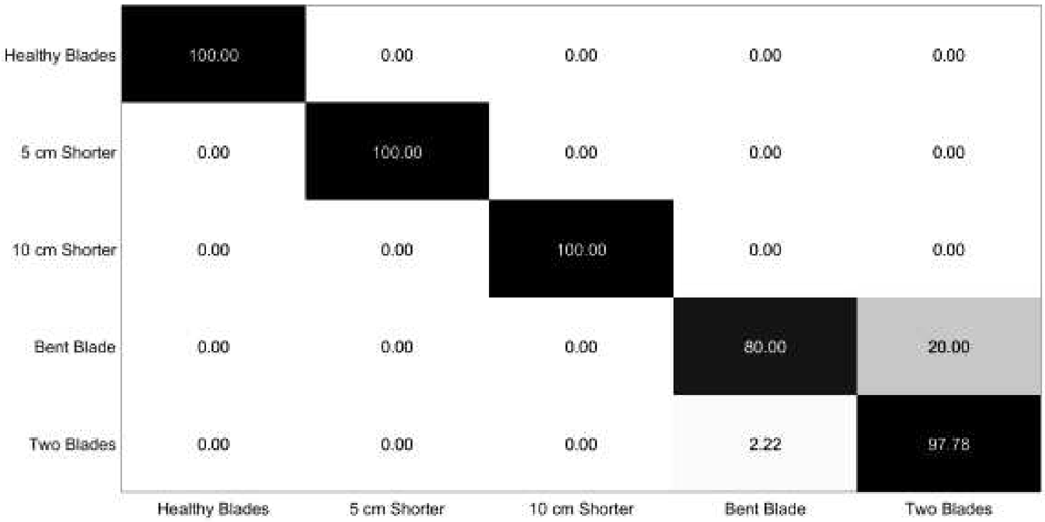

	Healthy Blades	5 cm Shorter	10 cm Shorter	Bent Blade	Two Blades
Healthy Blades	100.00	0.00	0.00	0.00	0.00
5 cm Shorter	0.00	100.00	0.00	0.00	0.00
10 cm Shorter	0.00	0.00	100.00	0.00	0.00
Bent Blade	0.00	0.00	0.00	80.00	20.00
Two Blades	0.00	0.00	0.00	2.22	97.78

(a)

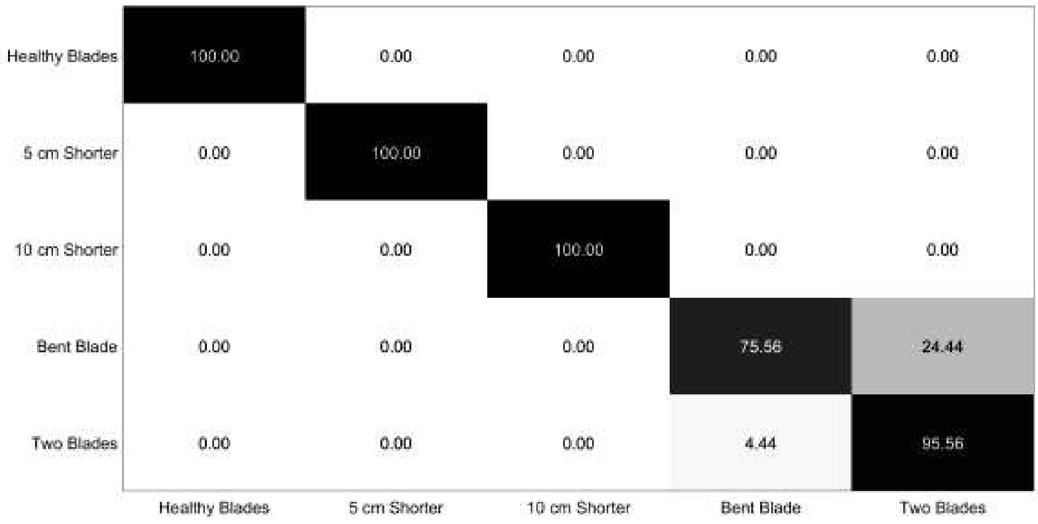

	Healthy Blades	5 cm Shorter	10 cm Shorter	Bent Blade	Two Blades
Healthy Blades	100.00	0.00	0.00	0.00	0.00
5 cm Shorter	0.00	100.00	0.00	0.00	0.00
10 cm Shorter	0.00	0.00	100.00	0.00	0.00
Bent Blade	0.00	0.00	0.00	75.56	24.44
Two Blades	0.00	0.00	0.00	4.44	95.56

(b)

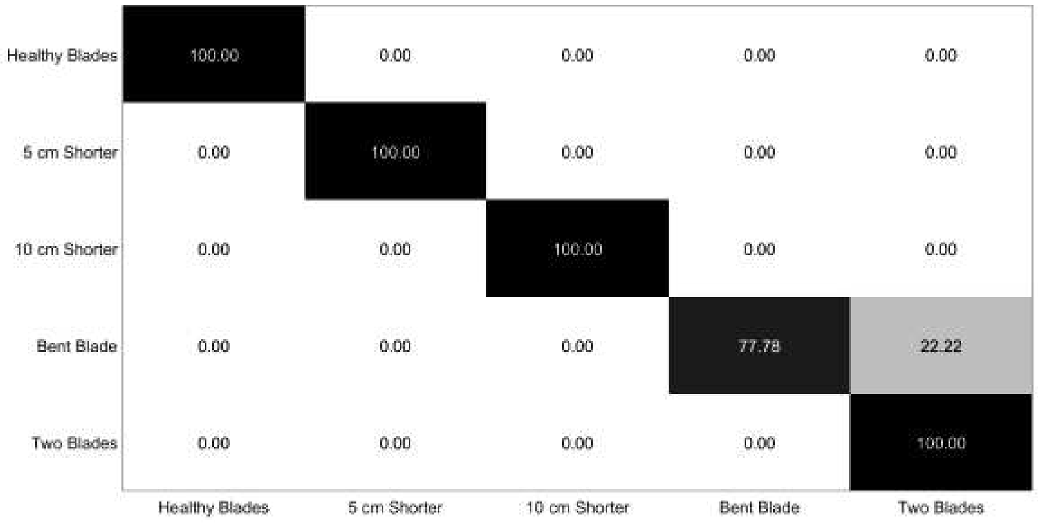

	Healthy Blades	5 cm Shorter	10 cm Shorter	Bent Blade	Two Blades
Healthy Blades	100.00	0.00	0.00	0.00	0.00
5 cm Shorter	0.00	100.00	0.00	0.00	0.00
10 cm Shorter	0.00	0.00	100.00	0.00	0.00
Bent Blade	0.00	0.00	0.00	77.78	22.22
Two Blades	0.00	0.00	0.00	0.00	100.00

(c)

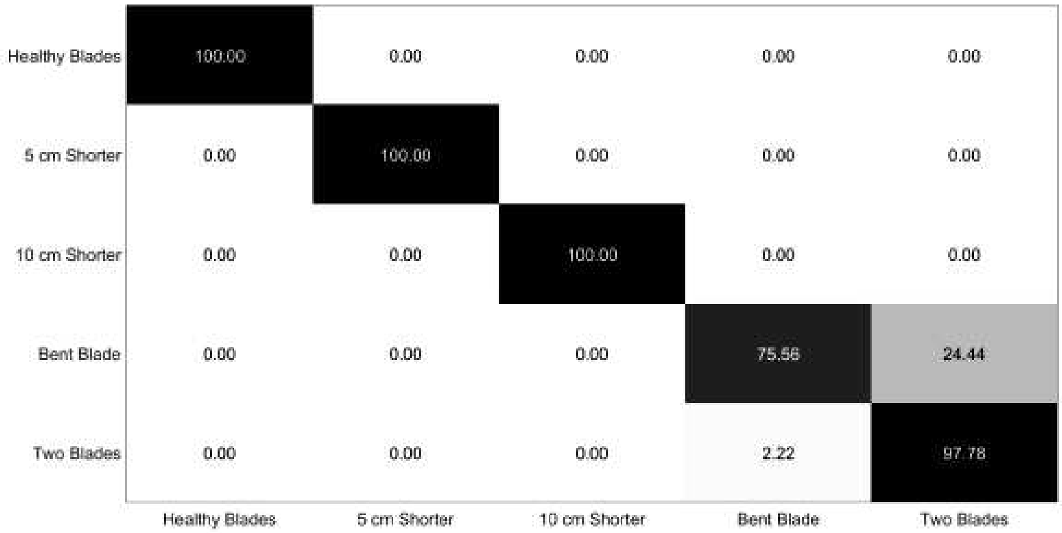

	Healthy Blades	5 cm Shorter	10 cm Shorter	Bent Blade	Two Blades
Healthy Blades	100.00	0.00	0.00	0.00	0.00
5 cm Shorter	0.00	100.00	0.00	0.00	0.00
10 cm Shorter	0.00	0.00	100.00	0.00	0.00
Bent Blade	0.00	0.00	0.00	75.56	24.44
Two Blades	0.00	0.00	0.00	2.22	97.78

(d)

Fig. 5.6: k-NN confusion matrices, Exp1. (a) *k=3*, (b) *k*=5, (c) *k=7*, (d) *k=9*.

In the case of Exp2, the classification is 100% accurate as Fig. 5.7 shows. However, this is because of the experiments were performed in ideal conditions (inside an anechoic chamber) and with a high SNR. The accuracy of the classification would drop in real conditions. This high degree of correct classification is due to the good separation between clusters in this particular experiment. The algorithm maintains its accuracy for different number of neighbours.

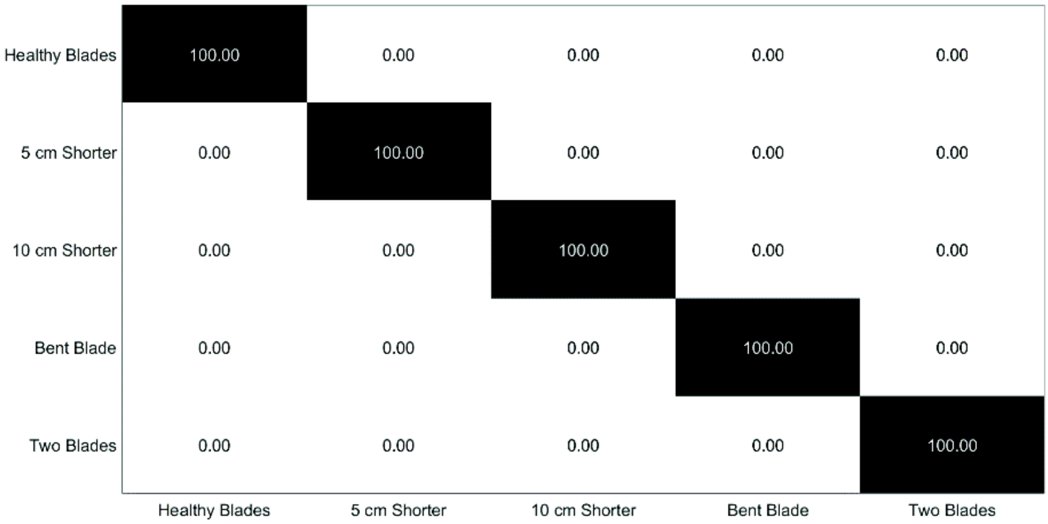

	Healthy Blades	5 cm Shorter	10 cm Shorter	Bent Blade	Two Blades
Healthy Blades	100.00	0.00	0.00	0.00	0.00
5 cm Shorter	0.00	100.00	0.00	0.00	0.00
10 cm Shorter	0.00	0.00	100.00	0.00	0.00
Bent Blade	0.00	0.00	0.00	100.00	0.00
Two Blades	0.00	0.00	0.00	0.00	100.00

Fig. 5.7: k-NN confusion matrix, Exp2. *k=5*.

The confusion matrices corresponding to Exp3 for different *k* is shown in Fig. 5.8. In this case, there is again a misclassification between two similar groups: *5 cm shorter blade* and *10 cm shorter blade*. The accuracy is high (above 90%) and the number of neighbours does not change the well behaviour of the algorithm.

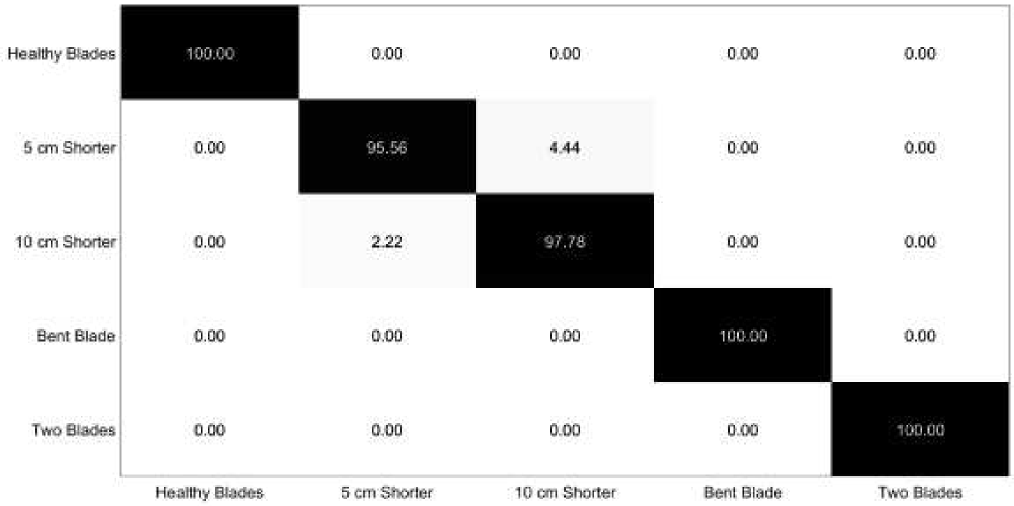

	Healthy Blades	5 cm Shorter	10 cm Shorter	Bent Blade	Two Blades
Healthy Blades	100.00	0.00	0.00	0.00	0.00
5 cm Shorter	0.00	95.56	4.44	0.00	0.00
10 cm Shorter	0.00	2.22	97.78	0.00	0.00
Bent Blade	0.00	0.00	0.00	100.00	0.00
Two Blades	0.00	0.00	0.00	0.00	100.00

(a)

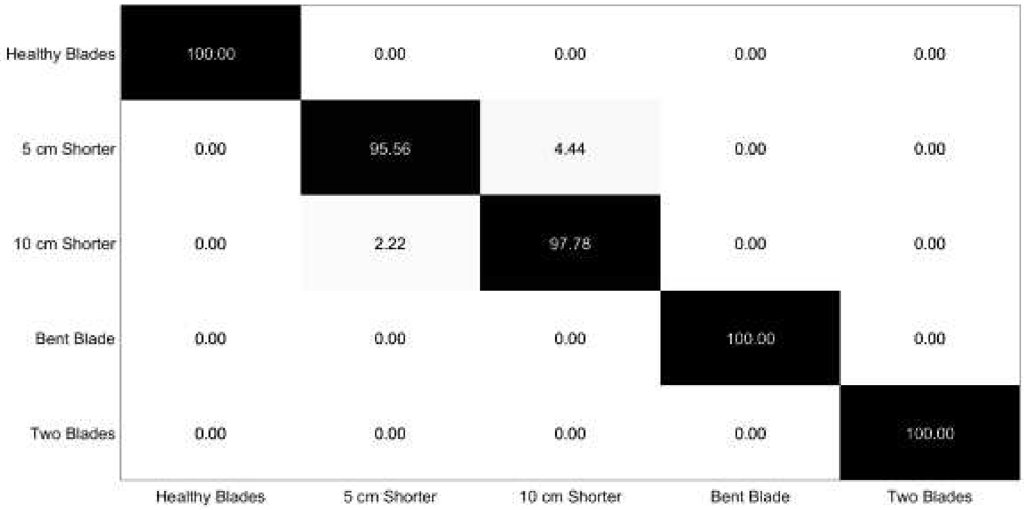

	Healthy Blades	5 cm Shorter	10 cm Shorter	Bent Blade	Two Blades
Healthy Blades	100.00	0.00	0.00	0.00	0.00
5 cm Shorter	0.00	95.56	4.44	0.00	0.00
10 cm Shorter	0.00	2.22	97.78	0.00	0.00
Bent Blade	0.00	0.00	0.00	100.00	0.00
Two Blades	0.00	0.00	0.00	0.00	100.00

(b)

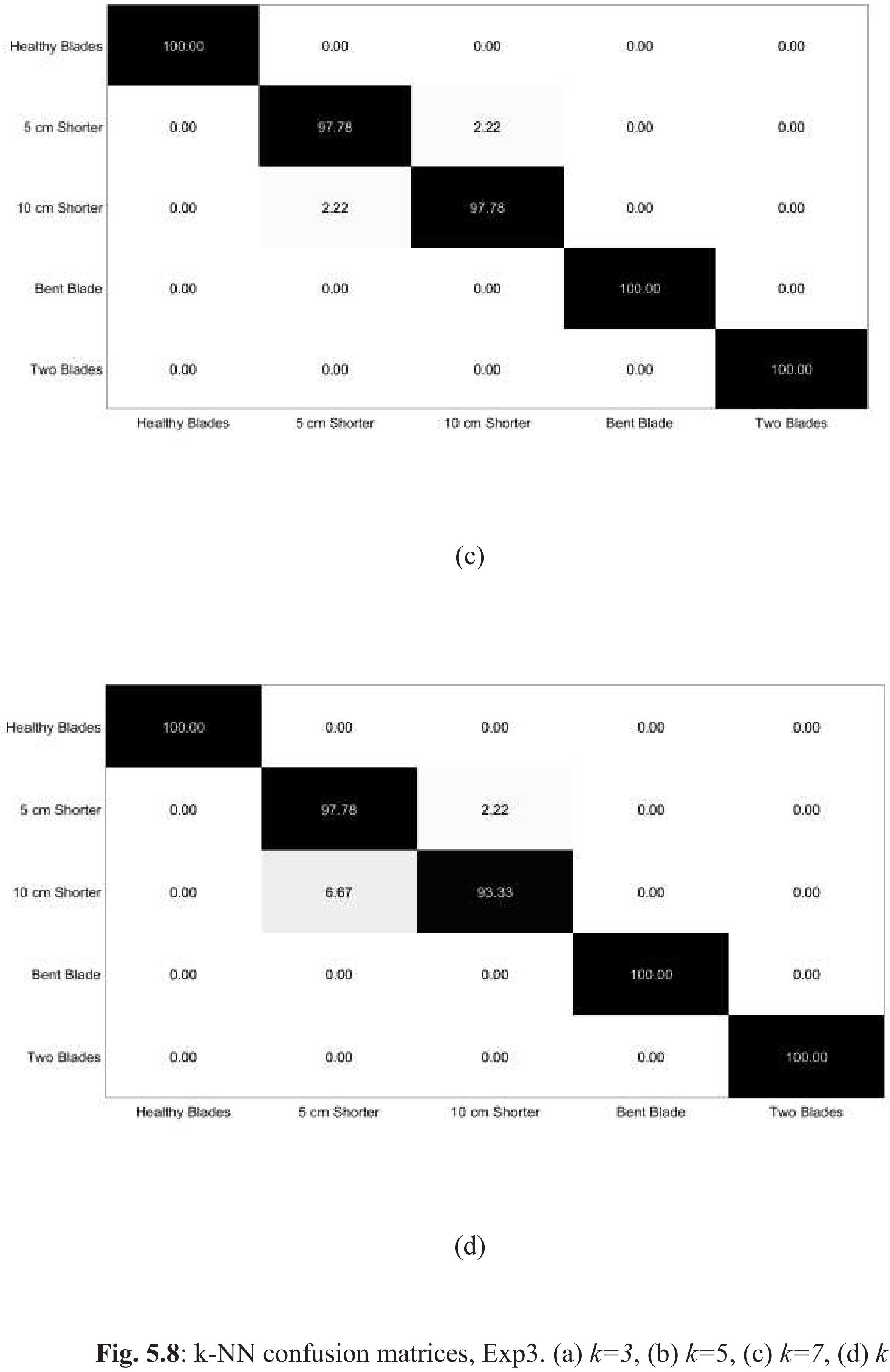

As it was expected by observing the clusters in the different feature spaces, the k-NN provides a high degree of accuracy (more than 80%). It can be concluded that for this small number of faults and for a particular position, the k-NN method offers a reliable classification in the time-domain for only two features with *k=5*.

If a third feature of coordinate in the feature space is included, the distinction between clusters is increased, as expected. However, this increment is not very significant and it improves slightly the classification results already shown.

The third statistical parameter considered was the standard deviation. Fig. 5.9 shows the clusters corresponding to Exp1, Exp2 and Exp3. For the sake of clarity, these experiments will be treated just as three different WT-radar configurations.

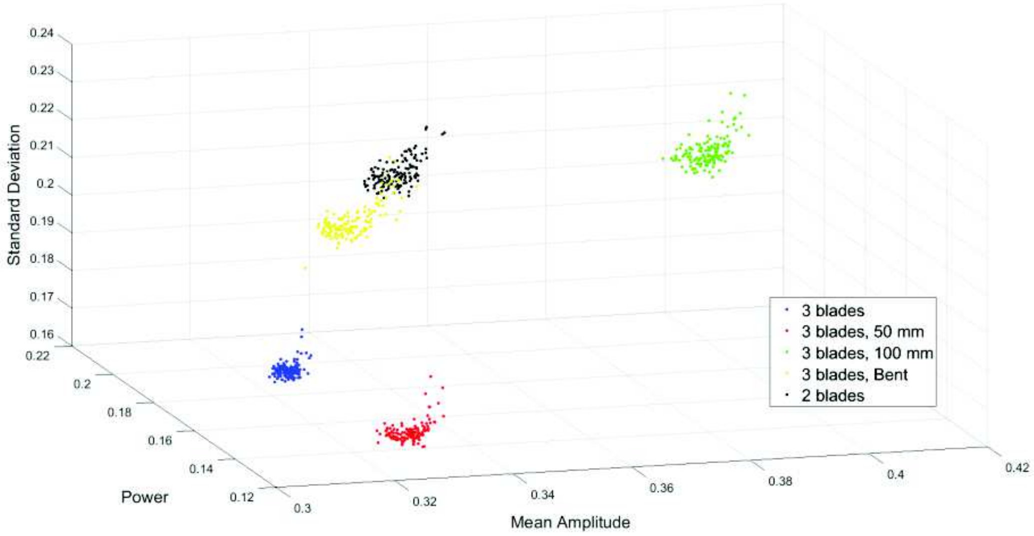

(a)

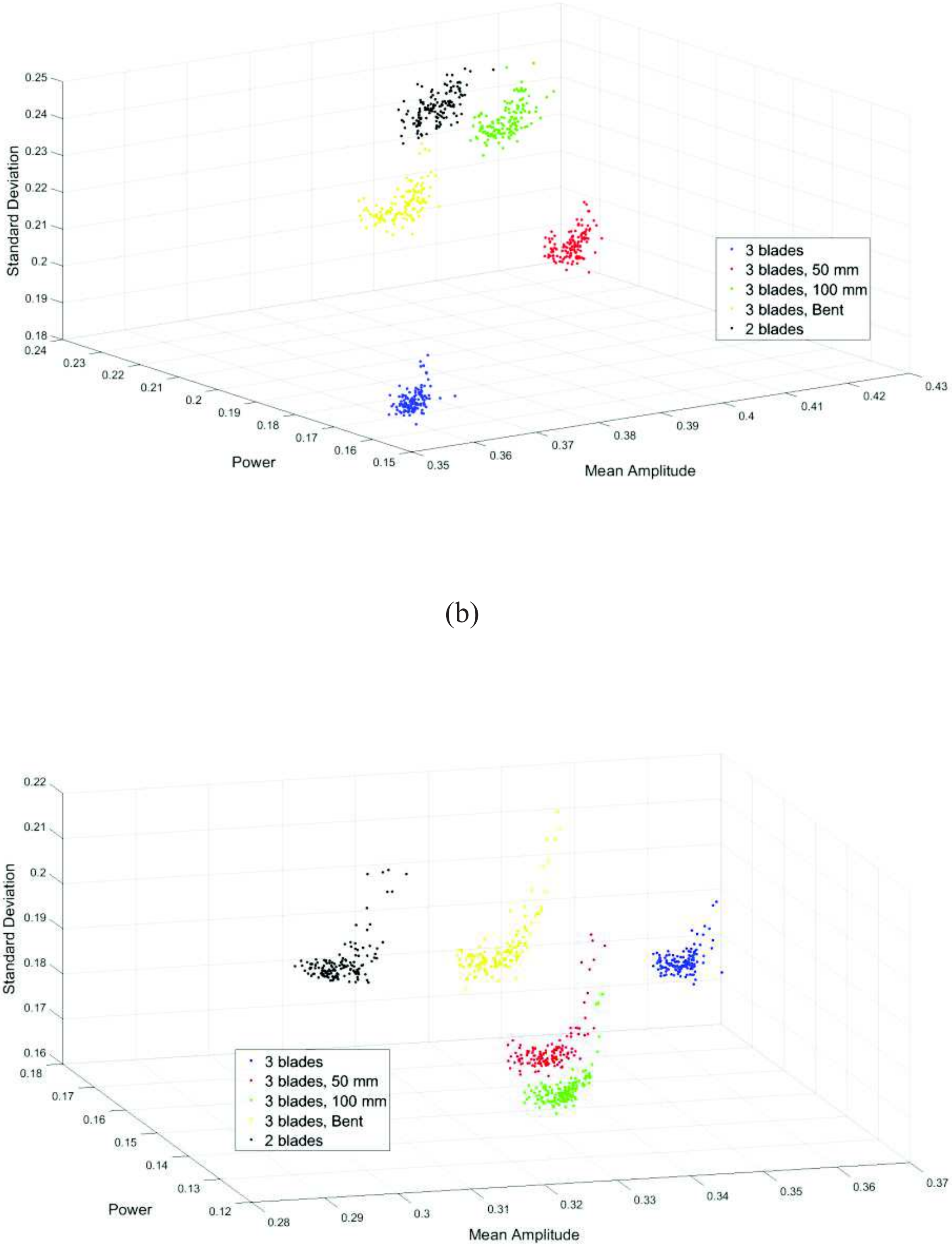

(b)

(c)

Fig. 5.9: 3D feature spaces corresponding to (a) Exp1, (b) Exp2 and (c) Exp3.

The confusion matrices in Fig. 5.10 show the classification accuracy of the k-NN algorithm applied to the features spaces of Fig. 5.9. The extra dimension does not improve the previous results since the accuracy was high enough in the 2D clustering.

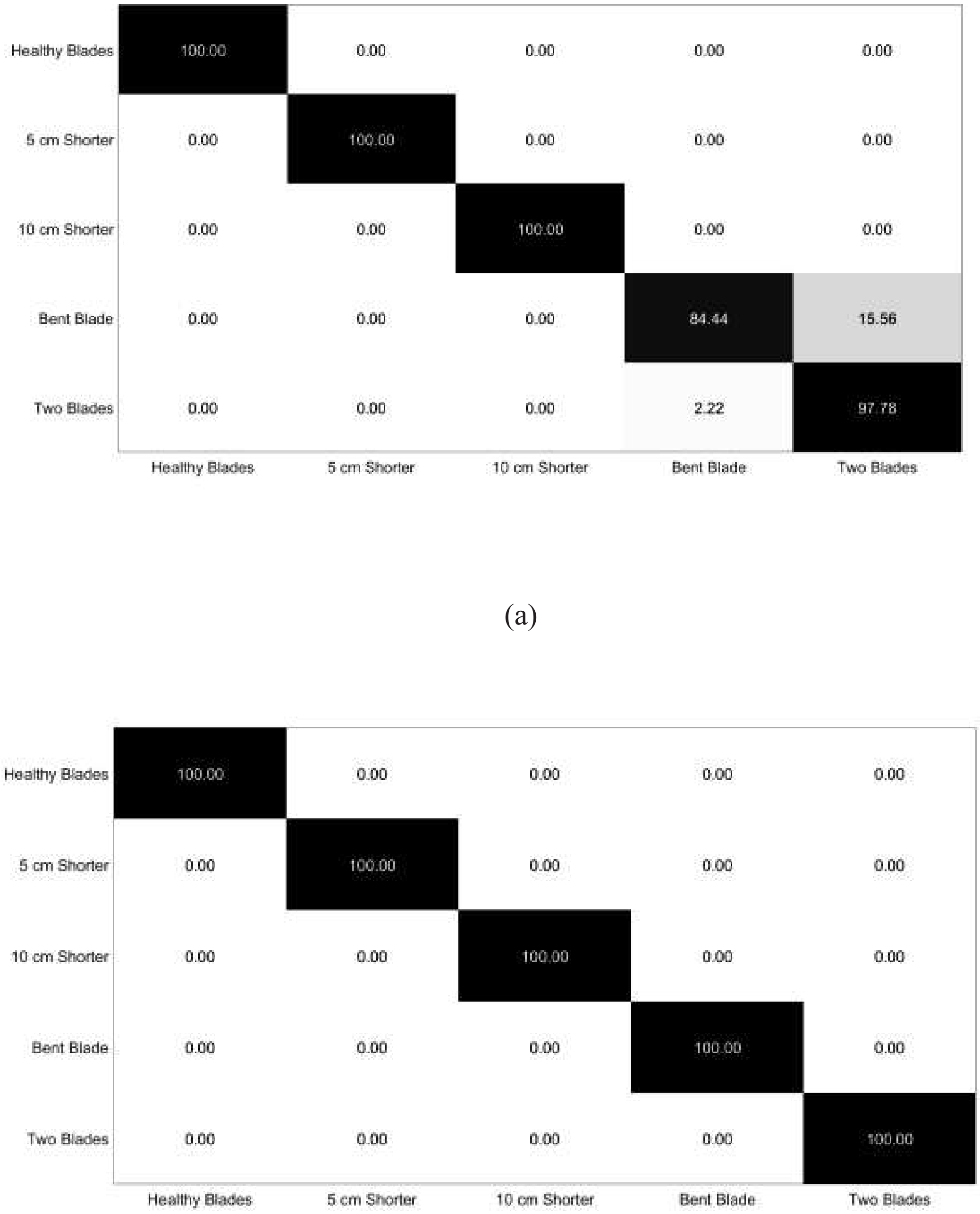

	Healthy Blades	5 cm Shorter	10 cm Shorter	Bent Blade	Two Blades
Healthy Blades	100.00	0.00	0.00	0.00	0.00
5 cm Shorter	0.00	100.00	0.00	0.00	0.00
10 cm Shorter	0.00	0.00	100.00	0.00	0.00
Bent Blade	0.00	0.00	0.00	84.44	15.56
Two Blades	0.00	0.00	0.00	2.22	97.78

(a)

	Healthy Blades	5 cm Shorter	10 cm Shorter	Bent Blade	Two Blades
Healthy Blades	100.00	0.00	0.00	0.00	0.00
5 cm Shorter	0.00	100.00	0.00	0.00	0.00
10 cm Shorter	0.00	0.00	100.00	0.00	0.00
Bent Blade	0.00	0.00	0.00	100.00	0.00
Two Blades	0.00	0.00	0.00	0.00	100.00

(b)

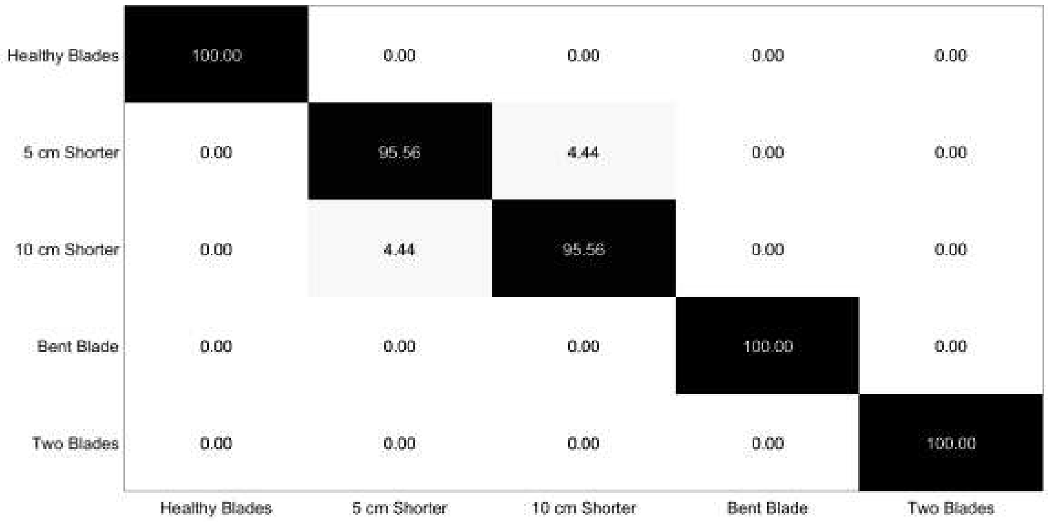

	Healthy Blades	5 cm Shorter	10 cm Shorter	Bent Blade	Two Blades
Healthy Blades	100.00	0.00	0.00	0.00	0.00
5 cm Shorter	0.00	95.56	4.44	0.00	0.00
10 cm Shorter	0.00	4.44	95.56	0.00	0.00
Bent Blade	0.00	0.00	0.00	100.00	0.00
Two Blades	0.00	0.00	0.00	0.00	100.00

(c)

Fig. 5.10: k-NN confusion matrices. (a) Exp1, (b) Exp2 and (c) Exp3. $k=5$.

Other parameters can be calculated from the signals, for example the maximum per revolution. If the maximum of the signal is used instead of the standard deviation to cluster the data, the result can be seen in Fig. 5.11, where the data from Exp2 have been used. The *5 cm shorter blade* and *10 cm shorter blade* groups are mixed in this case. However, the groups corresponding to the *healthy blades*, *bent blade* and *two blades* are still relatively well separated. This could be expected since the maximum of the signal is related to the reflectivity of the WT. In these three cases, the reflectivity differs due to the dramatic differences in the blade structure. However, in the case of *5 cm shorter blade* and *10 cm shorter blade* groups, the difference is not that pronounced. The addition of a third dimension improves the separation between clusters as observed in Fig. 5.11c.

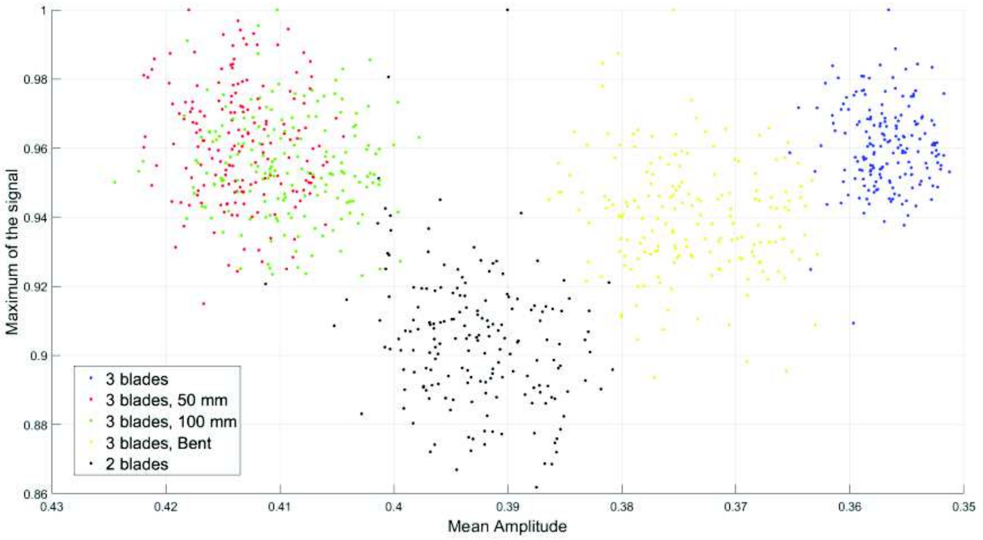
Maximum of the signal
1
0.98
0.96
0.94
0.92
0.9
0.88
0.86
0.43
0.42
0.41
0.4
0.39
0.38
0.37
0.36
0.35
Mean Amplitude
3 blades
3 blades, 50 mm
3 blades, 100 mm
3 blades, Bent
2 blades

(a)

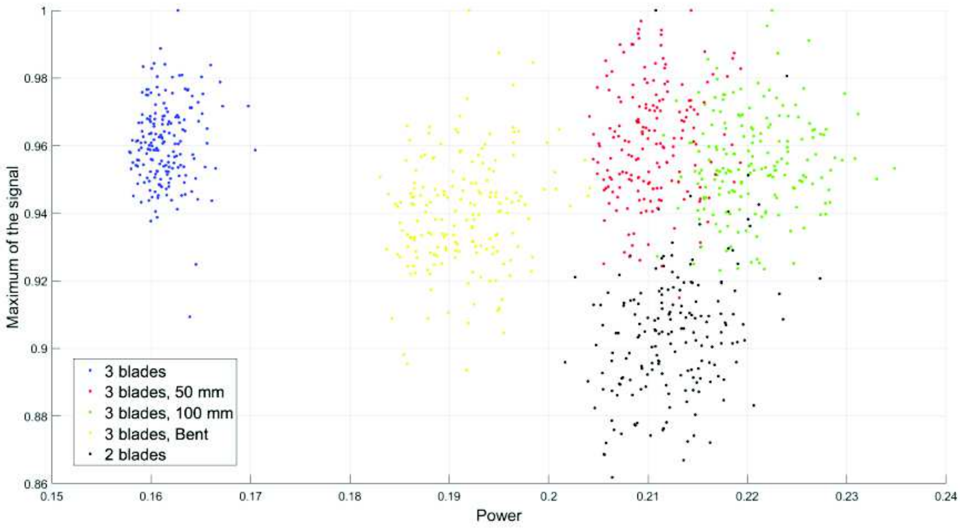
Maximum of the signal
1
0.98
0.96
0.94
0.92
0.9
0.88
0.86
0.15
0.16
0.17
0.18
0.19
0.2
0.21
0.22
0.23
0.24
Power
3 blades
3 blades, 50 mm
3 blades, 100 mm
3 blades, Bent
2 blades

(b)

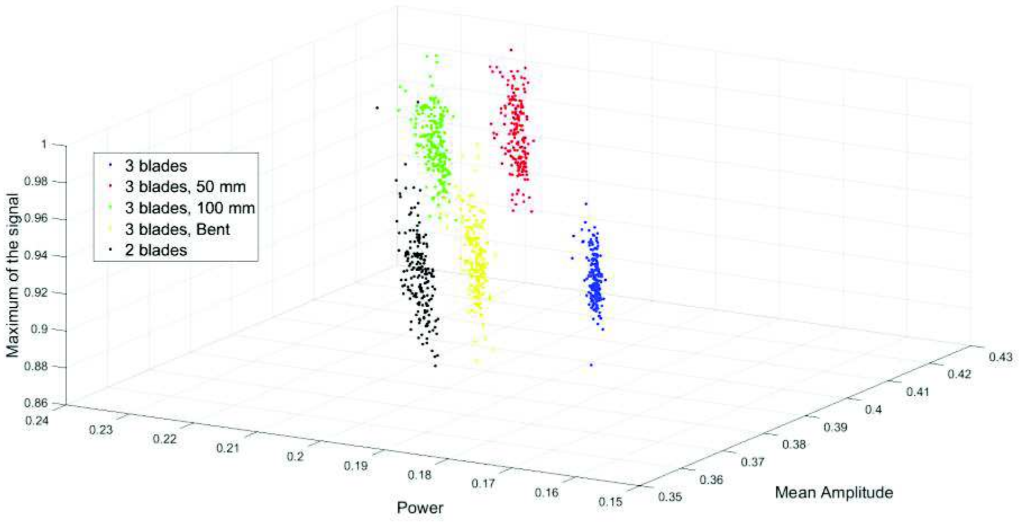

(c)

Fig. 5.11: Feature spaces, Exp2. (a) Maximum vs mean amplitude.(b) Maximum vs power. (c) Power vs mean amplitude vs maximum.

The confusion matrices corresponding to these configurations are shown in Fig. 5.12. The performance of the k-NN degrades dramatically when the maximum of the signals is combined with the corresponding mean amplitude. If the power is used instead of the mean amplitude, the accuracy is high enough but not as high as when the power and mean amplitude are combined together. As expected, the addition of a third dimension improves the performance of the classifier drastically. Similar results were obtained for the other two experiments, Exp1 and Exp3.

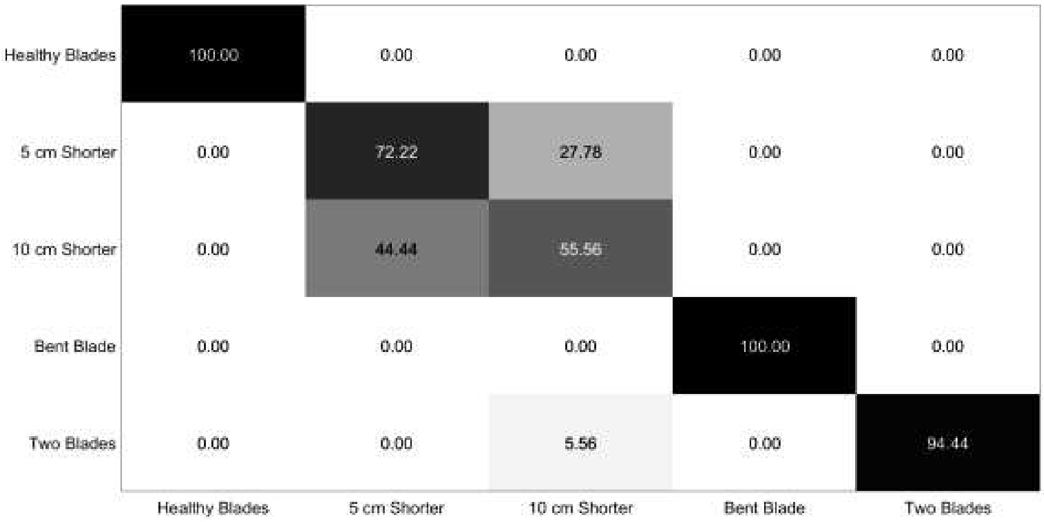

	Healthy Blades	5 cm Shorter	10 cm Shorter	Bent Blade	Two Blades
Healthy Blades	100.00	0.00	0.00	0.00	0.00
5 cm Shorter	0.00	72.22	27.78	0.00	0.00
10 cm Shorter	0.00	44.44	55.56	0.00	0.00
Bent Blade	0.00	0.00	0.00	100.00	0.00
Two Blades	0.00	0.00	5.56	0.00	94.44

(a)

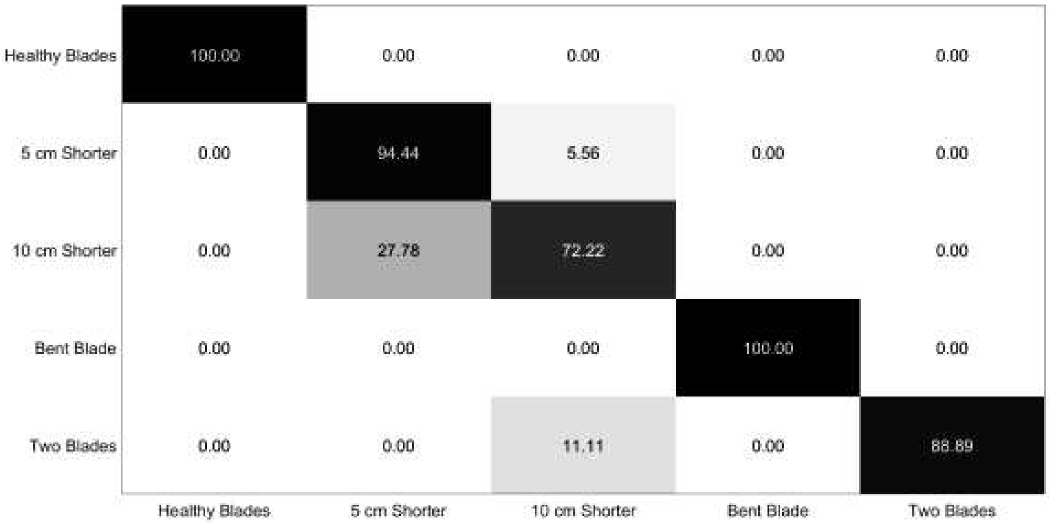

	Healthy Blades	5 cm Shorter	10 cm Shorter	Bent Blade	Two Blades
Healthy Blades	100.00	0.00	0.00	0.00	0.00
5 cm Shorter	0.00	94.44	5.56	0.00	0.00
10 cm Shorter	0.00	27.78	72.22	0.00	0.00
Bent Blade	0.00	0.00	0.00	100.00	0.00
Two Blades	0.00	0.00	11.11	0.00	88.89

(b)

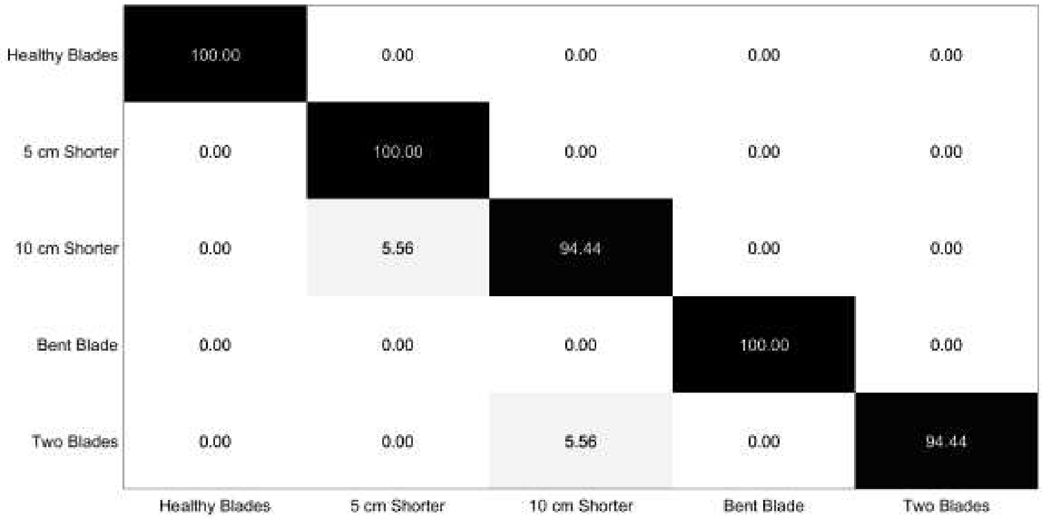

	Healthy Blades	5 cm Shorter	10 cm Shorter	Bent Blade	Two Blades
Healthy Blades	100.00	0.00	0.00	0.00	0.00
5 cm Shorter	0.00	100.00	0.00	0.00	0.00
10 cm Shorter	0.00	5.56	94.44	0.00	0.00
Bent Blade	0.00	0.00	0.00	100.00	0.00
Two Blades	0.00	0.00	5.56	0.00	94.44

(c)

Fig. 5.12: k-NN confusion matrices, Exp2. (a) Maximum vs mean amplitude. (b) Maximum vs power. (c) Power vs mean amplitude vs maximum. *k=5*.

The next step is to analyse the behaviour of the classifier when more types of faults are considered. In this case, apart from the mentioned faults, the following were added: *one blade 2.5 cm shorter*, *one blade 15 cm shorter* and *one blade scratched with sandpaper*. The same statistical parameters were calculated for this group of faults. The 2D feature space using the power and mean amplitude parameters can be seen in Fig. 5.13a. For this particular experiment, the *two blades* cluster and the *healthy blades* group are well separated from the others. This is expected since these are the two extreme cases. The rest of the clusters are dense and relatively well separated. The most interesting observation is that the *scratched blade* cluster is relatively well separated from the *healthy blades*. This indicates that such small defect can be potentially detected and classify correctly. This might rely on the fact that the rough surface of the blade changes the reflecting pattern resulting in an increment of the intensity of the signal.

Fig. 5.13b shows the clustering in 3D, using the standard deviation as a third component. The different types of faults are still well separated.

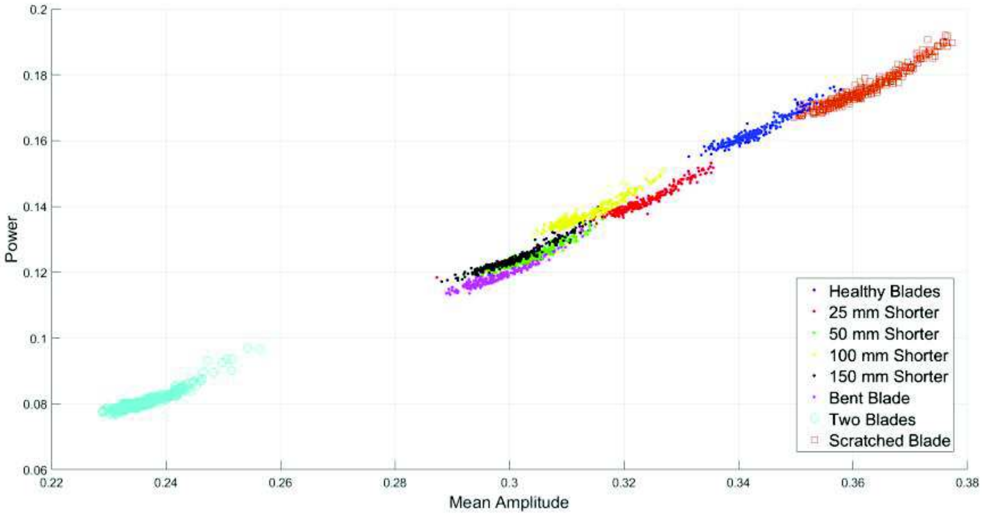

(a)

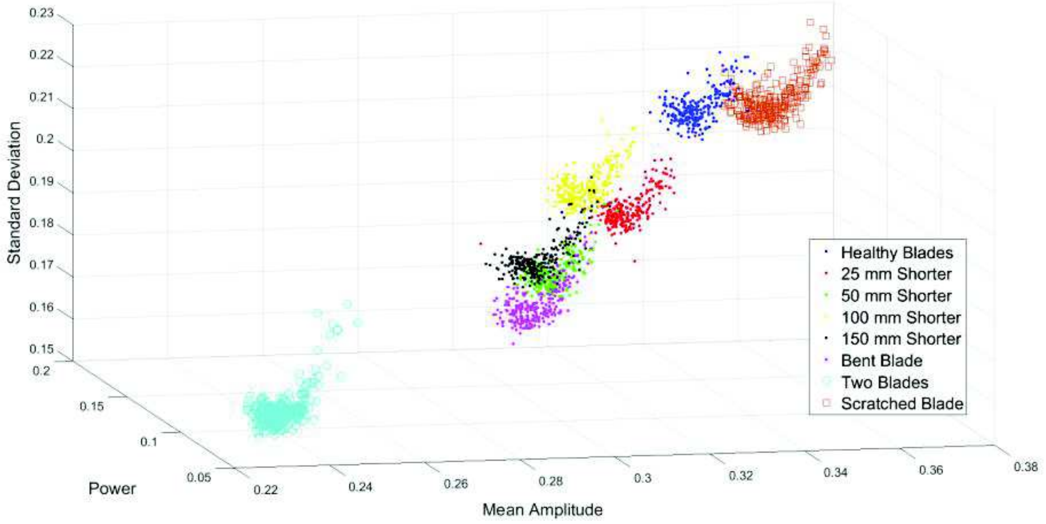

(b)

Fig. 5.13: Features spaces, seven WT faults. (a) Power vs mean amplitude. (b) Power vs mean amplitude vs standard deviation.

The performance of the k-NN method when seven faults are considered can be evaluated with the confusion matrices shown in Fig. 5.14-5.15. The confusion matrices for 2D and 3D were obtained using *k=5* and *k=9*. There is no a great difference between the two cases as well as it happened in the case of four faults. The degree of accuracy is high enough for *k=9*. Therefore, the classification is still fundamentally possible when seven faults are taken into account.

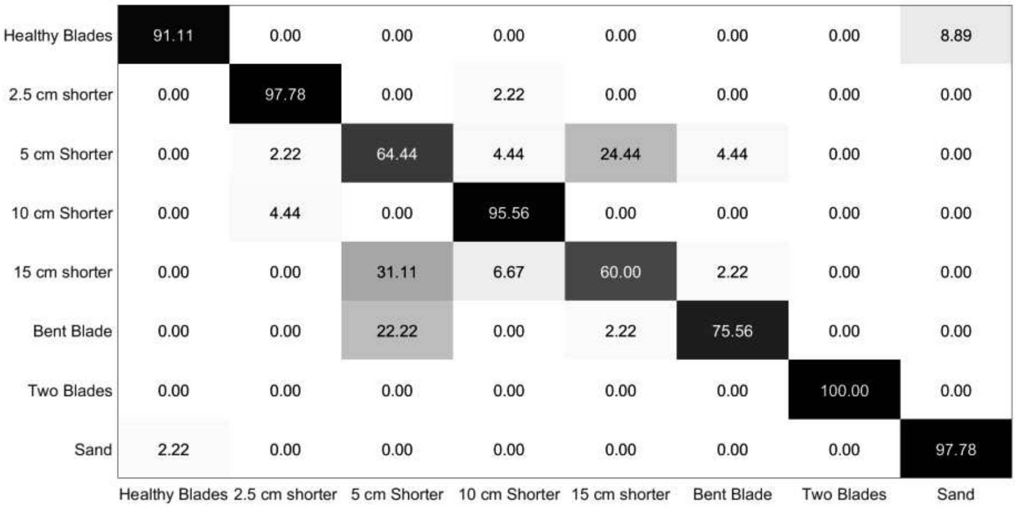

	Healthy Blades	2.5 cm shorter	5 cm Shorter	10 cm Shorter	15 cm shorter	Bent Blade	Two Blades	Sand
Healthy Blades	91.11	0.00	0.00	0.00	0.00	0.00	0.00	8.89
2.5 cm shorter	0.00	97.78	0.00	2.22	0.00	0.00	0.00	0.00
5 cm Shorter	0.00	2.22	64.44	4.44	24.44	4.44	0.00	0.00
10 cm Shorter	0.00	4.44	0.00	95.56	0.00	0.00	0.00	0.00
15 cm shorter	0.00	0.00	31.11	6.67	60.00	2.22	0.00	0.00
Bent Blade	0.00	0.00	22.22	0.00	2.22	75.56	0.00	0.00
Two Blades	0.00	0.00	0.00	0.00	0.00	0.00	100.00	0.00
Sand	2.22	0.00	0.00	0.00	0.00	0.00	0.00	97.78

(a)

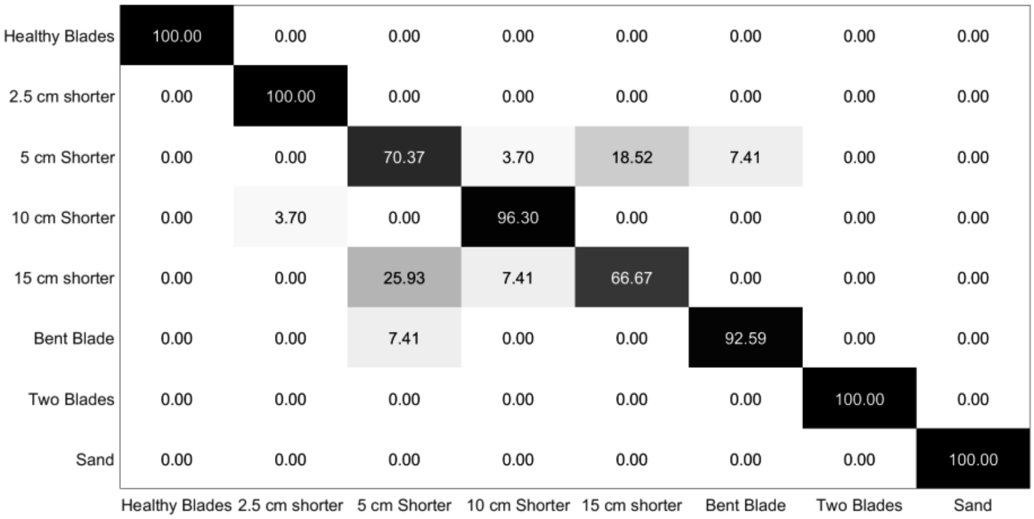

	Healthy Blades	2.5 cm shorter	5 cm Shorter	10 cm Shorter	15 cm shorter	Bent Blade	Two Blades	Sand
Healthy Blades	100.00	0.00	0.00	0.00	0.00	0.00	0.00	0.00
2.5 cm shorter	0.00	100.00	0.00	0.00	0.00	0.00	0.00	0.00
5 cm Shorter	0.00	0.00	70.37	3.70	18.52	7.41	0.00	0.00
10 cm Shorter	0.00	3.70	0.00	96.30	0.00	0.00	0.00	0.00
15 cm shorter	0.00	0.00	25.93	7.41	66.67	0.00	0.00	0.00
Bent Blade	0.00	0.00	7.41	0.00	0.00	92.59	0.00	0.00
Two Blades	0.00	0.00	0.00	0.00	0.00	0.00	100.00	0.00
Sand	0.00	0.00	0.00	0.00	0.00	0.00	0.00	100.00

(b)

Fig. 5.14: k-NN confusion matrix. Power vs. Mean amplitude. (a) *k=5* and (b) *k=9*.

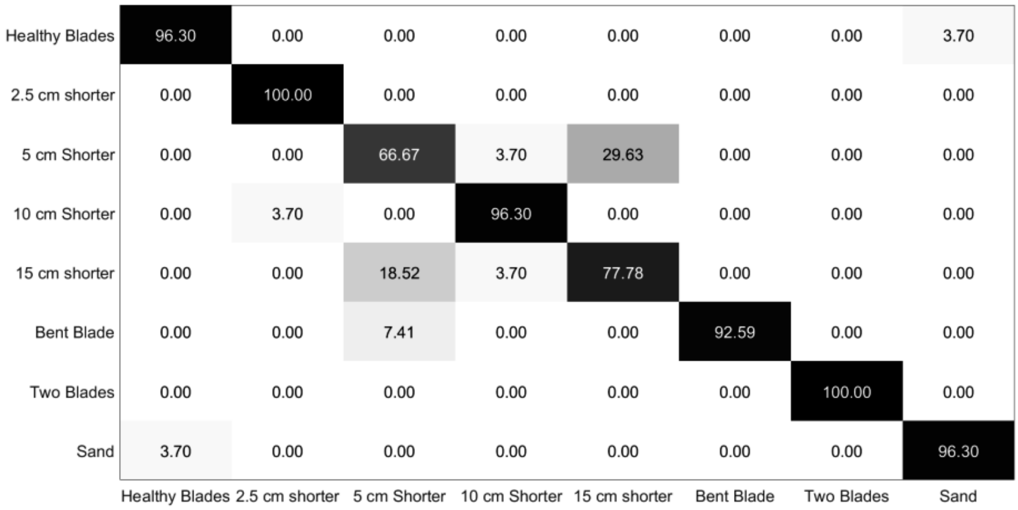

	Healthy Blades	2.5 cm shorter	5 cm Shorter	10 cm Shorter	15 cm shorter	Bent Blade	Two Blades	Sand
Healthy Blades	96.30	0.00	0.00	0.00	0.00	0.00	0.00	3.70
2.5 cm shorter	0.00	100.00	0.00	0.00	0.00	0.00	0.00	0.00
5 cm Shorter	0.00	0.00	66.67	3.70	29.63	0.00	0.00	0.00
10 cm Shorter	0.00	3.70	0.00	96.30	0.00	0.00	0.00	0.00
15 cm shorter	0.00	0.00	18.52	3.70	77.78	0.00	0.00	0.00
Bent Blade	0.00	0.00	7.41	0.00	0.00	92.59	0.00	0.00
Two Blades	0.00	0.00	0.00	0.00	0.00	0.00	100.00	0.00
Sand	3.70	0.00	0.00	0.00	0.00	0.00	0.00	96.30

(a)

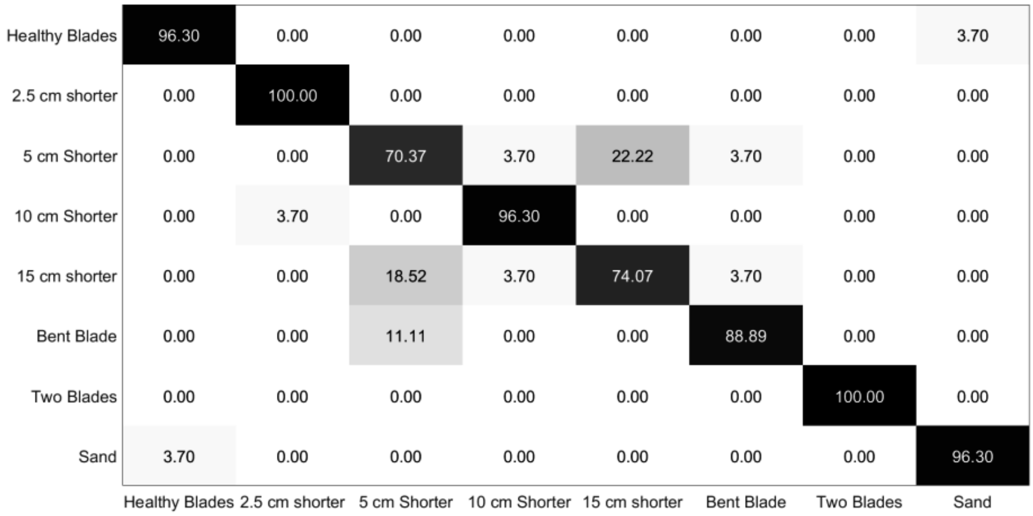

	Healthy Blades	2.5 cm shorter	5 cm Shorter	10 cm Shorter	15 cm shorter	Bent Blade	Two Blades	Sand
Healthy Blades	96.30	0.00	0.00	0.00	0.00	0.00	0.00	3.70
2.5 cm shorter	0.00	100.00	0.00	0.00	0.00	0.00	0.00	0.00
5 cm Shorter	0.00	0.00	70.37	3.70	22.22	3.70	0.00	0.00
10 cm Shorter	0.00	3.70	0.00	96.30	0.00	0.00	0.00	0.00
15 cm shorter	0.00	0.00	18.52	3.70	74.07	3.70	0.00	0.00
Bent Blade	0.00	0.00	11.11	0.00	0.00	88.89	0.00	0.00
Two Blades	0.00	0.00	0.00	0.00	0.00	0.00	100.00	0.00
Sand	3.70	0.00	0.00	0.00	0.00	0.00	0.00	96.30

(b)

Fig. 5.15: k-NN confusion matrix. Power vs. mean amplitude vs. standard deviation. (a) *k=5* and (b) *k=9*.

From the confusion matrices in Fig. 5.15 it can be concluded that the performance of the k-NN is degraded respect to the classification of four faults. This is somehow expected since there are more faults and therefore more clusters to distinguish. However, the accuracy of the classifier is highly acceptable in these experimental conditions.

In principle, the potential RF system deployed in the vicinity of a WT to monitor its structural health would be in a fixed position and the classification algorithm would be trained respect to that position. However, small changes can occur in the orientation of the sensor or its distance to the turbine. Therefore, it can be taken advantage of the inevitable small changes in the measurements to combine them and obtain a more robust classification system. Notice that the modifications introduced in the scaled experiments imply an important change in the results due to high frequency used. If the system is rescaled to a real situation, these changes would be much dramatic than the expected in a normal situation.

The data from Exp1, Exp2 and Exp3 have been combined and the resulting feature space using three statistical parameters has been plotted in Fig. 5.16. The size of the database is, in this case, $[(3 \cdot N) \times F] \times 3 = 2700 \times 3 = 8100$. In this particular situation, 50% of the database was used as training set. The power, mean amplitude and standard deviation of the signals were chosen as features. Each fault presents different clusters distributed in the feature space, which expected since this is a way of plotting the graphs Fig. 5.3-5.5 in a single chart. Fig. 5.17 shows the good performance of the k-NN as a classifier.

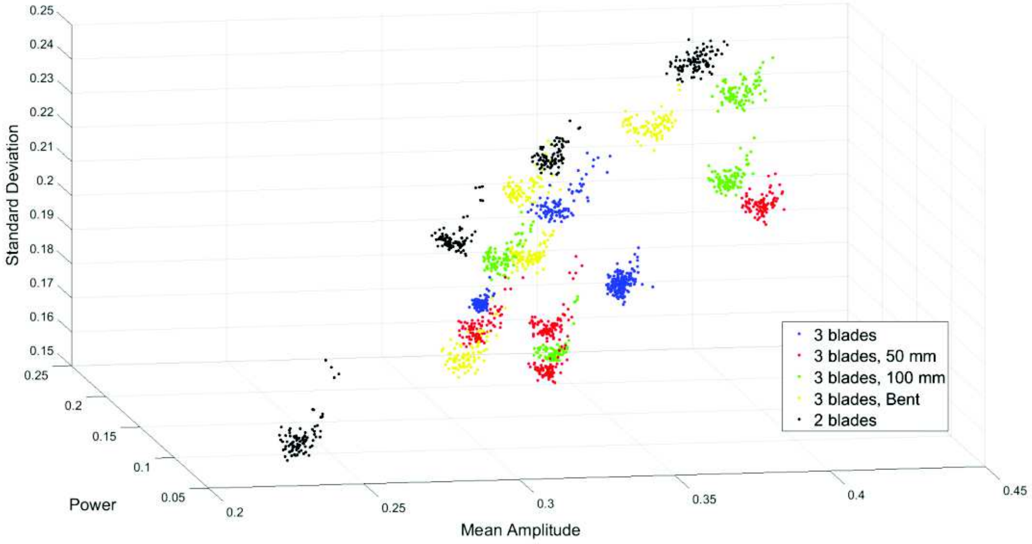

Fig. 5.16: Power vs. mean amplitude vs. standard deviation. Three different positions and four types of WT faults.

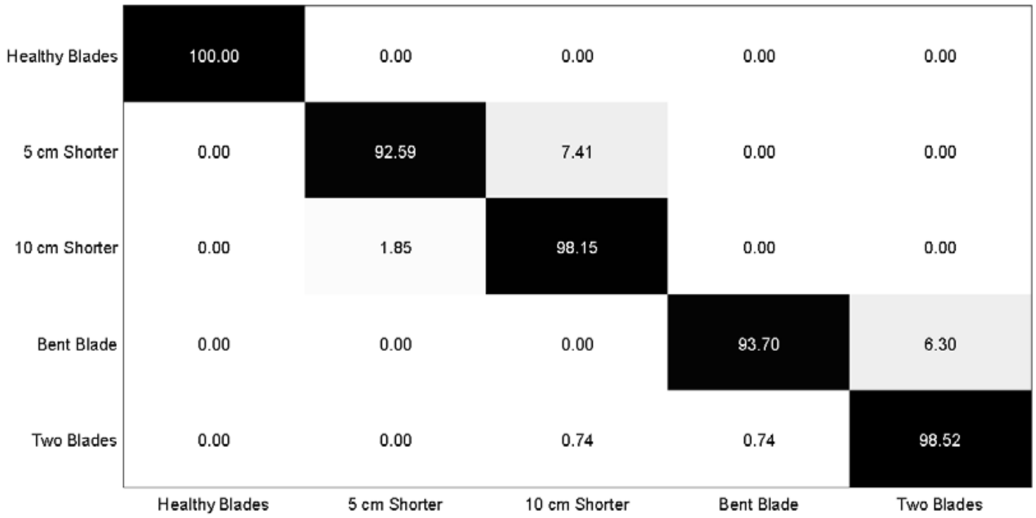

	Healthy Blades	5 cm Shorter	10 cm Shorter	Bent Blade	Two Blades
Healthy Blades	100.00	0.00	0.00	0.00	0.00
5 cm Shorter	0.00	92.59	7.41	0.00	0.00
10 cm Shorter	0.00	1.85	98.15	0.00	0.00
Bent Blade	0.00	0.00	0.00	93.70	6.30
Two Blades	0.00	0.00	0.74	0.74	98.52

Fig. 5.17: Confusion matrix for three different positions and four faults. *k=5*.

These results suggest that if a great variability is expected in the geometrical condition of the WT-radar system, different data should be taken for the expected range of positions. In this way, a database of enough positions could be used as training set to obtain a high accuracy in the classification.

5.5 Classification in the Frequency-domain. Principal Components Analysis

The PCA algorithm has been widely explained in literature. In this section, the theoretical introduction to this method will be similar to the analysis done in [1]. The goal of the PCA algorithm is two-fold: dimensionality reduction and feature extraction. The input of the PCA is a database in the form of a matrix whose rows are high-dimensional vectors. Each dimension represents a particular feature that can be any significant information extracted from the radar signature of the blades. Information from different types of sensors can also be used.

The training set is a subset of the database and it can be seen as formed by n d-dimensional samples $x_1, \dots, x_k, \dots, x_n$. In order to understand the logic behind the PCA algorithm, the problem of representing all these vectors by a single vector will be treated first. The objective is to find a vector x_0 such that the sum of the squared distances between x_0 and the various x_k is as small as possible. We define the squared-error criterion function $J_0(x_0)$ by

$$J_0(x_0) = \sum_{k=1}^{n} \|x_0 - x_k\|^2, \tag{5.1}$$

and seek the value of x_0 that minimizes J_0. It can be shown that the solution to this problem is given by $x_0 = m$, where m is the sample mean.

The sample mean is a zero-dimensional representation of the data set. It does not show any variability in the data. A more interesting, one-dimensional representation by projecting the data onto a line running through the sample mean can be obtained. Let e be a unit vector in the direction of that line. The equation of this line can be written as $x = m + ae$, where the scalar a corresponds to the distance of any point x from the mean m. If x_k is represented by $m + a_k e$, an optimal set of coefficients a_k can be found by minimizing the squared-error criterion function:

$$J_1(a_1, \dots, a_n, e) = \sum_{k=1}^{n} \|(m + a_k e) - x_k\|^2 \tag{5.2}$$

By definition $\|e\| = 1$, so after partially differentiating with respect to a_k and setting the derivative to zero, the coefficients are expressed by

$$a_k = e^t(x_k - m) \tag{5.3}$$

In order to find the best direction for the line of projection, a_k is substituted in the expression (5.2) to obtain

$$J_1(e) = -e^t S e + \sum_{k=1}^{n} \|x_k - m\|^2$$

(5.4)

where $S = \sum_{k=1}^{n} (x_k - m)(x_k - m)^t$ is the called *scatter matrix*.

The vector e that minimizes J_1 also maximizes the quadratic form $e^t S e$. So to do it, the method of Lagrange multipliers is used subject to the constraint $\|e\| = 1$. Therefore, e must be an eigenvector of the scatter matrix

$$Se = \lambda e$$

(5.5)

In particular, the eigenvector corresponding to the largest eigenvalue of the scatter matrix has to be selected.

If the problem has now to be extended to a c-dimensional one, the data point x can be written as

$$x = m + \sum_{i=1}^{c} a_i e_i,$$

(5.6)

where $c \leq d$. The criterion function

$$J_c = \sum_{k=1}^{n} \|(m + \sum_{i=1}^{c} a_{ki} e_i) - x_k\|^2$$

(5.7)

is minimized when the vectors $e_1, \dots, e_c$ are the c eigenvectors of the scatter matrix having the largest eigenvalues. Because the scatter matrix is real and symmetric, these eigenvectors are orthogonal. They form a natural set of basis vectors for representing any feature vector x. The coefficients a_i are the components of x in that basis, and are called the *principal components*. Geometrically, if the data points $x_1, \dots, x_n$ are pictured forming a d-dimensional hyperellipsoidally shaped cloud, the eigenvectors of the scatter matrix are the principal axes of that hyperellipsoid. PCA reduces the dimensionality of the feature space by restricting attention to those directions along which the scatter of the cloud is greatest. The PCA algorithm is able to detect features in these high-dimensional arrangements of data that would not be detectable by simple observation.

For classification purposes, a test $1 \times d$ data vector x is projected onto the k-dimensional subspace formed by the k eigenvectors that carry the relevant information. This means,

$$x^T W = x_p$$

(5.8)

where W is the matrix whose columns are the k eigenvectors (do not confuse with the k nearest neighbours).

In this research, PCA was implemented in the frequency-domain. The PSDs data from the different faulty WT signals served as inputs to construct the database. The size of the data base matrix was $(N \cdot F)\times d$, where N is the number of revolutions, F is the number of faults and d is the number of data points in the PSD. As an example, Fig. 5.18 represents the PSDs of the seven WT faults plus healthy blades (7+1 WT status). There are no features to differentiate faults for classification, so the use of a tool such as PCA is necessary for feature extraction (and dimensionality reduction). In this case, the number of frequencies in the PSDs was $d = 20$. As in the case of SPM, 90% of the database formed the training set and the rest formed the test set.

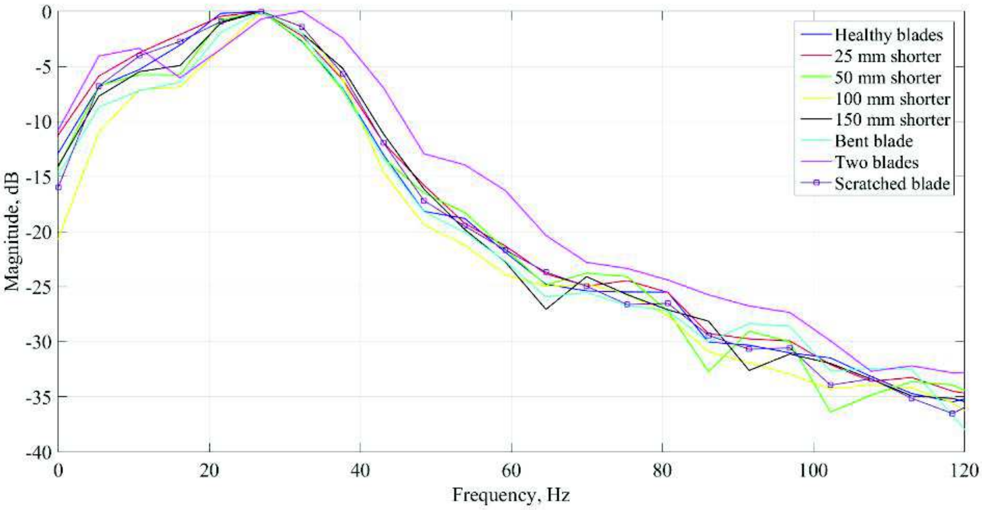

Fig. 5.18: PSDs of faulty WT signals. Seven types of faults plus the healthy blade signature.

The amplitudes per cycle of the time-domain signals were considered as features in the first instance. Although, as observed in section 4.6, there were visual differences in the signals of the different faults, the PCA algorithm was not able to detect patterns in the time-domain signatures to differentiate between WT faults. Fig. 5.19 corresponds to the feature space formed by using the time-domain signatures. The frequency-domain was the only option that provided satisfactory results.

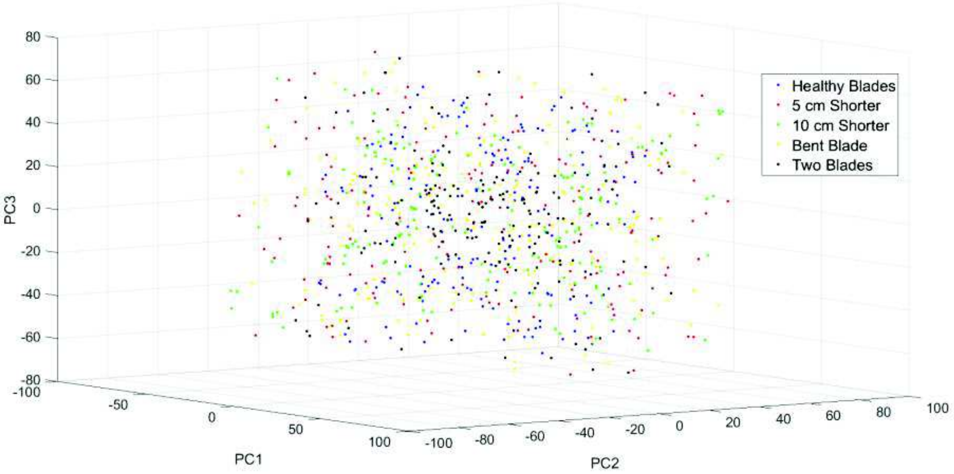

Fig. 5.19: PCA output. Time-domain signals used as inputs, Exp1.

The feature space of Fig. 5.20 was obtained after applying the PCA algorithm to the PSD of Exp1 signals. With just two principal components, the different types of faults form clusters that permit a relatively clear discrimination between them. Fig. 5.20a shows that the *5 cm shorter blade* and *10 cm shorter blade* groups are well-separated while the classes *two blades*, *healthy blades* and *bent blade* overlap. Although the time-domain signatures of these three faults were clearly different, their PSDs are not necessarily dissimilar too. Fig. 5.20b shows the PCA output when three principal components were used. In this case, the distinction between faults is clearer, as expected due to the extra dimension.

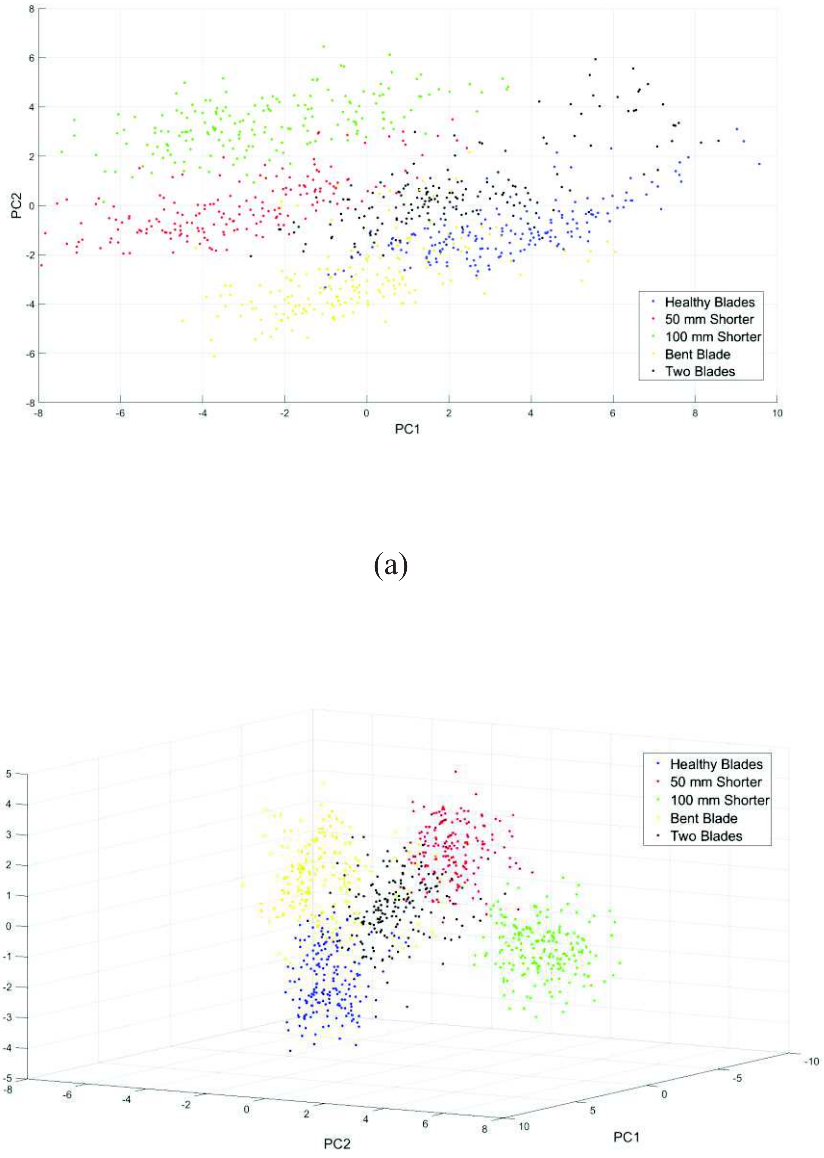

(a)

(b)

Fig. 5.20: PCA output. Four faults and healthy blades from Exp1. (a) Two principal components. (b) Three principal components.

Fig. 5.21 and Fig. 5.22 correspond to the PCA output from Exp2 and Exp3. The results are similar to Fig. 5.20.

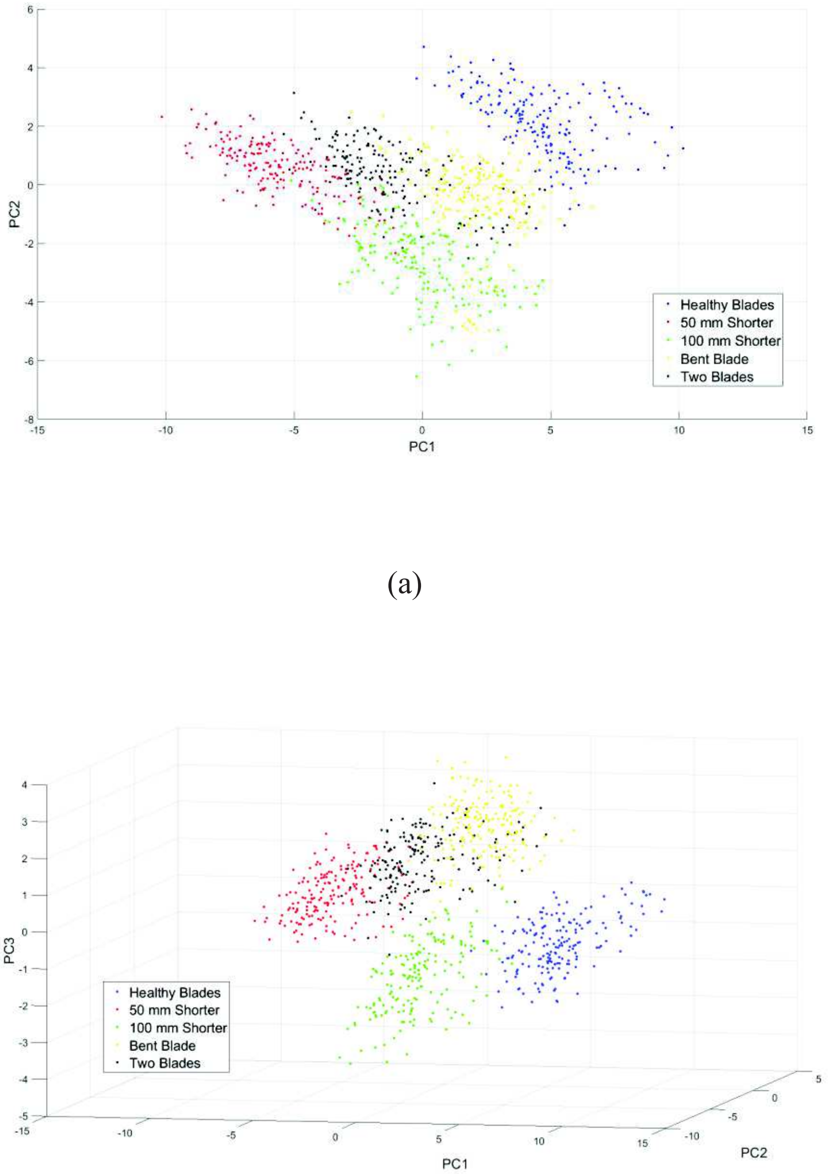

(a)

(b)

Fig. 5.21: PCA output. Four faults and healthy blades from Exp2. (a) Two principal components. (b) Three principal components.

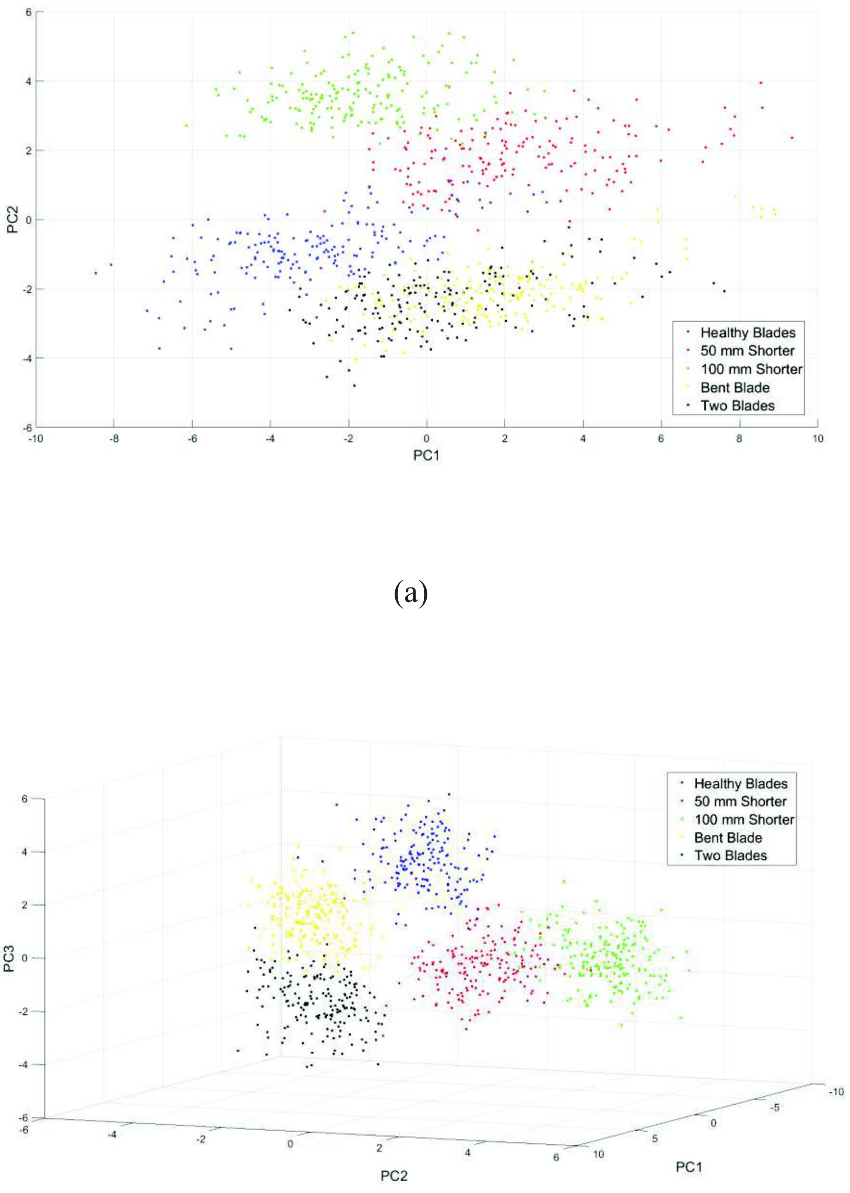

(a)

(b)

Fig. 5.22: PCA output. Four faults and healthy blades from Exp3. (a) Two principal components. (b) Three principal components.

The k-NN algorithm was used to classify the test points of the database. The confusion matrices in Fig. 5.23-5.25 assess the performance of the classifier in three different positions and for different numbers of neighbours *k* and principal components. The performance of the classifier in 2D (two principal components) is accurate enough (more than 70% correct classification), although it is less accurate than in the case of SPM. Increasing the number of neighbours, *k=5* and *k=9*, does not improve significantly the accuracy of the classifier.

The classification improves drastically if one more principal component is added. In the case of Fig. 5.23 (Exp1), the correct classification of the *two blades* samples is increased from 72% to 100% when *k=5*. However, also in this experiment, the correct classification of the *10 cm shorter blade* group is not improved by the addition of a third principal component. Similar behaviour is observed in the other two experiments, Exp2 and Exp3: a third principal component improves the correct classification of certain classes leaving others with the same rate of accuracy.

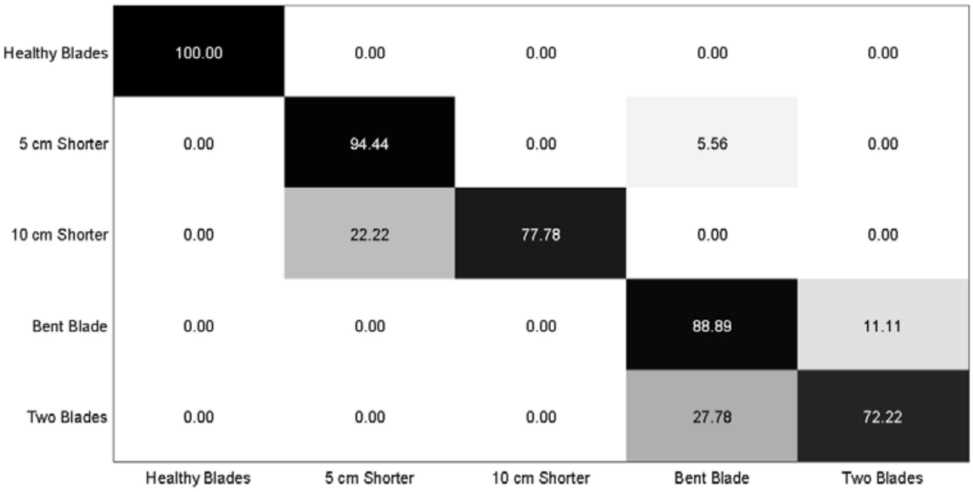

	Healthy Blades	5 cm Shorter	10 cm Shorter	Bent Blade	Two Blades
Healthy Blades	100.00	0.00	0.00	0.00	0.00
5 cm Shorter	0.00	94.44	0.00	5.56	0.00
10 cm Shorter	0.00	22.22	77.78	0.00	0.00
Bent Blade	0.00	0.00	0.00	88.89	11.11
Two Blades	0.00	0.00	0.00	27.78	72.22

(a)

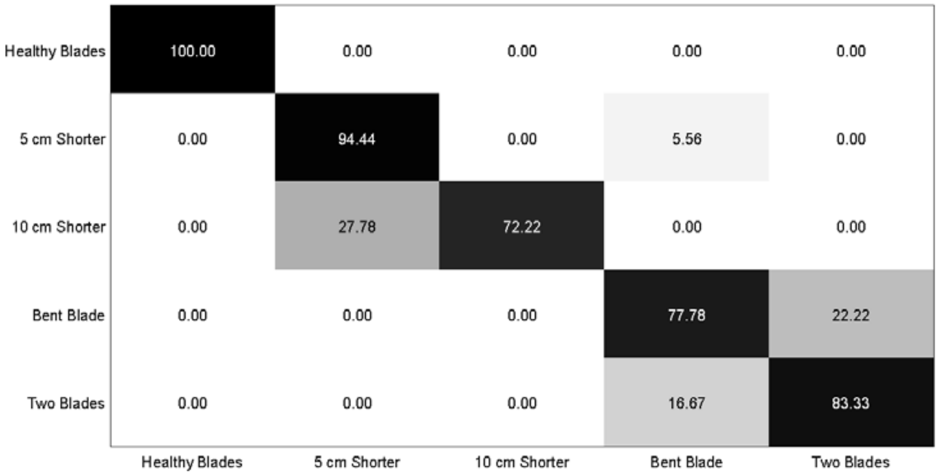

	Healthy Blades	5 cm Shorter	10 cm Shorter	Bent Blade	Two Blades
Healthy Blades	100.00	0.00	0.00	0.00	0.00
5 cm Shorter	0.00	94.44	0.00	5.56	0.00
10 cm Shorter	0.00	27.78	72.22	0.00	0.00
Bent Blade	0.00	0.00	0.00	77.78	22.22
Two Blades	0.00	0.00	0.00	16.67	83.33

(b)

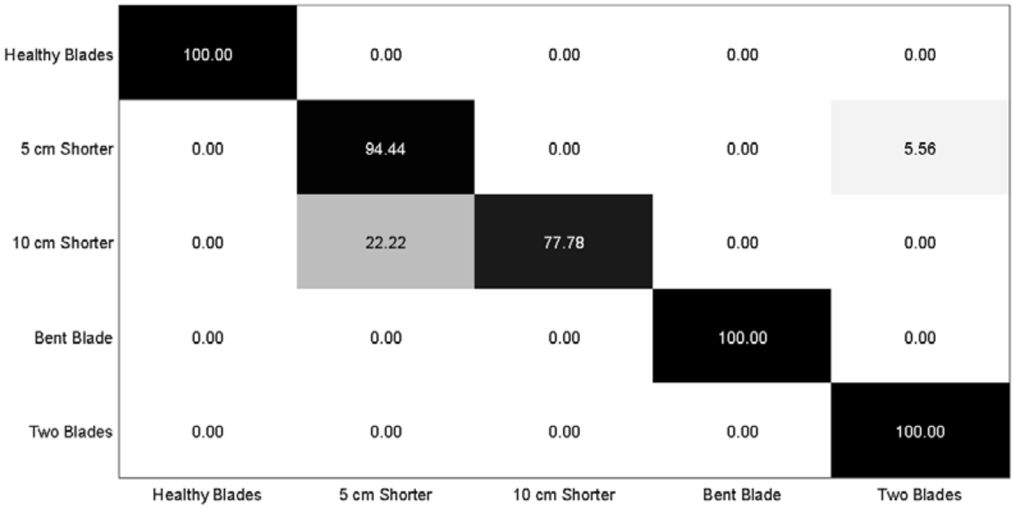

	Healthy Blades	5 cm Shorter	10 cm Shorter	Bent Blade	Two Blades
Healthy Blades	100.00	0.00	0.00	0.00	0.00
5 cm Shorter	0.00	94.44	0.00	0.00	5.56
10 cm Shorter	0.00	22.22	77.78	0.00	0.00
Bent Blade	0.00	0.00	0.00	100.00	0.00
Two Blades	0.00	0.00	0.00	0.00	100.00

(c)

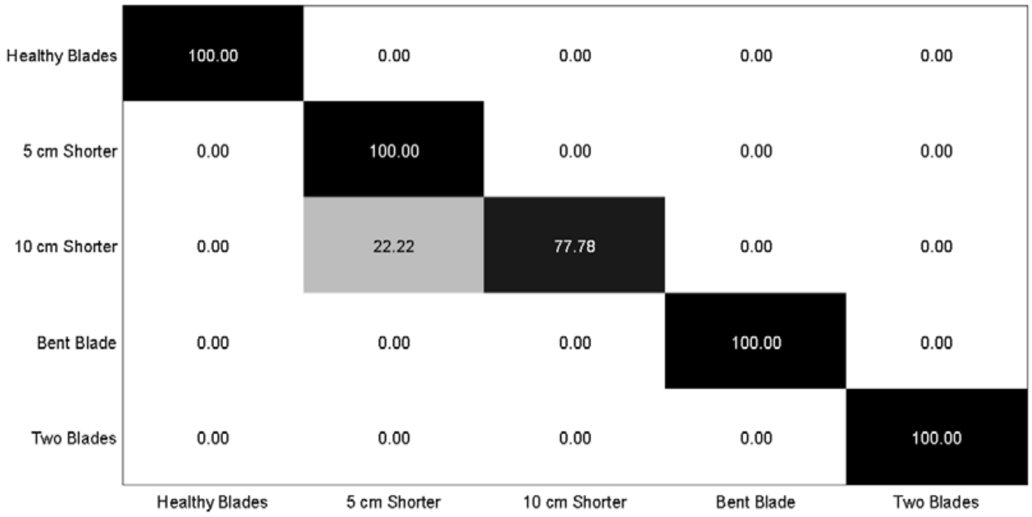

	Healthy Blades	5 cm Shorter	10 cm Shorter	Bent Blade	Two Blades
Healthy Blades	100.00	0.00	0.00	0.00	0.00
5 cm Shorter	0.00	100.00	0.00	0.00	0.00
10 cm Shorter	0.00	22.22	77.78	0.00	0.00
Bent Blade	0.00	0.00	0.00	100.00	0.00
Two Blades	0.00	0.00	0.00	0.00	100.00

(d)

Fig. 5.23: Confusion matrices, Exp1. Two principal components and (a) *k=5*, (b) *k=9*. Three principal components and (c) *k=5*, (d) *k=9*

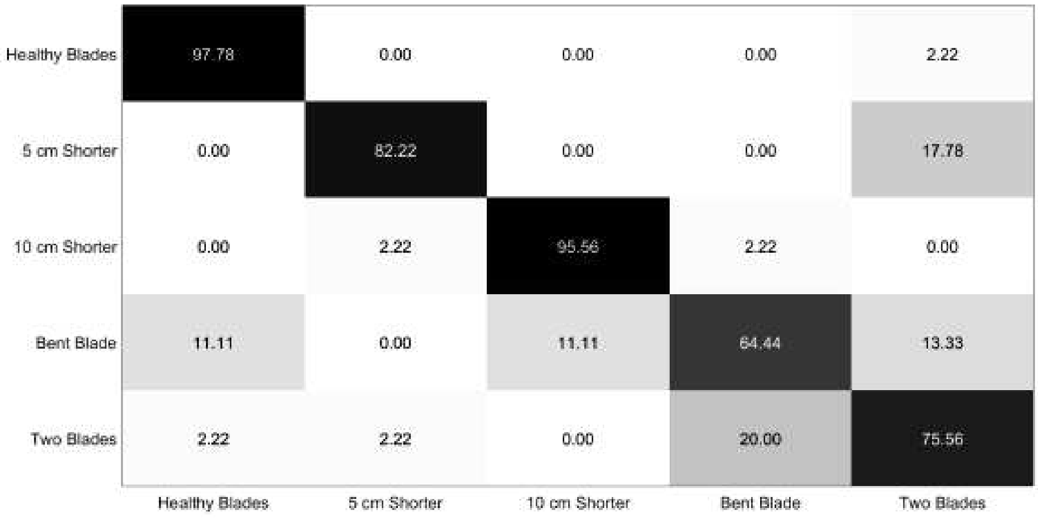

	Healthy Blades	5 cm Shorter	10 cm Shorter	Bent Blade	Two Blades
Healthy Blades	97.78	0.00	0.00	0.00	2.22
5 cm Shorter	0.00	82.22	0.00	0.00	17.78
10 cm Shorter	0.00	2.22	95.56	2.22	0.00
Bent Blade	11.11	0.00	11.11	64.44	13.33
Two Blades	2.22	2.22	0.00	20.00	75.56

(a)

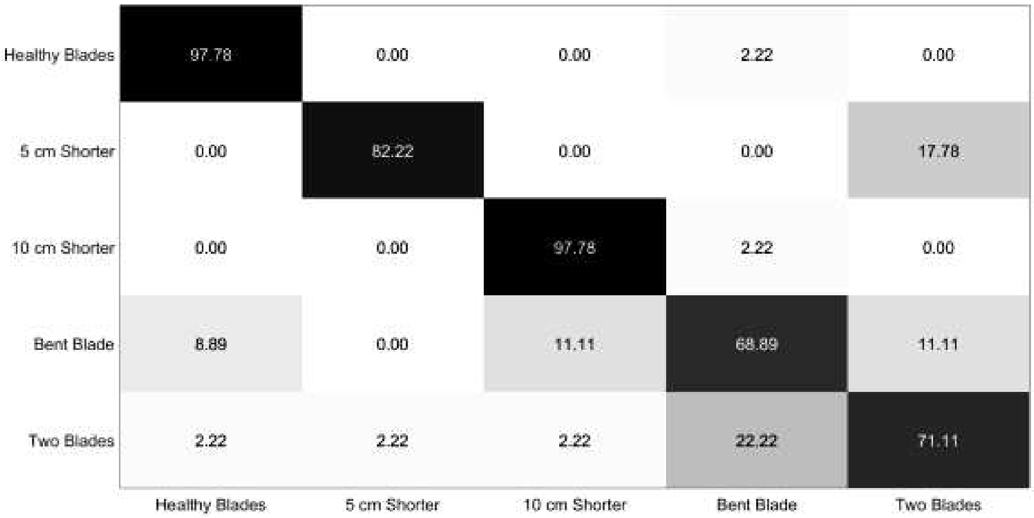

	Healthy Blades	5 cm Shorter	10 cm Shorter	Bent Blade	Two Blades
Healthy Blades	97.78	0.00	0.00	2.22	0.00
5 cm Shorter	0.00	82.22	0.00	0.00	17.78
10 cm Shorter	0.00	0.00	97.78	2.22	0.00
Bent Blade	8.89	0.00	11.11	68.89	11.11
Two Blades	2.22	2.22	2.22	22.22	71.11

(b)

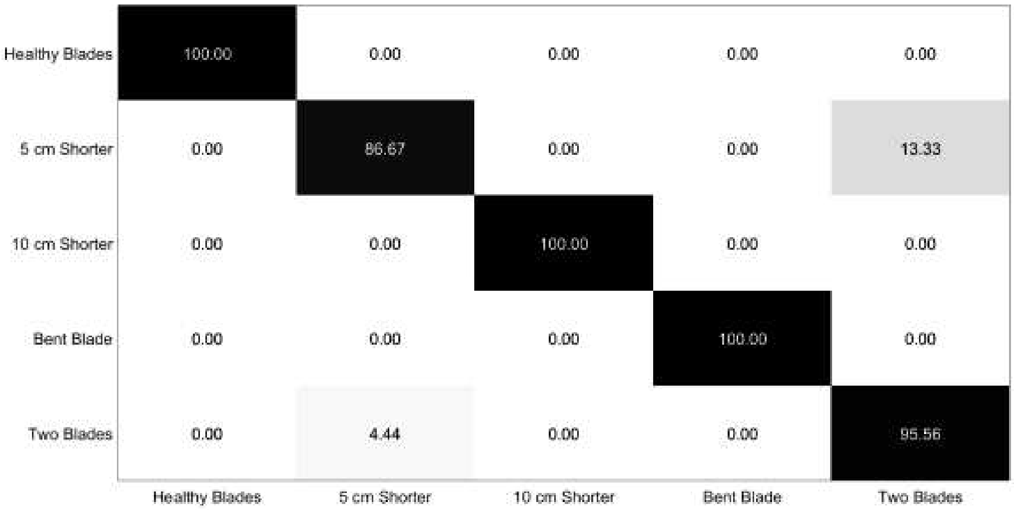

	Healthy Blades	5 cm Shorter	10 cm Shorter	Bent Blade	Two Blades
Healthy Blades	100.00	0.00	0.00	0.00	0.00
5 cm Shorter	0.00	86.67	0.00	0.00	13.33
10 cm Shorter	0.00	0.00	100.00	0.00	0.00
Bent Blade	0.00	0.00	0.00	100.00	0.00
Two Blades	0.00	4.44	0.00	0.00	95.56

(c)

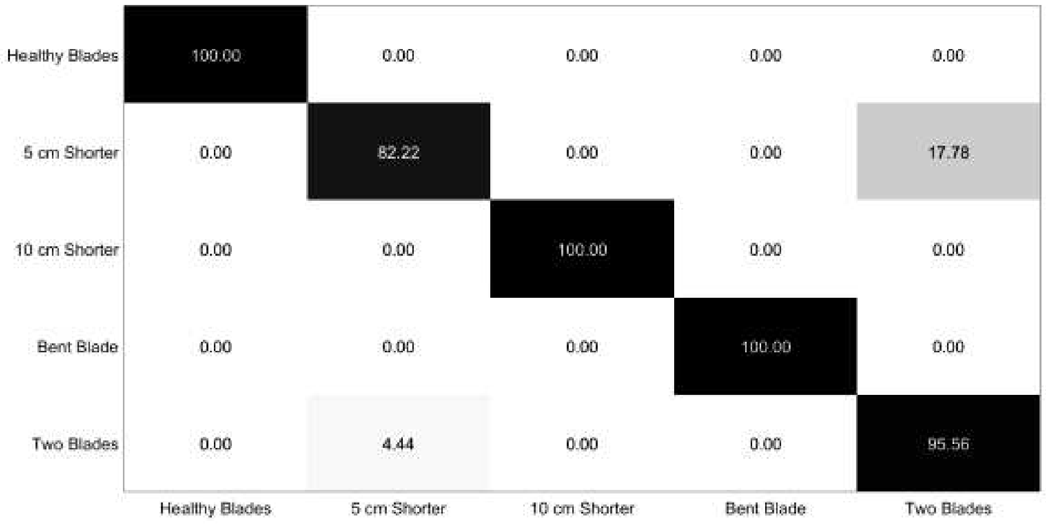

	Healthy Blades	5 cm Shorter	10 cm Shorter	Bent Blade	Two Blades
Healthy Blades	100.00	0.00	0.00	0.00	0.00
5 cm Shorter	0.00	82.22	0.00	0.00	17.78
10 cm Shorter	0.00	0.00	100.00	0.00	0.00
Bent Blade	0.00	0.00	0.00	100.00	0.00
Two Blades	0.00	4.44	0.00	0.00	95.56

(d)

Fig. 5.24: Confusion matrices, Exp2. Two principal components and (a) *k=5*, (b) *k=9*. Three principal components and (c) *k=5*, (d) *k=9*

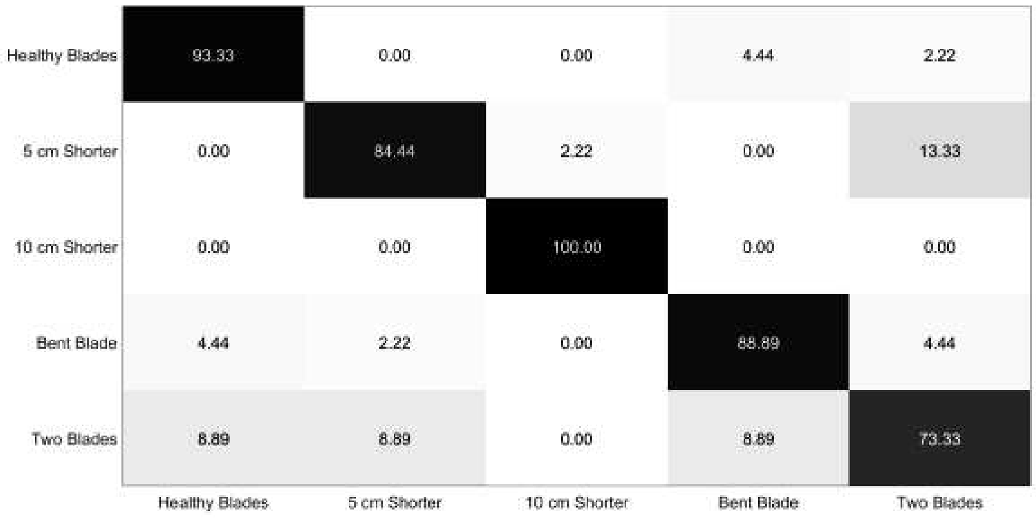

	Healthy Blades	5 cm Shorter	10 cm Shorter	Bent Blade	Two Blades
Healthy Blades	93.33	0.00	0.00	4.44	2.22
5 cm Shorter	0.00	84.44	2.22	0.00	13.33
10 cm Shorter	0.00	0.00	100.00	0.00	0.00
Bent Blade	4.44	2.22	0.00	88.89	4.44
Two Blades	8.89	8.89	0.00	8.89	73.33

(a)

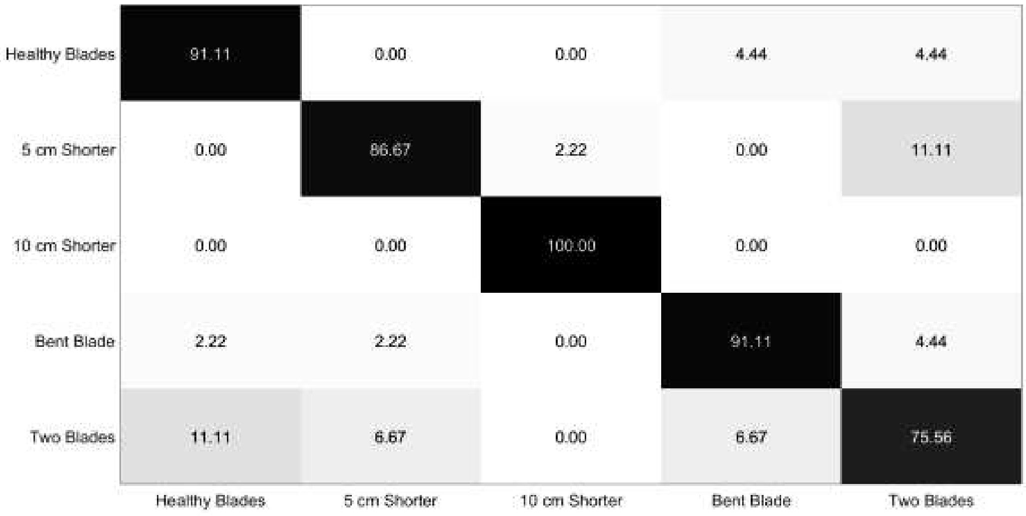

	Healthy Blades	5 cm Shorter	10 cm Shorter	Bent Blade	Two Blades
Healthy Blades	91.11	0.00	0.00	4.44	4.44
5 cm Shorter	0.00	86.67	2.22	0.00	11.11
10 cm Shorter	0.00	0.00	100.00	0.00	0.00
Bent Blade	2.22	2.22	0.00	91.11	4.44
Two Blades	11.11	6.67	0.00	6.67	75.56

(b)

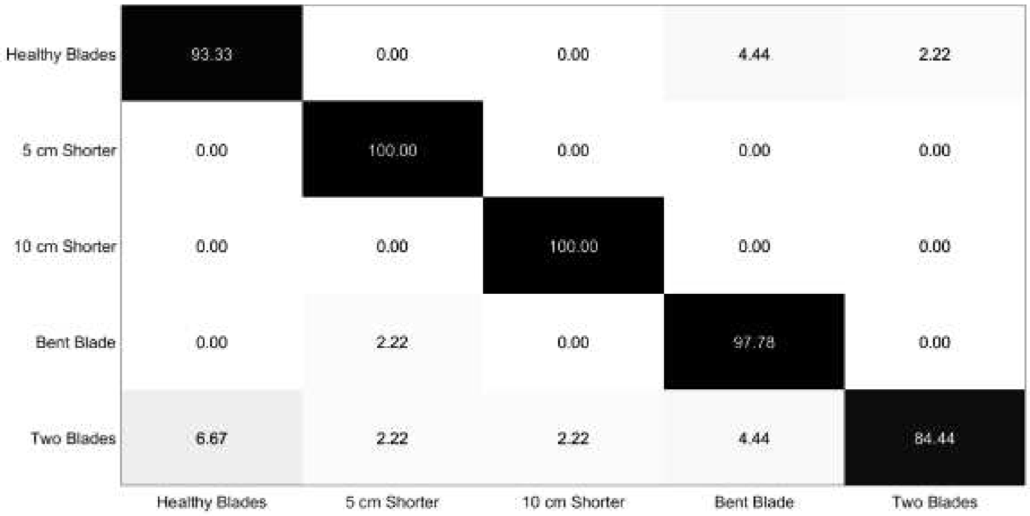

	Healthy Blades	5 cm Shorter	10 cm Shorter	Bent Blade	Two Blades
Healthy Blades	93.33	0.00	0.00	4.44	2.22
5 cm Shorter	0.00	100.00	0.00	0.00	0.00
10 cm Shorter	0.00	0.00	100.00	0.00	0.00
Bent Blade	0.00	2.22	0.00	97.78	0.00
Two Blades	6.67	2.22	2.22	4.44	84.44

(c)

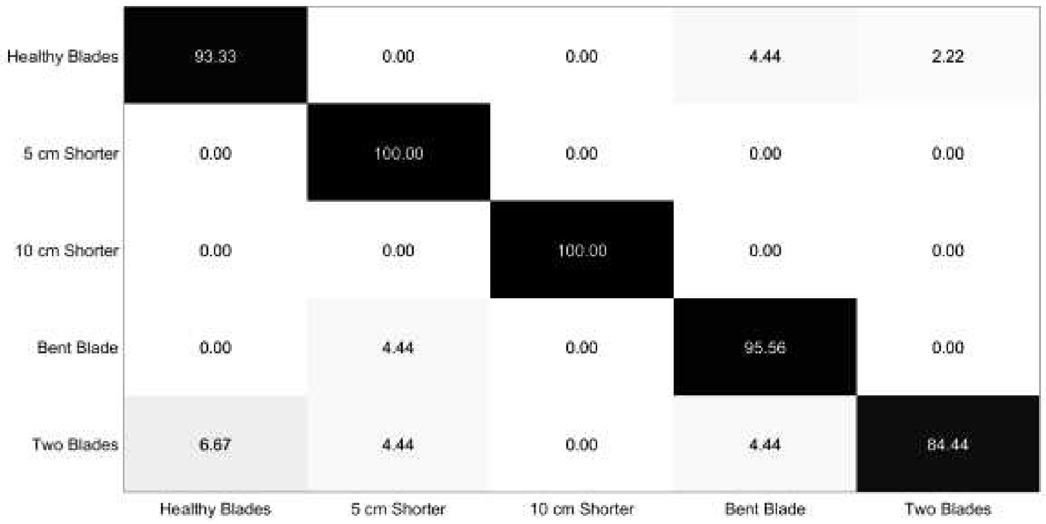

	Healthy Blades	5 cm Shorter	10 cm Shorter	Bent Blade	Two Blades
Healthy Blades	93.33	0.00	0.00	4.44	2.22
5 cm Shorter	0.00	100.00	0.00	0.00	0.00
10 cm Shorter	0.00	0.00	100.00	0.00	0.00
Bent Blade	0.00	4.44	0.00	95.56	0.00
Two Blades	6.67	4.44	0.00	4.44	84.44

(d)

Fig. 5.25: Confusion matrices, Exp3. Two principal components and (a) *k=5*, (b) *k=9*. Three principal components and (c) *k=5*, (d) *k=9*

The graphs in Fig. 5.26 correspond to the features spaces when seven faults plus healthy blades are considered. The data form relatively compact clusters for each type of fault. However, the distinction between them is not clear when only two principal components are used (Fig. 5.26a).

The clusters can be distinguished better from each other when three principal components are taken into account (Fig. 5.26b), although there are overlapping regions.

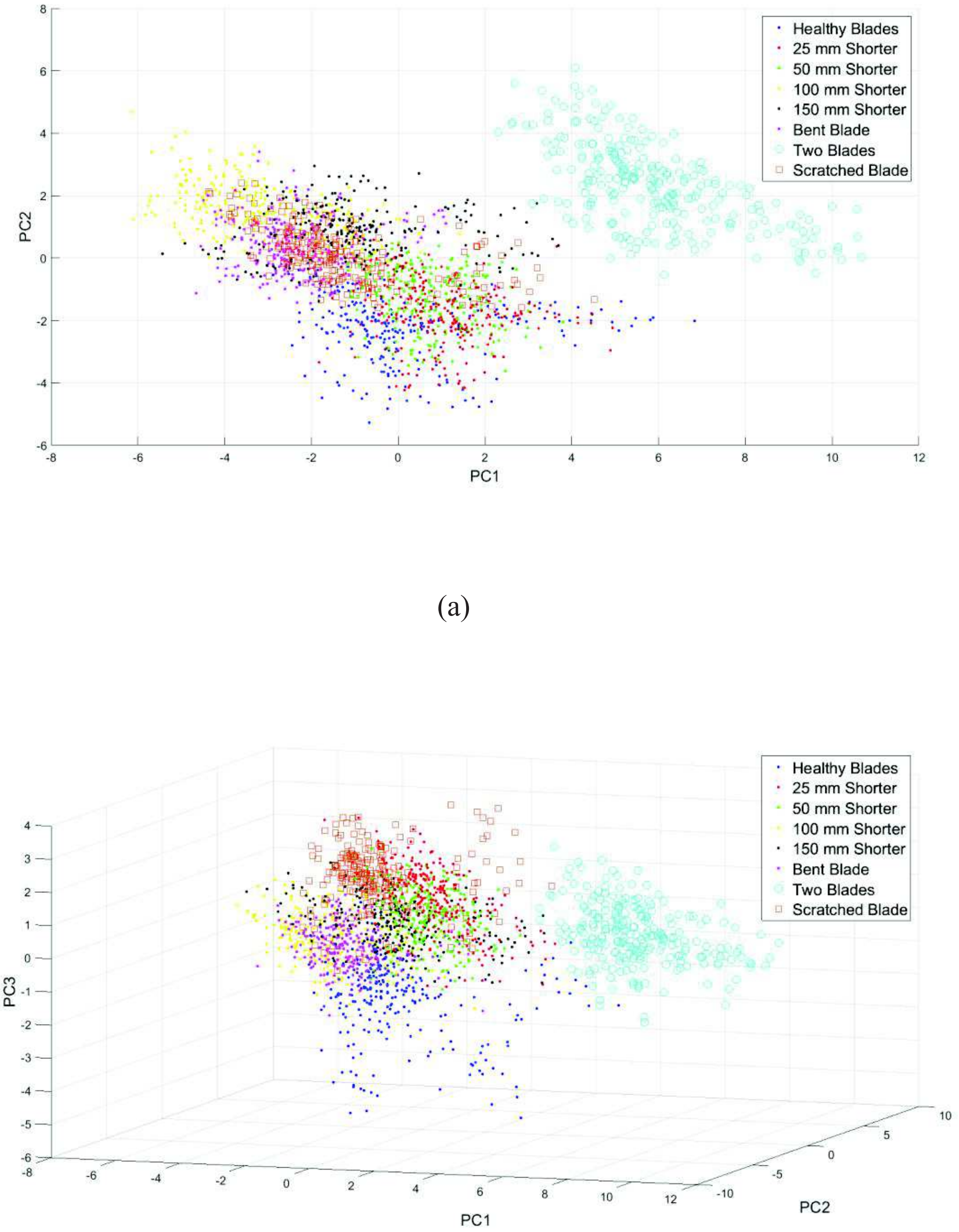

(a)

(b)

Fig. 5.26: PCA output. Seven faults and healthy blades. (a) Two principal components. (b) Three principal components.

Fig. 5.27 corresponds to the confusion matrices used to validate the accuracy of the k-NN classification when seven faults are considered. The performance of the classifier is not accurate when only two principal components are used (Fig. 5.27a-b). In fact, there is a high degree of misclassification between similar faults; for example, between the *2.5 cm shorter blade* and *5 cm shorter blade* classes. Increasing the number of neighbours (*k=5* in Fig. 5.27a and *k=9* in Fig. 5.27b) does not improve the results significantly. However, a better performance is obtained when three principal components are taken into account. There is a misclassification percentage in the *2.5 cm shorter blade* and *scratched blade* classes, but the degree of accuracy is more than 70% in the rest of the faults.

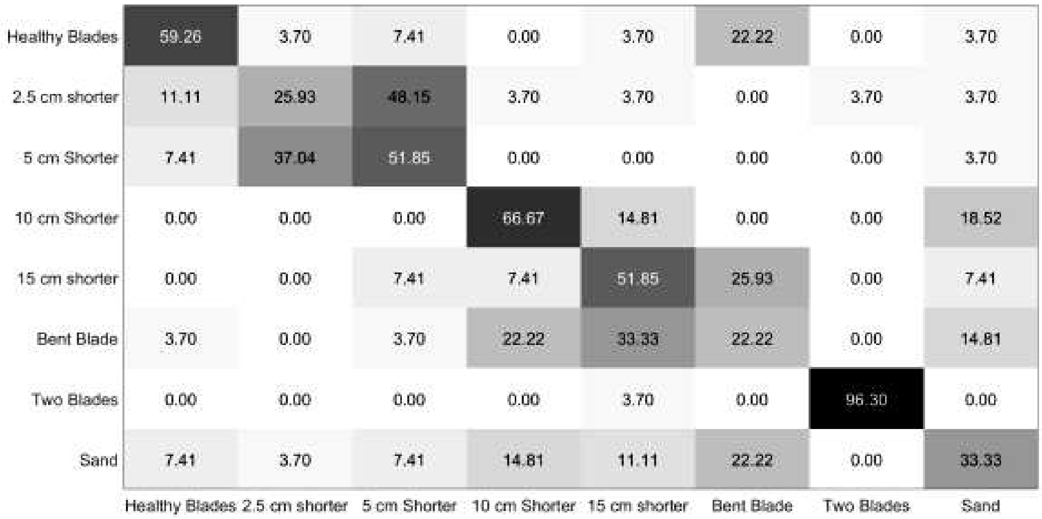

	Healthy Blades	2.5 cm shorter	5 cm Shorter	10 cm Shorter	15 cm shorter	Bent Blade	Two Blades	Sand
Healthy Blades	59.26	3.70	7.41	0.00	3.70	22.22	0.00	3.70
2.5 cm shorter	11.11	25.93	48.15	3.70	3.70	0.00	3.70	3.70
5 cm Shorter	7.41	37.04	51.85	0.00	0.00	0.00	0.00	3.70
10 cm Shorter	0.00	0.00	0.00	66.67	14.81	0.00	0.00	18.52
15 cm shorter	0.00	0.00	7.41	7.41	51.85	25.93	0.00	7.41
Bent Blade	3.70	0.00	3.70	22.22	33.33	22.22	0.00	14.81
Two Blades	0.00	0.00	0.00	0.00	3.70	0.00	96.30	0.00
Sand	7.41	3.70	7.41	14.81	11.11	22.22	0.00	33.33

(a)

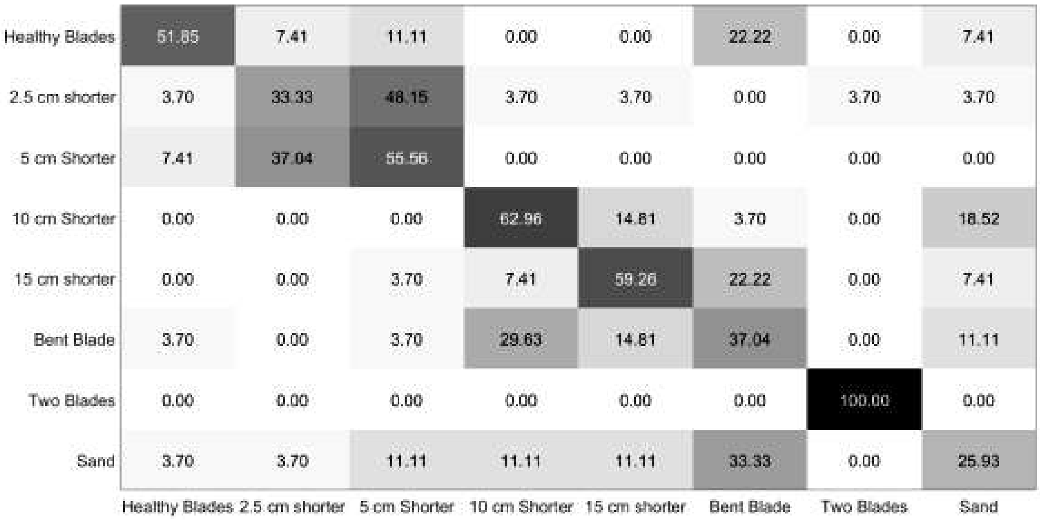

	Healthy Blades	2.5 cm shorter	5 cm Shorter	10 cm Shorter	15 cm shorter	Bent Blade	Two Blades	Sand
Healthy Blades	51.85	7.41	11.11	0.00	0.00	22.22	0.00	7.41
2.5 cm shorter	3.70	33.33	48.15	3.70	3.70	0.00	3.70	3.70
5 cm Shorter	7.41	37.04	55.56	0.00	0.00	0.00	0.00	0.00
10 cm Shorter	0.00	0.00	0.00	62.96	14.81	3.70	0.00	18.52
15 cm shorter	0.00	0.00	3.70	7.41	59.26	22.22	0.00	7.41
Bent Blade	3.70	0.00	3.70	29.63	14.81	37.04	0.00	11.11
Two Blades	0.00	0.00	0.00	0.00	0.00	0.00	100.00	0.00
Sand	3.70	3.70	11.11	11.11	11.11	33.33	0.00	25.93

(b)

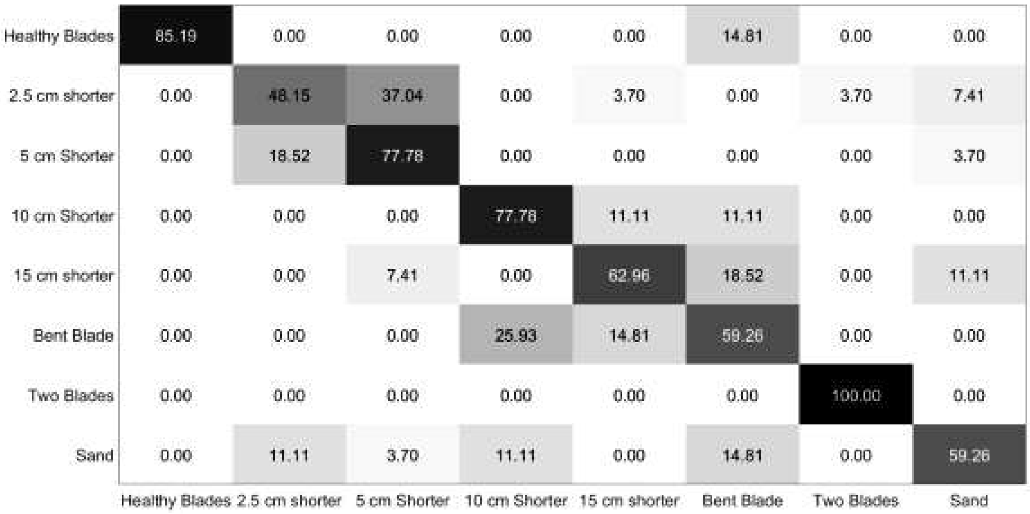

	Healthy Blades	2.5 cm shorter	5 cm Shorter	10 cm Shorter	15 cm shorter	Bent Blade	Two Blades	Sand
Healthy Blades	85.19	0.00	0.00	0.00	0.00	14.81	0.00	0.00
2.5 cm shorter	0.00	48.15	37.04	0.00	3.70	0.00	3.70	7.41
5 cm Shorter	0.00	18.52	77.78	0.00	0.00	0.00	0.00	3.70
10 cm Shorter	0.00	0.00	0.00	77.78	11.11	11.11	0.00	0.00
15 cm shorter	0.00	0.00	7.41	0.00	62.96	18.52	0.00	11.11
Bent Blade	0.00	0.00	0.00	25.93	14.81	59.26	0.00	0.00
Two Blades	0.00	0.00	0.00	0.00	0.00	0.00	100.00	0.00
Sand	0.00	11.11	3.70	11.11	0.00	14.81	0.00	59.26

(c)

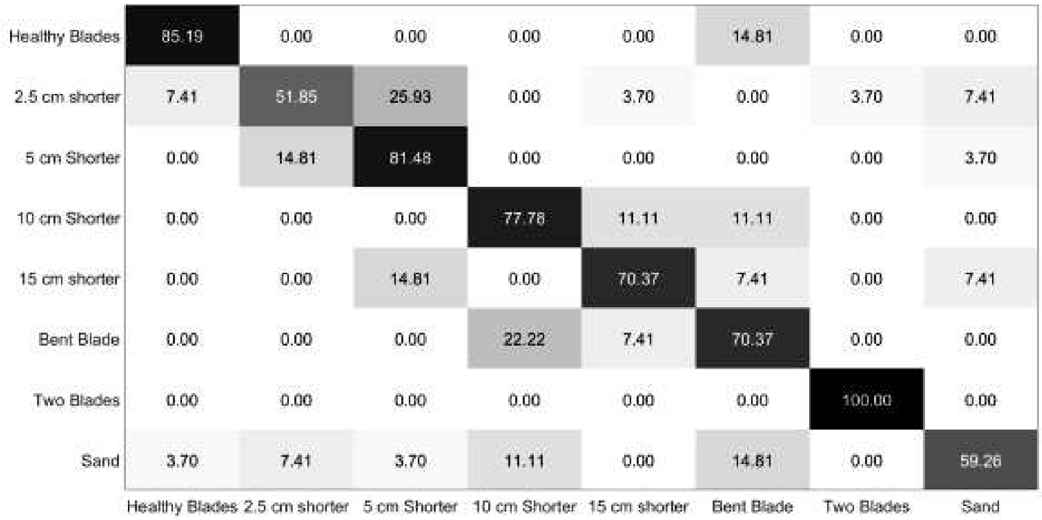

	Healthy Blades	2.5 cm shorter	5 cm Shorter	10 cm Shorter	15 cm shorter	Bent Blade	Two Blades	Sand
Healthy Blades	85.19	0.00	0.00	0.00	0.00	14.81	0.00	0.00
2.5 cm shorter	7.41	51.85	25.93	0.00	3.70	0.00	3.70	7.41
5 cm Shorter	0.00	14.81	81.48	0.00	0.00	0.00	0.00	3.70
10 cm Shorter	0.00	0.00	0.00	77.78	11.11	11.11	0.00	0.00
15 cm shorter	0.00	0.00	14.81	0.00	70.37	7.41	0.00	7.41
Bent Blade	0.00	0.00	0.00	22.22	7.41	70.37	0.00	0.00
Two Blades	0.00	0.00	0.00	0.00	0.00	0.00	100.00	0.00
Sand	3.70	7.41	3.70	11.11	0.00	14.81	0.00	59.26

(d)

Fig. 5.27: Confusion matrices, seven faults and healthy blades. Two principal components and (a) *k=5*, (b) *k=9*. Three principal components and (c) *k=5*, (d) *k=9*.

As was mentioned in the analysis of the results from SPM, a more robust classifier could be built by using several positions at the same time. Fig. 5.28 shows the PCA output when three different positions (Exp1, Exp2, Exp3) and four types of faults are considered. In this case, there are different subclusters for each type of fault. The exception is the *10 cm shorter blade* group whose data samples group well in a single cluster.

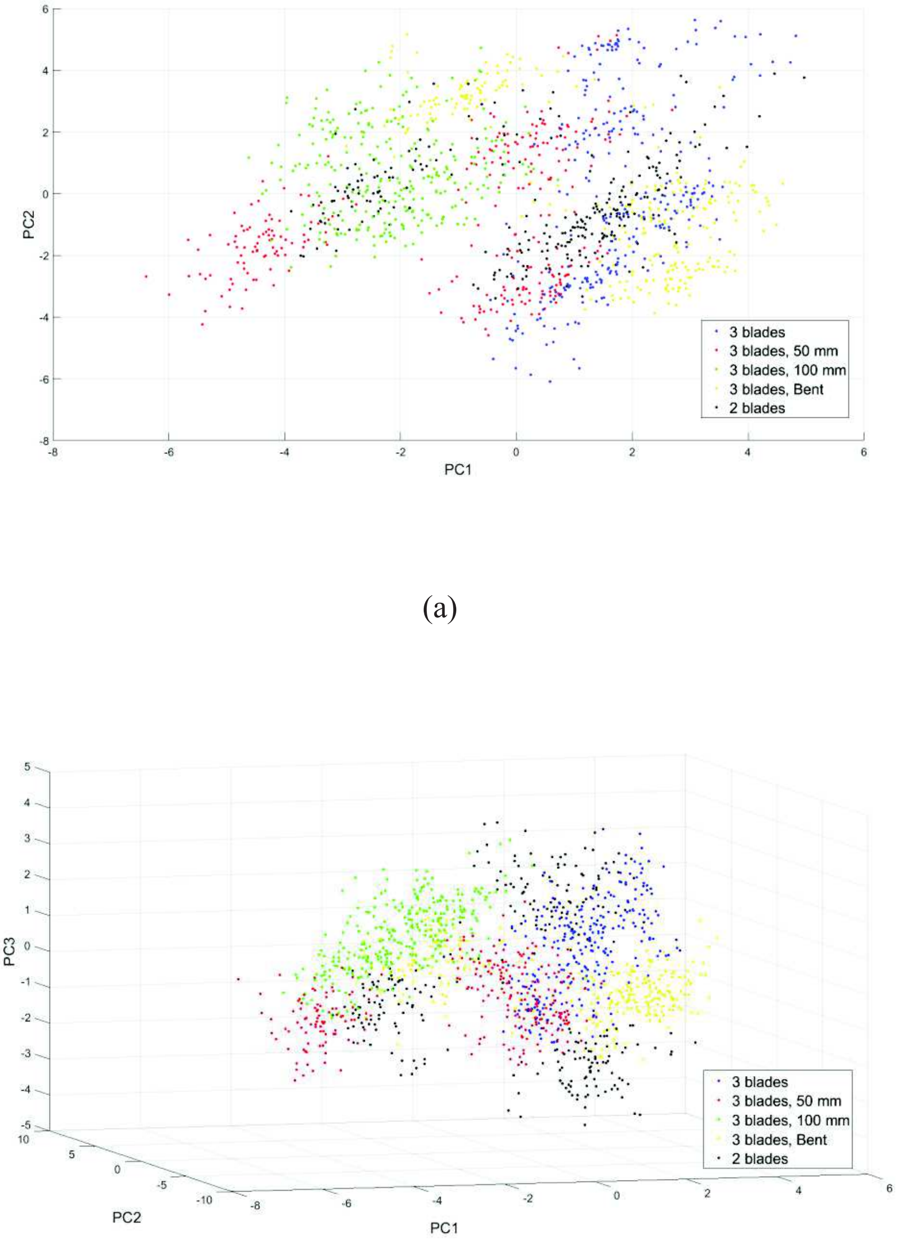

(a)

(b)

Fig. 5.28: PCA output. Three different positions and four types of faults. (a) Two principal components. (b) Three principal components.

Fig. 5.29 shows the confusion matrices used to validate the k-NN classification in this situation. In general, the degree of accuracy is more than 70% and the misclassification percentages are spread out between the different types of faults. This behaviour did not occur when a single position was considered. The reason for this may rely on the fact that the faults have one or several dense clusters and few samples in the space between. A test sample from a particular fault has more possibilities of falling well inside the correct cluster. However, statistically, there is a possibility that the test sample appears in the space between clusters and consequently it will be classified incorrectly as one of the other classes.

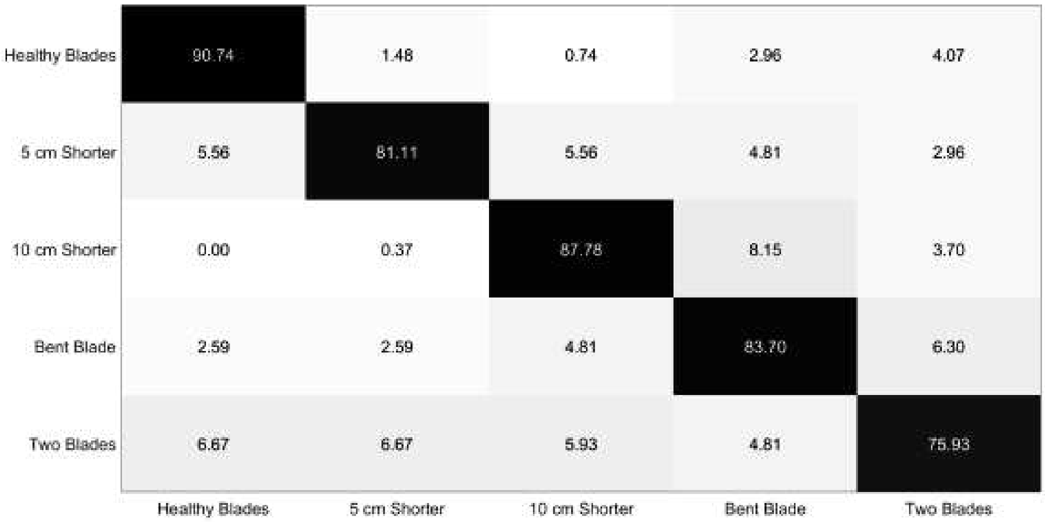

	Healthy Blades	5 cm Shorter	10 cm Shorter	Bent Blade	Two Blades
Healthy Blades	90.74	1.48	0.74	2.96	4.07
5 cm Shorter	5.56	81.11	5.56	4.81	2.96
10 cm Shorter	0.00	0.37	87.78	8.15	3.70
Bent Blade	2.59	2.59	4.81	83.70	6.30
Two Blades	6.67	6.67	5.93	4.81	75.93

(a)

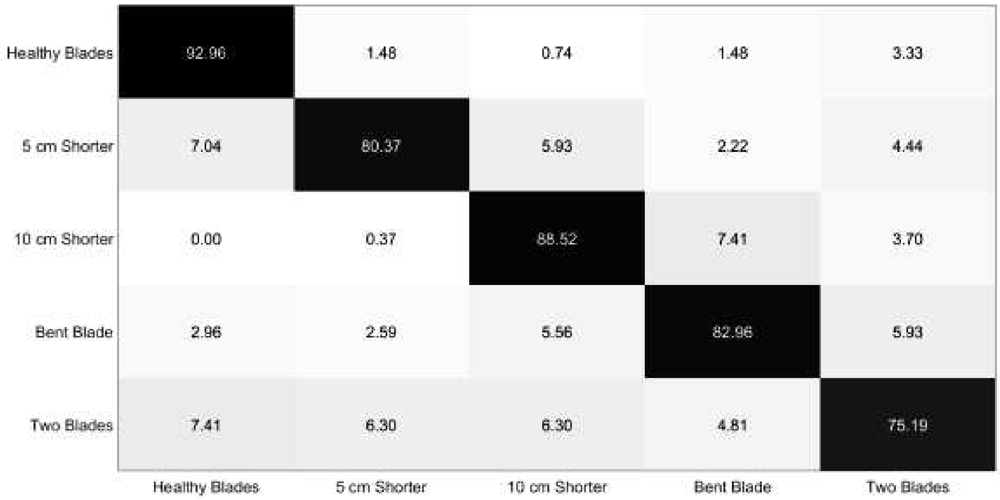

	Healthy Blades	5 cm Shorter	10 cm Shorter	Bent Blade	Two Blades
Healthy Blades	92.96	1.48	0.74	1.48	3.33
5 cm Shorter	7.04	80.37	5.93	2.22	4.44
10 cm Shorter	0.00	0.37	88.52	7.41	3.70
Bent Blade	2.96	2.59	5.56	82.96	5.93
Two Blades	7.41	6.30	6.30	4.81	75.19

(b)

Fig. 5.29: Confusion matrices. Three different positions WT-radar. *k=5*. (a) Two principal components. (b) Three principal components.

5.6 Classification of Wind Turbine Faults Using Artificial Neural-Network

The goal of a classification algorithm is to model the relationship between input and output data. The Neural-Network algorithm is a computational and mathematical model based on the biological process of a neuron [3]. A simple model of a neuron with multiple inputs can be mathematically expressed by

$$Y = f(1 + 2X_1 + 3X_2 + 5X_3 + 8X_4) \tag{5.9}$$

where Y is the *output* and X_1, X_2, X_3 and X_4 are the *input variables*. The 1 in equation (5.9) is the *bias* and the values *2, 3, 5* and *8* are the *weights*, w_i, of each input variable. Each input variable passes through a node in the *input layer* and it is multiplied by its weight. In the *output layer* all the weighted inputs and the bias are added by an *aggregation function* Σ forming the *net input* n of the *transfer function* f which produces the final neuron output Y. The graph in Fig. 5.30 represents the neuron model just described.

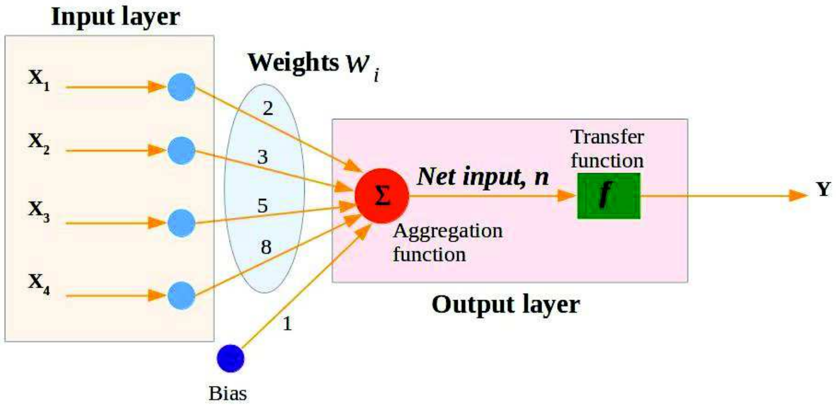

Fig. 5.30: Schematic model of a single neuron with several inputs.

The Neural-Network technique can model complex nonlinear relationships of the input variables and learn by some adaptive learning process [7]. This can be made by placing more layers called *hidden layers*. Fig. 5.31 shows a network with two layer apart from the input layer. The number of inputs is R. These are weighted by $w_{i,j,k}$, where i is the index for the hidden layer (1st layer, 2nd layer, etc.), j corresponds to the neuron in the hidden layer and k is the input index. These weighted inputs and the bias are added together by the corresponding aggregation function of each neuron in the hidden layer - for the sake of clarity, the different bias have not been plotted in Fig. 5.31.

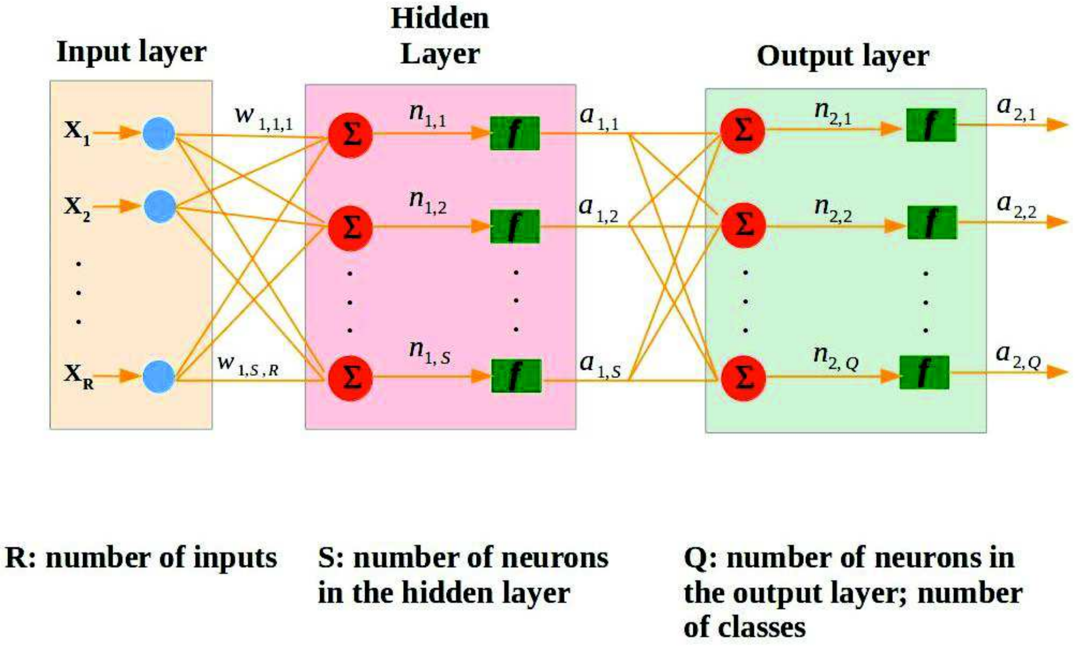

Fig. 5.31: Diagram of a neural network with two layers.

The number of neurons in the hidden layer is *S*. The outputs of the aggregation functions, the net inputs $n_{i,j}$, feed the transfer functions f. The results obtained from the transfer functions are $a_{i,j}$ which serve as inputs for the output layer. The indices for the net inputs and the transfer function outputs are the same: i is the index that labels the neuron layer (1 corresponds to the hidden layer in Fig. 5.31) and $j$is the corresponding neuron. The output layer has Q neurons with their own aggregation and transfer functions. The number of neurons in the output layer corresponds to the number of categories or classes to classify.

The Neural-Network algorithm is a more sophisticated classification technique compared to the k-NN. In order to build the network, the transfer functions in the hidden and output layers has to be chosen to fulfill the particularities of the system that the neural network is analysing.

Among the variety of transfer functions, the sigmoid function was used in the hidden layers of the neural network. This function combines nearly linear behaviour, non-linear behaviour and almost constant behaviour. Fig. 5.32 corresponds to the graph of the sigmoid function $f(x) = 1/(1 + e^{-x})$. As it can be seen, the behaviour of $f(x)$ depends on the value of x.Values of x in the centre of the domain produce a linear response while values of x in the extreme of the domain produce nearly constant response. Theoretically, the sigmoid function takes any real value as input and it squashes the output to the range 0-1. The sigmoid function represents many natural processes: rapid response in the beginning and stable response afterwards.

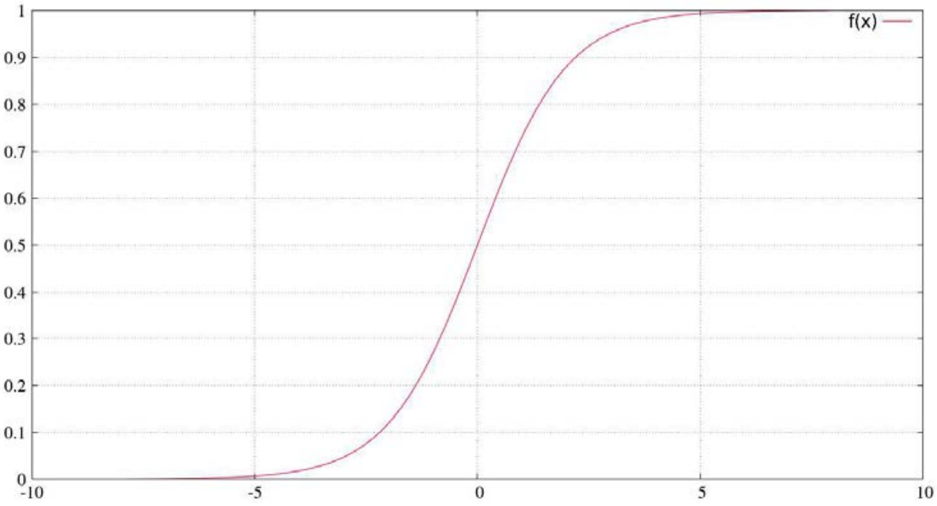

Fig. 5.32: Sigmoid function $f(x) = 1/(1 + e^{-x})$

The softmax function was employed in the output layer [7]-[9]. This transfer function is often used in artificial neural networks for multi-class classification, as it is the aim of this dissertation. The softmax function has the form $f(n_i) = exp(n_i)/\sum_{j=1}^{Q} exp(n_j)$, where n_i are the net inputs in the output layer. The total number of these inputs is Q which is the number of categories or faults. In the case of this transfer function, each neuron output is affected by all the net inputs n_i. The outputs of the softmax transfer function can be understood as the probabilities associated with each class. Each output will fall between 0 and 1, and the sum of the outputs will be 1 [9].

The sigmoid and softmax functions are available in the Neural-Networks MATLAB toolbox, so this tool was used to create the network. A two-layer feedforward network was built for the classification problem addressed here. The number of neurons in the hidden layer was set to 10 which provided satisfactory results and a computationally efficient algorithm. The network was trained using the scaled conjugate gradient backpropagation algorithm [10]. The features used in previous sections (statistical parameters and PSDs) were the inputs employed here to feed the network.

5.6.1 Statistical Parameters as Input for the Neural Network.

The three parameters of the signals used in section 5.4 (power, mean amplitude and standard deviation) were used as inputs for the neural network. The same database (same experiments) was used. 80% of the data points formed the training set, 10% was used to validate the results and the last 10% formed the test dataset to assess the performance of the network. Fig. 5.33 corresponds to the confusion matrices for training, validation, testing and overall accuracy for each of the three different experiments using four types of faults (Exp1, Exp2, Exp3). The results show that the degree of correct classification is more than 95%; the results are similar to those obtained with the k-NN algorithm.

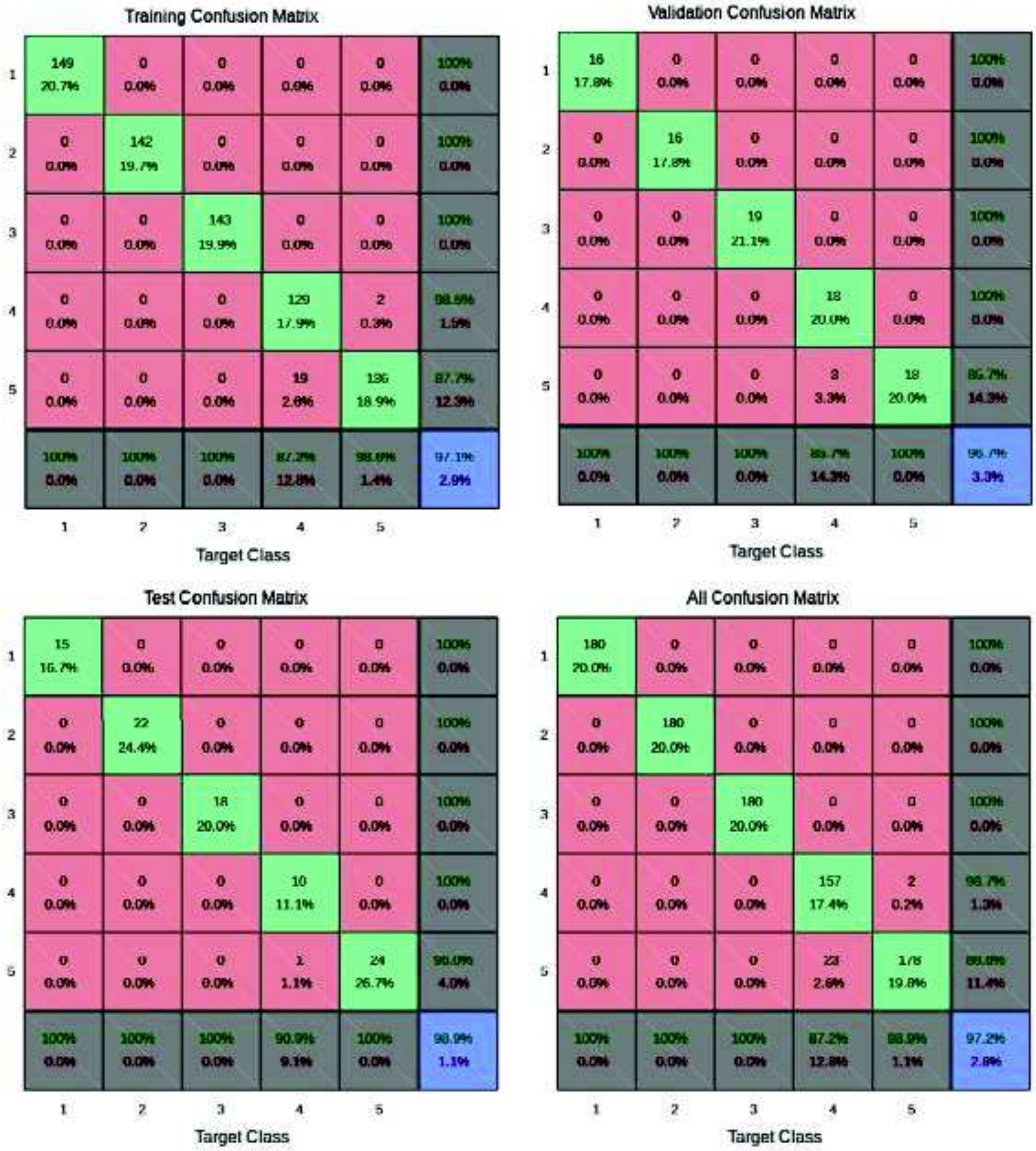

Training Confusion Matrix

1	149 20.7%	0 0.0%	0 0.0%	0 0.0%	0 0.0%	100% 0.0%
2	0 0.0%	142 19.7%	0 0.0%	0 0.0%	0 0.0%	100% 0.0%
3	0 0.0%	0 0.0%	143 19.9%	0 0.0%	0 0.0%	100% 0.0%
4	0 0.0%	0 0.0%	0 0.0%	129 17.9%	2 0.3%	98.5% 1.5%
5	0 0.0%	0 0.0%	0 0.0%	19 2.6%	136 18.9%	87.7% 12.3%
	100% 0.0%	100% 0.0%	100% 0.0%	87.2% 12.8%	98.6% 1.4%	97.1% 2.9%
	1	2	3	4	5	

Target Class

Validation Confusion Matrix

1	16 17.8%	0 0.0%	0 0.0%	0 0.0%	0 0.0%	100% 0.0%
2	0 0.0%	16 17.8%	0 0.0%	0 0.0%	0 0.0%	100% 0.0%
3	0 0.0%	0 0.0%	19 21.1%	0 0.0%	0 0.0%	100% 0.0%
4	0 0.0%	0 0.0%	0 0.0%	18 20.0%	0 0.0%	100% 0.0%
5	0 0.0%	0 0.0%	0 0.0%	3 3.3%	18 20.0%	85.7% 14.3%
	100% 0.0%	100% 0.0%	100% 0.0%	85.7% 14.3%	100% 0.0%	96.7% 3.3%
	1	2	3	4	5	

Target Class

Test Confusion Matrix

1	15 16.7%	0 0.0%	0 0.0%	0 0.0%	0 0.0%	100% 0.0%
2	0 0.0%	22 24.4%	0 0.0%	0 0.0%	0 0.0%	100% 0.0%
3	0 0.0%	0 0.0%	18 20.0%	0 0.0%	0 0.0%	100% 0.0%
4	0 0.0%	0 0.0%	0 0.0%	10 11.1%	0 0.0%	100% 0.0%
5	0 0.0%	0 0.0%	0 0.0%	1 1.1%	24 26.7%	96.0% 4.0%
	100% 0.0%	100% 0.0%	100% 0.0%	90.9% 9.1%	100% 0.0%	98.9% 1.1%
	1	2	3	4	5	

Target Class

All Confusion Matrix

1	180 20.0%	0 0.0%	0 0.0%	0 0.0%	0 0.0%	100% 0.0%
2	0 0.0%	180 20.0%	0 0.0%	0 0.0%	0 0.0%	100% 0.0%
3	0 0.0%	0 0.0%	180 20.0%	0 0.0%	0 0.0%	100% 0.0%
4	0 0.0%	0 0.0%	0 0.0%	157 17.4%	2 0.2%	98.7% 1.3%
5	0 0.0%	0 0.0%	0 0.0%	23 2.6%	178 19.8%	88.6% 11.4%
	100% 0.0%	100% 0.0%	100% 0.0%	87.2% 12.8%	98.9% 1.1%	97.2% 2.8%
	1	2	3	4	5	

Target Class

(a)

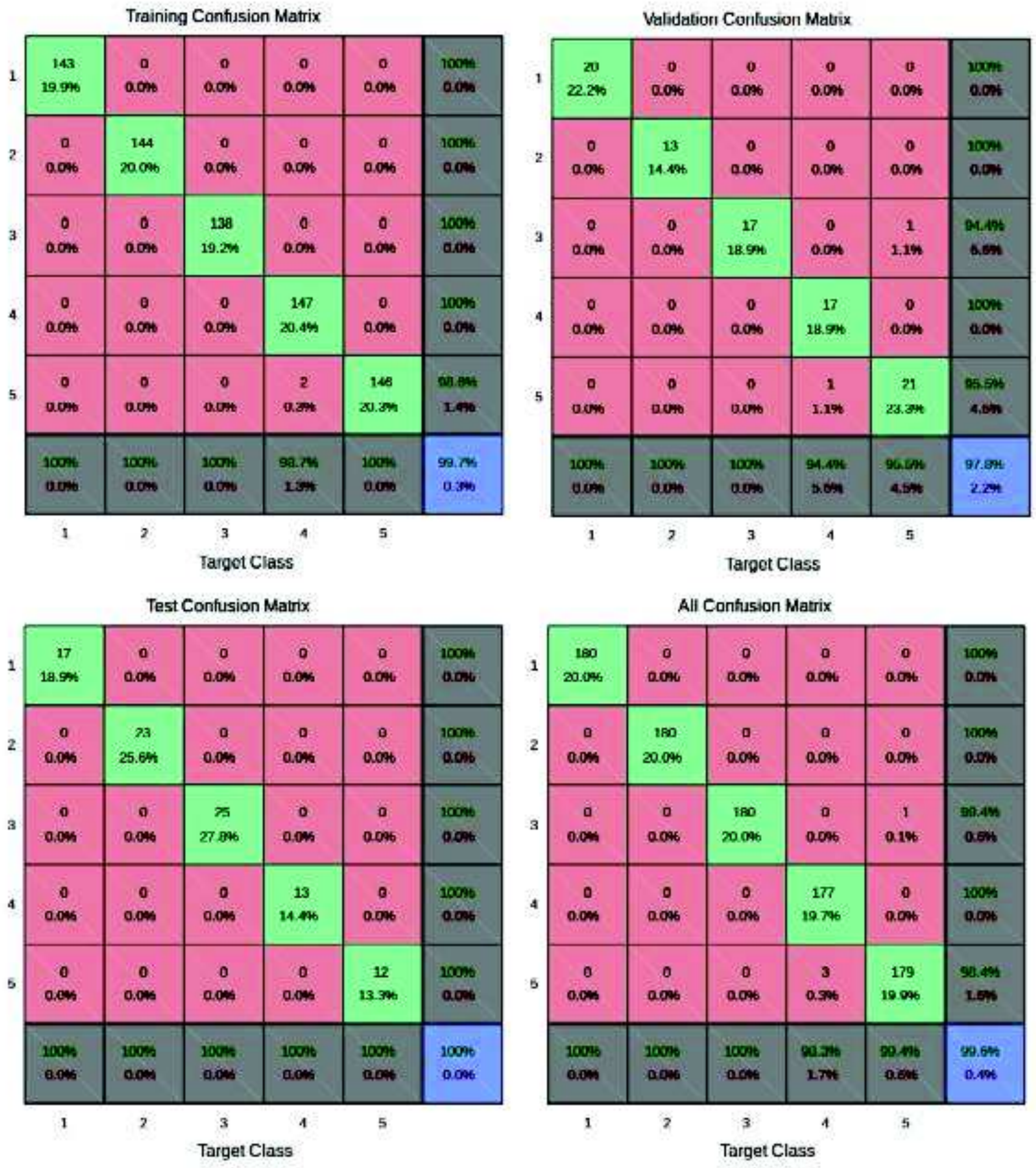

Training Confusion Matrix

	1	2	3	4	5	
1	143 19.9%	0 0.0%	0 0.0%	0 0.0%	0 0.0%	100% 0.0%
2	0 0.0%	144 20.0%	0 0.0%	0 0.0%	0 0.0%	100% 0.0%
3	0 0.0%	0 0.0%	138 19.2%	0 0.0%	0 0.0%	100% 0.0%
4	0 0.0%	0 0.0%	0 0.0%	147 20.4%	0 0.0%	100% 0.0%
5	0 0.0%	0 0.0%	0 0.0%	2 0.3%	146 20.3%	98.6% 1.4%
	100% 0.0%	100% 0.0%	100% 0.0%	98.7% 1.3%	100% 0.0%	99.7% 0.3%

Target Class

Validation Confusion Matrix

	1	2	3	4	5	
1	20 22.2%	0 0.0%	0 0.0%	0 0.0%	0 0.0%	100% 0.0%
2	0 0.0%	13 14.4%	0 0.0%	0 0.0%	0 0.0%	100% 0.0%
3	0 0.0%	0 0.0%	17 18.9%	0 0.0%	1 1.1%	94.4% 5.6%
4	0 0.0%	0 0.0%	0 0.0%	17 18.9%	0 0.0%	100% 0.0%
5	0 0.0%	0 0.0%	0 0.0%	1 1.1%	21 23.3%	95.5% 4.5%
	100% 0.0%	100% 0.0%	100% 0.0%	94.4% 5.6%	95.5% 4.5%	97.8% 2.2%

Target Class

Test Confusion Matrix

	1	2	3	4	5	
1	17 18.9%	0 0.0%	0 0.0%	0 0.0%	0 0.0%	100% 0.0%
2	0 0.0%	23 25.6%	0 0.0%	0 0.0%	0 0.0%	100% 0.0%
3	0 0.0%	0 0.0%	25 27.8%	0 0.0%	0 0.0%	100% 0.0%
4	0 0.0%	0 0.0%	0 0.0%	13 14.4%	0 0.0%	100% 0.0%
5	0 0.0%	0 0.0%	0 0.0%	0 0.0%	12 13.3%	100% 0.0%
	100% 0.0%	100% 0.0%	100% 0.0%	100% 0.0%	100% 0.0%	100% 0.0%

Target Class

All Confusion Matrix

	1	2	3	4	5	
1	180 20.0%	0 0.0%	0 0.0%	0 0.0%	0 0.0%	100% 0.0%
2	0 0.0%	180 20.0%	0 0.0%	0 0.0%	0 0.0%	100% 0.0%
3	0 0.0%	0 0.0%	180 20.0%	0 0.0%	1 0.1%	99.4% 0.6%
4	0 0.0%	0 0.0%	0 0.0%	177 19.7%	0 0.0%	100% 0.0%
5	0 0.0%	0 0.0%	0 0.0%	3 0.3%	179 19.9%	98.4% 1.6%
	100% 0.0%	100% 0.0%	100% 0.0%	98.3% 1.7%	99.4% 0.6%	99.6% 0.4%

Target Class

(b)

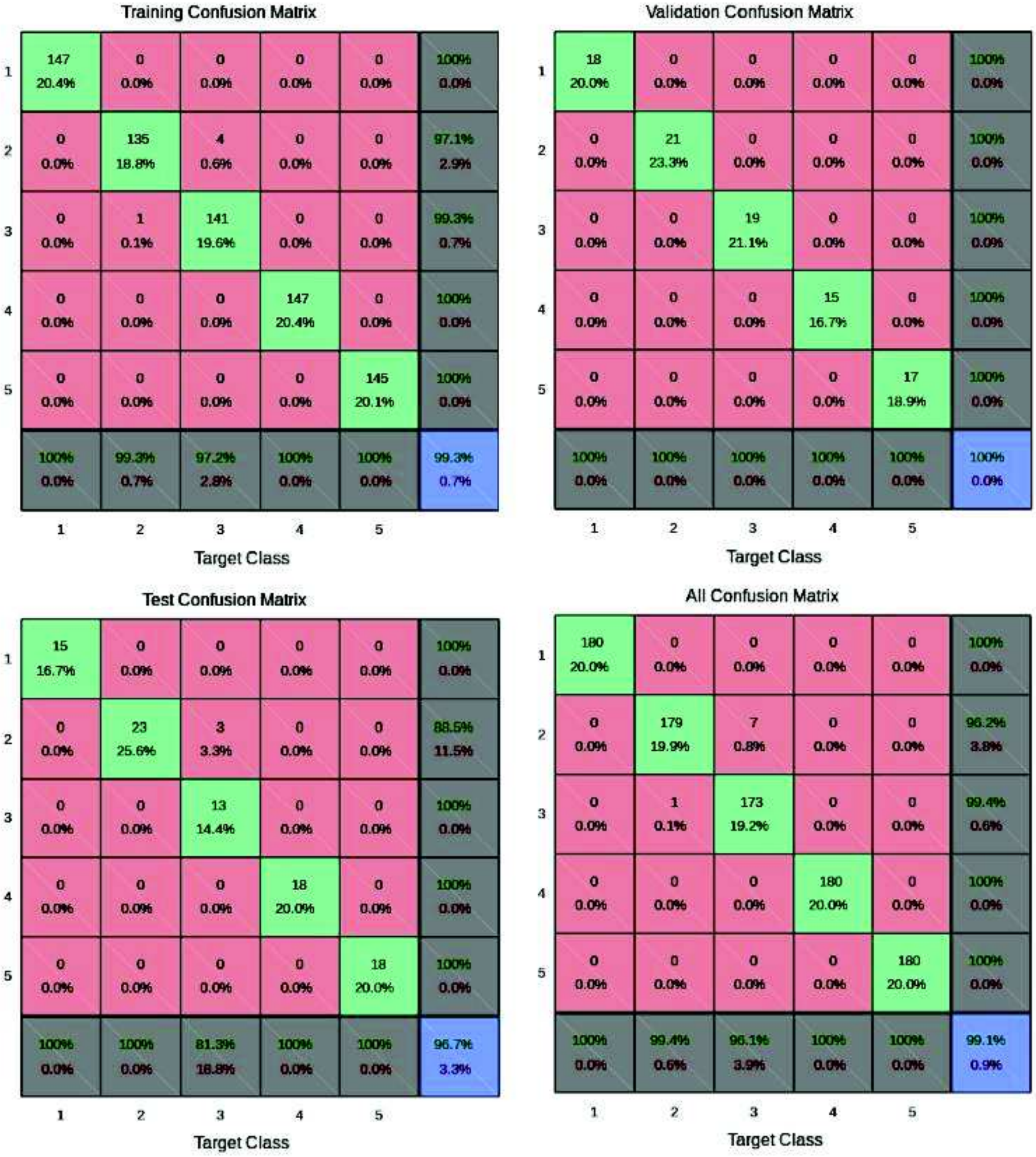

Training Confusion Matrix

	1	2	3	4	5	
1	147 20.4%	0 0.0%	0 0.0%	0 0.0%	0 0.0%	100% 0.0%
2	0 0.0%	135 18.8%	4 0.6%	0 0.0%	0 0.0%	97.1% 2.9%
3	0 0.0%	1 0.1%	141 19.6%	0 0.0%	0 0.0%	99.3% 0.7%
4	0 0.0%	0 0.0%	0 0.0%	147 20.4%	0 0.0%	100% 0.0%
5	0 0.0%	0 0.0%	0 0.0%	0 0.0%	145 20.1%	100% 0.0%
	100% 0.0%	99.3% 0.7%	97.2% 2.8%	100% 0.0%	100% 0.0%	99.3% 0.7%

Target Class

Validation Confusion Matrix

	1	2	3	4	5	
1	18 20.0%	0 0.0%	0 0.0%	0 0.0%	0 0.0%	100% 0.0%
2	0 0.0%	21 23.3%	0 0.0%	0 0.0%	0 0.0%	100% 0.0%
3	0 0.0%	0 0.0%	19 21.1%	0 0.0%	0 0.0%	100% 0.0%
4	0 0.0%	0 0.0%	0 0.0%	15 16.7%	0 0.0%	100% 0.0%
5	0 0.0%	0 0.0%	0 0.0%	0 0.0%	17 18.9%	100% 0.0%
	100% 0.0%	100% 0.0%	100% 0.0%	100% 0.0%	100% 0.0%	100% 0.0%

Target Class

Test Confusion Matrix

	1	2	3	4	5	
1	15 16.7%	0 0.0%	0 0.0%	0 0.0%	0 0.0%	100% 0.0%
2	0 0.0%	23 25.6%	3 3.3%	0 0.0%	0 0.0%	88.5% 11.5%
3	0 0.0%	0 0.0%	13 14.4%	0 0.0%	0 0.0%	100% 0.0%
4	0 0.0%	0 0.0%	0 0.0%	18 20.0%	0 0.0%	100% 0.0%
5	0 0.0%	0 0.0%	0 0.0%	0 0.0%	18 20.0%	100% 0.0%
	100% 0.0%	100% 0.0%	81.3% 18.8%	100% 0.0%	100% 0.0%	96.7% 3.3%

Target Class

All Confusion Matrix

	1	2	3	4	5	
1	180 20.0%	0 0.0%	0 0.0%	0 0.0%	0 0.0%	100% 0.0%
2	0 0.0%	179 19.9%	7 0.8%	0 0.0%	0 0.0%	96.2% 3.8%
3	0 0.0%	1 0.1%	173 19.2%	0 0.0%	0 0.0%	99.4% 0.6%
4	0 0.0%	0 0.0%	0 0.0%	180 20.0%	0 0.0%	100% 0.0%
5	0 0.0%	0 0.0%	0 0.0%	0 0.0%	180 20.0%	100% 0.0%
	100% 0.0%	99.4% 0.6%	96.1% 3.9%	100% 0.0%	100% 0.0%	99.1% 0.9%

Target Class

(c)

Fig. 5.33: Neural network confusion matrices. Three statistical parameters as input. (a) Exp1, (b) Exp2 and (c) Exp3.

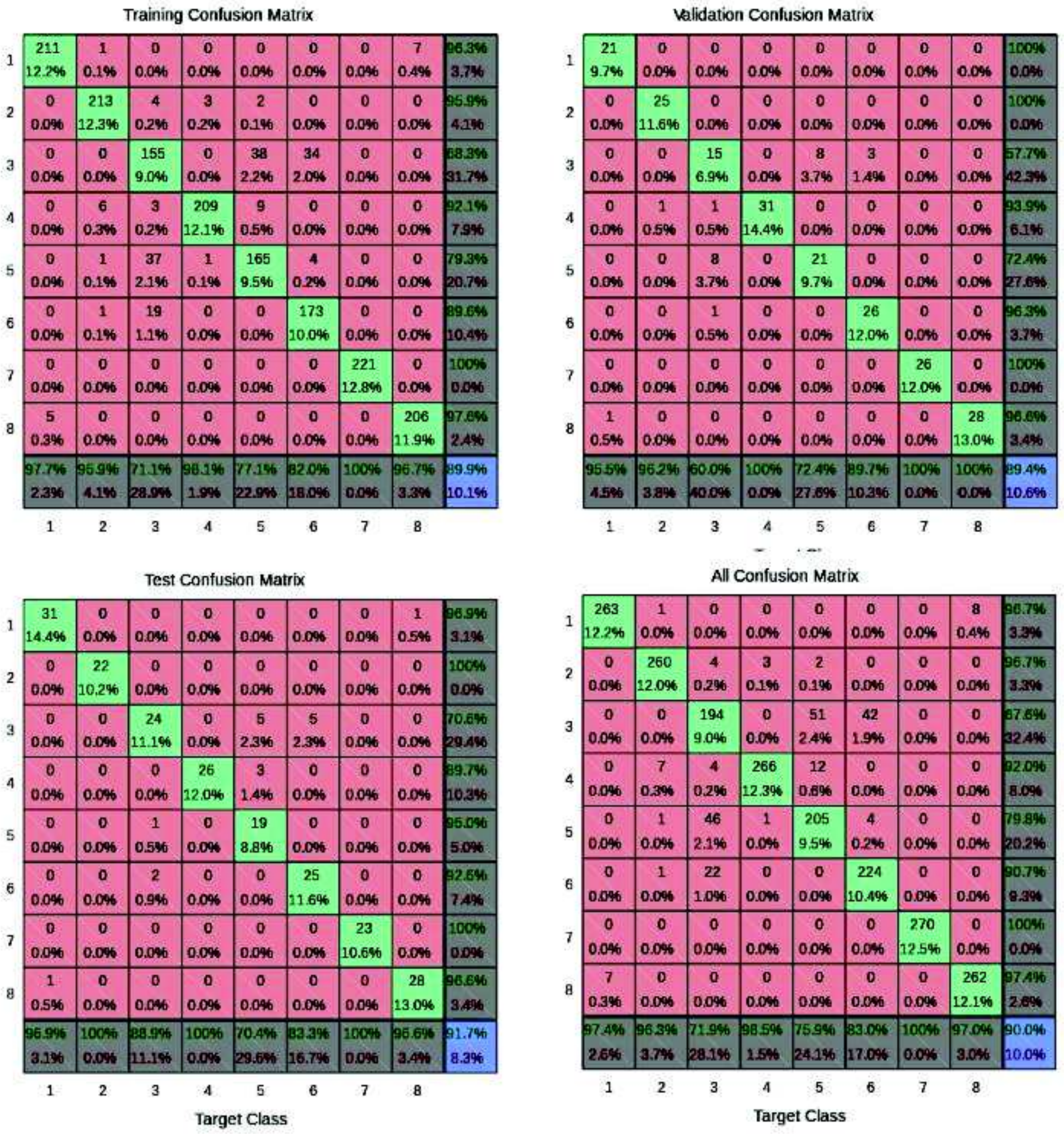

Training Confusion Matrix

1	211 12.2%	1 0.1%	0 0.0%	0 0.0%	0 0.0%	0 0.0%	0 0.0%	7 0.4%	96.3% 3.7%
2	0 0.0%	213 12.3%	4 0.2%	3 0.2%	2 0.1%	0 0.0%	0 0.0%	0 0.0%	95.9% 4.1%
3	0 0.0%	0 0.0%	155 9.0%	0 0.0%	38 2.2%	34 2.0%	0 0.0%	0 0.0%	68.3% 31.7%
4	0 0.0%	6 0.3%	3 0.2%	209 12.1%	9 0.5%	0 0.0%	0 0.0%	0 0.0%	92.1% 7.9%
5	0 0.0%	1 0.1%	37 2.1%	1 0.1%	165 9.5%	4 0.2%	0 0.0%	0 0.0%	79.3% 20.7%
6	0 0.0%	1 0.1%	19 1.1%	0 0.0%	0 0.0%	173 10.0%	0 0.0%	0 0.0%	89.6% 10.4%
7	0 0.0%	0 0.0%	0 0.0%	0 0.0%	0 0.0%	0 0.0%	221 12.8%	0 0.0%	100% 0.0%
8	5 0.3%	0 0.0%	0 0.0%	0 0.0%	0 0.0%	0 0.0%	0 0.0%	206 11.9%	97.6% 2.4%
	97.7% 2.3%	95.9% 4.1%	71.1% 28.9%	98.1% 1.9%	77.1% 22.9%	82.0% 18.0%	100% 0.0%	96.7% 3.3%	89.9% 10.1%
	1	2	3	4	5	6	7	8	

Validation Confusion Matrix

1	21 9.7%	0 0.0%	0 0.0%	0 0.0%	0 0.0%	0 0.0%	0 0.0%	0 0.0%	100% 0.0%
2	0 0.0%	25 11.6%	0 0.0%	0 0.0%	0 0.0%	0 0.0%	0 0.0%	0 0.0%	100% 0.0%
3	0 0.0%	0 0.0%	15 6.9%	0 0.0%	8 3.7%	3 1.4%	0 0.0%	0 0.0%	57.7% 42.3%
4	0 0.0%	1 0.5%	1 0.5%	31 14.4%	0 0.0%	0 0.0%	0 0.0%	0 0.0%	93.9% 6.1%
5	0 0.0%	0 0.0%	8 3.7%	0 0.0%	21 9.7%	0 0.0%	0 0.0%	0 0.0%	72.4% 27.6%
6	0 0.0%	0 0.0%	1 0.5%	0 0.0%	0 0.0%	26 12.0%	0 0.0%	0 0.0%	96.3% 3.7%
7	0 0.0%	0 0.0%	0 0.0%	0 0.0%	0 0.0%	0 0.0%	26 12.0%	0 0.0%	100% 0.0%
8	1 0.5%	0 0.0%	0 0.0%	0 0.0%	0 0.0%	0 0.0%	0 0.0%	28 13.0%	96.6% 3.4%
	95.5% 4.5%	96.2% 3.8%	60.0% 40.0%	100% 0.0%	72.4% 27.6%	89.7% 10.3%	100% 0.0%	100% 0.0%	89.4% 10.6%
	1	2	3	4	5	6	7	8	

Test Confusion Matrix

1	31 14.4%	0 0.0%	0 0.0%	0 0.0%	0 0.0%	0 0.0%	0 0.0%	1 0.5%	96.9% 3.1%
2	0 0.0%	22 10.2%	0 0.0%	0 0.0%	0 0.0%	0 0.0%	0 0.0%	0 0.0%	100% 0.0%
3	0 0.0%	0 0.0%	24 11.1%	0 0.0%	5 2.3%	5 2.3%	0 0.0%	0 0.0%	70.6% 29.4%
4	0 0.0%	0 0.0%	0 0.0%	26 12.0%	3 1.4%	0 0.0%	0 0.0%	0 0.0%	89.7% 10.3%
5	0 0.0%	0 0.0%	1 0.5%	0 0.0%	19 8.8%	0 0.0%	0 0.0%	0 0.0%	95.0% 5.0%
6	0 0.0%	0 0.0%	2 0.9%	0 0.0%	0 0.0%	25 11.6%	0 0.0%	0 0.0%	92.6% 7.4%
7	0 0.0%	0 0.0%	0 0.0%	0 0.0%	0 0.0%	0 0.0%	23 10.6%	0 0.0%	100% 0.0%
8	1 0.5%	0 0.0%	0 0.0%	0 0.0%	0 0.0%	0 0.0%	0 0.0%	28 13.0%	96.6% 3.4%
	96.9% 3.1%	100% 0.0%	88.9% 11.1%	100% 0.0%	70.4% 29.6%	83.3% 16.7%	100% 0.0%	96.6% 3.4%	91.7% 8.3%
	1	2	3	4	5	6	7	8	

Target Class

All Confusion Matrix

1	263 12.2%	1 0.0%	0 0.0%	0 0.0%	0 0.0%	0 0.0%	0 0.0%	8 0.4%	96.7% 3.3%
2	0 0.0%	260 12.0%	4 0.2%	3 0.1%	2 0.1%	0 0.0%	0 0.0%	0 0.0%	96.7% 3.3%
3	0 0.0%	0 0.0%	194 9.0%	0 0.0%	51 2.4%	42 1.9%	0 0.0%	0 0.0%	67.6% 32.4%
4	0 0.0%	7 0.3%	4 0.2%	266 12.3%	12 0.6%	0 0.0%	0 0.0%	0 0.0%	92.0% 8.0%
5	0 0.0%	1 0.0%	46 2.1%	1 0.0%	205 9.5%	4 0.2%	0 0.0%	0 0.0%	79.8% 20.2%
6	0 0.0%	1 0.0%	22 1.0%	0 0.0%	0 0.0%	224 10.4%	0 0.0%	0 0.0%	90.7% 9.3%
7	0 0.0%	0 0.0%	0 0.0%	0 0.0%	0 0.0%	0 0.0%	270 12.5%	0 0.0%	100% 0.0%
8	7 0.3%	0 0.0%	0 0.0%	0 0.0%	0 0.0%	0 0.0%	0 0.0%	262 12.1%	97.4% 2.6%
	97.4% 2.6%	96.3% 3.7%	71.9% 28.1%	98.5% 1.5%	75.9% 24.1%	83.0% 17.0%	100% 0.0%	97.0% 3.0%	90.0% 10.0%
	1	2	3	4	5	6	7	8	

Target Class

Fig. 5.34: Neural network confusion matrices. Three statistical parameters as input. Seven faults.

If more faults (categories) are included, the performance of the algorithm can be assessed with the help of the confusion matrices in Fig. 5.34. Comparing these results with the performance of the k-NN, the correct classification of the different types of faults is slightly better when neural networks are used, although the improvement is no more than 3-4%.

As it was done in sections 5.4 and 5.5, a combination of the three different positions and four types of faults can be tested using the neural network. The confusion matrices that correspond to this situation are shown in Fig. 5.35. In this case, the neural network does not improve significantly the accuracy of the classification obtained by selecting the features using the SPM.

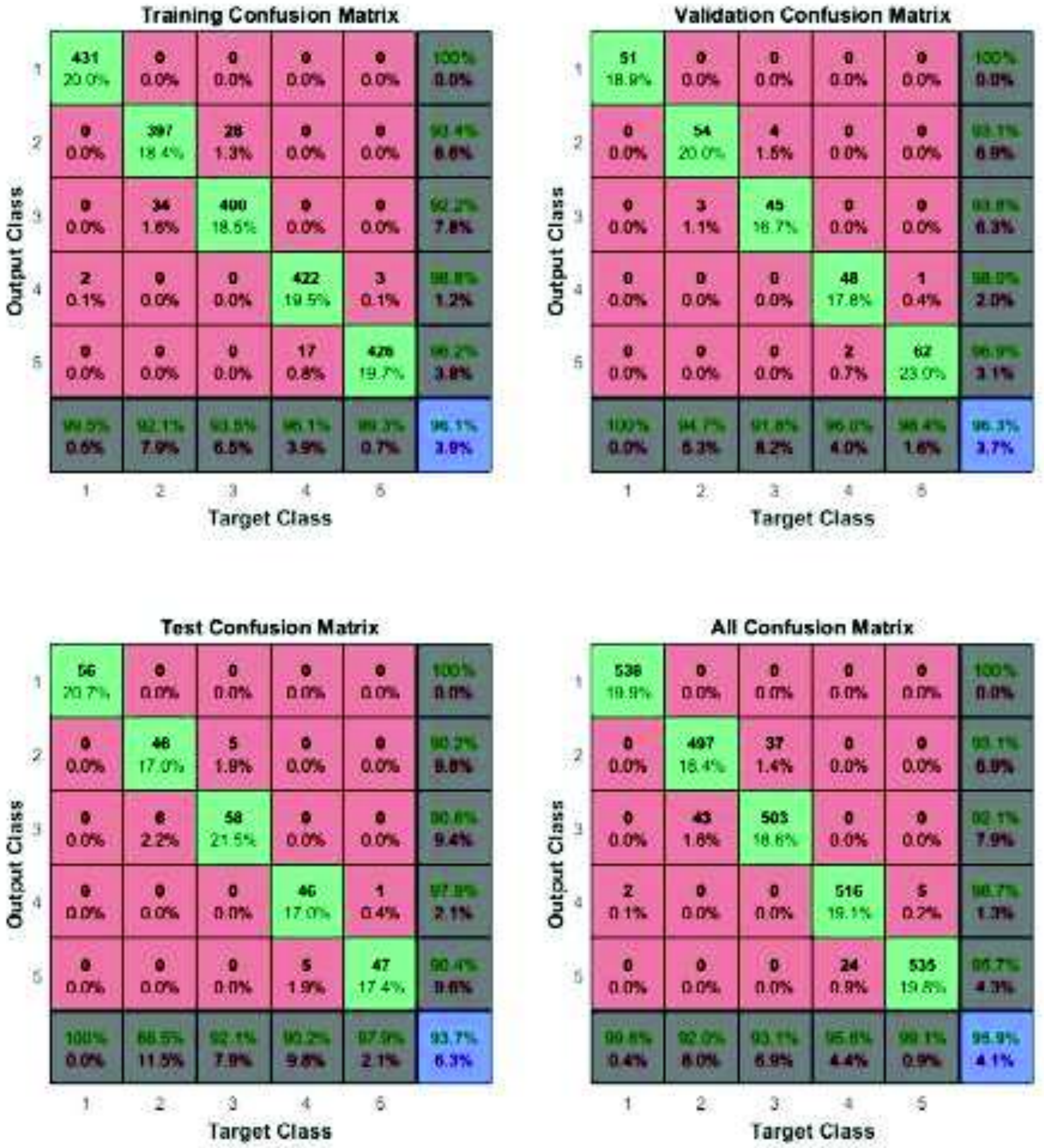

Training Confusion Matrix

Output Class	1	2	3	4	5	
1	431 20.0%	0 0.0%	0 0.0%	0 0.0%	0 0.0%	100% 0.0%
2	0 0.0%	397 18.4%	28 1.3%	0 0.0%	0 0.0%	93.4% 6.6%
3	0 0.0%	34 1.6%	400 18.5%	0 0.0%	0 0.0%	92.2% 7.8%
4	2 0.1%	0 0.0%	0 0.0%	422 19.5%	3 0.1%	98.8% 1.2%
5	0 0.0%	0 0.0%	0 0.0%	17 0.8%	426 19.7%	96.2% 3.8%
	99.5% 0.5%	92.1% 7.9%	93.5% 6.5%	96.1% 3.9%	99.3% 0.7%	96.1% 3.9%

Target Class

Validation Confusion Matrix

Output Class	1	2	3	4	5	
1	51 18.9%	0 0.0%	0 0.0%	0 0.0%	0 0.0%	100% 0.0%
2	0 0.0%	54 20.0%	4 1.5%	0 0.0%	0 0.0%	93.1% 6.9%
3	0 0.0%	3 1.1%	45 16.7%	0 0.0%	0 0.0%	93.8% 6.3%
4	0 0.0%	0 0.0%	0 0.0%	48 17.8%	1 0.4%	98.0% 2.0%
5	0 0.0%	0 0.0%	0 0.0%	2 0.7%	62 23.0%	96.9% 3.1%
	100% 0.0%	94.7% 5.3%	91.8% 8.2%	96.0% 4.0%	98.4% 1.6%	96.3% 3.7%

Target Class

Test Confusion Matrix

Output Class	1	2	3	4	5	
1	56 20.7%	0 0.0%	0 0.0%	0 0.0%	0 0.0%	100% 0.0%
2	0 0.0%	46 17.0%	5 1.9%	0 0.0%	0 0.0%	90.2% 9.8%
3	0 0.0%	6 2.2%	58 21.5%	0 0.0%	0 0.0%	90.6% 9.4%
4	0 0.0%	0 0.0%	0 0.0%	46 17.0%	1 0.4%	97.9% 2.1%
5	0 0.0%	0 0.0%	0 0.0%	5 1.9%	47 17.4%	90.4% 9.6%
	100% 0.0%	88.5% 11.5%	92.1% 7.9%	90.2% 9.8%	97.9% 2.1%	93.7% 6.3%

Target Class

All Confusion Matrix

Output Class	1	2	3	4	5	
1	538 19.9%	0 0.0%	0 0.0%	0 0.0%	0 0.0%	100% 0.0%
2	0 0.0%	497 18.4%	37 1.4%	0 0.0%	0 0.0%	93.1% 6.9%
3	0 0.0%	43 1.6%	503 18.6%	0 0.0%	0 0.0%	92.1% 7.9%
4	2 0.1%	0 0.0%	0 0.0%	516 19.1%	5 0.2%	98.7% 1.3%
5	0 0.0%	0 0.0%	0 0.0%	24 0.9%	535 19.8%	95.7% 4.3%
	99.6% 0.4%	92.0% 8.0%	93.1% 6.9%	95.6% 4.4%	99.1% 0.9%	95.9% 4.1%

Target Class

Fig. 5.35: Neural network confusion matrices. Three statistical parameters as input. Three different positions.

5.6.2 PSD as Input for the Neural Network.

Instead of statistical parameters, the PSDs of the faulty signals were used as inputs to the neural network. The performance of the network are presented in the confusion matrices seen in Fig. 5.36. The accuracy of the classifier is *100%*. In comparison with the k-NN using PCA, the improvement here is up to 15% for some of the faults. For example, the misclassification rate for the *two blades* class using three principal components was around 15% in the case of Exp3 (Fig. 5.25c-d). However, this high accuracy is not representative of the actual performance of the classifier. In real conditions, the number faults are more than four and the signal may probably exhibit noise or other characteristics that deviate it from its (controlled) experimental features. The use of four faults in the case of SPM and PCA is justified by the interest in testing the possibility of fault classification. However, for a powerful classification tool as Neural Network, this situation is "trivial" when the PSDs are used.

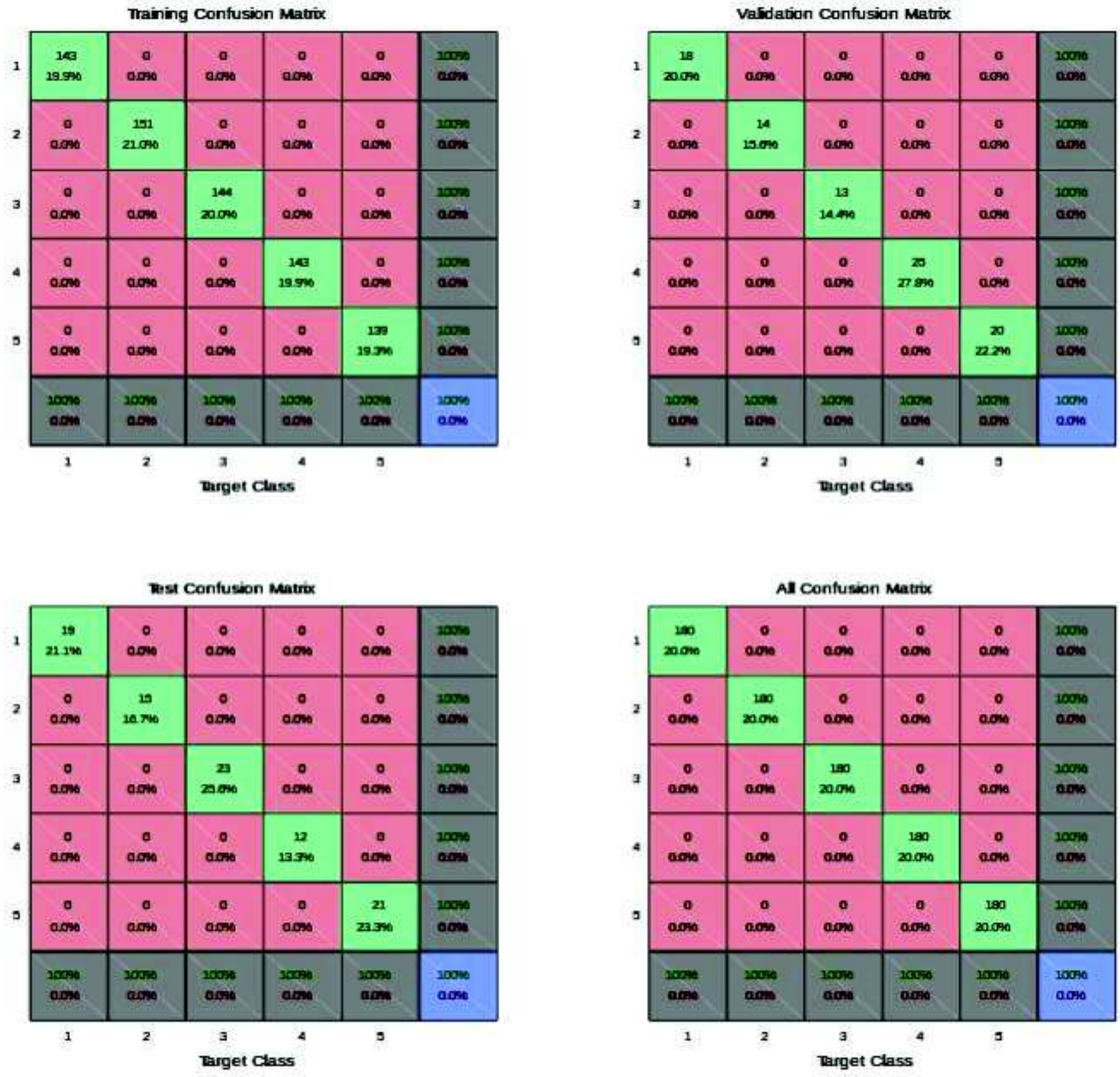

Fig. 5.36: Neural network confusion matrices. PSDs as inputs. Same results were obtained in the case of the three different positions.

When more faults are considered, the performance of the neural network resembled more to a potential realistic situation. It was shown in section 5.5 that, in the case of using seven types of faults, the performance of the k-NN algorithm using PSDs as features was not as accurate as in the case of only four faults. The Neural-Network algorithm improved the results for seven faults as can be seen in Fig. 5.37. The correct classification rate is over

90% in the case of Neural-Network, well above the accuracy of the k-NN method using PCA which was 51.85% for certain faults.

These results do not invalidate the usefulness of k-NN as classifier. It only suggests that, for WT faults classification in this geometric configuration, three principal components are not enough to obtain a high accuracy; three principal components do not carry enough information for a correct classification. It can be concluded that the Neural-Network algorithm is much more efficient in discovering patterns in the frequency-domain of the faulty signals than PCA was.

The performance of the neural network when PSDs are used as inputs is the best of all of the methods explored in this chapter. The reason for this may lie on the fact that, as it was explain in section 2.2, the magnitude of the spectral lines in the spectrum depends on the Bessel functions whose arguments are related to the physical characteristics of the system radar-WT, including the blades. This relation was an approximation and the true relationship may be much more complicated. However, the connection between the physical condition of the blades and the PSD has to be real. This relation is what the neural network algorithm has been capable of detecting.

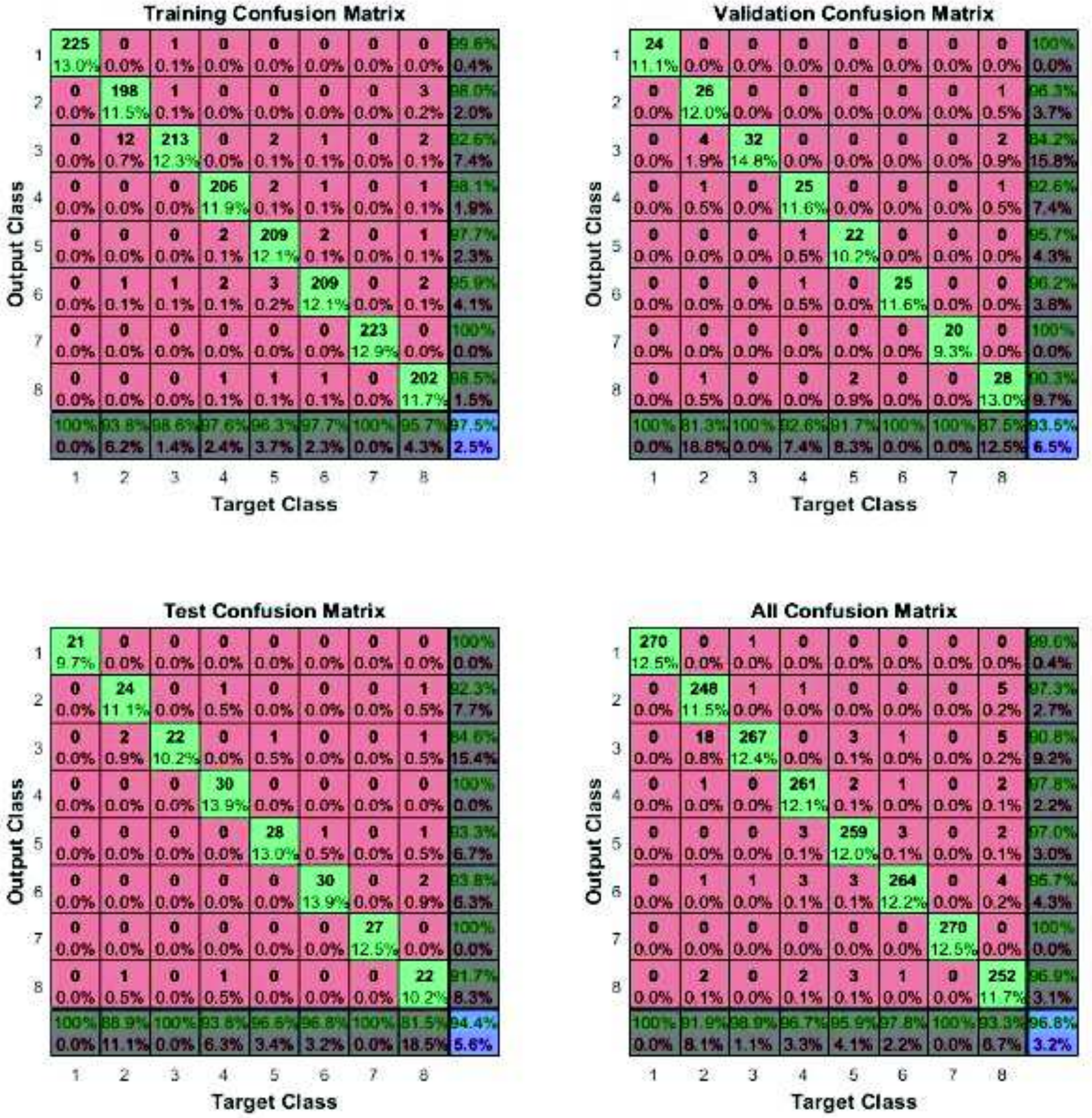

Training Confusion Matrix

	1	2	3	4	5	6	7	8	
1	225 13.0%	0 0.0%	1 0.1%	0 0.0%	0 0.0%	0 0.0%	0 0.0%	0 0.0%	99.6% 0.4%
2	0 0.0%	198 11.5%	1 0.1%	0 0.0%	0 0.0%	0 0.0%	0 0.0%	3 0.2%	98.0% 2.0%
3	0 0.0%	12 0.7%	213 12.3%	0 0.0%	2 0.1%	1 0.1%	0 0.0%	2 0.1%	92.6% 7.4%
4	0 0.0%	0 0.0%	0 0.0%	206 11.9%	2 0.1%	1 0.1%	0 0.0%	1 0.1%	98.1% 1.9%
5	0 0.0%	0 0.0%	0 0.0%	2 0.1%	209 12.1%	2 0.1%	0 0.0%	1 0.1%	97.7% 2.3%
6	0 0.0%	1 0.1%	1 0.1%	2 0.1%	3 0.2%	209 12.1%	0 0.0%	2 0.1%	95.9% 4.1%
7	0 0.0%	0 0.0%	0 0.0%	0 0.0%	0 0.0%	0 0.0%	223 12.9%	0 0.0%	100% 0.0%
8	0 0.0%	0 0.0%	0 0.0%	1 0.1%	1 0.1%	1 0.1%	0 0.0%	202 11.7%	98.5% 1.5%
	100% 0.0%	93.8% 6.2%	98.6% 1.4%	97.6% 2.4%	96.3% 3.7%	97.7% 2.3%	100% 0.0%	95.7% 4.3%	97.5% 2.5%

Validation Confusion Matrix

	1	2	3	4	5	6	7	8	
1	24 11.1%	0 0.0%	0 0.0%	0 0.0%	0 0.0%	0 0.0%	0 0.0%	0 0.0%	100% 0.0%
2	0 0.0%	26 12.0%	0 0.0%	0 0.0%	0 0.0%	0 0.0%	0 0.0%	1 0.5%	96.3% 3.7%
3	0 0.0%	4 1.9%	32 14.8%	0 0.0%	0 0.0%	0 0.0%	0 0.0%	2 0.9%	84.2% 15.8%
4	0 0.0%	1 0.5%	0 0.0%	25 11.6%	0 0.0%	0 0.0%	0 0.0%	1 0.5%	92.6% 7.4%
5	0 0.0%	0 0.0%	0 0.0%	1 0.5%	22 10.2%	0 0.0%	0 0.0%	0 0.0%	95.7% 4.3%
6	0 0.0%	0 0.0%	0 0.0%	1 0.5%	0 0.0%	25 11.6%	0 0.0%	0 0.0%	96.2% 3.8%
7	0 0.0%	0 0.0%	0 0.0%	0 0.0%	0 0.0%	0 0.0%	20 9.3%	0 0.0%	100% 0.0%
8	0 0.0%	1 0.5%	0 0.0%	0 0.0%	2 0.9%	0 0.0%	0 0.0%	28 13.0%	90.3% 9.7%
	100% 0.0%	81.3% 18.8%	100% 0.0%	92.6% 7.4%	91.7% 8.3%	100% 0.0%	100% 0.0%	87.5% 12.5%	93.5% 6.5%

Test Confusion Matrix

	1	2	3	4	5	6	7	8	
1	21 9.7%	0 0.0%	0 0.0%	0 0.0%	0 0.0%	0 0.0%	0 0.0%	0 0.0%	100% 0.0%
2	0 0.0%	24 11.1%	0 0.0%	1 0.5%	0 0.0%	0 0.0%	0 0.0%	1 0.5%	92.3% 7.7%
3	0 0.0%	2 0.9%	22 10.2%	0 0.0%	1 0.5%	0 0.0%	0 0.0%	1 0.5%	84.6% 15.4%
4	0 0.0%	0 0.0%	0 0.0%	30 13.9%	0 0.0%	0 0.0%	0 0.0%	0 0.0%	100% 0.0%
5	0 0.0%	0 0.0%	0 0.0%	0 0.0%	28 13.0%	1 0.5%	0 0.0%	1 0.5%	93.3% 6.7%
6	0 0.0%	0 0.0%	0 0.0%	0 0.0%	0 0.0%	30 13.9%	0 0.0%	2 0.9%	93.8% 6.3%
7	0 0.0%	0 0.0%	0 0.0%	0 0.0%	0 0.0%	0 0.0%	27 12.5%	0 0.0%	100% 0.0%
8	0 0.0%	1 0.5%	0 0.0%	1 0.5%	0 0.0%	0 0.0%	0 0.0%	22 10.2%	91.7% 8.3%
	100% 0.0%	88.9% 11.1%	100% 0.0%	93.8% 6.3%	96.6% 3.4%	96.8% 3.2%	100% 0.0%	81.5% 18.5%	94.4% 5.6%

All Confusion Matrix

	1	2	3	4	5	6	7	8	
1	270 12.5%	0 0.0%	1 0.0%	0 0.0%	0 0.0%	0 0.0%	0 0.0%	0 0.0%	99.6% 0.4%
2	0 0.0%	248 11.5%	1 0.0%	1 0.0%	0 0.0%	0 0.0%	0 0.0%	5 0.2%	97.3% 2.7%
3	0 0.0%	18 0.8%	267 12.4%	0 0.0%	3 0.1%	1 0.0%	0 0.0%	5 0.2%	90.8% 9.2%
4	0 0.0%	1 0.0%	0 0.0%	261 12.1%	2 0.1%	1 0.0%	0 0.0%	2 0.1%	97.8% 2.2%
5	0 0.0%	0 0.0%	0 0.0%	3 0.1%	259 12.0%	3 0.1%	0 0.0%	2 0.1%	97.0% 3.0%
6	0 0.0%	1 0.0%	1 0.0%	3 0.1%	3 0.1%	264 12.2%	0 0.0%	4 0.2%	95.7% 4.3%
7	0 0.0%	0 0.0%	0 0.0%	0 0.0%	0 0.0%	0 0.0%	270 12.5%	0 0.0%	100% 0.0%
8	0 0.0%	2 0.1%	0 0.0%	2 0.1%	3 0.1%	1 0.0%	0 0.0%	252 11.7%	96.9% 3.1%
	100% 0.0%	91.9% 8.1%	98.9% 1.1%	96.7% 3.3%	95.9% 4.1%	97.8% 2.2%	100% 0.0%	93.3% 6.7%	96.8% 3.2%

Fig. 5.37: Neural network confusion matrices. PSDs as inputs. Seven types of faults.

5.7 Summary

The possibility of automatically classifying WT faults has been explored in this chapter. Different methods have been applied to the time and frequency domains of faulty WT signals.

In the time-domain, the main statistical parameters of the signals have been employed as features to cluster the data points. Applied to these clusters, the k-NN algorithm has turned out to be accurate in classifying the different types of faults. Due to the fact that the statistical parameters noticeable depend on small variations in the radar-WT configuration, the performance of the classifier may be degraded if the experimental conditions are not well controlled. In a real situation, the sensitivity to the variations in the time-domain signal will depend on the particular configuration radar-WT and the radar frequency: a short wavelength compared to the characteristics geometrical changes in the WT (vibrations, pole bending, etc.) may probably degrade the performance of the classifier. On the other hand, the effects of these small changes could be "smooth out" by using an adequate wavelength, one sensitive only to the size of an actual mechanical fault. It seems clear that only investigations on actual WTs will determine whether or not this classifier based on the time-domain is adequate. These types of experiments have not been possible to be performed during this research due to the costs these actions would imply. However, the scaled experiments carried out in control circumstances have demonstrated the feasibility of detecting faults in WT blades and it will hopefully led to more experimentation in real operation situations.

Instead of working with the time-domain of the signals, their PSDs can be used to extract features related to the different types of faults. In this case, the PCA algorithm is employed to reduce the high dimensionality of such features and k-NN is used as classifier. Variations in the configuration radar-WT do not affect dramatically the performance of the PCA. In the case of only four faults, the clusters are relatively well-separated in the three positions tested. When seven faults are considered, the performance of the classifier degrades, although a high accuracy in the classification can be obtained for certain types of faults: the *25 mm shorter blade* and the *scratched blade* faults have a high percentage of misclassification. Therefore, it seems clear that three principal components are not enough to accurately classify this number of faults.

The last classifier analysed has been the Neural Network algorithm. This is the most powerful tool, even when the commercial Matlab toolbox is used: an algorithm made specifically for WT fault classification might fit the problem better, but at this stage of the research the two layers network has been enough to demonstrate the possibility of classification. The performance of the network is the highest of the three when seven WT faults are considered in the analysis and the PSDs are the input variables ($> 90\%$ of overall correct classification). Therefore, a simple neural network algorithm seems the most promising classifier of WT faults.

References

[1] R. O. Duda *et al.*, “Introduction” in *Pattern classification*, 2nd ed., New York, Chichester: Wiley, 2001, ch. 1, sec. 1.5, pp. 16-17.

[2] A. K. Jain *et al.*, “Statistical pattern recognition: a review,” *IEEE Trans. Pattern Anal. Mach. Intell.*, vol. 22, Iss. 1, pp. 4-37, Aug., 2002.

[3] V. Kotu and B. Deshpande, “Classification, k-Nearest Neighbours” in *Predictive Analytics and Data Mining*, 1st ed., Elsevier Science.

[4] S. Kulkarni and G. Harman, “The Nearest Neighbor Rule” in *An elementary introduction to statistical learning theory*, 1st ed., Hoboken, NJ: Wiley, 2011.

[5] T. M. Cover and P. E. Hart, “Nearest neighbor pattern classification,” *IEEE Trans. Inform. Theory*, vol. IT-13, pp. 21–27, 1967.

[6] P. Hall *et al.*, “Choice of neighbor order in nearest-neighbor classification”, *Ann. Statist.*, vol. 36, no. 5, pp. 2135-2152, 2008.

[7] M. Akbari *et al.*, “Artificial neural network and optimization” in *Advances in Friction-Stir Welding and Processing*, 2014, ch. 13, pp. 543-599.

[8] C. Bishop, “Neural Networks” in *Pattern recognition and Machine learning*, 1st ed., New York, NY: Springer, 2006.

[9] M. T. Hagan *et al.*, “Practical training issues” in *Neural Network Design*, 2nd ed., ch. 22, sec. 22-5.

[10] M. F. Moller, “A scaled conjugate gradient algorithm for fast supervised learning,” *Neural Networks*, vol. 6, pp. 525-533, Nov., 1991.

Chapter 6 Conclusions and Future Work

6.1 Conclusions

This thesis focuses on WT structural monitoring using RF sensors. The main goal of this research has been to investigate the feasibility of detecting and automatically classifying WT faults using radar and verify its performance. The idea is to place a short-range radar sensor in the vicinity of a WT and analyse its radar signature to detect and classify structural faults.

First of all, since the radar would be place near a WT, its radar signature in the near-field has been theoretically analysed. A first theoretical model has considered WT blades as a group of scattering points forming a rectangular plate. This model has established relationships between radar signal properties and WT mechanical properties. A second model has been developed to characterise radar returns from moving WT blades which can take into account the complexity of their shape. Both models have been tested in ideal and controlled, but representative experimental conditions within an anechoic chamber, showing a correlation coefficient of ~0.9 between theoretical and experimental results. The good agreement between theory and experiment confirms the validity of the theoretical framework. The model developed in this dissertation can be used to understand radar signatures of faulty blades in the near-field, and how the corresponding signal properties may be used to diagnose or classify a WT fault using a short-range radar sensor in the vicinity of the turbine blades.

The second part of this thesis has focused on the actual detection and classification of WT faults. The radar signatures from faulty WT's have been recorded and analysed. The results have shown that mechanical faults induced on WT blades clearly change the pattern of the time-domain signatures as well as the micro-Doppler signatures. Frequency-domain signatures do not show a clear and visual alteration. These experimental observations have demonstrated that radar sensors are capable of detecting mechanical faults that affect the structural health of WT's.

In order to classify different types of faults, several classification methods have been used in this research. These classification algorithms have employed two types of features. The first type have been the time-domain statistical parameters from faulty blades. The second type corresponds to frequency-domain features, where the well-known Principal Components Analysis (PCA) method has been employed to reduce the dimensionality of the database by automatically selecting the features that better help differentiate between WT faults. Two classification algorithms have been applied: k-Nearest Neighbours (k-NN) and Artificial Neural Networks (ANN). In order to assess the capacity of these algorithms to correctly classify WT faults, confusions matrices have been built for different configurations and number of faults. The results have shown a degree of correct classification over 70% in the worst case. The ANN proportionate the best results reaching 90% of correct classification even when 8 different classes or faults have been taken into account.

6.2 Future Work

Based on the results obtained, the recommendation for the next step is to conduct experiments with faulty blades outside the anechoic chamber to study how the classification algorithms are affected by real conditions. This investigation could include more types of faults such as rotor vibration and erosion. The experiments could also be done in a variety of weather conditions and for different geometrical configurations. They could also combine different types of faults.

Another interesting possibility is to conduct experiments with actual WT's. This would need the collaboration with the wind power industry since it is not possible to induce faults on real WT's. However, if permission is granted, it would be feasible to monitor a group of WT's and analyse how the radar signature is affected by real conditions, including phenomena such as ice accretion. By constantly monitoring real WT's, data from their actual faults could be analyse, giving extremely valuable information to improve the research presented in this thesis.

The ultimate goal of the project would be to use GNSS signals to monitor WT faults. This system would allow continuous monitoring anywhere in the world. Experiments in this direction could be performed if access to WT sites are granted. The MISL has the technology and experience to conduct these types of experiments.

GNSS monitoring is conceptually different: instead of the active radar system presented here, it would be a passive radar monitoring system. Another factor to consider would be the working frequency: it would be restricted to the L band. This would reduce the system resolution and the differet types of fault to be detected. For example, it would not be possible to distinguish between a blade with its length chipped 5% and one with its length 10% shorter.

The critical factor to consider would be the spectrum of the reflected signal from WT’s. The research presented in this thesis has shown that the spectrum contains information for classifying WT faults. Therefore, the quality of the signal in the frequency domain would be crucial for the success of a GNSS-based monitoring system.

Finally, it should also be stated here that this work is not limited to WT’s exclusively, but could potentially be applied to monitoring other rotating objects with short-range radar sensors, such as helicopter rotor blades.

Appendix A Wind Turbine Radar Signatures. Matlab Simulation Codes.

The codes implemented in MATLAB for simulation and classification purposes are presented in this Appendix. A.1 and A.2 corresponds to the codes used to simulate the theoretical radar signatures from flat and curved blades. A.3 and A.4 show the algorithms employed to classify WT faults in both time and frequency domains.

A.1 Flat blade radar signature

```
%% Scattering Centres Model of flat blades
% This code simulates the backscattered signal from a flat blade



%% Simulation parameters
c = 3e8;            % Speed of light
f0 = 24e9;          % Radar frequency
rn = 3.7;           % WT-radar radial distance
zn = 0.48;          % WT hub height
omega = 9.4;        % WT rotational speed
l = c/f0;           % Radar wavelength
lb = 0.5;           % Blade length
db = 0.02;          % Blade width

N = 300;            % Number of scattering points along the blade
M = 29;             % Number of scattering points across the blade
hv = lb/(N-1);      % Distance between two point-scatters along the blade
hh = db/(M-1);      % Distance between two point-scatters across the blade
%%%%%%



%%
Fs = 44.1e3;                    % Sampling frequency
dt = 1/Fs;                      % Sample time
T = n*2*pi/omega;               % Number n of blade revolutions
t = 0:dt:T-dt;                  % Time vector
L = length(t);                  % Length of signal
f = -Fs/2:Fs/L:Fs/2-Fs/L;       % Frequency vector
%%%%%%




%% Radar echo simulation. Equation (2.45), Chapter 2
% Signal vectors initialisation
```

```
s = 0.0*t;          % Three blades signal
s1 = 0.0*t;         % 1st blade signal
s2 = 0.0*t;         % 2nd blade signal
s3 = 0.0*t;         % 3rd blade signal


%% 3 blades together
for k=1:1
  for i=1:N-1
    for j=-(M-1)/2:(M-1)/2

      dm = hh*j;
      ln = hv*i;
      lmn = sqrt(dm^2+ln^2);

      alphamn = asin(dm/lmn);

      x = rn^2+lmn^2+2*lmn*zn*cos(omega*t+alphamn+2*pi/3*(k-1));
      r = sqrt(x);
      s = s+exp(-1i*4*pi/l*r);

    end
  end

  for j=-(M-1)/2:(M-1)/2

    dm = hh*j;

    x = rn^2+dm^2+2*dm*zn*cos(omega*t+2*pi/3*(k-1));
    r = sqrt(x);
    s = s+exp(-1i*4*pi/l*r);

  end
end
%%%%%%


%% One single blade
k = 1;              % 1st blade
% k = 2;            % 2nd blade
% k = 3;            % 3rd blade

for i=1:N-1
      for j=-(M-1)/2:(M-1)/2

            dm = hh*j;
            ln = hv*i;
```

```
        lmn = sqrt(dm^2+ln^2);

        alphamn = asin(dm/lmn);

        x = rn^2+lmn^2+2*lmn*zn*cos(omega*t+alphamn+2*pi/3*(k-1));
        r = sqrt(x);
        s1 = s1+exp(-1i*4*pi/l*r);

    end
end

for j=-(M-1)/2:(M-1)/2

    dm = hh*j;

    x = rn^2+dm^2+2*dm*zn*cos(omega*t+2*pi/3*(k-1));
    r = sqrt(x);
    s1 = s1+exp(-1i*4*pi/l*r);

end
%%%%%%%


%% Obtaining frequency-domain signatures
s_FT = fftshift(fft(s));            % Three blades
s_FT_1 = fftshift(fft(s1));         % One single blade
%%%%%%



%% The signal is filtered to emulate the two cascaded HF Butterworth filters
[b, a] = butter(1, [6/(44100/2) 92/(44100/2)]);

% Three blades
real_s_a = filter(b, a, real(s));
imag_s_a = filter(b, a, imag(s));

real_s_b = filter(b, a, real_s_a);
imag_s_b = filter(b, a, imag_s_a);

y = real_s_a+1i*iimag_s_b;

% Same procedure for a single blade
%%%%%%
```

```
%% Plotting signals in the time-domain
figure(1)
hold on
grid on

plot(t,20*log10((abs(s)./max(abs(s)))),'r','LineWidth',2)

xlim([* T])
ylim([-25 0])

xlabel('Time, s','fontsize',18)
ylabel('Amplitude','fontsize',18)


%% Plotting signals in the frequency-domain
figure(2)
grid on
hold on

plot(f,20*log10(abs(s_FT./max(s_FT))),'r')


xlim([-120 120])
ylim([-30 0])

xlabel('Frequency, Hz')
ylabel('Amplitude')
%%%%%%



%% Obtaining the joint time frequency domain. Micro-Doppler signature.

s_mD = s(*:*);                % Selecting part of the signal s

nfft =  128*60;                        % FFT length
noverlap = floor(nfft-0.05*nfft);    % 5% overlap
win = gausswin(nfft);                % Window used

[STFT,F,T,P] = spectrogram(s_mD,win,noverlap,nfft,Fs);


%% Plotting the spectrogram
figure(2)
```

```
imagesc(T,F-max(F)/2,fftshift(20*log10(abs(STFT)./max(max(abs(STFT)))),1), [-40 0])
xlabel('Time, s','fontsize',18); grid on; cbar = colorbar; colormap('jet'); ylim([-110 110])
ylabel('Frequency, Hz','fontsize',18);

cbar.Label.String = 'Power/Frequency, dB/Hz';
%%%%%%
```

A.2 Curved blade radar signature

```
% Curved Blades Radar Signature.
% This code simulates the radar signature of a curved blade.



%% WT blade points
S_measured = [*];          % S is a (Nx3) matrix formed by the coordinates of the points
                           % manually measured on a curved.
                           % Each column corresponds to a dimension (x,y,z).
                           % Each row is a measured point.



%% S_measured reorganised. Coordinates expressed in meters.
S(:,1) = (S_measured(:,1)-640.07)./1000; % 640.07 is the measurement system offset
S(:,2) = S_measured(:,3)./100;
S(:,3) = S_measured(:,2)./1000;



%% Plotting the blade surface S
plot3(S(:,1),S(:,2),S(:,3),'*r')
axis equal



%% Reading data from experimental signals.
[test,fs]=wavread('*.wav');          % Experimental file. fs: sample frequency.
left=test(:,1);
right=test(:,2);
time=(1/fs)*length(left);

% I and Q channels
I = left;
Q = right;

dtE = 1/fs;                          % Experimental sample time
tE = 0:dtE:time-dtE;                 % Experimental time vector
n = length(tE);
```

```
fE = -fs/2:fs/n:fs/2-fs/n;          % Experimental frequency vector



% Complex signal
s = I+cj.*Q;

% Signal high-pass filtering
s_hp = smooth(s,201);
%%%%%%



%% Simulation parameters
c = 3e8;            % Speed of light
f0 = 24e9;          % Radar frequency
rn = 3.7;           % WT-radar radial distance
zn = 0.48;          % WT hub height
omega = 9.4;        % WT rotational speed
l = c/f0;           % Radar wavelength
%%%%%%



%%
Fs = 44100;                         % Sample frequency
dt = 1/Fs;                          % Theoretical sample time
T = 2*pi/abs(omega);                % Rotational period
t = 0.0:dt:T-dt;                    % Theoretical time vector
L = length(t);
f = -Fs/2:Fs/L:Fs/2-Fs/L;           % Theoretical frequency vector


%% Radar echo simulation. Equation (3.35), Chapter 3
% Initial EM field vectors
Ex=0.0*t;
Ey=0.0*t;
Ez=0.0*t;

P = length(SF(:,1));        % Length in the x-direction

shift = *;                  % Angular shift.
                            % It was used to sinchronise experimental and theoretical signals


% Sort array by columns 1 and 2 (x and y coordinates)
SF = sortrows(SF,[1 2]);

% Initial directional derivatives
```

```
Dx=0.0;
Dy=0.0;
Dz=0.0;

alfa0 = *;           % Angular displacement
          % It was used to take into account the angular alignment between the radar and the WT


%% 1st Blade (same for the rest of the blades)
i = 1;     % Blade index

for j=1:P

      % Coordinates of the point P
      x = SF(j,1);
      y = SF(j,2);
      z = SF(j,3);

      lnO = sqrt(x^2+y^2+z^2);
      phiO = atan2(y,x);
      thetaO = acos(z/lnO);

      Xr = lnO*cos(phiO+2*pi/3*(i-1))*sin(thetaO+alfa);
      Yr = lnO*sin(phiO+2*pi/3*(i-1))*sin(thetaO+alfa);
      Zr = lnO*cos(thetaO+alfa);

      %% Base in x-direction
      % Reading the next point in the x-direction to calculate the base vector
      n = 1;
      while abs(x-SF(j+n,1))==0              % Same x coordinate
         n=n+1;
      end

      % Coordinates of the next point
      xx = SF(j+n,1);
      yy = SF(j+n,2);
      zz = SF(j+n,3);

      ln = sqrt(xx^2+yy^2+zz^2);
      phi = atan2(yy,xx);
      theta = acos(zz/ln);

      XXr = ln*cos(phi+2*pi/3*(i-1))*sin(theta+alfa);
      YYr = ln*sin(phi+2*pi/3*(i-1))*sin(theta+alfa);
      ZZr = ln*cos(theta+alfa);
```

```
% Base vector angle respect to x
beta_x = atan2((ZZr-Zr),(XXr-Xr));

% Base in the global X-coordinates
e_xx = 1.0*cos(beta_x);
e_xy = 0;
e_xz = 1.0*sin(beta_x);







% Vector module
e_x = sqrt(e_xx.^2+e_xy.^2+e_xz.^2);


%% Base in y-direction
xx = SF(j+1,1);
yy = SF(j+1,2);
zz = SF(j+1,3);

if abs(xx-x)==0       % Point with the same x-coordinate. Reading the surface in the y-direction

   ln = sqrt(xx^2+yy^2+zz^2);
   phi = atan2(yy,xx);
   theta = acos(zz/ln);

   XXr = ln*cos(phi+2*pi/3*(i-1))*sin(theta+alfa);
   YYr = ln*sin(phi+2*pi/3*(i-1))*sin(theta+alfa);
   ZZr = ln*cos(theta+alfa);

   % Base vector angle respect to y
   beta_y = atan2((ZZr-Zr),(YYr-Yr));

   % Base in the global Y-coordinates
   e_yx = 0;
   e_yy = 1.0*cos(beta_y);
   e_yz = 1.0*sin(beta_y);

   % Vector module
   e_y = sqrt(e_yx.^2+e_yy.^2+e_yz.^2);

else

   Dy = 0.0;             % If the x coordinate is different, ignore.
```

```
        end


        %% Observation vector. Distance radar-scattering point.
        Rx = -lnO*cos(phiO-omega*t-shift+2*pi/3*(i-1))*sin(thetaO+alfa);
        Ry = -zn-lnO*sin(phiO-omega*t-shift+2*pi/3*(i-1))*sin(thetaO+alfa);
        Rz = sqrt(rn^2-zn^2)-lnO*cos(thetaO+alfa);

        % Module of the radial vector
        R = sqrt(Rx.^2+Ry.^2+Rz.^2);


        %% Vector of the electric dipole moment in terms of the basis vectors
        px = e_xx/e_x.*cos(omega*t+shift)+e_yx/e_y.*sin(omega*t+shift);
        py = e_xy/e_x.*cos(omega*t+shift)+e_yy/e_y.*sin(omega*t+shift);
        pz = e_xz/e_x.*cos(omega*t+shift)+e_yz/e_y.*sin(omega*t+shift);

        p = sqrt(px.^2+py.^2+pz.^2);


        %% Electric field vector
        Ex = Ex+3*2*pi*f0^2/c^2/(8.85^-12)./R.^3./p.*(-Rz.*(Rx.*pz-Rz.*px)-Ry.*(Rx.*py-
    Ry.*px)).*exp(1i*4*pi*f0/c*R);

        Ey = Ey-3*2*pi*f0^2/c^2/(8.85^-12)./R.^3./p.*(Rz.*(Ry.*pz-Rz.*py)-Rx.*(Rx.*py-
    Ry.*px)).*exp(1i*4*pi*f0/c*R);

        Ez = Ez+3*2*pi*f0^2/c^2/(8.85^-12)./R.^3./p.*(Ry.*(Ry.*pz-Rz.*py)+Rx.*(Rx.*pz-
    Rz.*px)).*exp(1i*4*pi*f0/c*R);

    end



    %%%%%%
    %% Same procedure for the other two blades (i=2, i=3)
    %%%%%%


    %% The signal is filtered to emulate the two cascaded HF Butterworth filters
    [b, a] = butter(1, 6/(44100/2), 'high');        % Cut-off frequency: 6 Hz

    rExa = filter(b, a, real(Ex));
    iExa = filter(b, a, imag(Ex));
```

```
rExaa = filter(b, a, rExa);
iExaa = filter(b, a, iExa);

% Filtered electric field. x-component.
Ex = rExaa+cj.*iExaa;



%% Plotting signals in the time-domain
figure(1)
hold on
grid on

% Theoretical signal
plot(t,20*log10((abs(Ex)./max(abs(Ex)))),'--r','LineWidth',2)

% Experimental signal
plot(tE(*:*),20*log10((abs(s_hp(*:*))./max(abs(s_hp(*:*))))),'b','LineWidth',2)
% (*,*) selects a particular period of the signal



xlim([* T])
ylim([-25 0])

xlabel('Time, s','fontsize',18)
ylabel('Amplitude','fontsize',18)


%% Obtaining frequency-domain signatures
Ex_FT = fftshift(fft(Ex));
s_hp_FT = fftshift(fft(s_hp));

%% Plotting signals in the frequency-domain
figure(2)
grid on
hold on

% Theoretical signal
plot(f,20*log10(abs(Ex_FT./max(Ex_FT))),'r')

% Experimental signal
plot(fE,20*log10(abs(s_hp_FT./max(s_hp_FT))),'b')


xlim([-120 120])
```

```
ylim([-30 0])

xlabel('Frequency, Hz')
ylabel('Amplitude')


%% Obtaining the joint time frequency domain. Micro-Doppler signature.

% Theoretical spectrogram
Ex_mD = Ex(*:*); % Selecting part of the theoretical signal

nfft =  128*60; % FFT length
noverlap = floor(nfft-0.05*nfft);    % 5% overlap
win = gausswin(nfft);                % Window used

[STFT,F,T,P] = spectrogram(Ex_mD,win,noverlap,nfft,Fs);


%% Plotting the theoretical spectrogram
figure(3)
imagesc(T,F-max(F)/2,fftshift(20*log10(abs(STFT)./max(max(abs(STFT)))),1), [-40 0])
xlabel('Time, s','fontsize',18); grid on; cbar = colorbar; colormap('jet'); ylim([-110 110])
ylabel('Frequency, Hz','fontsize',18);

cbar.Label.String = 'Power/Frequency, dB/Hz';



% Experimental spectrogram
s_hp_mD = s_hp(*:*);     % Selecting part of the experimental signal

[STFT,F,T,P] = spectrogram(s_hp_mD,win,noverlap,nfft,Fs);


%% Plotting the experimental spectrogram
figure(4)
imagesc(T,F-max(F)/2,fftshift(20*log10(abs(STFT)./max(max(abs(STFT)))),1), [-40 0])
xlabel('Time, s','fontsize',18); grid on; cbar = colorbar; colormap('jet'); ylim([-110 110])%; xlim([0
TT])
ylabel('Frequency, Hz','fontsize',18);

cbar.Label.String = 'Power/Frequency, dB/Hz';
%%%%%%
```

A.3 Wind Turbine Faults Classification Using Statistical Parameters Method and k-NN

```
% Statistical Parameters Method
% This code extracts features from the time-domain signatures
% to classify WT faults.


%% Reading the data from the different faults
[test,fs]=wavread('*.wav');          % File data name
left=test(:,1);
right=test(:,2);

I = left;
Q = right;

cj = sqrt(-1);

s1 = I+cj.*Q;                        % Healthy signal
s1_hp = smooth(s1,201);              % High-pass filter

Sn1 = abs(s1_hp)./max(abs(s1_hp));      % Signal amplitude

% s2 corresponds to the second fault: blade 2.5 cm shorter
% Same procedure for the rest of the faulty blade signals

clear I Q left right s1 s1_hp
%%%%%%


%% Creating the data matrix X
N = 450;                             % Number of rows: number of WT revolutions
M = 20;                              % Number of points from the PSD

T = round(2*pi/9.4/dt);              % Number of points in each revolution

X = zeros(N*8,3);                    % Initialising the data matrix


%% Calculating the different statistical parameters from
% the time-domain signatures

% Mean amplitude
n = 0;
```

```
for i=1:N

   n0 = n;
   n = n+T;

   X(i,1) = mean(Sn1(n0+1:n));
   X(N+i,1) = mean(Sn2(n0+1:n));
   X(2*N+i,1) = mean(Sn3(n0+1:n));
   X(3*N+i,1) = mean(Sn4(n0+1:n));
   X(4*N+i,1) = mean(Sn5(n0+1:n));
   X(5*N+i,1) = mean(Sn6(n0+1:n));
   X(6*N+i,1) = mean(Sn7(n0+1:n));
   X(7*N+i,1) = mean(Sn8(n0+1:n));

end


% Maximum of the signal
n = 0;

for i=1:N

    n0 = n;
    n = n+T;

    X(i,3) = max(Sn1(n0+1:n));
    X(i+N,3) = max(Sn2(n0+1:n));
    X(i+2*N,3) = max(Sn3(n0+1:n));
    X(i+3*N,3) = max(Sn4(n0+1:n));
    X(i+4*N,3) = max(Sn5(n0+1:n));
    X(i+5*N,3) = max(Sn6(n0+1:n));
    X(i+6*N,3) = max(Sn7(n0+1:n));
    X(i+7*N,3) = max(Sn8(n0+1:n));

end


% Power per revolution
n = 0;

for i=1:N

   n0 = n;
   n = n+T;

   X(i,2) = sum(Sn1(n0+1:n).^2)/length(Sn1(n0+1:n));
   X(i+N,2) = sum(Sn2(n0+1:n).^2)/length(Sn2(n0+1:n));
```

```
    X(i+2*N,2) = sum(Sn3(n0+1:n).^2)/length(Sn3(n0+1:n));
    X(i+3*N,2) = sum(Sn4(n0+1:n).^2)/length(Sn4(n0+1:n));
    X(i+4*N,2) = sum(Sn5(n0+1:n).^2)/length(Sn5(n0+1:n));
    X(i+5*N,2) = sum(Sn6(n0+1:n).^2)/length(Sn6(n0+1:n));
    X(i+6*N,2) = sum(Sn7(n0+1:n).^2)/length(Sn7(n0+1:n));
    X(i+7*N,2) = sum(Sn8(n0+1:n).^2)/length(Sn8(n0+1:n));

end


% Standard deviation
n = 0;

for i=1:N

    n0 = n;
    n = n+T;

    X(i,3) = std(Sn1(n0+1:n));
    X(i+N,3) = std(Sn2(n0+1:n));
    X(i+2*N,3) = std(Sn3(n0+1:n));
    X(i+3*N,3) = std(Sn4(n0+1:n));
    X(i+4*N,3) = std(Sn5(n0+1:n));
    X(i+5*N,3) = std(Sn6(n0+1:n));
    X(i+6*N,3) = std(Sn7(n0+1:n));
    X(i+7*N,3) = std(Sn8(n0+1:n));

end


clear Sn1 Sn2 Sn3 Sn4 Sn5 Sn6 Sn7 Sn8
%%%%%%


%% Selecting randomly 90% of the data to create the training dataset

[Xr,Xc] = size(X);

% Row vectors containing a random permutation of the integers from 1 to N
Rp1 = randperm(N);
Rp2 = N+randperm(N);
Rp3 = 2*N+randperm(N);
Rp4 = 3*N+randperm(N);
Rp5 = 4*N+randperm(N);
Rp6 = 5*N+randperm(N);
Rp7 = 6*N+randperm(N);
Rp8 = 7*N+randperm(N);
```

```
percT = round(0.9*N);              % Number of data points in the training dataset
                                   % 90% of the total data.


% Creating the training matrix

XT = zeros(8*percT,Xc);

XT(1:percT,:) = X(Rp1(1:percT),:);         % Selecting randomly 90% of the data points.
XT(percT+1:2*percT,:) = X(Rp2(1:percT),:);
XT(2*percT+1:3*percT,:) = X(Rp3(1:percT),:);
XT(3*percT+1:4*percT,:) = X(Rp4(1:percT),:);
XT(4*percT+1:5*percT,:) = X(Rp5(1:percT),:);
XT(5*percT+1:6*percT,:) = X(Rp6(1:percT),:);
XT(6*percT+1:7*percT,:) = X(Rp7(1:percT),:);
XT(7*percT+1:8*percT,:) = X(Rp8(1:percT),:);
%%%%%%



%% Plotting the Feature Space
IndX = 1;
IndY = 2;
IndZ = 3;

figure
axes
hold all
grid on

NT = percT;

plot3(XT(1:NT,IndX),XT(1:NT,IndY),XT(1:NT,IndZ), '.b','MarkerSize',10)
plot3(XT(NT+1:2*NT,IndX),XT(NT+1:2*NT,IndY),XT(NT+1:2*NT,IndZ), '.r','MarkerSize',10)
plot3(XT(2*NT+1:3*NT,IndX),XT(2*NT+1:3*NT,IndY),XT(2*NT+1:3*NT,IndZ), '.g','MarkerSize',10)
plot3(XT(3*NT+1:4*NT,IndX),XT(3*NT+1:4*NT,IndY),XT(3*NT+1:4*NT,IndZ), '.y','MarkerSize',10)
plot3(XT(4*NT+1:5*NT,IndX),XT(4*NT+1:5*NT,IndY),XT(4*NT+1:5*NT,IndZ), '.k','MarkerSize',10)
plot3(XT(5*NT+1:6*NT,IndX),XT(5*NT+1:6*NT,IndY),XT(5*NT+1:6*NT,IndZ), '.m','MarkerSize',10)
plot3(XT(6*NT+1:7*NT,IndX),XT(6*NT+1:7*NT,IndY),XT(6*NT+1:7*NT,IndZ), 'oc','MarkerSize',10)
plot3(XT(7*NT+1:8*NT,IndX),XT(7*NT+1:8*NT,IndY),XT(7*NT+1:8*NT,IndZ), '+r','MarkerSize',10)

set(gca,'fontsize',15)

legend({'Healthy Blades','25 mm Shorter','50 mm Shorter','100 mm Shorter','150 mm Shorter',...
   'Bent Blade','Two Blades','Scratched Blade'},'fontsize',20);

xlabel('Mean Amplitude','fontsize',20)
```

```
ylabel('Power','fontsize',20)
zlabel('Standard Deviation','fontsize',20)
%%%%%%




%% Searching the k nearest neighbours
% The F matrix assigns a label to the training data points

F(1:NT) = 1;                    % Healthy blades
F(NT+1:2*NT) = 2;               % 25 mm shorter
F(2*NT+1:3*NT) = 3;             % 50 mm shorter
F(3*NT+1:4*NT) = 4;             % 100 mm shorter
F(4*NT+1:5*NT) = 5;             % 150 mm shorter
F(5*NT+1:6*NT) = 6;             % Bent blade
F(6*NT+1:7*NT) = 7;             % Two blades
F(7*NT+1:8*NT) = 8;             % Scratched blade

%% Number of test points
Ntest = N-NT;

% Creating the test dataset
XTest = zeros(8*Ntest,Xc);

% Selecting the points that were not included in the training dataset
XTest(1:Ntest,:) = X(Rp1(percT+1:N),:);
XTest(Ntest+1:2*Ntest,:) = X(Rp2(percT+1:N),:);
XTest(2*Ntest+1:3*Ntest,:) = X(Rp3(percT+1:N),:);
XTest(3*Ntest+1:4*Ntest,:) = X(Rp4(percT+1:N),:);
XTest(4*Ntest+1:5*Ntest,:) = X(Rp5(percT+1:N),:);
XTest(5*Ntest+1:6*Ntest,:) = X(Rp6(percT+1:N),:);
XTest(6*Ntest+1:7*Ntest,:) = X(Rp7(percT+1:N),:);
XTest(7*Ntest+1:8*Ntest,:) = X(Rp8(percT+1:N),:);

%% Obtaining the k nearest neighbours
[IDX,Dis] = knnsearch(XT(:,1:3),XTest(:,1:3),'k',5);

N_IDX = size(IDX,1);

%% Assigning a label based on the nearest neighbours
for i=1:N_IDX

   Fhat(i) = mode(F(IDX(i,:)));

end

%% Assining a class label to the test points
```

```
FF(1:Ntest) = 1;
FF(Ntest+1:2*Ntest) = 2;
FF(2*Ntest+1:3*Ntest) = 3;
FF(3*Ntest+1:4*Ntest) = 4;
FF(4*Ntest+1:5*Ntest) = 5;
FF(5*Ntest+1:6*Ntest) = 6;
FF(6*Ntest+1:7*Ntest) = 7;
FF(7*Ntest+1:8*Ntest) = 8;
%%%%%%


%% Confusion matrix. Comparing the known classes to the predicted ones
[C,order] = confusionmat(FF',Fhat)
%%%%%%




%% Plotting the confusion matrix
num_class = 8;

mat = C./Ntest.*100;            % A 8-by-8 matrix of random values from 0 to 1 find percentage
format('bank')
figure,imagesc(mat);            % Create a colored plot of the matrix values
colormap(flipud(gray));         % Change the colormap to gray (so higher values are
                                % black and lower values are white)

textStrings = num2str(mat(:),'%0.2f');          % Create strings from the matrix values
                                                % with percentage symbol
textStrings = strtrim(cellstr(textStrings));    % Remove any space padding
[x,y] = meshgrid(1:num_class);                  % Create x and y coordinates for the strings
hStrings = text(x(:),y(:),textStrings(:),...    % Plot the strings
            'HorizontalAlignment','center');
midValue = mean(get(gca,'CLim'));               % Get the middle value of the color range
textColors = repmat(mat(:) > midValue,1,3);     % Choose white or black for the
                                                % text color of the strings so
                                                % they can be easily seen over
                                                % the background color

set(hStrings,{'Color'},num2cell(textColors,2),'fontsize',20);          % Change the text colors

set(gca,'XTick',1:num_class,...                 % Change the axes tick marks
      'XTickLabel',{'Healthy Blades','25 mm shorter','50 mm Shorter','100 mm Shorter','150 mm
shorter','Bent Blade','Two Blades','Sand'},...   %  and tick labels
      'YTick',1:num_class,...
      'YTickLabel',{'Healthy Blades','25 mm shorter','50 mm Shorter','100 mm Shorter','150 mm
shorter','Bent Blade','Two Blades','Sand'},...
```

```
    'TickLength',[0 0],'fontsize',20);

format('short')
%%%%%%
```

A.4 Wind Turbine Faults Classification Using Principal Components Analysis and k-NN

```
% Principal Components Analysis in the frequency-domain

%% Reading the data from the different faults
[test,fs]=wavread('*.wav');          % File data name
left=test(:,1);
right=test(:,2);

time=(1/fs)*length(left);

I = left;
Q = right;

cj = sqrt(-1);

s1 = I+cj.*Q;               % Healthy signal
s1 = smooth(s1,201);        % High-pass filter

% s2 corresponds to the second fault: blade 25 mm shorter
% Same procedure for the rest of the faulty blade signals

clear I Q left right
%%%%%%


%% Creating the data matrix X
N = 450;            % Number of rows: number of WT revolutions
M = 20;             % Number of points from the PSD

T_s = round(2*pi/9.4/dt);

a = size(real(s1(1:T_s)));           % Number of rows: number of data points in one revolution

X = zeros(8*N,a);                    % Initialising the matrix

% Creating the rows
k = 0;
```

```
for i=1:N

    k0 = k;
    k = k+T_s;

    X(i,:) = real(s1(k0+1:k));

end

clear s1

% Same procedure for the rest of the signals
%%%%%%

% Creating the PCA matrix: 'powspec'
for j=1:N

    [px1,f1] = pwelch(X(j,:));
    P1=10*log10(px1/max(px1));
    powspec(j,:)=P1(1:M)';
    clear P1

end



% Plotting the PSD
figure(1)
plot(f1(1:M),powspec(1:j,:),'b')
hold

% Same procedure for the rest of the signals
%%%%%%


%% Obtaining the vectors expressed in the base of the Principal Components
[coefs,score,latent] = princomp(zscore(powspec));

clear X;
%%%%%%


%% Selecting randomly 90% of the data to create the training dataset

X = score(:,1:3);              % Three Principal Components
```

```
[Xr,Xc] = size(X);


% Row vectors containing a random permutation of the integers from 1 to N
Rp1 = randperm(N);
Rp2 = N+randperm(N);
Rp3 = 2*N+randperm(N);
Rp4 = 3*N+randperm(N);
Rp5 = 4*N+randperm(N);
Rp6 = 5*N+randperm(N);
Rp7 = 6*N+randperm(N);
Rp8 = 7*N+randperm(N);

percT = round(0.9*N);                 % Number of data points in the training dataset
                                      % 90% of the total data.


% Creating the training matrix

XT = zeros(8*percT,Xc);

XT(1:percT,:) = X(Rp1(1:percT),:);          % Selecting randomly 90% of the data points.
XT(percT+1:2*percT,:) = X(Rp2(1:percT),:);
XT(2*percT+1:3*percT,:) = X(Rp3(1:percT),:);
XT(3*percT+1:4*percT,:) = X(Rp4(1:percT),:);
XT(4*percT+1:5*percT,:) = X(Rp5(1:percT),:);
XT(5*percT+1:6*percT,:) = X(Rp6(1:percT),:);
XT(6*percT+1:7*percT,:) = X(Rp7(1:percT),:);
XT(7*percT+1:8*percT,:) = X(Rp8(1:percT),:);
%%%%%%



%% Plotting the Feature Space
figure
axes
hold all
grid on

IndX = 1;
IndY = 2;
IndZ = 3;

NT = percT;

plot3(XT(1:NT,IndX),XT(1:NT,IndY),XT(1:NT,IndZ), '.b','MarkerSize',10)
plot3(XT(NT+1:2*NT,IndX),XT(NT+1:2*NT,IndY),XT(NT+1:2*NT,IndZ), '.r','MarkerSize',10)
```

```
plot3(XT(2*NT+1:3*NT,IndX),XT(2*NT+1:3*NT,IndY),XT(2*NT+1:3*NT,IndZ), '.g','MarkerSize',10)
plot3(XT(3*NT+1:4*NT,IndX),XT(3*NT+1:4*NT,IndY),XT(3*NT+1:4*NT,IndZ), '.y','MarkerSize',10)
plot3(XT(4*NT+1:5*NT,IndX),XT(4*NT+1:5*NT,IndY),XT(4*NT+1:5*NT,IndZ), '.k','MarkerSize',10)
plot3(XT(5*NT+1:6*NT,IndX),XT(5*NT+1:6*NT,IndY),XT(5*NT+1:6*NT,IndZ), '.m','MarkerSize',10)
plot3(XT(6*NT+1:7*NT,IndX),XT(6*NT+1:7*NT,IndY),XT(6*NT+1:7*NT,IndZ), 'oc','MarkerSize',10)
plot3(XT(7*NT+1:8*NT,IndX),XT(7*NT+1:8*NT,IndY),XT(7*NT+1:8*NT,IndZ), '+r','MarkerSize',10)

set(gca,'fontsize',15)

legend({'Healthy Blades','25 mm Shorter','50 mm Shorter','100 mm Shorter','150 mm Shorter',...
   'Bent Blade','Two Blades','Scratched Blade'},'fontsize',20);



xlabel('PC1','fontsize',20)
ylabel('PC2','fontsize',20)
zlabel('PC3','fontsize',20)
%%%%%%



%% Searching the k nearest neighbours
% The F matrix assigns a label to the training data points
F(1:NT) = 1;                        % Healthy blades
F(NT+1:2*NT) = 2;                   % 25 mm shorter
F(2*NT+1:3*NT) = 3;                 % 50 mm shorter
F(3*NT+1:4*NT) = 4;                 % 100 mm shorter
F(4*NT+1:5*NT) = 5;                 % 150 mm shorter
F(5*NT+1:6*NT) = 6;                 % Bent blade
F(6*NT+1:7*NT) = 7;                 % Two blades
F(7*NT+1:8*NT) = 8;                 % Scratched blade

%% Number of test points
Ntest = N-NT;

% Creating the test dataset
XTest = zeros(8*Ntest,Xc);

% Selecting the points that were not included in the training dataset
XTest(1:Ntest,:) = X(Rp1(percT+1:N),:);
XTest(Ntest+1:2*Ntest,:) = X(Rp2(percT+1:N),:);
XTest(2*Ntest+1:3*Ntest,:) = X(Rp3(percT+1:N),:);
XTest(3*Ntest+1:4*Ntest,:) = X(Rp4(percT+1:N),:);
XTest(4*Ntest+1:5*Ntest,:) = X(Rp5(percT+1:N),:);
XTest(5*Ntest+1:6*Ntest,:) = X(Rp6(percT+1:N),:);
XTest(6*Ntest+1:7*Ntest,:) = X(Rp7(percT+1:N),:);
XTest(7*Ntest+1:8*Ntest,:) = X(Rp8(percT+1:N),:);

%% Obtaining the k nearest neighbours
[IDX,Dis] = knnsearch(XT(:,1:3),XTest(:,1:3),'k',5);
```

```
N_IDX = size(IDX,1);

%% Assigning a label based on the nearest neighbours
for i=1:N_IDX

   Fhat(i) = mode(F(IDX(i,:)));

end

%% Assining a class label to the test points
FF(1:Ntest) = 1;
FF(Ntest+1:2*Ntest) = 2;
FF(2*Ntest+1:3*Ntest) = 3;
FF(3*Ntest+1:4*Ntest) = 4;
FF(4*Ntest+1:5*Ntest) = 5;
FF(5*Ntest+1:6*Ntest) = 6;
FF(6*Ntest+1:7*Ntest) = 7;
FF(7*Ntest+1:8*Ntest) = 8;



%% Confusion matrix. Comparing the known classes to the predicted ones
[C,order] = confusionmat(FF',Fhat)
%%%%%%

%% Plotting the confusion matrix
num_class = 8;

mat = C./Ntest.*100;               % A 8-by-8 matrix of random values from 0 to 1 find percentage
format('bank')
figure,imagesc(mat);               % Create a colored plot of the matrix values
colormap(flipud(gray));            % Change the colormap to gray (so higher values are
                                   % black and lower values are white)

textStrings = num2str(mat(:),'%0.2f');           % Create strings from the matrix values
                                                 % with percentage symbol
textStrings = strtrim(cellstr(textStrings));     % Remove any space padding
[x,y] = meshgrid(1:num_class);                   % Create x and y coordinates for the strings
hStrings = text(x(:),y(:),textStrings(:),...     % Plot the strings
            'HorizontalAlignment','center');
midValue = mean(get(gca,'CLim'));                % Get the middle value of the color range
textColors = repmat(mat(:) > midValue,1,3);      % Choose white or black for the
                                                 % text color of the strings so
                                                 % they can be easily seen over
                                                 % the background color

set(hStrings,{'Color'},num2cell(textColors,2),'fontsize',20);          % Change the text colors
```

```
set(gca,'XTick',1:num_class,...                         % Change the axes tick marks
        'XTickLabel',{'Healthy Blades','25 mm shorter','50 mm Shorter','100 mm Shorter','150 mm
shorter','Bent Blade','Two Blades','Sand'},...          %  and tick labels
        'YTick',1:num_class,...
        'YTickLabel',{'Healthy Blades','25 mm shorter','50 mm Shorter','100 mm Shorter','150 mm
shorter','Bent Blade','Two Blades','Sand'},...
        'TickLength',[0 0],'fontsize',20);

format('short')
%%%%%%
```

Appendix B Publication List

- Crespo-Ballesteros, M.; Antoniou, M. (2014). “Wind Turbine Radar Signature Analysis in the Near-Field,” International Radar Conference, Lille, France, Oct. 2014

- Crespo-Ballesteros, M.; Antoniou, M. (2015). “Automatic Classification of Wind Turbine Structural Faults Using Doppler Radar: Proof of concept study,” IEEE Radar Conference, Arlington, USA, May 2015.

- Crespo-Ballesteros, M.; Antoniou, M.; Cherniakov, M. “Wind Turbine Blade Radar Signature in the Near-Field: Theory and Experimental Confirmation,” IEEE Transactions on Aerospace and Electronic Systems, Feb. 2017.